Molecular Beam Laser Spectroscopy of the Molecules Cu_2, CuAg and Ag_2

by

Andrew Moray James

A thesis presented for the degree of
Doctor of Philosophy in the
Faculty of Science at the
University of Edinburgh
1990

Declaration

This thesis was composed by myself and is based on work carried out whilst a member of the molecular beam laser spectroscopy group in the Chemistry Department at the University of Edinburgh.

In memory of my parents.

"Publish and be damned !"
-Arthur Wellesley, First Duke of Wellington

Abstract

Transition metal clusters were generated by laser vaporisation in the throat of a pulsed supersonic expansion. Detection was accomplished by pulsed laser photoionisation in the source of a time-of-flight mass spectrometer (University of Edinburgh), or by laser-induced fluorescence (LIF) using a ring dye laser (National Research Council of Canada, Ottawa).

A variety of metal cluster systems from the first and second transition periods were probed using laser photoionisation time-of-flight mass spectrometry.

Resonant two photon ionisation (R2PI) spectroscopy was performed on the A←X system of CuAg, and the A state conclusively demonstrated to have 0^+ symmetry. Rotational analysis yielded r_e'' = 2.3664(71) Å and r_e' = 2.508(14) Å for $^{63}Cu^{107}Ag$. The collision-free lifetime for the v = 0 level of the A state was determined to be 32 ± 2 ns. Congested ultraviolet band systems lying at twice the A←X transition energy were probed using vibronic R2PI spectroscopy.

Ring dye laser fluorescence spectroscopy was used to probe the A←X system of Ag_2 with Doppler-limited resolution. A rotational analysis gave r_e'' = 2.53118(28) Å and r_e' = 2.65537(31) Å.

The adiabatic ionisation potentials of Cu_2 and CuAg were determined using threshold ionisation spectroscopy (TIS) to be 7.90426(42) eV and 7.78058(54) eV respectively. The dissociation energies of the ion ground states were accordingly determined to be 1.83(08) eV (Cu_2^+) and 1.56(10) eV ($CuAg^+$). Rich autoionisation structure in the post-threshold region was observed for both these systems.

Electronic excitation in the Group 1b transition metal dimers is discussed in the light of the R2PI, LIF and TIS results.

Acknowledgements

None of the following would have been possible without the help of a number of people.

Firstly, I must thank the Carnegie Trust for the Universities of Scotland for the award of a three-year research studentship. During the fourth year of my Ph. D., I was funded largely by a charitable endowment from the Bankers' Benevolent Fund, of Cheapside, London, to whom I am particularly indebted.

I thank my supervisor, Dr. Pat Langridge-Smith, for nurturing my interest in molecular spectroscopy, and for his support and enthusiasm over the last four years.

Special thanks are extended to two former co-workers. Dr. Andrew Butler developed and maintained the control software for the experiments described here, and was always willing to incorporate modifications. Dr. Peter Cartwright adopted an exemplary approach to the theory and practice of these experiments, which I have tried to emulate wherever possible.

I should like to express my gratitude to Drs. Peter Hackett and Benoit Simard for their invitation to work for a month at the National Research Council of Canada, Ottawa, a sojourn which proved valuable and productive. Also, to Dr. Claire Callender for her generous hospitality during my visit there.

In Edinburgh, Dr. George Lemire provided invaluable electronics expertise at a crucial juncture, and Dr. Trevor Ridley was always willing to advise and assist

with the finer details of high resolution dye laser operation. Many thanks to both.

Dr. George Keenan and Dr. Kevin Costello, who were responsible for the design of the Reflectron instrument, are gratefully acknowledged for furnishing technical details. Jim MacDonald is thanked for his assistance with some of the experiments described here.

Of the workshop staff, Stewart Mains and John Ashfield (Mechanical); and Alan King, Gordon Waugh and Duncan McLean (Electronics) are thanked for providing an excellent construction and maintenance service.

Moving to the realm of theory, I am indebted to Dr. Kenneth Lawley for his time and constructive criticism of Chapters 5-8. Also, thanks to Phil Jewsbury for providing working versions of the Franck Condon factor programs described in Appendix D.

Finally, I should like to thank my girlfriend, Kathleen, for her confidence-boosting support and encouragement, even during the darkest hours of failed experiments.

List of Tables

Table 4.1 MB1 linear TOFMS performance 96

Table 4.2 MB2 reflectron schematic 110

Table 5.1 CuAg spectroscopic constants by thermal emission spectroscopy 142

Table 5.2 Bandhead positions and vibrational constants for the A←X system of CuAg 156

Table 5.3 Line positions and rotational constants for the CuAg A←X (0-0) band 172

Table 5.4 Line positions and rotational constants for the CuAg A←X (1-0) band 174

Table 5.5 Isotope shifts in the A←X system of CuAg 176

Table 5.6 Rotational constants for the A and X states of CuAg 178

Table 5.7 Experimental and theoretical spectroscopic constants of the $X(^1\Sigma^+)$ state of $^{63}Cu^{107}Ag$ 186

Table 5.8 Atomic and ionic dissociation limits of Cu and Ag 190

Table 5.9 (a) $^{63}Cu^{107}Ag$ ultraviolet band positions 205

Table 5.9 (b) $^{63}Cu^{109}Ag$ and $^{65}Cu^{107}Ag$ ultraviolet band positions 207

Table 6.1 Threshold ionisation measurements on $^{63}Cu^{107}Ag$ 250

Table 6.2 Autoionising Rydberg states of $^{63}Cu^{107}Ag$ 263

Table 6.3 Threshold ionisation measurements on $^{63}Cu^{63}Cu$ 274

Table 7.1 Spectroscopic constants of the Ag_2 molecule 285

Table 7.2 Observed and calculated rotational line positions for the $^{107}Ag^{109}Ag$ $A(0_u^+)\leftarrow X(^1\Sigma_g^+)$ (0-0) band 310

Table 7.3 Rotational constants for the A and X states of $^{107}Ag^{109}Ag$ 314

Table 7.4 Theoretical determinations of the Ag_2 ground state spectroscopic parameters 316

Table 7.5 Lowest ^2P and ^2D limits of silver 323

Table 8.1 Orbital radii of the Group 1b atoms 332

Table 8.2 Spectroscopic constants for the Cu,Ag dimer ground states 333

Table 8.3 Ionisation potentials of the Cu,Ag dimers 337

Table 8.4 Dissociation energies of excited Cu,Ag dimers 342

Table 8.5 Spectroscopic constants of Au-containing dimers 346

List of Figures

Figure 2.1 "Hole burning" in a helium pulse profile 15

Figure 2.2 Maxwellian velocity distribution for helium at 5 K and 300 K 18

Figure 2.3 Photoionisation schemes 21

Figure 2.4 TOF mass spectra of Mo_2 isotopomers 32

Figure 2.5 Dye laser cavity configurations 34

Figure 3.1 Schematic of the MB1 apparatus 39

Figure 3.2 Schematic of the MB2 apparatus 43

Figure 3.3 Detail of the cluster source 46

Figure 3.4 Ion extraction optics for the linear TOF mass spectrometer 50

Figure 3.5 Ion extraction optics and mirror for the RETOF mass spectrometer 51

Figure 3.6 Block diagram of the experimental control hardware 62

Figure 3.7 Line driver circuit diagram 64

Figure 3.8 Timing delays in a typical cluster experiment 69

Figure 4.1 Prototypical time-of-flight mass spectrometers 74

Figure 4.2 Mass transmission function of the MB2 linear TOF mass spectrometer 91

Figure 4.3 Ion flight time vs. position of formation in the source of the MB1 linear TOF instrument 93

Figure 4.4 Ion flight time vs. initial ion velocity for the MB1 linear TOF instrument 94

Figure 4.5 TOF mass spectrum of molybdenum isotopes recorded on the MB1 linear instrument 95

Figure 4.6 Contour plot of the potential distribution in the source region of the MB1 linear instrument 97

Figure 4.7 Schematic of the reflecting field TOF mass spectrometer 100

Figure 4.8 (a) TOF mass spectrum of niobium clusters recorded on the MB2 linear instrument 107

Figure 4.8 (b) TOF mass spectrum of niobium clusters recorded on the MB2 reflectron instrument 108

Figure 4.9 TOF mass spectrum of molybdenum isotopes recorded on the MB2

reflectron instrument 111
Figure 4.10 Contour plot of the potential distribution in the source region of the MB2 reflectron instrument 112
Figure 4.11 Contour plot of the potential distribution in the source region of the MB2 reflectron ion mirror 113
Figure 4.12 (a) TOF mass spectrum of copper clusters optimised for Cu_9^+ 118
Figure 4.12 (b) TOF mass spectrum of copper clusters optimised for high mass clusters 119
Figure 4.13 TOF mass spectrum of silver clusters 120
Figure 4.14 TOF mass spectrum of copper- and silver-containing clusters 121
Figure 4.15 TOF mass spectrum of aluminium clusters 129
Figure 4.16 (a) TOF mass spectrum of niobium clusters recorded using 266 nm ionisation 132
Figure 4.16 (b) TOF mass spectrum of niobium clusters recorded using 193 nm ionisation 133
Figure 4.17 TOF mass spectrum of iron clusters 134
Figure 4.18 TOF mass spectrum of nickel clusters 135
Figure 5.1 TOF mass spectrum of CuAg isotopomers 150
Figure 5.2 (a) Vibronic R2PI spectrum of the A←X system of $^{63}Cu^{107}Ag$ 152
Figure 5.2 (b) Vibronic R2PI spectrum of the A←X system of $^{63}Cu^{109}Ag$ and $^{65}Cu^{107}Ag$ 153
Figure 5.3 Excitation decay profile for the $v_A = 0$ level of $^{63}Cu^{107}Ag$ 157
Figure 5.4 (a) Rotationally-resolved R2PI spectrum of the (0-0) band of the A←X system of $^{63}Cu^{107}Ag$ 160
Figure 5.4 (b) Rotationally-resolved R2PI spectrum of the (0-0) bands of the A←X system of $^{63}Cu^{109}Ag$ and $^{65}Cu^{107}Ag$ 161
Figure 5.4 (c) Rotationally-resolved R2PI spectrum of the (0-0) band of the A←X system of $^{65}Cu^{109}Ag$ 162
Figure 5.4 (d) Experimental and simulated spectra of the (0-0) band of the A←X system of $^{63}Cu^{107}Ag$ 163
Figure 5.5 (a) Rotationally-resolved R2PI spectrum of the (1-0) band of the A←X system of $^{63}Cu^{107}Ag$ 164
Figure 5.5 (b) Rotationally-resolved R2PI spectrum of the (1-0) bands of the

A←X system of $^{63}Cu^{109}Ag$ and $^{65}Cu^{109}Ag$ 165

Figure 5.5 (c) Rotationally-resolved R2PI spectrum of the (1-0) band of the A←X system of $^{65}Cu^{109}Ag$ 166

Figure 5.5 (d) Experimental and simulated spectra of the (1-0) band of the A←X system of $^{63}Cu^{107}Ag$ 167

Figure 5.6 Nonrelativistic Hartree-Fock orbital energies for the $^2S_{1/2}$ states of copper and silver 183

Figure 5.7 RKR potential curves for CuAg 189

Figure 5.8 1 colour, 3 photon ionisation spectrum of the A←X system of $^{63}Cu^{107}Ag$ 200

Figure 5.9 REMPI processes in the 3 photon ionisation of CuAg 201

Figure 5.10 (a) 1 colour R2PI spectrum of ultraviolet systems of $^{63}Cu^{107}Ag$ 203

Figure 5.10 (b) 1 colour R2PI spectrum of ultraviolet systems of $^{63}Cu^{109}Ag$ and $^{65}Cu^{107}Ag$ 204

Figure 5.11 (a) Power dependence plot for the 3 photon ionisation of the CuAg A←X (3-0) band 211

Figure 5.11 (b) Power dependence plot for the 3 photon ionisation of the CuAg A←X (4-0) band 212

Figure 6.1 Ionisation threshold lowering by a static field 229

Figure 6.2 PIE curve for $^{63}Cu^{107}Ag$, ionising from $v_A = 0$ in a static field of $\simeq$ 270 V cm^{-1} 235

Figure 6.3 CuAg ionisation threshold as a function of applied static field 238

Figure 6.4 High voltage pulser circuit schematic 241

Figure 6.5 Temporal profile of the high voltage pulse 243

Figure 6.6 PIE curve for $^{63}Cu^{107}Ag$, ionising from $v_A = 0$ in zero static field (Δt = 300 ns) 245

Figure 6.7 PIE curve for $^{63}Cu^{107}Ag$, ionising from $v_A = 0$ in zero static field (Δt = 60 ns) 248

Figure 6.8 PIE curve for $^{63}Cu^{107}Ag$, ionising from $v_A = 1$ in zero static field (Δt = 300 ns) 251

Figure 6.9 Franck Condon factors for the CuAg $v_+ = 0 \leftarrow v_A = 0$ transition 259

Figure 6.10 Vibrational autoionisation schematic 261

Figure 6.11 Rotationally-resolved R2PI spectrum of the (1-0) band of the A←X

system of $^{63}Cu^{63}Cu$ 271

Figure 6.12 PIE curve for $^{63}Cu^{63}Cu$, ionising from $v_A = 1$ in zero static field ($\Delta t = 60$ ns) 272

Figure 6.13 Franck Condon factors for the Cu_2 $v_+ = 0,1 \leftarrow v_A = 1$ transitions 275

Figure 6.14 Electronic autoionisation schematic 277

Figure 7.1 Schematic of the molecular beam-ring dye laser apparatus 290

Figure 7.2 Ring dye laser optical layout 294

Figure 7.3 Ring laser LIF spectrum of the (0-0) band of the A←X system in Ag_2 (P-branch) 305

Figure 7.4 Ring laser LIF spectrum of the (0-0) band of the A←X system of Ag_2 (R-bandhead) 306

Figure 7.5 RKR potential curves for Ag_2 321

Figure A.1 One colour R2PI spectrum of the E←X system of Al_2 352

Table of Contents

1 Introduction 1
1.1 Outline of thesis 9
References 10
2 Experimental Principles: Essential Background 12
2.1 The experimental cycle 12
2.2 The laser vaporisation process 13
2.3 Supersonic expansion of clusters 16
2.4 Laser photoionisation processes 19
2.5 Spectral linewidths 26
2.6 Fluorescence versus photoionisation spectroscopy 29
References 37
3 Cluster Photoionisation Experimental Details 38
3.1 MB1 vacuum system 38
3.2 MB2 vacuum system 42
3.3 Cluster source 45
3.4 TOFMS ion optics 49
3.5 Ion signal detection 53
3.6 Laser systems 54
3.6.1 JK HyperYAG HY750 Nd:YAG laser 54
3.6.2 Quanta Ray Nd:YAG-pumped dye laser system 55
3.6.3 Lumonics TE-861-T excimer laser 57
3.6.4 Lambda Physik excimer pumped dye laser system 58
3.7 Experimental control and data acquisition 60
3.7.1 Control hardware 61
3.7.2 Control software 67
References 72
4 Time-of-Flight Mass Spectrometry of Elemental Clusters 73
4.1 Introduction 73
4.2 Resolution 77
4.2.1 Spatial resolution 77
4.2.2 Kinetic energy resolution 78
4.2.3 Time resolution 79
4.2.4 Detector Response Time 80
4.2.5 Space charge effects 80
4.3 The Wiley-McLaren spatial focusing TOFMS 81
4.3.1 Spatial focusing conditions 81
4.3.2 Energy resolution 86
4.3.3 Overall resolution: practical design considerations 87
4.4 The Mamyrin reflecting field TOFMS 99
4.4.1 Energy focusing in the RETOFMS 99
4.4.2 Overall resolution and system performance 105
4.5 Ion transmission function 115
4.6 Photoionisation TOF mass spectra of Group 1b metal clusters 117
4.7 Photoionisation TOF mass spectra other transition metal clusters 130
References 139
5 Photoionisation Spectroscopy of the $A(0^+) \leftarrow X(^1\Sigma^+)$ System of CuAg 140

5.1 Introduction 140
5.2 Experimental considerations 144
5.2.1 Copper-silver alloy rod fabrication 145
5.2.2 Experimental setup for R2PI spectroscopy 146
5.3 R2PI spectroscopy of the A←X system in CuAg 149
5.3.1 Vibronic spectroscopy 149
5.3.2 Lifetime measurements 155
5.3.3 Rotationally-resolved spectroscopy 159
5.3.4 Rovibronic spectral simulations 177
5.4 Discussion 181
5.4.1 The X($^1\Sigma^+$) state 181
5.4.2 The A(0^+) excited state 185
5.4.3 Conclusion 197
5.4.4 Results of Morse and co-workers 197
5.5 Observation of new ultraviolet band systems in CuAg 198
References 214
6 Threshold Photoionisation Spectroscopy of CuAg and Cu_2 216
6.1 Introduction 216
6.2 Autoionisation processes 224
6.2.1 Electronic autoionisation 224
6.2.2 Vibrational autoionisation 225
6.2.3 Rotational autoionisation 227
6.3 Field ionisation 228
6.4 Threshold photoionisation spectroscopy of CuAg 232
6.4.1 Experimental details 233
6.4.2 Field dependence of the ionisation threshold 234
6.4.3 Experimental modifications for zero-field threshold ionisation studies 240
6.4.4 Zero-field threshold ionisation measurements on CuAg 244
6.4.5 Assignment of the adiabatic ionisation threshold in CuAg 252
6.4.6 The dissociation energy of $CuAg^+$ 264
6.5 Threshold photoionisation spectroscopy of Cu_2 265
6.5.1 Zero-field threshold ionisation measurements on Cu_2 270
References 279
7 Laser Induced Fluorescence Spectroscopy of the A(0_u^+)←X($^1\Sigma_g^+$) System in Ag_2 282
7.1 Introduction 282
7.2 Experimental setup 289
7.2.1 Vacuum system 291
7.2.2 Cluster source 291
7.2.3 Ring dye laser system 292
7.2.4 Fluorescence detection and experimental control 299
7.3 Results and Data Analysis 304
7.4 Discussion 315
7.4.1 The X($^1\Sigma_g^+$) ground state 315
7.4.2 The A(0_u^+) excited state 319
References 326
8 Bonding in the group 1b transition metal dimers 328
8.1 Bonding in copper and silver dimers 331

8.1.1 The $X(^1\Sigma_g^+)$ ground states 331
8.1.2 Adiabatic ionisation potentials 335
8.1.3 Dissociation energies of neutral and ionic ground states 336
8.1.4 Excited states 341
8.2 Bonding in gold-containing dimers 344
8.3 Critical Evaluation 348
References 350
A The $E(^3\Sigma_g^-)$←$X(^3\pi_u)$ system of Al_2 **351**
References 353
B Generation of electrostatic potential maps **354**
References 356
C The RKR method for generating potential curves **357**
References 358
D Calculation of Franck Condon factors **359**
References 361
E Nuclear spin statistics **362**
References 364
F Courses and Conferences Attended **365**

Chapter 1
Introduction

In the context of this thesis, a "metal cluster" is defined as an unligated aggregate of metal atoms, M_N, in the 2-200 atom size regime. Much of the work which will be described here concerns the extreme lower limit of this definition: transition metal dimers. The reader may immediately query the misappropriation of the term "cluster" to describe an entity which only barely scrapes into the category of "molecule". However, it can be justified on the grounds that the dimer represents a prototypical system, many of whose characteristics appear, to varying extents, in larger clusters. A gradation in physical and chemical properties is observed with increasing size, as the growing clusters gradually lose their molecular identity and start to exhibit properties characteristic of the bulk phase. A classic example of these trends is the variation in ionisation potential (IP) with increasing cluster size. For typical metal systems, the ionisation potential drops off fairly smoothly, reaching a limiting value of the bulk work function. [1]- [3] Discontinuities occur most noticeably only for smaller clusters ($N < 50$), reflecting the existence of discrete electronic structure. [4]

Small clusters of the transition metals are of particular interest due to the presence of filled, or partially filled d shells. These shells are considerably contracted with respect to the valence shell as one moves across a transition period, and thus they interact to a varying degree upon bond formation. Much of the catalytic activity in the transition metals stems from the involvement of these d orbitals as electron donors and acceptors. Spectroscopic investigation of dimeric and trimeric transition metal molecules can yield much useful

information on d orbital participation in the metal-metal bond. For larger clusters, much of the impetus towards probing their electronic structure stems from the perceived similarities between them and the metallic aggregates believed to be of central importance in catalysis. [5] In fact, gas phase transition metal clusters have been suggested as the ultimate catalytic models, providing an ultra-clean surface on which chemisorption may occur.

Modelling the catalytic action of real surfaces or ligated polynuclear cluster complexes at an *ab initio* molecular level exceeds the scope of theory at present. However, the problem can be simplified by spectroscopic and theoretical studies of bare transition metal clusters in the gas phase: information may be obtained on the properties of the true metal-metal bond in the absence of perturbing effects caused by neighbouring ligands or molecules. Specifically, the bonding interactions involving catalytically-significant frontier orbitals, especially the d shell, may be investigated.

Historically, while there was clear motivation for studying the physical and chemical properties of transition metal clusters, the field remained something of a backwater until the start of the last decade. This was due to the refractory nature of the transition metals, and the consequent difficulty of preparing clusters of them. Conventional sources of low vapour pressure species, such as heated ovens, were restricted largely to lower boiling metals such as the alkalis. [7] Here, the vapour pressure is sufficiently high for the atomic species to be expanded through an orifice to form a molecular beam. Use of an inert carrier gas facilitates cluster growth, and cools the molecules adiabatically during expansion, presenting the possibility of making molecular beams of large clusters with low

internal temperatures. However, for the more refractory transition metals, cooling of the oven source by the carrier itself leads to unacceptably low vapour pressures, and inhibits cluster growth beyond the dimer. Despite these limitations, the dimers Ag_2 and CuAg were generated using pure oven sources, and the emissions from thermally populated electronic excited states were a useful initial guide in the spectroscopic experiments performed here (see Chapters 5 and 7). Thermal sources have proved more useful in the determination of metal cluster dissociation energies using Knudsen effusion mass spectrometry. [8]

The use of furnace emission spectroscopy to investigate transition metal dimers is not generally very informative. The low Boltzmann population in all but the lowest excited states reduces the spectral range of systems which can be observed with any intensity in emission. The complementary technique of absorption spectroscopy offers more scope in this respect, but is hampered by its inherent low sensitivity. Discharge sources can circumvent the problems of low excited state populations, but transition metal dimers are not easily produced using this method, and spectral interpretation is complicated by congestion.

Clusters trapped in cryogenic rare gas matrices persist for long periods and are thus amenable to examination by insensitive spectroscopic techniques. For example, extended X-ray absorption fine structure (EXAFS) [9]; electron spin resonance (ESR) [10]; electronic absorption [11]; magnetic circular dichroism (MCD) [12] and Raman spectroscopy [13] have all been employed to probe small transition metal clusters trapped in inert gas matrices. Matrix isolation techniques can trap out refractory metal atoms (usually formed by electric

discharge) at a low temperature. With the relatively long aggregation times and cold matrix environment, the probability of producing clusters larger than the dimer is enhanced.

However, matrix techniques suffer from a number of severe disadvantages which limit their usefulness when applied to metal clusters systems. One of the principal difficulties rests with the problem of assigning observed spectroscopic features to particular carriers. The lack of mass selectivity is especially problematic when an uncharacterised distribution of metal clusters is entrapped. Arduous and not always reliable control experiments are required to assign the observed signals to carriers. Further problems arise because of the interaction between the clusters and the host matrix. Perturbations are introduced which can shift band origins by several 1000 cm^{-1}, and features become broad due to interactions with matrix lattice vibrations. Spectroscopic detail is further obscured by the trapping of guest molecules in more than one matrix site, and removal of electronic degeneracy by lower symmetry host environments results in splitting of bands. The utility of matrix methods as applied to metal clusters is therefore limited. ESR spectroscopy is probably the most worthwhile matrix technique with its ability, through hyperfine isotopic interactions, to provide definitive transition assignments. ESR can yield a large number of spectroscopic parameters, enabling state symmetries and orbital characteristics to be determined. It is, of course, limited to paramagnetic species.

Thus at the beginning of the 1980s, transition metal cluster spectroscopy was a tantalising field, not yet adequately served by experiment. The deficiencies of matrix spectroscopy were such that theoretical methods exceeded the capabilities

of experimentation to provide verification. The subject was dragged out of the doldrums largely by the development of laser vaporisation-supersonic expansion techniques by Smalley and co-workers. [14] Here, a high power pulsed laser is used to locally heat a metal target to plasma temperatures. The vapour produced is quenched and entrained in an inert carrier to promote clustering, prior to adiabatic expansion into vacuum to generate a cold cluster beam. The marriage of these techniques led to a veritable renaissance of metal dimer spectroscopy. [15] The problem of refractory sources was immediately overcome by the rapid and intense heating possible with a pulsed laser. Collisional removal of metal-metal bond formation energy by the carrier gas facilitated the formation of intense beams of large clusters, as in the hot oven alkali clustering experiments. The prospects for spectroscopy of small clusters were also greatly enhanced. Molecules cooled to the lowest rovibronic states during expansion could be probed using fluorescence and photoionisation spectroscopy, with the analysis considerably simplified by the low internal temperatures. Moreover, the use of mass selective photoion detection eliminates the problems of overlapping spectra due to different isotopomers. A host of work on dimers of the first transition period has appeared, with the groups of Smalley [16] [17] and Morse [20] [21] prominent. At the time of writing, experiment has regained the lead over theory, with a substantial body of data on electronically excited transition metal dimers not yet tackled by theory. Trimeric and higher systems have proved more elusive, with definitive spectroscopic investigations of only Cu_3 [22]- [24] and Ag_3. [25]

While molecular spectroscopists and *ab initio* theoreticians continue to derive

much satisfaction from the small cluster end of the scale, the surface science and solid state physics communities are greatly intrigued by larger clusters in the range N = 3-1000. Conventional electronic spectroscopy of neutral clusters larger than the dimer has proved difficult, due to the increasingly high density of states, and the removal of excitation energy by fast relaxation processes. Conspicuously greater success in studying larger clusters has been achieved by photoelectron spectroscopies involving electron detachment from cluster negative ions. [26] Here, information on the developing band structure may be obtained directly by photodetachment of electrons from valence s and core d orbitals over a range of cluster sizes. [27] This field is complimented by ionisation potential measurements on the corresponding neutral clusters, which can also reveal information on the development of electronic shell structure. [1]- [3] [28] *Ab initio* treatments have developed along parallel lines, and some suggest from density of states calculations that the electronic properties of clusters closely resemble those of the bulk when N is as low as 10. [29]

The larger transition metal clusters have also been the subject of extensive studies on their size-dependent chemical reactivity. Laser-vaporisation prepared clusters are reacted with catalytically-important adsorbates such as H_2 and CO, detecting the chemisorption products using time of flight mass spectrometry. Much elegant experimental work has been carried out, [30]- [34] although thus far only tenuous links with models of chemical reactivity have been made.

At this juncture, the "traditional" field of high resolution transition metal dimer spectroscopy is nearing maturity, although there are many unsolved problems. An extension of high level theoretical calculations to excited states would be very

welcome. The other areas, while hardly in their infancy, have still to be matched by theory. The development of mass selective beam instruments and applications of high mass resolution ion cyclotron resonance methods should open up new avenues for probing larger clusters. In the near future, it may be possible to select clusters of a particular mass, neutralise them by charge exchange, and deposit them on surfaces for direct structural probing by techniques such as Scanning Tunnelling Microscopy.

The foregoing discussion pointed up the attractions of studying d orbital interactions in transition metal clusters. Why then do we propose to investigate transition metal dimers of the Group 1b coinage triad? Copper, silver and gold, with their $(n-1)d^{10}s^{1}$ ground state electronic configurations, bond primarily through valence s atomic orbitals. The fully-occupied and contracted d orbitals behave as cores, with only a minimal involvement in bonding. These lustrous metals seem positively dull alongside species such as V (d^3s^2) and Cr (d^5s^1) which are bristling with partially-occupied d orbitals capable of strong bonding interactions. Nevertheless, there are many examples of catalytic action in the coinage triad, most notably the role which silver clusters play in the formation of photographic latent images. [35]

On a more fundamental level, justification for studying the coinage dimers comes from the sheer electronic complexity of transition metal dimers with open d shells. A good example of this is furnished by comparing the lowest electronic states of nickel and copper dimer, which have the ground state configurations $d^{18}(s\sigma)^2$ and $d^{20}(s\sigma)^2$ respectively. There are calculated to be $\simeq$ 30 excited states of Ni_2 within 1 eV of the ground state, [36] which has not yet been

definitively identified. [17] The multiplicity of states arises from the numerous ways in which the two d core holes may be correlated in the molecule. In Cu_2, by contrast, the first excited state lies $\simeq 2$ eV away, [37] and the density of states is very sparse, facilitating spectroscopic interpretation. Theoreticians are better able to cope with systems where the d orbital interaction is both weak and does not lead to such a high multiplicity of electronic states. In the coinage dimers, the d cores may be treated outwith the valence space, a valuable simplification permitting ready extension to higher clusters. An N-electron problem is formulated, where N is the number of atoms in the cluster. Thus dimers of the coinage triad may be regarded as model systems which can be used to test *ab initio* methodology. Any failure to provide satisfactory agreement with these, the simplest valence-bonded transition metal clusters, indicates that the model is likely to fail generally.

Our specific interest in the silver dimer molecule stems partly from a desire on the part of theoreticians to have an experimental determination of the equilibrium internuclear separation in the ground state. [38] This has hitherto eluded experimentalists because of the small rotational constants. Similar motivation applies in the case of the heteronuclear dimer CuAg, where both experimental and theoretical data is even more scarce. On a broader note, the scientific literature currently lacks many cogent theoretical descriptions of electronic excitation in transition metal dimers. The initiation of a comprehensive study of the spectroscopy of electronically-excited Group 1b dimers and their ions will hopefully stimulate theoreticians to redouble their efforts in this area.

1.1 Outline of thesis

The following structure has been adopted:

Chapter 2 discusses the principles underlying cluster generation, supersonic expansion, laser induced fluorescence and photoionisation spectroscopy.

Chapter 3 contains a description of the experimental equipment used to carry out the photoionisation experiments described in Chapters 4-6.

Chapter 4 is concerned with the principles of time of flight mass spectrometry, and describes various cluster generation experiments.

Chapter 5 centres mainly on the rotationally-resolved two colour photoionisation spectroscopy of the A←X system in CuAg. Some additional work on ultraviolet band systems of this molecule is also described.

Chapter 6 describes the measurements of adiabatic ionisation potentials of CuAg and Cu_2 using two colour threshold photoionisation spectroscopy, and the evidence for autoionisation structure in the post-threshold region.

Chapter 7 discusses the Doppler-limited laser fluorescence spectroscopy of the A←X system in Ag_2, carried out at the National Research Council of Canada, Ottawa.

Chapter 8 draws together the material presented in the earlier chapters with a comparison of spectroscopic properties of Cu_2, Ag_2 and CuAg. In addition, gold-containing coinage dimers are compared with the Cu,Ag trio.

References

[1] Rohlfing E. A., Cox D. M., Kaldor, Chem. Phys. Lett., **99**, p 161, (1983)

[2] Rohlfing E. A., Cox D. M., Kaldor A., J. Phys. Chem., **88**, p 4497, (1984)

[3] Whetten R. L., Zakin M. R., Cox D. M., Trevor D. J., Kaldor A., J. Chem. Phys., **85**, p 1697, (1986)

[4] Powers D. E., Hansen S. G., Geusic M. E., Michalopolous D. L., Smalley R. E., J. Chem. Phys., **78**, p 2866, (1983)

[5] Kaldor A., Cox D. M., Zakin M. R., Adv. Chem. Phys., **70(2)**, p 211, (1988)

[6] Moskovits M. (ed.), *Metal Clusters*, John Wiley, New York, 1986.

[7] Herrmann A., Leutwyler S., Schumacher E., Wöste L., Helv. Chim. Acta, **61**, p 453, (1978)

[8] Hilpert K., Ber. Bunsenges. Phys. Chem., **83**, p 161, (1979)

[9] Montano P. A., Zhao J., Ramanathan M., Shenoy G. K., Schulze W., Urban J., Chem. Phys. Lett., **164**, p 126, (1989)

[10] van Zee R. J., Weltner W. Jr., Chem. Phys. Lett., **162**, p 437, (1989)

[11] Ozin G. A., Huber H., McIntosh D., Mitchell S., Norman J. G. Jr., Noodleman L., J. Am. Chem. Soc., **101**, p 3504, (1979)

[12] Grinter R., Armstrong S., Jayasooriya U. A., McCombie J., Norris D., Spingall J. P., Far. Symp. Chem. Soc., **14**, p 94, (1980)

[13] Schulze W., Abe H., Far. Symp. Chem. Soc., **14**, p 87, (1980)

[14] Dietz T. G., Duncan M. A., Powers D. E., Smalley R. E., J. Chem. Phys., **74**, p 6511, (1981)

[15] Morse M. D., Chem. Rev., **86**, p 1049, (1986)

[16] Michalopolous D. L., Geusic M. E., Hansen S. G., Powers D. E., Smalley R. E., J. Phys. Chem, **86**, p 3914, (1982)

[17] Morse M. D., Hansen G. P., Langridge-Smith P. R. R., Zheng L.-S., Geusic M. E., Michalopolous D. L., Smalley R. E., J. Chem. Phys., **80**, p 5400, (1984)

[18] Rohlfing E. A., Valentini J. J., J. Chem. Phys., **84**, p 6560, (1985)

[19] Preuss D. R., Pace S. A., Gole J. L., J. Chem. Phys., **71**, p 3553, (1979)

[20] Fu Zh., Morse M. D., J. Chem. Phys., **90**, p 3417, (1989)

[21] Bishea G. A., Morse M. D., Chem. Phys. Lett., **171**, p 430, (1990)

[22] Morse M. D., Hopkins J. B., Langridge-Smith P. R. R., Smalley R. E., J. Chem. Phys., **79**, p 5316, (1983)

[23] Rohlfing E. A., Valentini J. J., Chem. Phys. Lett, **126**, p 113, (1986)

[24] Morse M. D., Chem. Phys. Lett., **133**, p 8, (1987)

[25] Cheng P. Y., Duncan M. A., Chem. Phys. Lett., **152**, p 341, (1988)

[26] Leopold D. G., Ho J., Lineberger W. C., J. Chem. Phys., **86**, p 1715, (1987)

[27] Cheshnovsky O., Taylor K. J., Conceicao J., Smalley R. E., Phys. Rev. Lett., **64**, p 1785, (1990)

[28] Martin T. P., Bergman T., Göhlich H., Lange T., Chem. Phys. Lett., **172**, p 209, (1990)

[29] Fripiat J. G., Chow K. J., Boudart M., Diamond J. R., Johnson K. H., J. Mol. Catal., **1**, p 59, (1975)

[30] Zakin M. R., Cox D. M., Kaldor A., J. Phys. Chem., **91**, p 5224, (1987)

[31] Zakin M. R., Cox D. M., Whetten R. L., Trevor D. J., Kaldor A., Chem. Phys. Lett., **135**, p 223, (1987)
[32] Parks E. K., Weiller B. H., Bechtold P. S., Hoffmann W. F., Nieman G. C., Pobo L. G., Riley S. J., J. Chem. Phys., **88**, p 1622, (1988)
[33] Whetten R. L., Cox D. M., Trevor D. J., Kaldor A., J. Phys. Chem., **89**, p 566, (1985)
[34] Morse M. D., Geusic M. E., Heath J. R., Smalley R. E., J. Chem. Phys., **83**, p 2293, (1985)
[35] Sayhun M. R. V., Photogr. Sci. Eng., **22**, p 317, (1978)
[36] Noell J. O., Newton M. D., Hay P. J., Martin R. L., Bobrowicz F. W., J. Chem. Phys., **73**, p 2360, (1980)
[37] Bondybey V. E., J. Chem. Phys., **77**, p 3771, (1982)
[38] Martin R. L., J. Chem. Phys., **86**, p 5027, (1989)

Chapter 2
Experimental Principles: Essential Background

This chapter describes the principles underlying jet spectroscopy of transition metal clusters. Detailed descriptions of the experimental equipment employed can be found in Chapters 3 and 7.

2.1 The experimental cycle

Transition metal molecules were generated by pulsed laser vaporisation of a metal target rod in the throat of a helium supersonic expansion produced by a pulsed valve. The carrier gas quenches the metal plasma and assists cluster growth by acting as the third body in the clustering process. The cluster-helium mixture is expanded into vacuum, forming an adiabatically-cooled molecular beam.

In this work, two widely-differing techniques were employed to probe electronically excited states in particular transition metal clusters. For the majority of the experiments carried out, a pulsed dye laser excited the species of interest in the presence of a second laser capable of achieving one photon ionisation out of the excited state. The photoions created were detected in a time of flight mass spectrometer (TOFMS). This experimental system was based at the University of Edinburgh. For the experiments described in Chapter 7, silver dimer molecules, also prepared using a laser vaporisation source, were excited using a ring dye laser, with the resulting fluorescence detected by an off-axis photomultiplier tube. These molecular beam LIF experiments were performed at

the National Research Council of Canada, Ottawa.

In both cases the experiments were run in fully-pulsed mode at a rate of 10 experimental timing cycles (of vaporisation-signal acquisition) per second. In the case of the LIF experiments, the ring dye laser provided continuous excitation of the molecular beam, with fluorescence detection synchronised to the laser vaporisation pulse.

2.2 The laser vaporisation process

Laser irradiation of the surface of a metal target can lead to ablation of material in the liquid, gaseous or plasma phases, depending on the power density of the laser pulse employed. Several distinct material removal processes have been identified by Ready. [1] Below 10^5 W cm^{-2}, the dominant mechanism is melting of the surface accompanied by ejection of liquid droplets. In the region 10^6-10^8 W cm^{-2}, material is ablated mainly as vapour, while still higher powers result in a plasma pluming out from the surface.

Excimer and Q-switched Nd:YAG lasers have been used extensively as vaporisation sources. The use of these short pulse duration lasers (typically 10-25 ns pulsewidth) to generate high laser powers does not at first appear to be the optimum solution. Only a small amount of metal is vaporised by the leading edge of such a short pulse. The dense vapour cloud, strongly heated by the following portion of the pulse, soon becomes ionised and forms an opaque, superheated plasma. This shields the surface from further ablation by the remainder of the pulse. The plasma, in which the temperature may be many

thousands of degrees above the boiling point of the metal, must be quenched completely by the carrier gas before the nucleation process can occur with any probability of success.

However, long pulses (100-1000 μs) ablate mainly liquid droplets rather than vapour. These droplets serve as nucleation centres for any atomic species present, using up the supply of metal atoms for molecular cluster growth. [2] This latter difficulty is much more intractable than that of a quenching a hot plasma with helium. Hence our approach, in common with other workers in the field, is to employ short-pulse radiation from a Q-switched Nd:YAG laser (Edinburgh), or a noble gas-halogen excimer laser (NRCC). Short duration pulses do not lead to deep pitting of the target. However, continual ablation of the same region gradually drills a surface depression, whose walls can act to quench the nascent plasma emanating from the bottom of the well. To prevent this, the target rod is rotated and translated continuously during operation, so that a fresh surface is always presented to the ablating laser pulse.

The metal plasma tends to stream out from the target surface along the laser axis, driven by the hydrodynamic pressure gradient between the plasma and surroundings. Thus in the immediate vicinity of the target region, the carrier gas density is quite low as it is blown out of the beam. This process is illustrated in Figure 2.1. The upper trace shows the helium pulse profile from a molecular beam valve, recorded by nonresonant photoionisation during a typical copper clustering experiment. The distinct discontinuity in the plateau flags the time at which the vaporisation laser is fired into the beam. The local reduction in gas density is preserved as the pulse translates to the ionisation region. This is

Figure 2.1 : "Hole burning" in a helium pulse profile

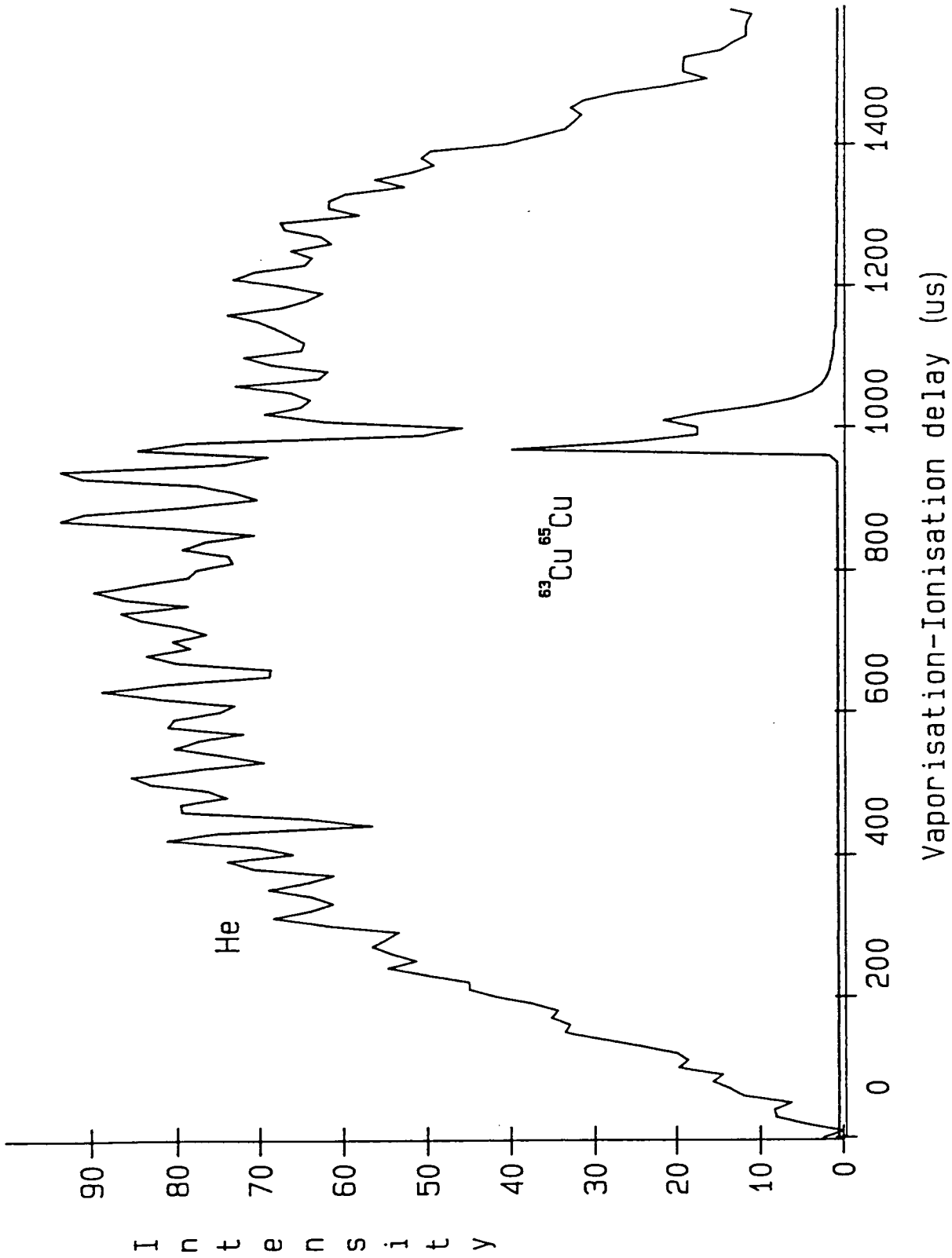

confirmed by the lower trace which shows the corresponding temporal distribution of copper dimer species recorded simultaneously. The peak of this arrival time distribution coincides with the dip in the helium intensity. The carrier gas then quenches the plasma collisionally allowing clustering between atoms of the cooled vapour to take place. This aggregation process probably proceeds by stepwise single atom addition to growing cluster nuclei, with the enthalpy of metal-metal bond formation removed by further collisions with the bulk carrier gas. Confinement of the nascent cluster distribution to a narrow channel prior to expansion into vacuum maintains the high carrier gas number density necessary to promote efficient clustering.

2.3 Supersonic expansion of clusters

A molecular sample, when seeded in an inert carrier and expanded into vacuum, provides the experimentalist with an almost ideal spectroscopic sample. Kantrowitz and Grey [3]- [4] originally proposed the supersonic nozzle as a means of increasing beam intensities over effusive sources. However, its ubiquity in molecular spectroscopy today owes more to the utility of the internal cooling which accompanies expansion. [5]

The molecular species of interest, in this case a distribution of metal clusters, is present in an excess of inert carrier gas. This gas expands through an orifice whose diameter greatly exceeds the mean free path of molecules upstream of the nozzle. The numerous collisions which occur in the orifice region convert enthalpy associated with random translation of the carrier into directed mass

flow. The translational temperature of the carrier thus falls dramatically as the expansion proceeds adiabatically. Since the local speed of sound drops below the beam velocity, the expansion becomes supersonic. Seed molecules undergo an aerodynamic acceleration to approximately the velocity of the carrier gas. The narrowing of the velocity distribution which accompanies this process is depicted in Figure 2.2. A highly directional molecular beam is formed, whose density distribution is much more axially-concentrated than an effusive source.

The rate at which the internal molecular modes equilibrate with the cooling translational bath depends on the efficiency with which energy may be transferred. The rotational manifold may be cooled efficiently since the size of rotational quanta removed in collisions is fairly small. Vibration is less rapidly cooled, since the quanta which must be removed in collisions are substantially larger. During the expansion, the density, and thus the collision rate are continually falling until a point is reached when no further collisions take place. The energy distributions in the various manifolds are then frozen in. Typical regimes of temperature attained are: T_t = 0.5-20 K, T_{rot} = 2-50 K, T_{vib} = 10-100 K, reflecting the differing cross sections for collisional quenching of each manifold. [6] Helium is preferred as the carrier gas due to its low polarisability, which precludes formation of van der Waals' complexes either with itself or with the metal species.

Cooling of molecules to the lowest quantum states greatly reduces spectral congestion. Low rotational temperatures are particularly appealing in this work since the transition metal diatomics have small rotational constants and potentially cluttered spectra. Increased population of the lowest states means

Figure 2.2 : Maxwellian velocity distribution for helium at 5 K and 300 K

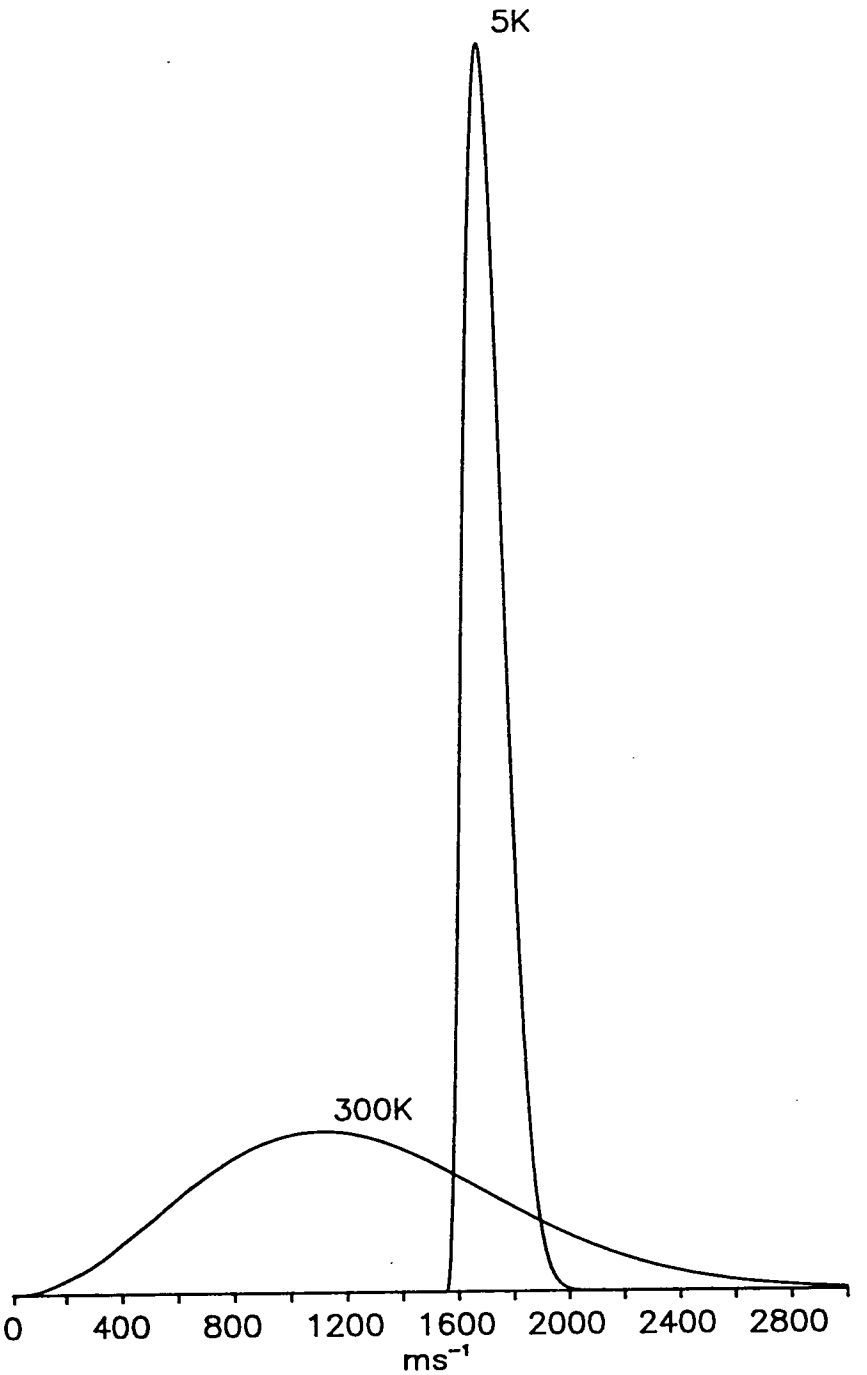

that the intensity of specific rovibronic transitions arising from these levels is enhanced.

Narrowing of the translational velocity distribution of molecules in the beam has important consequences for spectroscopy with cw ring dye lasers, since Doppler-limited spectroscopy can be performed readily with these narrow line sources. It is desirable to cool the beam as much as possible to reduce the Doppler line width, which is proportional to $T^{1/2}$. Such considerations do not apply to the pulsed laser photoionisation sources employed where the laser bandwidth exceeds the Doppler width by an order of magnitude.

2.4 Laser photoionisation processes

In the photoionisation mass spectroscopy discussed in Chapter 4, cluster species were all one- or two-photon nonresonantly ionised from their electronic ground states. When a molecule in its ground state absorbs a photon of sufficient energy to carry it above the vertical ionisation potential, the molecular photoion and a photoelectron are created. Such a process can often be strongly allowed since the photoelectron can remove energy and angular momentum, facilitating a whole range of transitions to the continuum (see Figure 2.3 (a)). [7] The rate equation for this process is:

$$W = \sigma_1 I \qquad (2.1)$$

where

W = transition rate in s^{-1}

σ_1 = single photon absorption cross section in cm^{-2}

I = radiation flux in photons cm^{-2} s^{-1}.

Single photon absorption cross sections lie typically in the range 10^{-16} - 10^{-22} cm^{-2}. [8] An alternative and equivalent way of expressing the transition rate is in terms of ρ, the spectral energy density, and B, the Einstein coefficient for stimulated absorption. [9] In this case, σI is replaced by $B\rho$ in the transition rate expression.

It should be noted that this completely general expression applies equally to single photon excitation of bound eigenstates of the molecule, in addition to transitions to the continuum. In this, and all other cases mentioned, references to transitions involving continuum states and real, bound states are entirely interchangeable.

When the molecular ionisation potential lies between the energy of one and two laser photons from the same laser field, two-photon nonresonant ionisation can occur (see Figure 2.3 (b)). Such a process involves the simultaneous absorption of two photons from the same radiation field, which is not surprisingly a far less probable process than single photon absorption. For a pure two-photon absorption, the second photon must be absorbed within 10^{-15} s, the lifetime of the hypothetical virtual intermediate state which lies at the energy of the first laser photon. This state is formed from an energy weighted summation over all real bound and continuum states of the molecule. The transition rate here depends quadratically on the laser flux, reflecting the requirement for

Figure 2.3 : Photoionisation schemes

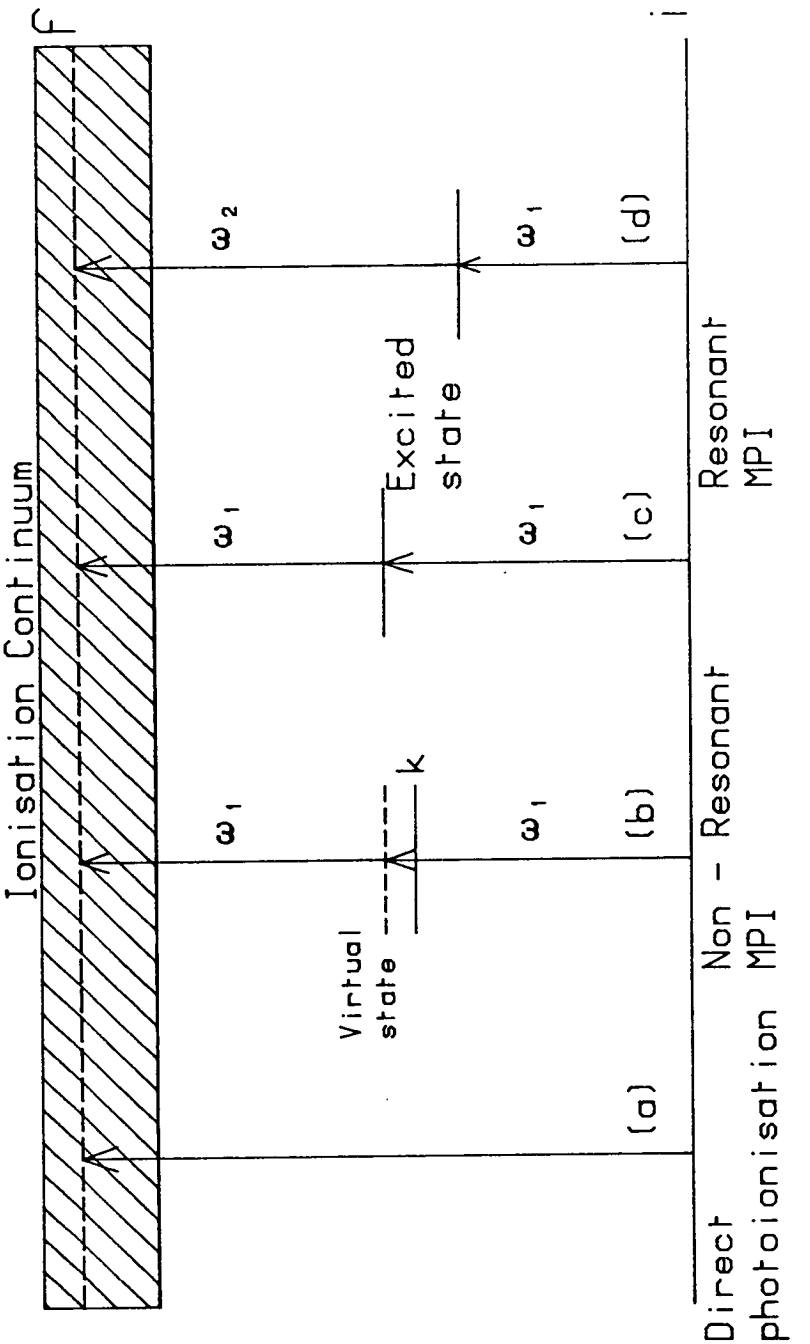

simultaneous two-photon interaction with the molecule: [8]

$$W = \sigma_2 I^2 \qquad (2.2)$$

where

σ_2 = the two-photon absorption cross section in cm^4 s,

the other terms being as described previously.

Cross sections for pure two-photon processes, unperturbed by any near-resonances at the one photon level, are many orders of magnitude smaller than those for single photon processes. They lie typically in the range 10^{-48} - 10^{-58} cm^4 s, and require concomitantly higher laser powers to produce appreciable transition rates. [8]

Equations (2.1), (2.2) and analogous expressions for higher order ionisation processes are frequently utilised in crude determinations of cluster ionisation potentials (IPs) using fixed frequency laser sources. [10] If a cluster is n-photon ionised at a particular photon energy $\hbar\omega_1$, then the ionisation signal should show an n-photon dependence on the laser intensity. This is most easily seen when an equation such as (2.2) is cast in a logarithmic form:

$$\ln W = \ln\sigma_2 + n \ln I. \qquad (2.3)$$

The slope of this "power dependence" plot should be an integral quantity n. Clearly the cluster IP then lies in the range $(n-1)\hbar\omega_1 < IP < n\hbar\omega_1$. Replacing the original laser source with one of higher photon energy ($\hbar\omega_2$) may cause the

order of the ionisation process to go from n→n-1, which is reflected in a change in the slope of the power dependence plot. The IP can then be "bracketed" in the range $(n-1)\hbar\omega_1 < IP < (n-1)\hbar\omega_2$.

For the nonresonant cluster photoionisation work reported here, substantial ion signals could be obtained without focusing the laser to increase the photon flux. Indeed, it was desirable to avoid excessive laser fluxes since the probability of subsequent photon absorption by the molecular ion is then increased. This can lead to excitation to dissociative continua in the ion, resulting in fragmentation. Under such circumstances, the interpretation of photoionisation mass spectra as a faithful representation of neutral cluster intensity distributions becomes fraught with uncertainty. This point is discussed further in relation to some anomalous intensities observed in copper cluster distributions in Chapter 4.

Under certain circumstances, two photon transition intensities may be augmented by perturbations caused by near resonance at the one photon level with real molecular eigenstates. The two photon transition probability, calculated by second order perturbation theory is: [6] [11]

$$A_{if} = C_{if}\left[\sum_k R_{ik}.e_1.R_{kf}.e_2/(\omega_{ki}-\omega_1)\right]^2 I^2 \qquad (2.4)$$

where

C_{if} is the spectral line profile of the two photon transition

R_{ik}, R_{kf} are the matrix elements for the transitions i→k, k→f

e_1, e_2 are the polarisation vectors

ω_1 is the laser frequency

ω_{ki} is the transition frequency for the process i→k.

Although the summation which generates the virtual level extends over all k states, clearly those which lie close to the photon energy will dominate the expression and lead to high transition probabilities (Figure 2.3 (b)). Examples of such near-resonance enhancement in CuAg are discussed in Chapter 5.

In the special case of the first photon being in resonance with the intermediate state k, the results of the perturbation treatment suggest that the cross section for such resonant absorption or ionisation should be many orders of magnitude higher. The simplest case occurs when the real excited state lies more than half way to the ionisation potential (Figure 2.3 (c)). Absorption of one photon carries the molecule to the intermediate state which will be substantially longer lived than the fleeting virtual state of the nonresonant two photon process. Absorption of a second photon from the same laser field can now occur, driving the molecule into the ionisation continuum. The resulting large two photon resonant absorption cross section reflects the much lower laser flux needed for efficient ionisation. Molecules may dwell in the long lived intermediate state while awaiting the arrival of the second photon. Such intermediate resonances alter the power law dependence to I^q, where q is normally some nonintegral

number less than n. [8] States of the CuAg molecule in the ultraviolet spectral region were probed using this one colour, resonant two photon ionisation (R2PI) technique (see Chapter 5).

When the resonant excited state lies less than half way to the ionisation potential, a more energetic photon from a different laser field is required to induce single photon ionisation out of this state (see Figure 2.3 (d)). The principles are identical to the one colour resonant ionisation scheme described above. This two colour technique is central to the investigation of low-lying excited states of transition metal dimers, since these invariably lie at less than half the ionisation energy. An ultraviolet radiation source (excimer laser) is required to stimulate excited state ionisation. Exploiting the differences between resonant and nonresonant transition rates to record excitation spectra is easily accomplished. The exciting and ionising lasers are aligned spatially and temporally in the ion source of the TOFMS. Scanning the excitation laser while monitoring the photoion signal produces an isotopically-resolved "quasi-absorption" spectrum. When the exciting laser is off-resonance with a molecular transition, the ion signal is low since it arises from low probability nonresonant n-photon ionisation from each laser. When the exciting laser comes into resonance with a molecular transition, facile resonant two photon ionisation can occur, with consequent enhancement in the ion signal. Scanning the first laser in the presence of the second, ionising laser then maps out rovibronic structure in the excited state, provided the bandwidth of the first laser is narrow enough. The foregoing description has ignored the fate of the ion as the exciting laser energy is scanned. Since the ionising photon normally carries the molecule well above the threshold

limit into a region with a high state density, the ionisation cross section should not vary markedly over the limited scanning ranges. [12]

Applications of two colour R2PI to study the spectroscopy of states of CuAg in the visible region of the spectrum are presented in Chapter 5. A variation of R2PI, in which the fixed frequency ionising laser is replaced by a tunable dye laser, is used in the technique of threshold ionisation spectroscopy (TIS), the subject of Chapter 6. Here the exciting laser is tuned to some intermediate resonance while a frequency-doubled dye laser is scanned across the ionisation threshold, to provide information on the ion. The same principles apply here. When the second laser crosses the ionisation threshold, the ion signal rises dramatically as two photon nonresonant ionisation at the second step switches to single photon ionisation.

2.5 Spectral linewidths

The useful information content of any laser excitation spectrum is largely determined by the bandwidth of the excitation source. A considerable part of this work involved recording rotationally-resolved electronic spectra of transition metal dimers (see Chapters 5 and 7). The small (typically 0.05 - 0.1 cm^{-1}) rotational constants of these species lead to spectra which can be highly congested, even when jet-cooled. Many rovibronic transitions can lie within a few cm^{-1} spacing, and detail is often obscured by inadequate laser resolution. An evaluation of those factors determining spectral linewidths, other than the laser bandwidth, is thus appropriate at this juncture.

Spontaneous emission of radiation from a molecular state in the gas phase gives rise to a homogeneous Lorentzian line profile, whose width is inversely proportional to the lifetime of the state. Normally this profile is concealed by other broadening mechanisms.

A major contribution at low pressures arises from Doppler broadening, which is due to the thermal motion of molecules with respect to the interacting light wave. The halfwidth of a Doppler line profile is given by: [6]

$$\Delta\omega_d = (\omega_0/c)(8kT\ln 2/m)^{1/2} \qquad (2.5)$$

where

ω_0 = the centre frequency of transition

c = the speed of light

k = Boltzmann's constant

T = the temperature

m = the molecular mass.

A Doppler broadened spectral line cannot be represented by a pure Gaussian but by a convolution of the Lorentzian profile with a Gaussian. The result is known as a Voigt profile. Since the halfwidth varies as $T^{1/2}$, Doppler broadening can be reduced in the low temperature environment of a molecular beam. Its effects can only be eliminated completely in highly specialised situations [6].

All the experiments described in this thesis were performed in a molecular beam environment, which was fairly well expanded into the collisionless regime. Such a

spectroscopic sample would not be affected by elastic or inelastic collisional broadening mechanisms.

If the interaction time of the laser field with the molecular species is very small compared to the spontaneous lifetime of the transition, transit time broadening of the spectral line may occur. [6] Since the interaction time of the laser pulse with the molecules is on the order of 10 ns, the resulting contribution to line broadening would be about 100 MHz. As the pulsed laser sources used here had bandwidths of 1200 MHz at best, this broadening effect would not be observable. When using cw laser sources, the relatively long interaction time between the laser field and molecular beam make this effect negligible.

If the radiation flux incident on a molecular absorber is sufficiently high, saturation of the transition, and consequent broadening of the spectral line profile may occur. Under conditions of saturation, the populations in the upper and lower states in the transition become equalised and stationary, since the overall rates of absorption and emission from each level are the same.

The transition rate for an induced absorption process (W_{12}) is related to the spectral energy density of the exciting laser (ρ) through the Einstein coefficient for stimulated absorption: [6]

$$W_{12} = B_{12}\rho \tag{2.6}$$

where W_{12} has units of s^{-1}. The probability of a molecule undergoing the transition 1→2 during the laser pulse is given by:

$$P_{12} = W_{12}\Delta t \qquad (2.7)$$

where Δt is the laser pulse duration. Saturation of the transition requires that the absorption probability is $\simeq 1/2$, to equalise the populations in the upper and lower states. The rates of induced absorption and emission increase with the laser pumping power. Consequently, the time a molecule resides in either level before undergoing a transition is reduced, and the spectral linewidth increases accordingly, as given by the Uncertainty Principle.

The effects of kinetic saturation on rotational linewidths can be severe, particularly in the cases of congested R2PI spectra recorded with relatively broadband pulsed dye laser sources.

In resonance enhanced multiphoton ionisation (REMPI) experiments, high laser intensities can dramatically foreshorten the excited state lifetime, since the ionisation step is usually more probable than the two photon excitation step. Focusing of the laser beam to achieve the power densities required for these processes can lead to geometric saturation with further spectral line broadening contributions. [13]

2.6 Fluorescence versus photoionisation spectroscopy

Molecular beam fluorescence may be excited by crossing the beam with the output of a tunable dye laser. The LIF signal is collected perpendicular to the plane of intersection of these two beams. The expansion can be interrogated close to the jet orifice, sampling regions of high number density. The substantial

number of molecules in the laser-molecular beam interaction zone, coupled with the high laser power density, facilitates the recording of intense fluorescence with high signal-to-noise ratios. This is to be contrasted with the case of photoionisation using mass spectrometric detection. The source region of the mass spectrometer requires the maintenance of a low pressure ($< 10^{-6}$ mbar) to prevent electrical arcing, collisional ionisation and detector degradation (see Chapter 3). Although the core of the molecular beam is skimmed prior to entering the ion source of the TOFMS, vacuum pumping requirements dictate that this region be located well downstream of the point of expansion. The axial beam number density follows a $1 / r^{-2}$ dependence on distance from the nozzle. Hence the density in the ion source region can be dramatically less than in the fluorescence zone, in our case by a factor of $> 10^3$. This somewhat negates the inherent collection sensitivity advantage which photoionisation possesses over fluorescence.

From a practical standpoint, the constraints of experimental timing control are less rigorous for fluorescence detection than for photoionisation. The LIF signal can be detected using a fairly high ohmic coupling on the photomultiplier tube. The resulting long time constant of the decay trace makes for easy gating of the signal for averaging purposes. Two colour photoionisation *via* a short-lived excited state can be seriously compromised if there is any jitter between the exciting and ionising laser pulses, which results in noisy two colour signals.

However there are some disadvantages associated with fluorescence techniques in general, which can be quite crippling under some circumstances. Since the technique lacks any means of mass discrimination, assignment of the carrier of an

observed electronic transition is often difficult. Conversely, photoionisation detection of excited states coupled with mass selective detection in a quadrupole or TOF mass spectrometer facilitates ready identification of the carrier. A related problem is that of spectral congestion due to blending of spectra due to different isotopomers. Where there are small isotope shifts between the various species, or where there are a large number of possible isotopic combinations, this problem can be severe. The latter is particularly acute for many of the transition metals which have rich distributions of natural isotopes. By detecting photoions mass selectively, separate spectra can be recorded for all isotopomers simultaneously, greatly simplifying the analysis. An extreme example of the multi-isotope problem is illustrated in Figure 2.4, which shows the isotopomer distribution for molybdenum dimer obtained by nonresonant photoionisation TOF mass spectrometry (see Chapter 4). Without selective isotopic enrichment of the source of molybdenum, unravelling the LIF spectroscopy of this molecule would be impossible. Even mass-resolved photoionisation spectroscopy is complicated by blending, since there are many isobaric interferences between different isotopomers of the same mass.

Optimising cluster source and beam conditions is easier in photoionisation experiments, since cluster species may be nonresonantly ionised. This removes the requirement, present in LIF, for excitation of some known atomic or molecular transition which is used to monitor beam intensity during optimisation.

A pulsed dye laser was used as the excitation source in all the wavelength-resolved photoionisation experiments. Such lasers have a

Figure 2.4 : TOF mass spectrum of Mo_2 isotopomers

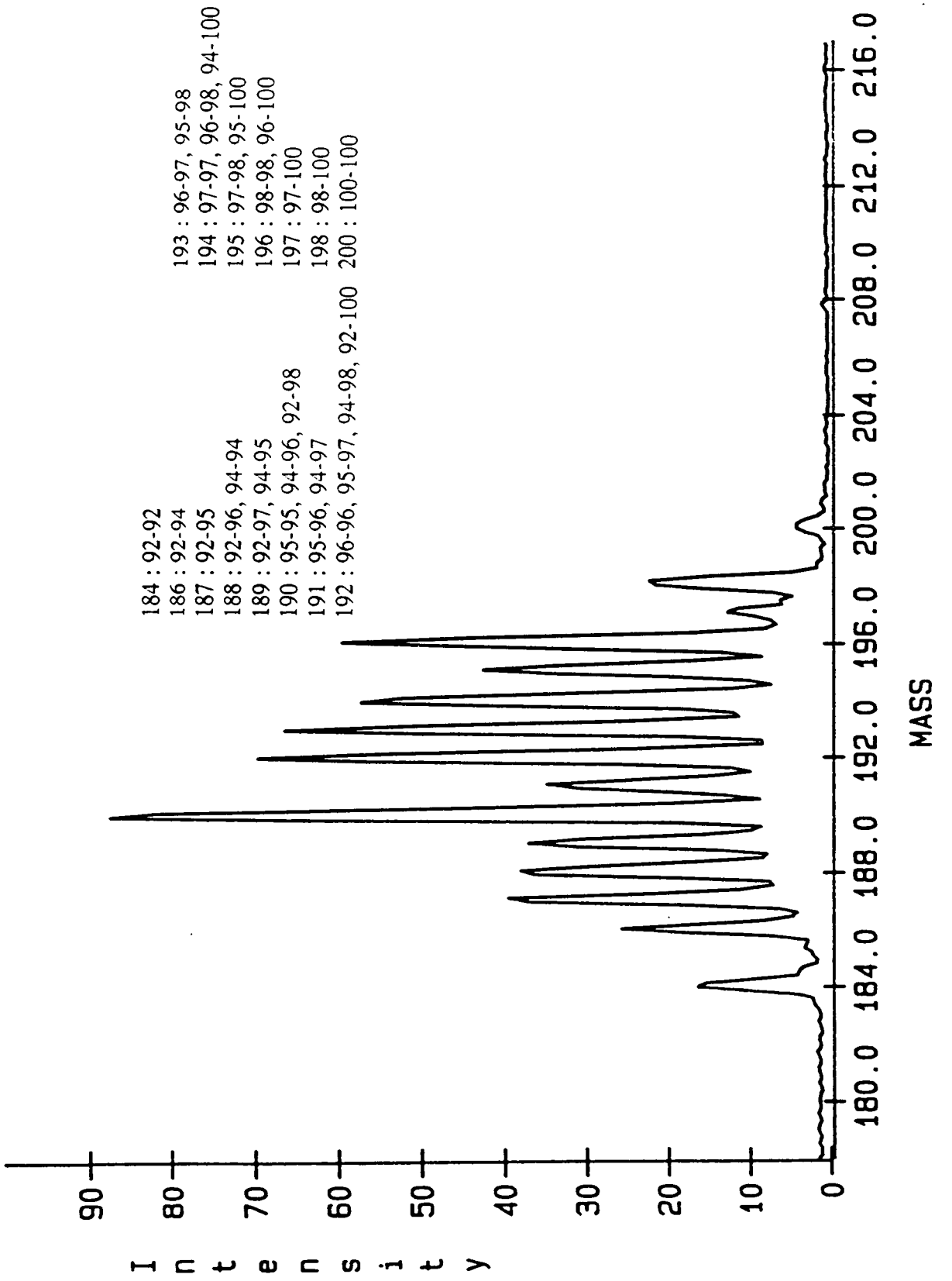

conventional cavity supporting standing wave oscillation as depicted in Figure 2.5 (a). Linewidths are limited in standing wave dye lasers by spatial holeburning in the gain medium. [14] The standing wave laser resonator is effectively a Fabry-Perot etalon with a large spacing between the reflecting surfaces. The reflected intensity is a maximum when the cavity length is equal to an integral number of half wavelengths:

$$d = n\lambda/2. \tag{2.8}$$

In other words, there are nodes in the wave intensity at the end mirrors. Clearly, the nodal pattern extends into the gain medium. Dye molecules located at these nodes are not stimulated by lasing oscillation in the cavity. The gain of these regions can be high enough to sustain lasing at different wavelengths from the original oscillation. These new wavelengths do not have nodes in the electric field intensity at the original node locations. Hence the standing wave oscillation is multimodal, with gain distributed over many longitudinal modes, and intracavity line narrowing elements must be inserted to reduce the bandwidth. However, these high loss devices, coupled with the distribution of gain over many modes, seriously limit the spectral power density. The narrowest bandwidth that could be achieved with the lasers available here was 1200 MHz (0.04 cm^{-1}) [15] which is just adequate to rotationally resolve silver dimer electronic spectra. However, the pulsed laser is relatively easy to operate and is capable of rapid scanning over several nm. It is the most suitable laser for spectroscopic survey work, whether fluorescence or photoionisation methods are being employed.

The continuous wave ring laser offers much enhanced spectral resolution at high

Figure 2.5 : Dye laser cavity configurations

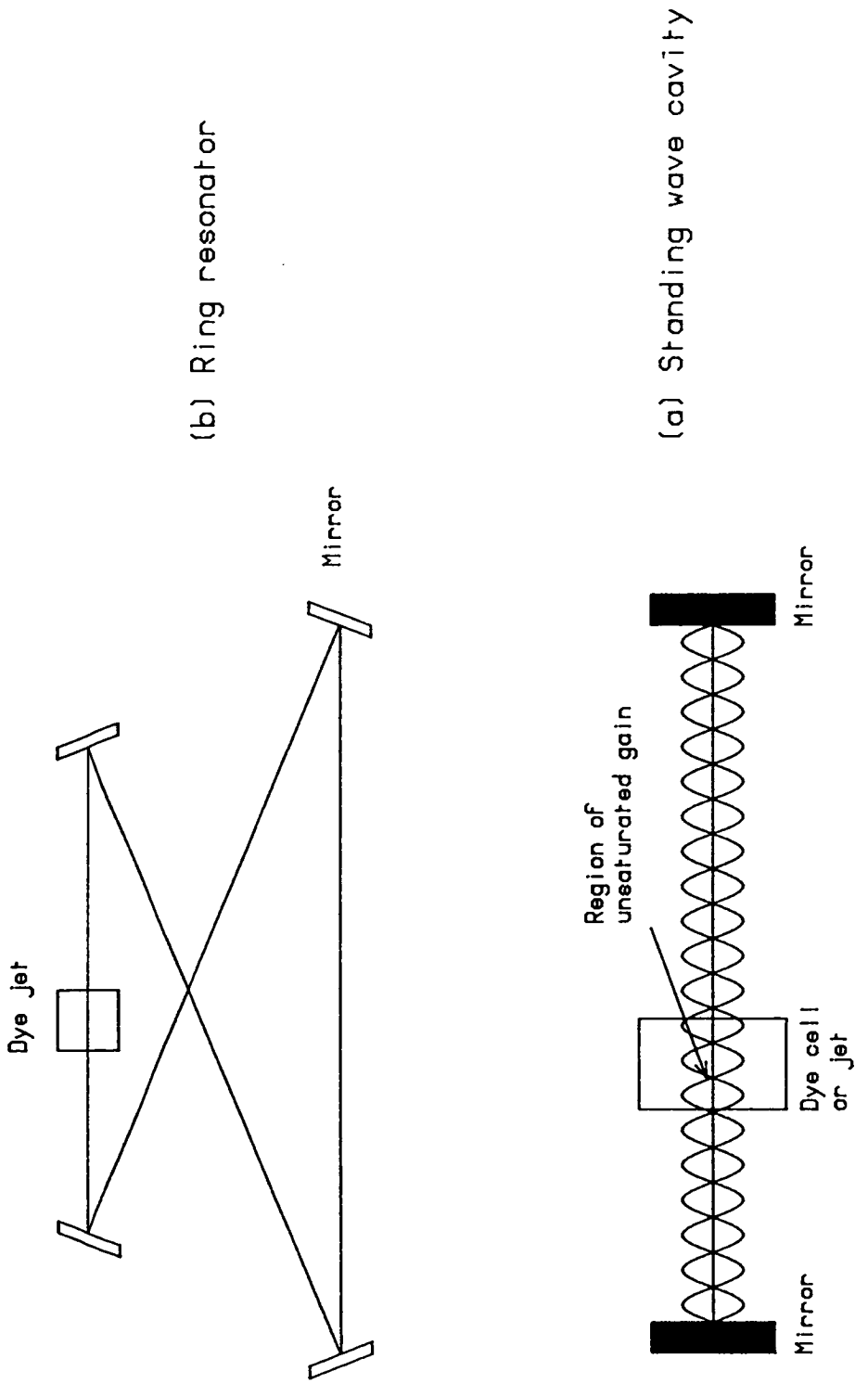

power, with all available gain concentrated in a single cavity mode. In a ring resonator, a travelling wave propagates without spatial node structure (Figure 2.5 (b)), the only requirement being that it constructively interferes after each pass round the cavity:

$$L = m\lambda \tag{2.9}$$

where

L = ring cavity length

λ = wavelength

m = an integer.

This travelling wave samples all regions of gain in the lasing medium, and thus the problem of spatial hole burning is removed. A single longitudinal mode will propagate instantaneously when a wavelength selecting device (birefringent filter) and unidirectional device (Faraday rotator) are inserted. Low loss, low finesse etalons are utilised to select a single mode for lasing operation. The homogeneously broadened linewidth which results should be a few Hz. Acoustic and mechanical disturbances which change the cavity length will alter the frequency of this mode. Scanning linewidths are thus limited in practice to about 1 MHz. [16] This is substantially less than typical molecular beam Doppler widths of around 100 MHz. Doppler-limited electronic spectroscopy thus becomes viable, the narrow linewidth permitting complete rotational resolution of multi-isotope spectra almost as far as the bandhead. One major disadvantage of the ring laser is that it is extremely difficult to operate compared to a pulsed

dye laser, and cannot scan rapidly over a wide spectral range. It is therefore wholly unsuited to survey scanning applications, but is the system of choice when molecules with small rotational constants ($< 0.05\ cm^{-1}$) or complex hyperfine structure are under investigation. In practice, the position of electronic band systems require to be first located by rapid scanning techniques. In the present work on silver dimer, mass resolved photoionisation spectroscopy was first carried out to obtain vibronic band positions, rotational constants and isotope shifts to moderate precision. Doppler-limited spectra obtained using the ring laser then permitted highly accurate determinations of the rotational constants, the photoionisation data assisting in assignment of the multi-isotopomer LIF spectra.

It should be clear that neither technique alone offers a solution to all the problems of high resolution electronic spectroscopy in molecular beams. The photoionisation technique is clearly more versatile, however. The ultimate experimental goal would be to couple a cw ring laser as the excitation source, with photoionisation from the continuously excited state using a pulsed laser, detecting ions mass selectively.

References

[1] Ready J. F., *Industrial Applications of Lasers*, Academic Press, New York, 1978.

[2] Powers D. E., Hansen S. G., Puiu A. C., Hopkins J. B., Dietz T. G., Duncan M. A., Langridge-Smith P. R. R., Smalley R. E., J. Phys. Chem., **86**, p 2556, (1982)

[3] Kantrowitz A., Grey J., Rev. Sci. Instrum., **22**, p 328, (1951)

[4] Kantrowitz A., Grey J., Rev. Sci. Instrum., **22**, p 333, (1951)

[5] Smalley R. E., Wharton L., Levy D. H., Acc. Chem. Res., **10**, p 139, (1977)

[6] Demtröder W., *Laser Spectroscopy: Basic Concepts and Instrumentation*, Springer Verlag, Berlin, 1982.

[7] Hollas J. M., *High Resolution Spectroscopy*, Butterworths, London, 1982.

[8] Parker D. H., *Ultrasensitive Laser Spectroscopy (ed. Kliger D. S.)*, Academic Press, New York, 1983.

[9] Atkins P. W., *Molecular Quantum Mechanics*, 2nd. edition, Oxford University Press, 1983.

[10] Rohlfing E. A., Cox D. M., Kaldor A., J. Chem. Phys., **81**, p 3322, (1984)

[11] Göppert-Mayer M., Ann. Phys., **9**, p 273, (1931)

[12] Antonov V. S., Letokhov V. S., *Laser Analytical Spectrochemistry (ed. Letokhov V. S.)*, Adam Hilger, Bristol, 1986.

[13] Johnson P. M., Otis C. E., Ann. Rev. Phys. Chem., **32**, p 139, (1981)

[14] Divens W. G., Jarrett S. M., Rev. Sci. Instrum., **53**, p 1363, (1982)

[15] Lambda Physik, *FL3001/2 Instruction Manual*, Gottingen, 1986.

[16] Coherent Inc., *CR-699-21 Instruction Manual*, Palo Alto, Ca., 1984.

Chapter 3
Cluster Photoionisation Experimental Details

This chapter describes the laser systems, metal cluster source, and the two different types of molecular beam apparatus, referred to henceforth as MB1 and MB2, which were used in the present work. A brief description of the experimental data acquisition software and hardware is also given. MB1, the first generation cluster beam rig at Edinburgh, featured a linear TOFMS, and was used primarily for the clustering studies described in Chapter 4. MB2, the second generation Edinburgh instrument, possessed interchangeable linear and reflecting field TOF mass spectrometers. This system was employed for the R2PI experiments and the threshold photoionisation studies described in Chapters 5 and 6. The ring laser LIF system at NRCC Ottawa was used exclusively for studies of silver dimer spectroscopy. It is described separately in Chapter 7.

3.1 MB1 vacuum system

The MB1 vacuum system is shown schematically in Figure 3.1. It consisted of three chambers constructed from 304 stainless steel, equipped with demountable side flanges. These flanges were also of 304 stainless steel, apart from those on the main chamber, which were fabricated from aluminium. Each chamber was pumped independently by a rotary-backed oil diffusion pump.

The MB1 main chamber, which had a volume of 68 l, housed the cluster source fixtures, molecular beam valve and skimmer mount. The side flanges on this chamber were equipped with ports on which quartz windows were mounted to

Figure 3.1 : Schematic of the MB1 apparatus

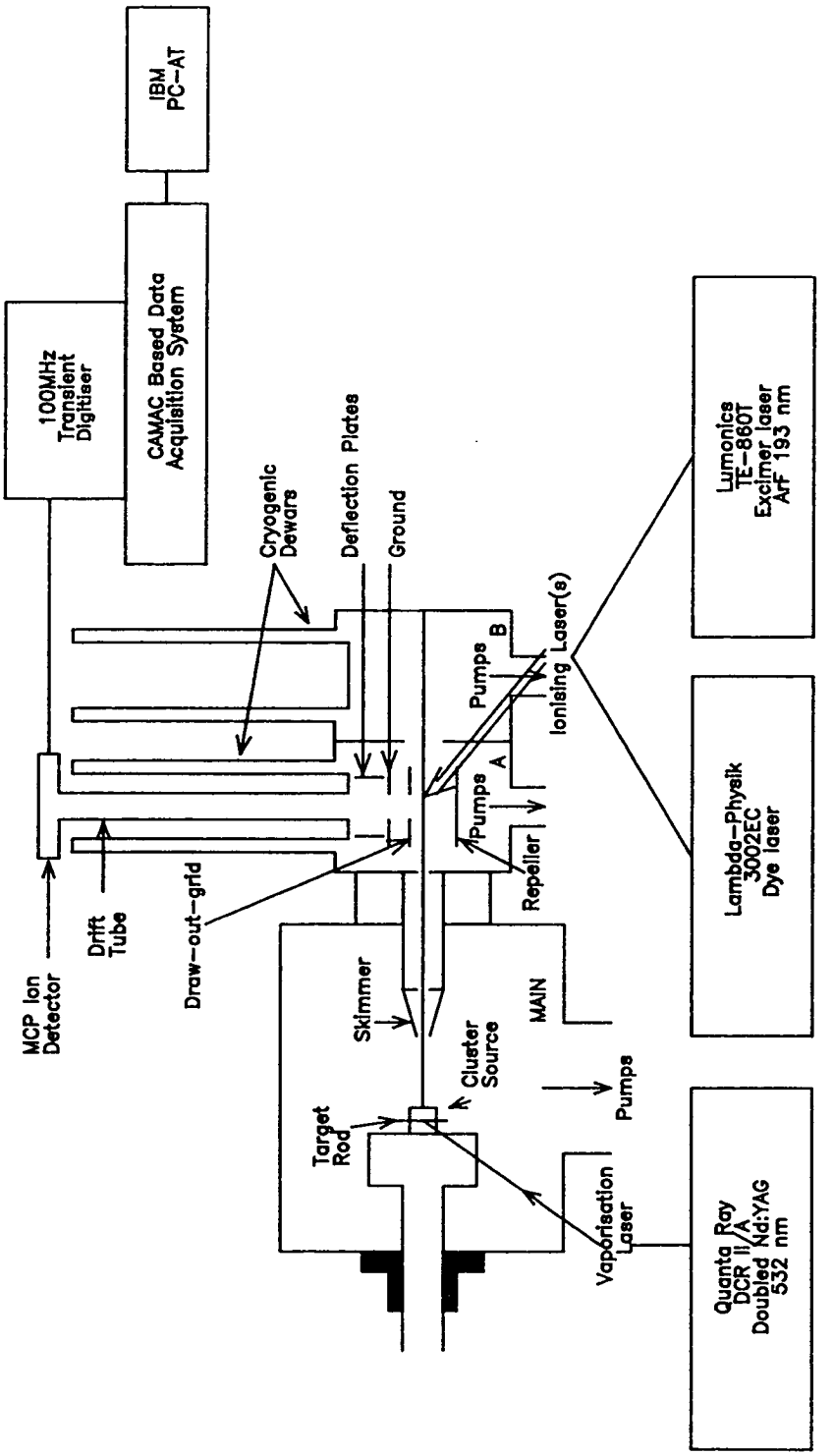

allow passage of the laser vaporisation beam. Deposition of vaporised material on the laser entrance window proved to be a problem, requiring this window to be stood-off the flange on a 30 cm long tube. This chamber was pumped by a half-chevron baffled CVC PBA-1000 oil diffusion pump, using Convoil 20 pump fluid. The unbaffled pumping speed of 5300 ls^{-1} (for air up to 1 x 10^{-3} mbar) was reduced by the baffle to 2690 ls^{-1}. The base pressure in this chamber with the molecular beam valve off was 1.2 x 10^{-6} mbar. This rose to 1.2 x 10^{-3} mbar under typical running conditions of 10 bar helium backing pressure at 10 Hz. (All subsequent references to "running conditions" relate to these parameters.) The diffusion pump was backed by a rotary-booster combination (Edwards E2M40/EH250) capable of pumping 8.5 mbar ls^{-1} at a foreline pressure of 0.1 mbar. Pressures were measured in this chamber by Edwards Pirani (PRL 010) and Penning (CP25-K) gauges covering the ranges 10-10^{-4} mbar and 10^{-2}-10^{-7} mbar respectively. The main chamber could be isolated from the A chamber and the diffusion pump by pneumatically-operated gate valves. This isolation capability, a feature common to MB1 and MB2, was desirable to facilitate the rapid changing of target rods without breaking the high vacuum in the ion source region. The main chamber also housed the skimmer mount. This was stood-off the wall of the A chamber to minimise the disruption effects on the beam core caused by the wings striking the chamber walls. Two alternative designs of skimmer (Beam Dynamics) were used: one with a 3mm aperture, 50° included angle, and one with a 5 mm and 30° included angle. Skimming of the beam between the main and A chambers allowed low pressures (< 10^{-5} mbar helium) to be maintained in the A chamber during operation.

The MB1 A chamber, a 17 l 304 stainless steel cube, housed the ion extraction optics, flight tube and microchannel plate detector of the linear TOFMS. It was pumped by a baffled Edwards E09 oil diffusion pump (Edwards L9 pump fluid). The unbaffled pumping speed was 3300 ls^{-1} for hydrogen. This pump was backed by a parallel combination of Edwards E2M18 rotary pumps which also backed the B chamber oil diffusion pump through a common foreline. The side flanges were equipped with quartz windows to admit the various laser beams. The drift tube of the TOFMS (132 cm long, 4 cm internal diameter) was mounted on the top flange of the A chamber. The lower 66 cm portion of this tube was surrounded by a double-skinned liquid nitrogen dewar, whose base penetrated into the A chamber by 6.4 cm. The ion extraction optics were mounted inside a copper cryoshield which was affixed to the dewar base. This cryoshield was provided with 4 x 40 mm diameter holes to allow passage of the laser and molecular beams into the ion source. The cryopumping effect of the dewar and cryoshield reduced the pressure in the A chamber by an order of magnitude. Base pressure in the A chamber was 1.2×10^{-7} mbar, while the operating pressure was typically 6×10^{-6} mbar. At the top of the flight tube was mounted the microchannel plate detector (MCP), isolatable from the A chamber by a pneumatically-operated gate valve.

The MB1 B chamber, identical to the A chamber apart from the lack of a flight tube, was pumped by an Edwards Diffstak 160/700C oil diffusion pump (Edwards L9 fluid) with a pumping speed of 700 ls^{-1}. This chamber was used as a dump tank for the molecular beam after it had traversed the A chamber. The B chamber pressures were typically 7.2×10^{-8} mbar (base) and 3×10^{-6} mbar (

running) . Pressures were measured in both the A and B chambers by Balzers TPR 010 Pirani gauges (100 - 5.6 x 10^{-4} mbar) and Balzers IKR 020 cold cathode ionisation gauges (5 x 10^{-3} - 4 x 10^{-10} mbar).

3.2 MB2 vacuum system

The MB2 vacuum system was similar in construction to MB1, and is shown in Figure 3.2. The main chamber, which had a volume of 43.7 l, was constructed from 304 stainless steel in the manner of MB1, and also housed the cluster source, molecular beam valve and skimmer mount. A 30 cm stand-off tube was used for admittance of the laser vaporisation beam. This chamber was pumped by a half-chevron baffled 10" diffusion pump (CVC PMC-10), with a baffled pumping speed on air of 2600 ls^{-1} (Convoil 20 pump fluid). The rotary-booster backing pump system for this chamber was the same as that for MB1 (Edwards E2M40/EH250). An Edwards CP25K Penning ionisation gauge was used to monitor the pressure in this chamber, base pressure 1.4 x 10^{-5} mbar rising to 2.4 x 10^{-3} mbar when operating. The 3 mm aperture, 50° included angle skimmer was used in all the MB2 experiments described. Manually-operated gate valves isolated the main chamber from the diffusion pump and the A chamber.

The MB2 A chamber housed the ion extraction optics, flight tube and detector of the linear TOF mass spectrometer. (The flight tube is perpendicular to the plane of Figure 3.2.) This chamber, a 17 l cube of 304 stainless steel identical to the A chamber in the MB1 system, was pumped by an Edwards EM160/700 oil diffusion pump, with a speed of 700 ls^{-1} on air (Edwards L9 pump fluid). The diffusion pump was backed by an Edwards E2M18 rotary pump, which also

Figure 3.2 : Schematic of the MB2 apparatus

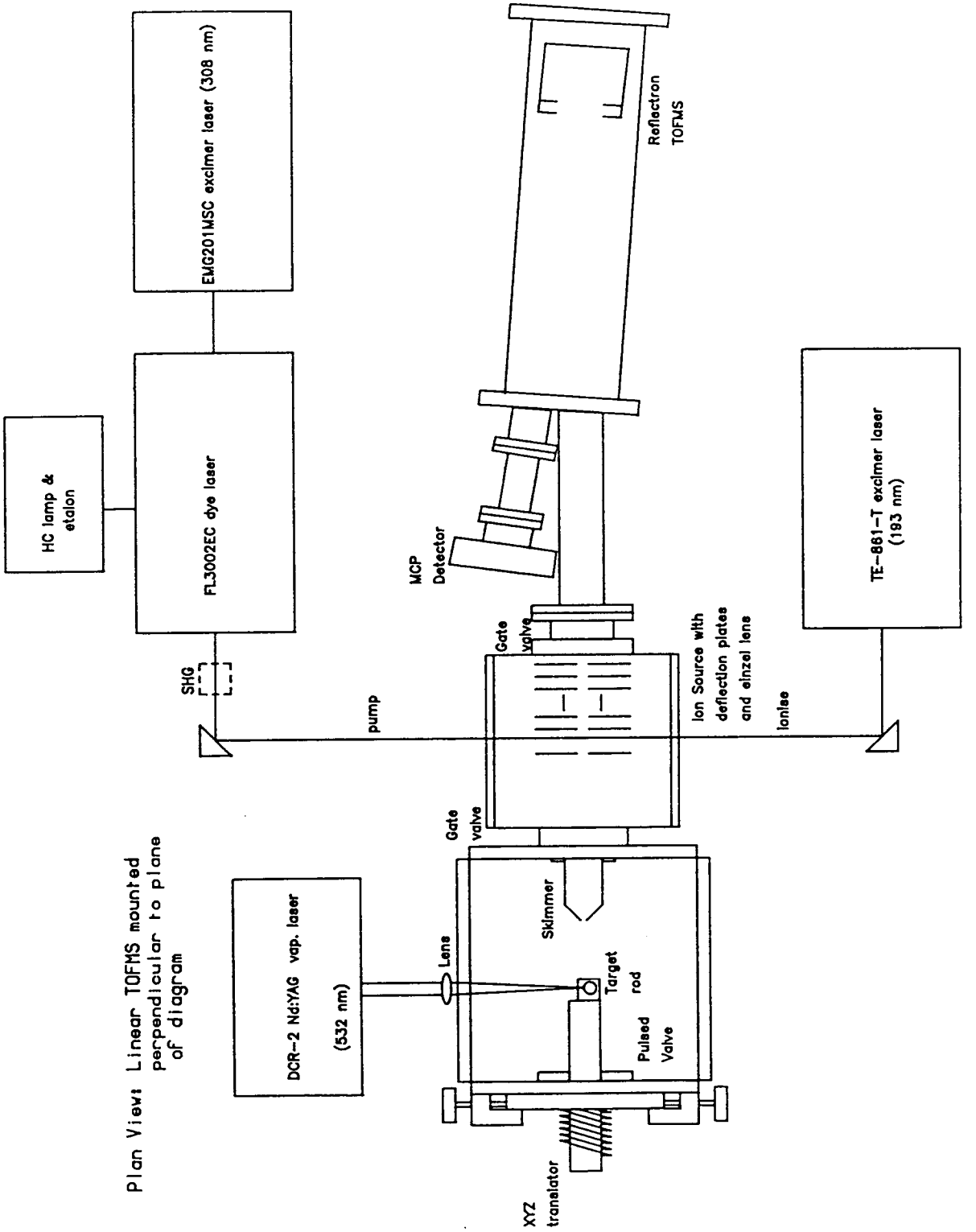

backed the reflectron chamber diffusion pump *via* a common foreline trunking. The flight tube, 132 cm long, with an internal diameter of 4 cm, was surrounded by a 60 cm double skinned liquid nitrogen dewar. A microchannel plate detector was mated to a flange at the top of this flight tube. In the case of the MB2 rig, the base of the cryopump did not penetrate into the A chamber interior appreciably, to facilitate easy mounting of different ion extraction optic geometries. The ion optics for the linear or reflectron TOF configurations were mounted on bed bars running along the base of the A chamber. Neither set was equipped with a cryoshield. This had a slightly adverse effect on the base pressure in the MB2 ion source compared to MB1, but did not prove to be a major problem. The stainless steel side flanges on the A chamber were equipped with a dual set of quartz window ports for laser beam admittance. Pressures were measured in this chamber by Edwards CP25K Penning and PRL10 Pirani gauges. A typical base pressure was 1.2×10^{-7} mbar, the running pressure being 3.5×10^{-6} mbar.

The MB2 reflectron chamber (R) was constructed from 304 stainless steel and had a volume of 24.7 l (63.5 cm long by 19 cm internal diameter). This chamber was connected to the A chamber *via* a stand-off section (30 cm by 6.3 cm diameter), which mated with a manually-operated gate valve isolating the R chamber from the A chamber. The ion mirror optics were mounted off the back flange of this chamber, tilted at 4° to the common molecular beam-ion extraction axis, to direct ions down the second arm of the flight tube. The axis of this second drift region was angled at 8° with respect to the first (see Figure 4.7). Another stand off section (22 cm by 6.3 cm internal diameter), also angled at

8° to the beam axis, connected the R chamber to a second MCP detector. The chamber was pumped by an Edwards CR160 diffusion pump with a pumping speed of 700 ls^{-1} for air. A double skinned liquid nitrogen dewar was mounted on top of the R chamber for cryopumping purposes. R chamber pressures, monitored by an Edwards CP25K Penning gauge were 1.2 x 10^{-7} mbar (base) and 5.9 x 10^{-7} mbar (running).

3.3 Cluster source

The cluster source, which was common to both systems, can be logically divided into two basic components: the molecular beam valve and the target rod mounting fixture, the latter being mounted over the snout of the molecular beam valve. The complete assembly could be translated in three dimensions by an XYZ translator. A detailed cutaway schematic of the cluster source is shown in Figure 3.3.

Two types of commercial molecular beam valve were used for the experiments described here: a Newport Research Corporation BV100 and a General Valve Series 9 valve. The BV100 valve was of the double solenoid type with a soft iron actuator, as described by Adams *et al.*. [1] When the valve was "off", current flowed continuously through the "close" coil, forcing a viton tip seal against a 500 µm orifice. When the valve was triggered to open, the close current dropped to zero and the current pulse supplied to the open coil drew the actuator back, breaking the seal and allowing gas to escape through the orifice. Varying the open pulse duration altered the stroke length of the actuator and the intensity of the gas pulse generated. Following the open pulse time-out, a large current pulse

Figure 3.3 : Detail of the cluster source

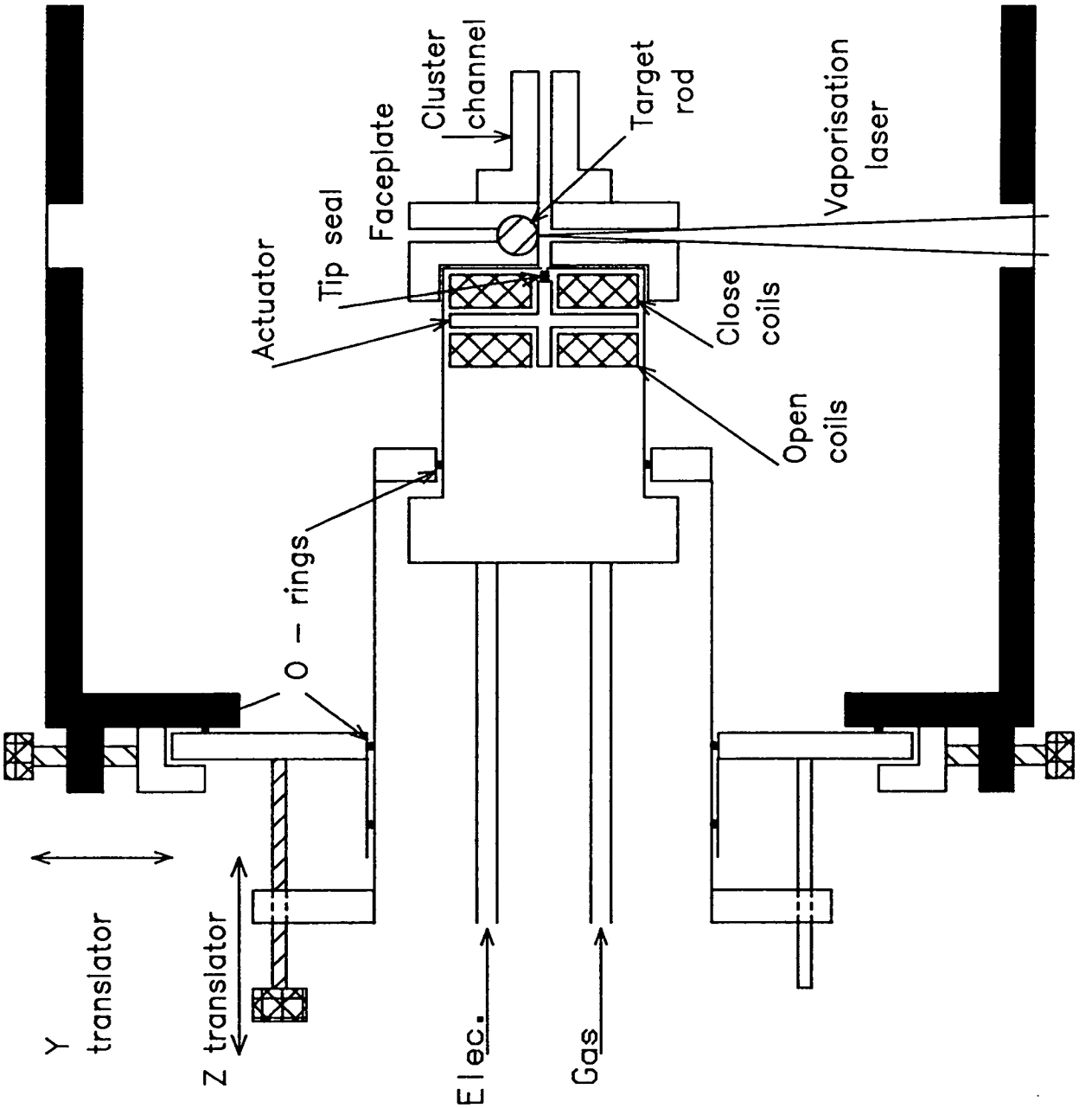

was supplied to the close coil to seal the valve shut again. The advantage of this design was that very high intensity gas pulses could be delivered. However, this valve proved very unreliable in long term operation, particularly when generating pulses of shorter than 900 μs duration at high backing pressures. Normal operating conditions involved the generation of 900 μs duration pulses at 6-10 bar backing pressure of helium. The throughput of this valve was approximately 0.77 mbar l $pulse^{-1}$. The use of this valve was confined chiefly to clustering studies on the MB1 rig (see Chapter 4).

The General Valve Series 9 was of a simpler and much more reliable design. This valve used a single solenoid to draw an iron actuator back against the retaining action of a spring which held a teflon tip seal against a 500 μm orifice. This valve worked reliably down to 250 μs duration pulse lengths. The overall gas pulse intensity was noticeably less than that from the NRC BV100, probably a consequence of shorter stroke length and the conical geometry of the tip which restricted the conductance. This valve was less suited to cluster studies, but proved more useful for the spectroscopic experiments where its greater reliability and pulse-to-pulse reproducibility were of more importance.

The cluster source faceplate followed the designs of Smalley and others. [2] It provided, in essence, a means of mounting the target rod close to the helium flowstream while vaporising, to maximise cluster intensity. A variety of different faceplate designs were used with the two valves, but all had a number of common features. The basic fixture consisted of a block of aluminium or brass with three mutually perpendicular, intersecting channels drilled through it. This block was mounted over the valve so that the clustering channel (1 mm diameter) aligned

with the valve orifice. In order to improve clustering, by maximising the number of collisions occurring before free expansion, extender channels of varying lengths (8-45 mm) and internal diameters (1.3-2 mm) were epoxied on to the outlet of the clustering channel. A typical configuration featured a 33 mm extender of 1.3 mm internal diameter. The number density in this channel at 10 bar backing pressure was approximately $3.6 \times 10^{+19}$ cm^{-3}, and a cluster formed at the beginning of the channel would undergo about 10^5 collisions before free expansion. A second channel, approximately 3mm in diameter, was drilled right through the faceplate in the horizontal plane. This channel admitted the laser vaporisation beam to the target region. A significant fraction of the gas pulse was diverted down the laser channel reducing the amount available for clustering. With the low-throughput General Valve nozzle, this necessitated narrowing the laser channel by inserting a steel slug drilled through to 1 mm internal diameter. In this way the conductance of the laser channel was reduced relative to the clustering channel, and less gas was lost. A third channel, 5 mm in diameter, was drilled vertically through the fixture at right angles to the other two. This channel accomodated the target rod and was displaced from the molecular beam axis so that the rod surface just grazed the gas flow, and did not interrupt the flowstream. The metal target rods, purchased with nominal 5 or 6 mm diameter, were turned down with emery cloth until they slip-fitted the rod channel. During an experiment, rods were continuously rotated and translated by a screw mechanism driven by a stepper motor (McLennan 34 HS-106 driving an 8-32 UNF rod). The motor speed and direction were controlled by a module in the CAMAC crate (see section 3.7). Limit switches were employed to define the region of the rod being vaporised.

3.4 TOFMS ion optics

Schematics of the ion extraction optics used for the linear and reflecting geometry TOF instruments are shown in Figures 3.4 and 3.5. The grid assembly for both the MB1 and MB2 linear TOF configurations followed the design of Wiley and McLaren [3] for a double field spatial focusing TOFMS (see Chapter 4). For the MB1 rig, the repeller, draw out and flight grid plates were fabricated from 72 mm square, 0.5 mm thick stainless steel. Holes (40 mm diameter) were cut in the draw out and flight grids to transmit the ions. To improve the field homogeneity around these plates, nickel mesh (Buckbee Mears, 90% transmission) was placed over the holes and held in place by electrically-conducting paint. Deflection plates were fabricated from 1/4" aluminium plate. The complete assembly was mounted on a 4-rod support frame, the plates being spaced at the correct distances by insulating Delrin rod.

The ion extraction optics for the MB2 linear TOFMS were fabricated in a similar manner, using the same mesh. Here, gold-plated aluminium was used for the plates (1.75 mm thick for the extraction set, 3 mm thick for the deflectors). The deflector plates could be replaced, if desired, by a three-element, cylindrical einzel lens (not used here). There was insufficient clearance to mount both the deflectors and the einzel lens together in the linear configuration. The complete assembly was mounted on a plinth which slotted over the bed bars. The plinth could be translated on the bars to the desired position before being locked in place by a clamping stock.

The extraction optics for the reflectron TOFMS geometry followed the same

Figure 3.4 : Ion extraction optics for the linear TOF mass spectrometers

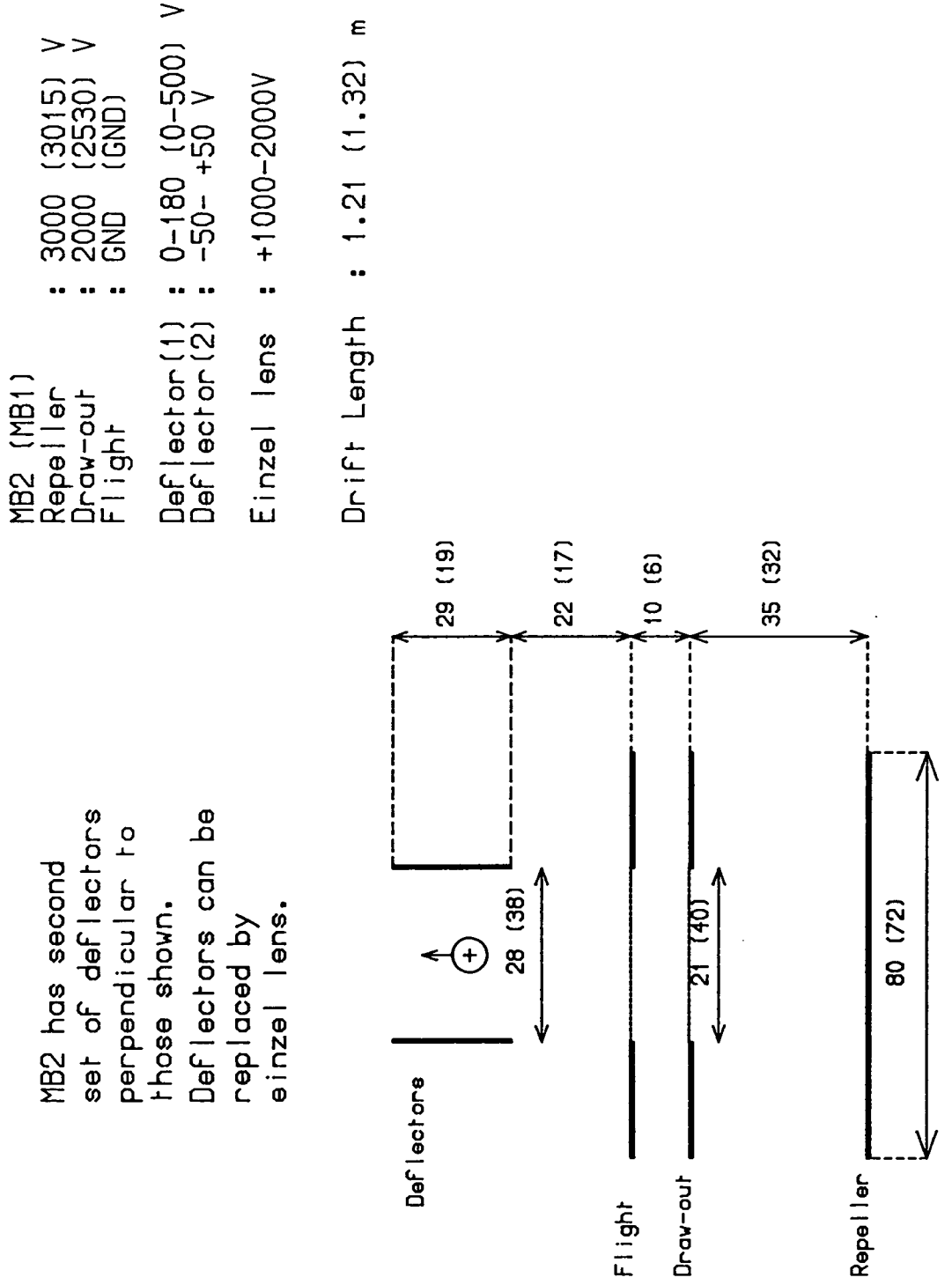

Figure 3.5 : Ion extraction optics and mirror for the RETOF mass spectrometer

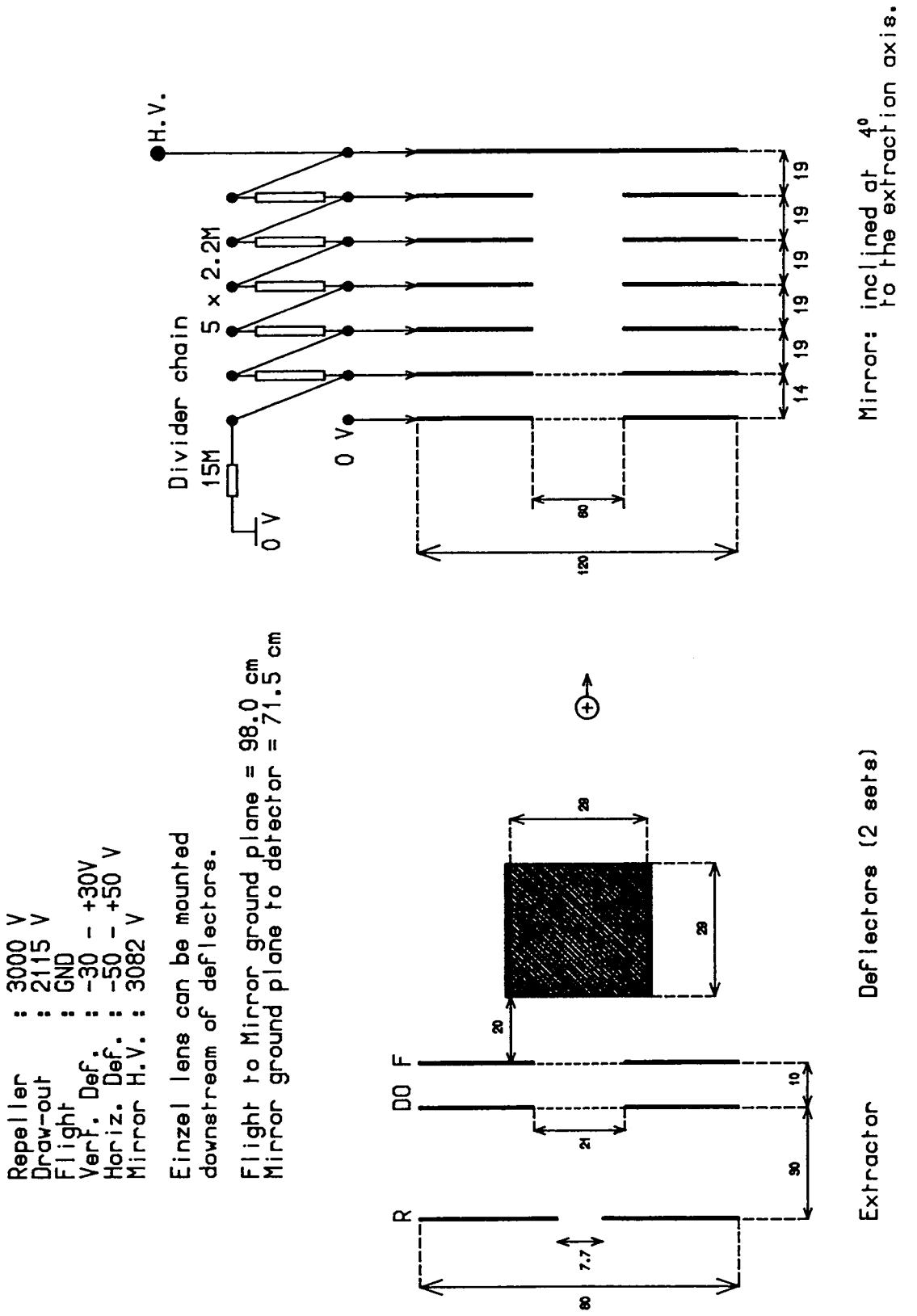

design, except that the repeller plate had a .77 cm hole cut in it to admit the molecular beam to the ion source. The aperture was not covered with mesh as this was found to cut down the molecular beam transmission considerably. The extraction assembly, including deflectors was plinth-mounted as described above.

The ion mirror for the reflectron TOFMS consisted of six stainless steel toroidal rings (12 cm outer diameter, 6 cm aperture). The apertures of the first and second rings were covered by grids (Buckbee Mears, 90% transmission), while the remainder simply acted as guard rings to improve the field homogeneity between the backplane and the mirror entrance. These optics were mounted off the mirror backplane as shown in Figure 3.5. The entrance ring was kept at ground potential to define the field free drift path. The supply voltage was dropped across these rings by a resistor network as shown. The voltage ratio between the two stages could be varied by changing the external resistance, which was mounted outside the vacuum chamber.

Voltages were supplied to the various elements for the two TOFMS configurations described above by a variety of power supplies which were changed around frequently. The types employed are listed here:

MB1:

- Repeller:- Le Croy 2415 (CAMAC crate-stationed)
- Draw out:- Power Designs 1570
- Deflection plates:- Power Designs 2K20A
- MCP detector:- Power Designs 1556C

MB2:

- Repeller:- Brandenburg 507R / Stanford PS350

- Draw out:- Brandenburg 475R / Stanford PS350 / Power Designs 1570
- Deflection plates:- Brandenburg 475R / Stanford PS325 / Power Designs 2K20A
- Ion mirror: Stanford PS350 / EG & G Ortec 556
- MCP detector:- Stanford PS350 / Fluke 408B

Voltages were delivered to the plates *via* MHV vacuum electrical feedthroughs to which fishplated wires were connected. The chambers themselves were held at ground potential in common with the extraction flight grids and supply earths.

3.5 Ion signal detection

The TOFMS ion signal was detected by a dual microchannel plate [4] (MCP) and amplified before being recorded by the digitiser. The MCP (R. M. Jordan Co.) was of a dual chevron type, with two Galileo MCP-18B plates. The active detection area was 2.48 cm^2. Individual channels in the array were 10 µm diameter, with a 12.5 µm spacing between centres. A divider chain was constructed to drop a maximum of 1000V across each plate. The gain per plate was 10^3 at 1000V, dropping to $\simeq 10^2$ with typical operating plate voltages of 700 V. The MCP was operated in grounded anode mode. [4] This means of operation made for easy coupling of the signal to the amplifier, since there was no need to capacitively-decouple the anode when it was biassed at 0 V. It also has the advantage of increased gain, since the ions are accelerated in to the MCP to strike the first plate, which is negatively biased. [5] However, it requires a grounded entrance grid to be placed in front of the biased plates to define the end of the field free drift region of the TOFMS. The transmission of this grid (82 %) reduces the overall sensitivity. The ion signal at the MCP anode was

amplified 100 times by a fast video preamplifier (Pacific Instruments 2A50). This non-inverting device had 50 Ω input and output impedances, matching the MCP anode and digitiser input.

3.6 Laser systems

3.6.1 JK HyperYAG HY750 Nd:YAG laser

The HY750 was a pulsed Nd:YAG laser used for vaporisation and pumping a dye laser. Specified output of this folded geometry, oscillator-amplifier system was 800 mJ $pulse^{-1}$ at the fundamental wavelength (1064 nm), at a 10 Hz repetition rate. Both Q-switched and fixed-Q radiation could be generated. A thermally-stabilised oven housed CD^*A and KD^*P doubling crystals for the generation of second (532 nm) and third harmonic (355 nm) radiation. Two Brewster-angled gull wing prisms enabled the various harmonics to be separated and the desired output wavelength to be selected. Pulse energies for the 2nd. and 3rd. harmonic outputs were 320 and 170 mJ $pulse^{-1}$ respectively. The laser required two 15 V trigger pulses for external control. The first triggered the flashlamps, and the second, the Q-switch. The Q-switched pulse energy could be varied by altering the time delay between the two trigger pulses. This method of varying the pulse energy was preferable to varying the flashlamp charging voltages as this could lead to thermal lensing detuning in the Nd:YAG rods. When used as a vaporisation laser, Q-switched radiation (typically 20-40 mJ in a 10 ns pulse) was focused to a 1 mm^2 spot by a 100 cm BK7 plano-convex pyrex lens. The laser vaporisation power density on the target was thus 2-4 x 10^8 W cm^{-2}. The laser power was measured before the focusing lens by a Photon

Control calorimeter calibrated at 532 nm.

3.6.2 Quanta Ray Nd:YAG-pumped dye laser system

This was a complete Nd:YAG-pumped dye laser system, consisting of a DCR-2A Nd:YAG pump laser, a PDL-2 dye laser and a WEX-1c frequency doubling and mixing accessory. The DCR-2A Nd:YAG laser had a conventional in-line oscillator-amplifier geometry, with a "doughnut"-type output coupler in the oscillator cavity. The laser could be operated in Q-switched or fixed-Q mode, and was capable of delivering 800 mJ of 1064 nm fundamental radiation in a 9 ns pulse at 10 Hz. KD^*P doubling and mixing crystals for generating 2nd. and 3rd. harmonic wavelengths were located in a thermally-stabilised oven. Specified output pulse energies were 360 mJ and 150 mJ for the 2nd. and 3rd. harmonics respectively. A Pellin-Broca prism was used to spatially separate the different wavelengths. The laser required a total of three trigger pulses for full external control. A TTL pulse initialised the firing sequence, switching high voltage on to the Pockels cell (Q-switch). A second TTL pulse, delayed by 3 ms relative to the first, triggered the flashlamps, while a third TTL pulse triggered the Q-switch. Varying the delay between the second and third pulses (over the range 130-200 μs) enabled the output pulse energy to be varied. Although this laser was intended to be used to pump the PDL-2 dye laser, it was used more extensively in the present work as a vaporisation laser. This was due to its superiority over the HY750 as regards shot-to-shot power fluctuations and beam pointing stability. When used for vaporisation, the beam was focused as for the HY750 with a 100 cm BK7 plano-convex pyrex lens. The lens-target rod distances required for a particular incident power density were slightly different because of the differing

beam divergences of the two Nd:YAG lasers. Again, the laser power was measured with a 532 nm-calibrated Photon Control calorimeter.

The PDL-2 dye laser had a conventional oscillator-amplifier layout, with an optional preamplifier. The amplifier could be pumped either longitudinally or transversely, and a 2.5 ns optical delay line could be installed if pumping dyes with high amplified spontaneous emission (ASE) levels. The grating could be tuned between 380 and 900 nm, the output bandwidth being 0.4 cm^{-1} at 500 nm. A computer-controlled stepper motor was used to drive the grating, although this could be disengaged for manual adjustment. The laser bandwidth was too large to rotationally-resolve transition metal dimer electronic spectra. Thus it was used principally as the pump laser in the two colour threshold photoionisation experiments of Chapter 6, where the grating was set on bandheads of vibronic features. In these experiments the PDL-2 was pumped by the HY750 Nd:YAG laser, since the DCR-2A was used for vaporisation. The pumping efficiency with which either Nd:YAG laser could pump the PDL-2 dye laser was approximately the same.

The WEX-1c accessory contained a range of frequency doubling and mixing crystals to extend the tuning range of the dye laser system. Dye laser radiation could be frequency doubled using one of a range of KDP (potassium dihydrogen phosphate) or $KD^{*}P$ (potassium dideuterium phosphate) nonlinear crystals. In the experiments described here, sole use was made of a KDP crystal cut at 83° to generate 4th. harmonic Nd:YAG radiation (266 nm) by doubling the 2nd. harmonic output of a Nd:YAG laser (JK HY 750). To maintain the correct phase matching relationships between the beam direction and crystal axis [6], the

crystals could be angled tuned mechanically using an integral d.c. motor. A photodiode sensor circuit was servo-locked to the tilting motor to maintain the correct tuning angle during scanning. For the fixed frequency application used here, it was desirable to utilise this facility as it guarded against thermal detuning of the doubling crystal. Dye laser and ultraviolet pulse energies were measured by a Coherent 210 average power meter.

3.6.3 Lumonics TE-861-T excimer laser

The TE-861-T excimer laser was used as a general purpose photoionisation laser. The cluster generation experiments described in Chapter 4 and the two colour R2PI spectroscopy studies described in Chapter 5 were all carried out using this laser to provide the ionising photon. This thyratron-switched laser was capable of operating on a variety of noble gas-halogen mixtures. For all the experiments performed here, it was run on the ArF line (193 nm). Specified output energy at 193 nm was 100 mJ $pulse^{-1}$ in a 8-10 ns pulse, as measured by a Photon Control calorimeter calibrated for this wavelength. As time elapsed, the Al coating on the MgF_2 rear reflector became badly etched, with a deleterious effect on performance. This necessitated changing the reflector and output coupler for a quartz set, which was used for the experiments described in Chapter 5. The laser required two 15 V trigger pulses for external operation. The first "charge on demand" pulse initialised the capacitor charging cycle, while the second pulse, delayed by 12 ms, triggered the thyratron. Varying the charging period or the peak charging voltage altered the output pulse energy.

3.6.4 Lambda Physik excimer pumped dye laser system

This laser system was employed chiefly as the excitation source in the rotationally-resolved spectroscopy of CuAg described in Chapter 5. It consisted of a EMG201MSC, thyratron-switched, excimer laser pumping a triply-amplified, etalon line-narrowed dye laser. The excimer pump laser was operated on XeCl gas mix, delivering 400 mJ of 308 nm radiation at a 1 Hz repetition rate, as measured by a pyroelectric joulemeter (Gentec ED200). At 10 Hz the pulse energy could drop to about half this value. The FL3002EC dye laser comprised an oscillator and a chain of three transversely-pumped amplification stages. 5 % of the 308 nm pump beam was split off to transversely pump the oscillator dye cuvette, which was located in a Hänsch type cavity, with a 66 x prismatic beam expander. The lasing wavelength was selected by a grating (600 lines / mm, 2.7 μ blaze) which could be tilted between Littrow angles of 42.5° and 72.5°. The laser bandwidth (0.18 cm^{-1} at 500 nm) could be narrowed by the insertion of an air-spaced intracavity etalon (ICE). [7] This etalon (free spectral range 1 cm^{-1}, finesse 25-30) narrowed the bandwidth to approximately 0.04 cm^{-1} at 500 nm, which was sufficient for recording rotationally-resolved electronic spectra of the first and second row transition metal dimers. When scanning, the etalon was angle-tuned synchronously with the grating over a maximum tuning range of 1 nm. A confocal monitor etalon accessory [7] (free spectral range 0.67 cm^{-1}, finesse 10) was used in conjunction with a diffuser and 100 cm diverging lens to verify single mode operation of the etalon-narrowed laser by projection of the interference fringe pattern on to a screen. Another integral confocal etalon (free spectral range 0.1 cm^{-1}, finesse 25) was used for recording etalon transmission

peaks for the purpose of calibrating rotationally-resolved spectra. The oscillator cuvette, used in a double-pass configuration, also served as a preamplifier, with 5 % of the pump laser used for transverse pumping. The vertically-polarised output was further amplified by passage through a second, transversely-pumped amplifier cuvette, before being expanded by a Galilean telescope (magnification = 5) into the final amplifier cuvette. Up to 12 mJ of line-narrowed output could be obtained from a dye such as Coumarin 102 lasing at 480 nm. A Gentec ED200 pyroelectric joulemeter was again used as a pulse energy monitor.

This laser system also possessed second harmonic generation (SHG) capabilities. Tunable ultraviolet radiation could be generated using the FL532B crystal tilter accessory, on which nonlinear frequency-doubling crystals were mounted. This device employed angle tuning to maintain the phase matching relationship between fundamental wave, crystal symmetry axis and second harmonic wave while scanning the fundamental wavelength. [6] The FL532B comprised a motor-driven spindle connected by a cam to an idling spindle. All the experiments described here, which involved second harmonic generation, were carried out using a thermally-stabilised β-Barium Borate (BBO) crystal (Lambda Physik FL37), which covered the range 220-305 nm. This crystal offered much higher doubling efficiencies than the alternative Potassium Penta-Borate (KPB) crystals. The doubling crystal was mounted on the first spindle, and a quartz plate was mounted on the second to compensate for beam displacement as the crystal rotated. As the fundamental wavelength was altered by the grating, the doubling crystal was tilted synchronously to maintain the correct phase angle between crystal axis and input beam. Calibration of the tilt angle-wavelength

relationship was achieved by determining the maximum intensity of the second harmonic radiation at various wavelengths across the desired tuning range. A control program stored in the dedicated microprocessor provided with the dye laser fitted a polynomial through these points, using it to calculate the correct tilt angle for all wavelengths when scanning. Separation of the fundamental from the second harmonic radiation was achieved by a harmonic separator consisting of four near-Brewster angled Pellin-Broca prisms.

3.7 Experimental control and data acquisition

These pulsed molecular beam photoionisation experiments, involving precise timing of experimental events and rapid data logging, required the development of a sophisticated computer-driven control system. Controlling the experiments was a quite formidable task, since this necessitated a great deal of interfacing between the computer and real-world hardware such as the laser instrumentation. The CAMAC (computer automated measurement and control) system, a widely-used standard in real-time experimental control, was adopted for these experiments. [8] This approach involves the use of a range of modular instruments located in a crate, controlled by software run on a microcomputer. Such an approach, in which much of the control and signal processing is carried out by dedicated devices external to the computer itself, greatly reduces the burden placed on the software itself. The control code can be written in a high level language such ac C or FORTRAN, calling machine language routines only when necessary, which convert this code into the binary format required to drive the CAMAC modules.

3.7.1 Control hardware

The onerous task of developing and integrating the hardware and software for experimental control was carried out by a colleague, A. M. Butler. [9] A block diagram of the control system architecture is shown in Figure 3.6.

The control and measurement modules conformed to the IEEE CAMAC standard. This control protocol was based on a crate (WES FHD-DV3), which provided power and data communication lines, into which CAMAC modules were slotted. A common dataway of 24 read/write lines was used to transmit data to and from the instruments. Other lines directed specific commands to the correct subaddress locations of particular module stations, acknowledged the receipt of information, or generated requests for module attention. The structure of the data bus was such that all lines except for the station address and attention request lines were connected in parallel to all stations. The crate controller (DSP 6002) was located in the rightmost slot of the crate. This accepted commands issued through the dataway from the microcomputer (IBM PC-AT) and passed instructions to the appropriate crate modules. It also transferred data recorded by modules back down the dataway to the computer for further processing.

Experimental timing control was provided by two CAMAC pulse generators. A Kinetic Systems 3655 pulse delay generator provided eight sequential TTL level pulses, each of 200 ns duration. This device was triggered by an instruction sent through the CAMAC dataway. The minimum step size which could be set between pulses was 1 μs, determined by the internal clock frequency of the pulse

Figure 3.6 : Block diagram of the experimental control hardware

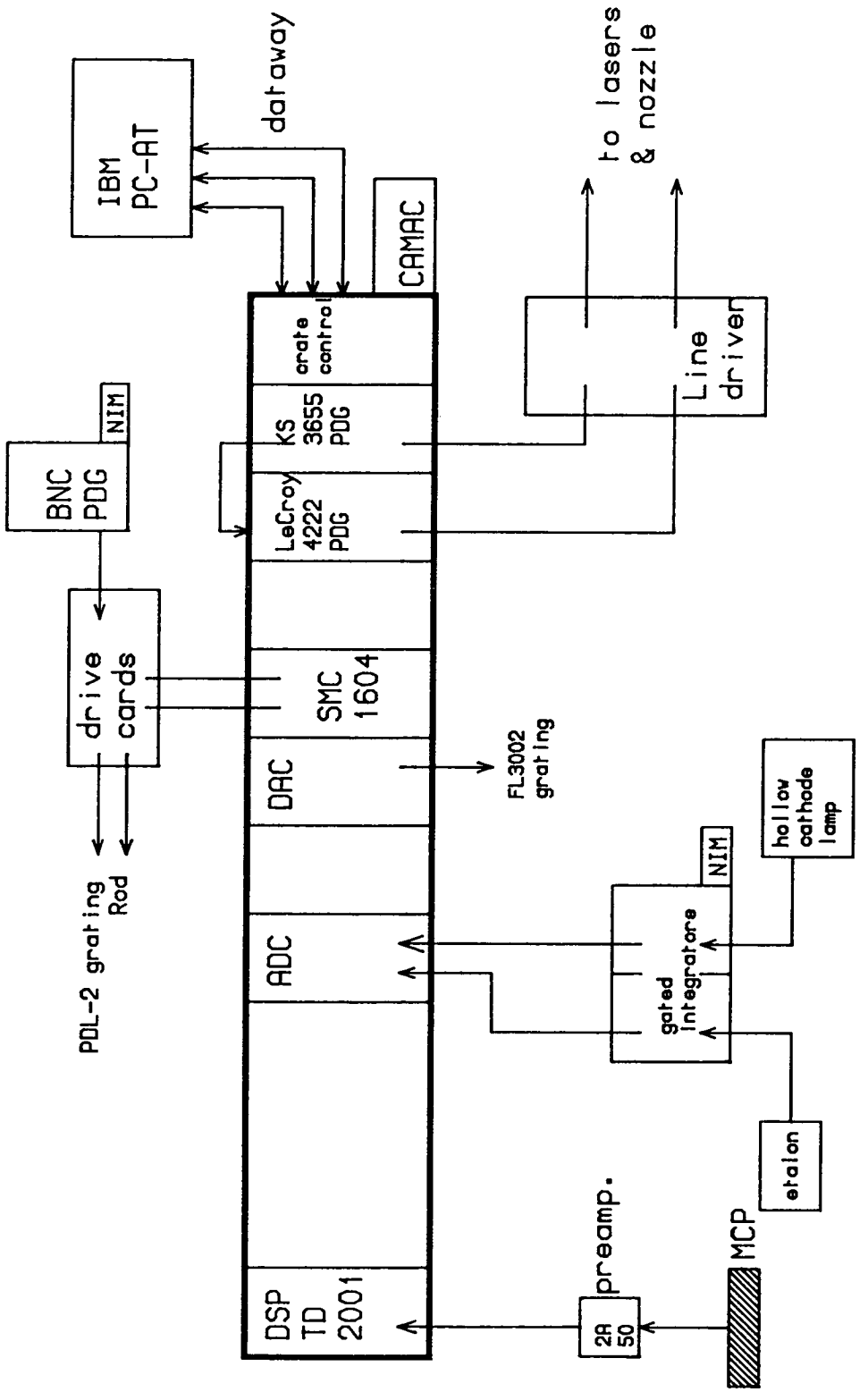

generator. The jitter between these pulses was approximately 1 ns. This module was used to trigger those devices whose relative timing in the experimental cycle was not particularly critical. For example, the molecular beam valve and vaporisation laser Q-switch were triggered by the KS 3655.

One of the channels of the KS 3655 was used to trigger a Le Croy 4222 pulse delay generator located in the neighbouring CAMAC station. This module employed fast emitter-coupled logic to generate four 100 ns duration TTL pulses of 1 ns accuracy, which could be issued in any order. Timing jitter between pulses was better than 170 ps. The 4222 pulse generator was dedicated to controlling events where very precise control of the timing was required. For example, the pump and ionisation lasers in two colour R2PI experiments and the digitiser were all triggered by the 4222.

The TTL pulses produced by both these modules did not source sufficient current to drive 50 Ω loads over long lengths of coaxial cable, as was required by the experiment. Furthermore, many devices had trigger thresholds in excess of 10 V and required trigger pulses of greater than 200 ns duration. It was therefore necessary to construct a multichannel line-driving unit capable of generating current- and voltage-boosted trigger pulses upon receipt of delay generator trigger pulses, with minimal jitter and insertion delay. Figure 3.7 shows a schematic of a single channel of the custom-built line driver unit. A TTL pulse from one of the delay generators triggered a 74221 monostable multivibrator, providing an output pulse whose length was determined by the value of the external RC time constant, either 10 or 50 µs. The 10 µs pulse was fed to trigger a 7417 driver (5 V) and the 50 µs pulse to a CMOS 40107 driver (15 V). The

Figure 3.7 : Line driver circuit diagram

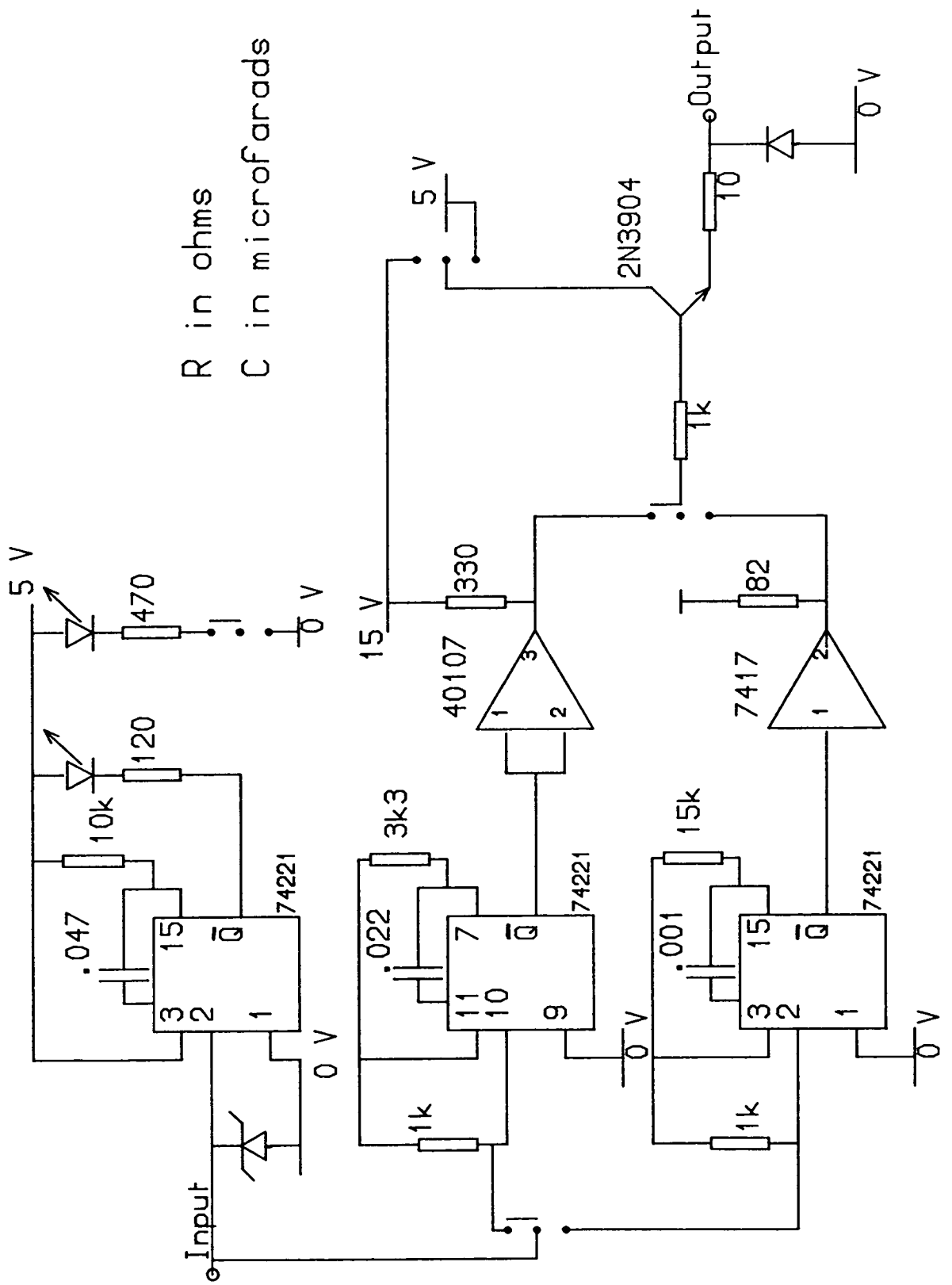

outputs from these chips drove a 2N3904 transistor with collector voltage also switchable between 5 and 15 V. These transistors were capable of driving a 50 Ω load. This circuit was replicated in a 12-channel module housed in a NIM rack. The outputs of each channel were switch-selectable between 5 V, 10 µs and 15 V, 50 µs pulses. Individual channels could be modified by changing the external resistor-capacitor network or rail voltage for specialised triggering requirements.

Control of the stepper motors which drove the PDL-2 dye laser grating and the rod translator was accomplished by a four channel CAMAC stepper motor controller (Hytec SMC 1604). The SMC 1604 supplied pulses to chopped bipolar drive cards (McLennan TM162C, 2A/phase) located in a 19" rack unit. Alternatively, the TM162C card driving the rod translator could be driven by a pulse generator external to the CAMAC system (Berkeley Nucleonics 8010). This was useful when optimising cluster signal intensity, as an important parameter was the rod rotation rate. It often proved more convenient to be able to adjust the rate manually using the 8010 pulse generator than to exit the mass spectral acquisition routine of the control program to change the SMC-determined rod rotation rate. When frequency scanning with the PDL-2, the grating was moved typically every 35 cycles (or "shots"). Stepping the grating discontinuously facilitated the accumulation of a number of single shot mass spectra at a particular wavelength before moving the grating on. Thus an improvement in the signal to noise ratio could be obtained. The SMC 1604 sent a burst of stepping pulses to the motor on every 35th. cycle. The number of single step pulses sent in each burst determined the wavelength increment.

The FL3002EC grating was driven by a single pulse from a BiRa 5408 digital to

analogue convertor (DAC). The 5408 was an eight-channel device delivering 0-10 V at 5 mA with 12 bit vertical resolution. Scanning control of the FL3002EC was provided almost entirely by its own dedicated microprocessor, with grating, intracavity etalon and crystal tilter control all programmed into a dedicated E2PROM. Driving the FL3002EC during a frequency scan required only a single pulse supplied by the DAC, the grating and associated scanning elements dwelling at rest until the next pulse was received.

The waveform generated by ions striking the microchannel plate detector consisted of a series of negative-going current pulses. Fast sampling of these electron bunches, which could be as narrow as 30-40 ns, was accomplished by a DSP 2001 transient digitiser. This CAMAC module could sample the waveform at a range of frequencies from 100 MHz to 1 MHz with a 3 ns sampling window. The maximum word length which could be stored was 32 Kb, although the maximum size which could be processed by the control program at 10 Hz was 2 Kb. The dynamic signal range was 512 mV, with 8 bit resolution on the vertical axis (0.39 %). Sampling was continuous with the digitiser continually overwriting its memory until an external "stop" trigger pulse was received. The next 2 Kb of samples recorded after this trigger pulse then became valid data for readout through the dataway. The 2001 also featured a pre-trigger sampling option whereby the digitiser could store samples received before the stop pulse, as well as those arriving after it. Since the maximum word length was 2 Kb, only a 20.48 µs time window of the complete mass spectrum could be examined at 100 MHz. Times of flight for the heaviest ions transmitted by the spectrometer could be as long as 100 µs, so recording complete mass spectra required operating the

digitiser at a lower sampling rate, with consequent loss of resolution. Portions of the high mass region could be examined under high resolution by inserting a delay between the trigger pulse for the ionisation laser and the digitiser stop trigger.

Slowly varying signals, such as those from monitor photodiodes measuring laser powers or etalon transmission fringes, were sampled by a BiRa 5303 analogue to digital convertor (ADC). The 5303 was an eight channel device with 12 bit vertical resolution. Signals from the photodiodes were first sent to NIM-housed gated integrators (Stanford Research Systems SR250) to be averaged. The averaged outputs from the SR250s were then fed to the ADC for storage.

Controlling software was run on an IBM PC-AT microcomputer, whose processors were clocked at 8 Mhz. A CAMAC interface card communicated through a ribbon cable with the crate controller. A high resolution graphics display (640 x 350 pixels) driven by an EGA 256 Kb graphics adaptor, allowed data to be displayed while the experiment was running. Data was stored on a 20 Mb fixed disk drive and could be backed up using a 5 1/4" floppy drive.

3.7.2 Control software

The control programs were written by A. M. Butler, using the C high level programming language. Some assembler functions were included to speed up certain parts of the program. [9] A constant repetition rate in the experiment was desirable to guard against thermal lensing effects detuning the Nd:YAG lasers, resulting in unnecessary fluctuations in the cluster beam intensity. Using the interrupt mechanism of the PC-AT ensured that any changes in experimental

parameters were made during the dead time between shots. This was easier than trying to synchronise the computer to the experiment using some external clock source. The interrupts were called at twice the 10 Hz repetition rate. When an interrupt was received, one of two functions was called alternately. The first function, known as TIC, armed the digitiser, loaded the time delays into the delay generators and triggered the KS3655 to initialise the experimental cycle. Once the TIC routine was completed, the processor returned to the task it was performing before interruption. A typical timing sequence as used in a two colour R2PI experiment, is shown in Figure 3.8, and is discussed in more detail below. The second function, TOC, was executed after a TIC to read data from the digitiser and ADC.

There were three modes of operation in which the experiment could be run by the control program. The simplest of these involved the display of mass spectra on the graphics display as the experiment was running. A number of single shot spectra could be accumulated before the screen was refreshed, and cumulative mass spectra could be displayed as they were progressively summed up. The horizontal scale on the time of flight display could be recalibrated into mass units if desired.

In these experiments it was crucial to establish the correct time interval between various experimental control events. Some of these, such as the delay between two pulses required to trigger a particular laser were known *a priori*. Other delays, such as those between the vaporisation laser and the peak of the cluster distribution arriving in the ion source (when the ionisation laser actually fired), could only be estimated crudely. They could only be determined accurately by

Figure 3.8 : Timing delays in a typical cluster experiment

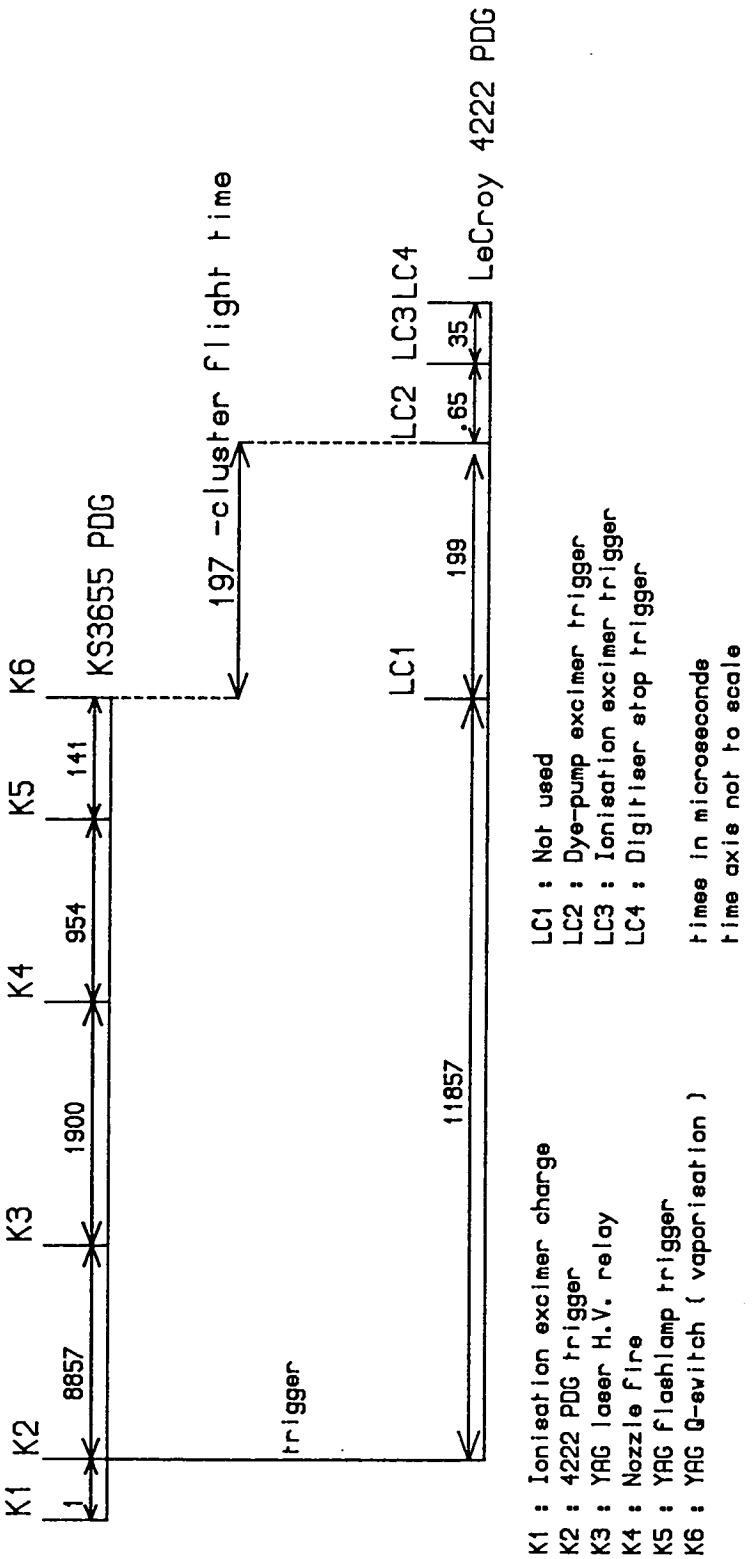

experiment. All the delays between pulses could be changed using the software while running the experiment. New delay values were simply loaded into the pulse generators during execution of the TIC function. In "timescan" mode, the control program could scan one pulse in time relative to the other pulses in the timing network, while monitoring the ion signal of a particular species. In this mode, the digitiser was used simply as a gated integrator. The time channels corresponding to a particular isotopomer peak were first determined from the mass spectrum and loaded into the signal definition routine. Up to ten different mass peaks could be monitored with this facility while some delay was scanned by recording the variation in signal in these channels. The display showed the changing ion signal as a function of the time delay. An example of scanning an important delay is given in Figure 3.8. Here, scanning the Channel 9 delay is equivalent to altering the delay between when the vaporisation laser and ionisation laser fire. In this way, the time of arrival profile of different cluster species can be mapped out (see Figure 2.1).

The timescanning technique could be very easily adapted to examining the lifetime of electronically-excited states in two colour R2PI experiments. Scanning the ionisation laser in time relative to the excitation laser mapped out the decay profile of the excited state level. The time delay corresponding to maximum ion signal could be easily found from such scans. This delay simply represented the two laser pulses being correctly overlapped in time in the ion source, giving rise to a large photoion signal as the excited state is ionised before it has had time to decay.

The third mode of control, "frequency" scanning, was very similar in principle to

the timescan facility. To record a resonant ionisation spectrum, the time channels of the species of interest were determined from the mass spectrum and loaded into the signal definition registers. The various parameters related to scanning of the PDL-2 or FL3002EC dye laser gratings were then keyed into the frequency scanning routine. In the case of the FL3002EC, since all control, apart from the grating stepping pulse, was provided by the dedicated microprocessor on the laser, the values were entered purely for consistency between the laser and the control program. The number of single shot mass spectra to be accumulated at each position of the grating was also entered. When a scan was started, the laser grating was moved under computer control while the changing mass spectrum was displayed on-screen. The average signal recorded in the time window defining a particular mass peak could also be displayed while scanning. ADC-recorded signals, such as those of the photodiodes monitoring etalon transmission fringes and the laser power, could also be displayed.

Since the transient digitiser sampling window was only open for 3 ns at each sampling point, the averaged signal which is recorded in a frequency scan is not a true reflection of the ion packet intensity. Thus frequency scanning was always carried out at the highest sampling rate (100 MHz) to maximise the number of points at which a peak was sampled, hence improving the recorded average signal.

References

[1] Adams T. E., Rockney B. H., Morrison R. J. S., Grant E. R., Rev. Sci. Instrum., **52**, p 1469, (1981)

[2] Powers D. E., Hansen S. G., Geusic M. E., Puiu A. C., Hopkins J. B., Dietz T. G., Duncan M. A., Langridge-Smith P. R. R., Smalley R. E., J. Phys. Chem., **86**, p 2556, (1982)

[3] Wiley W. C., McLaren I. H., Rev. Sci. Instrum., **26**, p 1150, (1955)

[4] Wiza J. L., Nucl. Instrum. Methods, **162**, p 587, (1979)

[5] Hellsing J. L., Karrison L., Andren H. O., Norden H., J. Phys. E: Sci. Instrum., **18**, p 920, (1985)

[6] Baldwin G. C., *An Introduction to Non-Linear Optics*, Plenum Press, New York, 1969.

[7] Demtröder W., *Laser Spectroscopy: Basic Concepts and Instrumentation*, Springer Verlag, Berlin, 1981.

[8] Costrell L., IEEE Trans. Nuc. Sci., **20**, p 557, (1973)

[9] Butler A. M., *Ph. D. thesis*, Edinburgh University, 1989.

Chapter 4
Time-of-Flight Mass Spectrometry of Elemental Clusters

4.1 Introduction

A central aspect of this work was the use of Time-of-Flight Mass Spectrometry (TOFMS) as a means of detecting laser-photoionised elemental clusters. This chapter opens with a description of the principles and operational limitations of the linear and reflecting field time-of-flight mass spectrometers which were employed in this work. The remainder of the chapter is devoted to a discussion of various cluster generation experiments in which metal atom clusters were non-resonantly photoionised and detected by TOFMS.

TOFMS is one of the simplest and most versatile techniques for the separation of ions according to mass. [1] A schematic of a prototypical time of flight instrument is given in Figure 4.1 (a). Ions are accelerated through a fixed potential difference and enter a field free drift region. Since the ions all extract the same kinetic energy from the electrostatic field, ions of different masses travel at different velocities through the drift region. It is easily shown, using Newton's equations of motion, that for any combination of extraction fields, the flight time (T) depends on the ion mass (m) according to:

$$T = Km^{1/2}, \tag{4.1}$$

where K is a constant containing terms dependent on the extraction fields, drift length, position of ionisation and charge on the ion. The lighter, faster moving

Figure 4.1 : Prototypical time-of-flight mass spectrometers

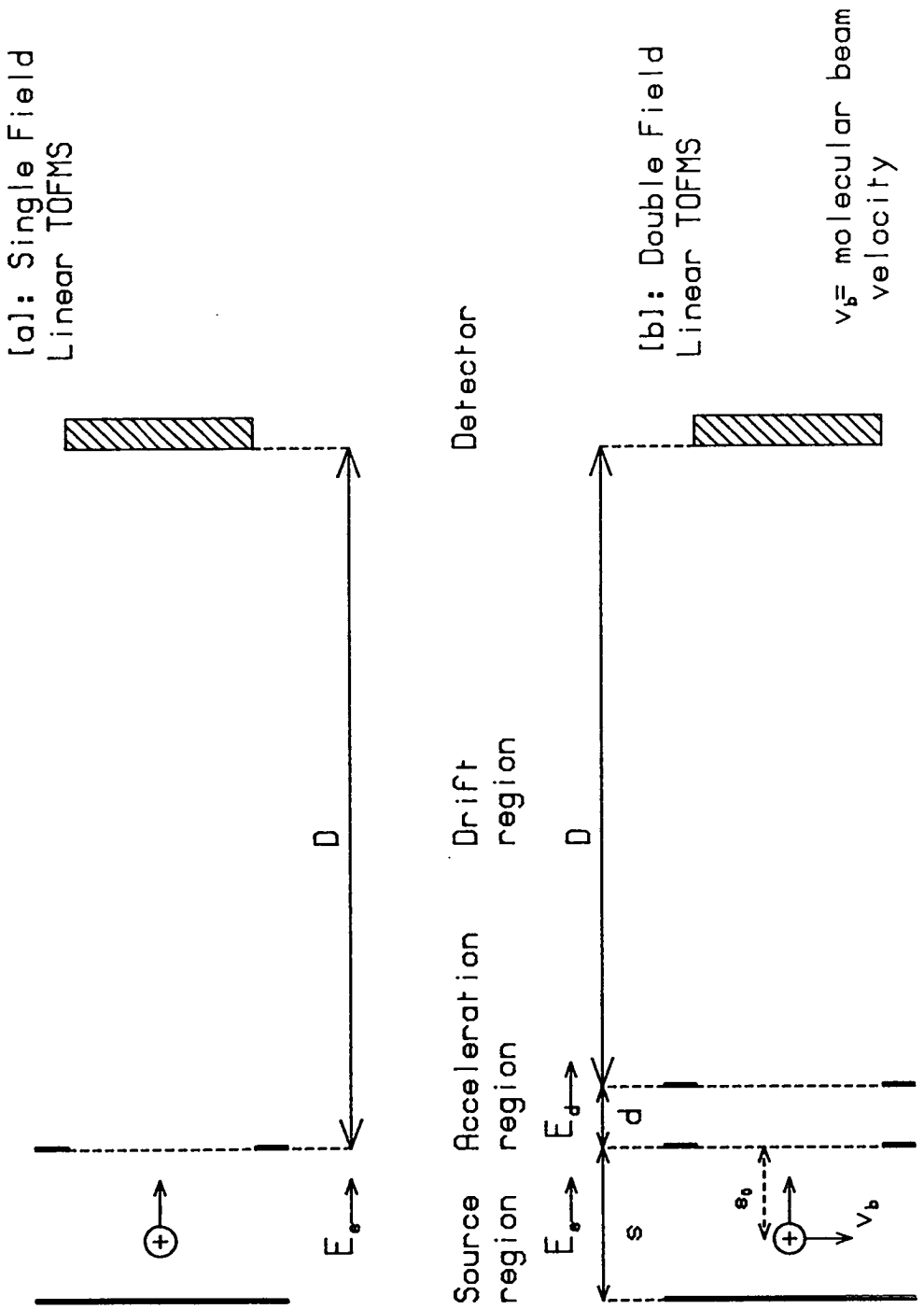

ions reach the detector before the heavier, slower ones. A spectrum of all the ion masses present is generated by recording the ion intensity as a function of time, a mass peak being recorded when a packet of ions of a particular mass arrives at the detector.

One advantage which TOFMS possesses over other mass spectrometric techniques (e.g. electric and magnetic sector or quadrupole instruments) is immediately apparent: a complete mass spectrum can be recorded for each ionisation event. Sector and quadrupole instruments are normally coupled to continuous ion sources, and detection of a range of masses relies on scanning of electric or magnetic fields so that ions of different mass impinge on the detector. Such instruments are clearly inapplicable to low duty cycle, pulsed experiments such as those described here. With a pulsed source of ions, the fields would have to be be scanned sufficiently slowly to ensure that an adequate number of experimental cycles are completed at each mass point. By contrast, TOFMS offers rapid acquisition of the complete mass range: 100 μs for a mass range of 1000 amu being typical of the acquisition time for our instruments. Furthermore, the ability of TOFMS to display a complete mass spectrum for each experimental cycle greatly facilitates the optimisation of clustering conditions, since the intensity distribution over the whole mass range can change markedly as clustering parameters are altered.

Sector and quadrupole instruments also suffer from an inherent lack of sensitivity compared to time-of-flight instruments. Owing to their spatial, as opposed to temporal separation of ions of different masses, these instruments reject all those ions not focused on the detector at a particular field setting.

When the instrument is scanned to record a mass spectrum, only a fraction of all the ions of a particular mass will be focused on the detector, at the point when the field parameters are correctly adjusted to transmit these ions to the detector. The transmitted ion intensity in TOFMS is potentially much higher. A mass spectrum is recorded without altering any field parameters, and all the ions of a particular mass are extracted along essentially the same trajectory, roughly collinear with the spectrometer axis. Thus the sensitivity of ion collection is much higher in TOFMS, in an idealised situation being limited only by the transmission efficiency of the grids defining the extraction fields.

Many quadrupole instruments have undesirably sharp mass transmission functions. An idealised TOF instrument has a much less mass-dependent transmission function, and theoretically there is no upper limit to the mass detected. (Practical constraints in a molecular beam-TOF system which affect the mass transmission are discussed later.) The open design of TOF ion source regions permits easy access by laser and molecular beams, an important consideration when designing these experiments. Also, ions can be extracted from a large area in the source, improving the sensitivity.

Apart from these considerations, a major factor in favour of TOF instrumentation is its simple construction and ease of operation. The stringent design constraints of precise mechanical alignment and uniformity of magnetic fields required for sector instruments are not necessary in the design of a TOFMS instrument.

The principal disadvantage of TOFMS compared to the other techniques is that

of its limited resolution, which in the past restricted its range of applications. Sector instruments can attain a resolving power of 100,000, while the resolution of early TOF designs was closer to 100. Those factors which determine the resolving power of a TOF mass spectrometer are now considered in detail.

4.2 Resolution

The ability of a TOF mass spectrometer to resolve two adjacent mass peaks depends on two factors: (1) the difference in arrival times at the detector between the two peaks, and (2) the temporal width of an individual peak.

Considering the first factor, since $T = Km^{1/2}$, the difference in flight times between peaks of neighbouring masses decreases as the mass increases. In other words, the mass spectral peaks "concertina" together at higher mass, with an associated degradation in the resolving power of the instrument. Secondly, the temporal width of an individual peak is related to a variety of factors which contribute to broadening and loss of resolution. Mass resolution is defined as:

$$R = m/\Delta m = T/2\Delta T, \tag{4.2}$$

for an ion of mass m, with flight time T, and overall temporal packet width ΔT. The effects of those factors which contribute to ΔT are now discussed.

4.2.1 Spatial resolution

Ionisation in the source region of a TOFMS must occur over a finite spatial volume. Consider two ions with the same mass-to-charge ratio and initial kinetic

energy, formed at the same time but at different positions on the spectrometer axis in a simple single field TOF mass spectrometer (see Figure 4.1(a)). Since they were formed at different positions along the axis, the two ions will acquire different kinetic energies from the static field, and enter the drift region with different velocities. The ion which started furthest from the draw out grid will extract the greater kinetic energy and arrive at the detector before the other ion, provided that the drift tube is sufficiently long. This difference in arrival times, due to formation of ions which sample a range of accelerating potentials, broadens the temporal profile of the ion packet arriving in the detector plane. Clearly, the use of a spatially-restricted ionisation source, such as an apertured or focused pulsed laser beam, will limit the range of ion extraction and hence also the spatial broadening contribution. However, tight focusing can lead to excessive space-charge repulsion which introduces further peak broadening. The problems of spatial effects on resolution have been elegantly solved by the development of a double field, spatial focusing instrument by Wiley and McLaren in 1955. [2] The principles of operation of the Wiley-McLaren instrument, which was mounted in both the MB1 and MB2 cluster beam rigs, is described in detail in section 4.3 below.

4.2.2 Kinetic energy resolution

Consider again two ions of the same mass-to-charge ratio, formed at the same position in the ion source, with velocities directed oppositely along the spectrometer axis. The ion which is initially travelling away from the detector must be decelerated to zero before being re-accelerated towards the detector. The two ions thus reach the detector at different times, creating additional peak

broadening. In a simple, single field instrument the effects of the initial kinetic energy on the resolution can be minimised by using a higher extraction field to increase the ratio of the ion energy to the kinetic energy spread, although the drift tube would have to be lengthened to maintain adequate time separation between adjacent masses. The narrow transverse velocity distribution afforded by a molecular beam propagating perpendicular to the spectrometer axis clearly improves kinetic energy resolution.

Wiley and McLaren, in their seminal paper on the double-field TOF mass spectrometer, described a means of energy focusing whereby a delay was introduced between the ionising pulse and the application of a pulsed extraction field. However, the gain in energy resolution is offset by a loss of spatial resolution, since the TOF mass spectrometer had to be operated away from space-focusing conditions (see Section 4.3 below).

4.2.3 Time resolution

Suppose that a laser pulse of duration Δt is used as the ionising source. Consider two ions, with identical initial positions and velocities, formed respectively by the leading and trailing edges of the light pulse. These ions necessarily arrive at the detector separated in time by an interval Δt, ignoring all other broadening contributions. When the first TOF mass spectrometers were developed, obtaining short pulses from electron beam sources, which were commonly employed for electron impact ionisation, was a considerable problem, and consequently high mass resolution was difficult to attain. With the advent of short pulse duration laser sources (10-20 ns pulses), a dramatic improvement in

time resolution was obtained. With picosecond lasers time resolution can be improved still further, although other resolution-limiting factors may then become significant.

4.2.4 Detector Response Time

Any detector will have a finite response time to the signal generated by an ion packet. In the case of microchannel plate detectors, which have found wide application in TOF mass spectrometry, this risetime is in the sub-nanosecond regime. [3] Further broadening of the ion peak may be introduced by in-line amplifiers used to boost the signal prior to sampling. Additionally, mismatching of the impedance between the detector anode, cabling, amplifier and the waveform recording instrumentation may also contribute to temporal broadening. If the final ion signal is recorded by high frequency sampling using a transient digitiser, the overall resolution will be limited by the speed at which the waveform is sampled. For example, an ion peak which is 10 ns broad (4σ width) would be detected as having a width of 20 ns if sampled at 50 MHz, and might not be registered at all if it fell between two sampling points. Similarly, fully-resolved adjacent mass peaks may, owing to the limited rate of sampling, be detected as single broad peaks.

4.2.5 Space charge effects

The temporal width of the ion packet may also be degraded due to electrostatic repulsion between ions. Parker [4] estimates that these space-charge effects become significant at ion number densities of 10^6-10^8 cm^{-3}. In the experiments

described here, the ion number density was calculated to have an upper limit of 2×10^6 cm^{-3} (see Section 4.5 below), so that space-charge effects should have a minor effect on the resolution.

4.3 The Wiley-McLaren spatial focusing TOFMS

The objective of introducing focusing conditions is to try to eliminate the dependence of the flight time of an ion on its position of formation and initial velocity. A design which eliminates the spatial dependence was realised by Wiley and McLaren over thirty years ago. [2] This section describes the focusing action of their instrument.

4.3.1 Spatial focusing conditions

Consider by way of introduction the simple, single-field TOF mass spectrometer depicted in Figure 4.1 (a). The flight time of an ion formed in the source region is given by the sum of the times spent in the acceleration and drift regions. Applying Newton's equations of motion yields the following result for the time of flight of the ion:

$$T(U_0, s_0) = (2m)^{1/2}/qE_s \, [\, U_{tot}^{1/2} + U_0^{1/2}] \; + (2m)^{1/2} D/2U_{tot}^{1/2}, \qquad (4.3)$$

where

U_0 = the initial kinetic energy of the ion

s_0 = the distance of the ion from the draw out grid

m = the ion mass

q = the ion charge

E_s = the electric field strength in the source

D = the drift length

$U_{tot} = U_0 + qs_0E_s$

If the ions are to be spatially focused after traversing the drift tube, then it is clear that a value for D must be found which satisfies the equation $(dT/ds_0)_{U0} = 0$. In other words, the flight time to the detector becomes independent of the initial ion position to a first order approximation. Qualitatively, the action of space focusing can be visualised by considering two ions with the same initial kinetic energy, formed at different positions in the source, separated by a distance Δs. The ion nearer the draw out grid enters the drift region first, but is overtaken by the other ion which acquires a higher kinetic energy (ΔsqE_s) from the field. The point in space and time at which the two ions are equidistant from the source represents the position of the spatial focus. Differentiating Equation (4.3) with respect to s_0 and setting the result to zero gives the condition for first order spatial focusing:

$$D = 2s_0. \qquad (4.4)$$

This is a purely geometric focusing condition of limited practical utility. For

example, if the position of ionisation alters, space-focusing can only be re-established by moving the detector plane to alter the drift tube length in accordance with Equation (4.4). First order spatial focusing gives drift lengths over which the ion flight times are far too short for adequate time separation of peaks. Wiley and McLaren sought a solution to the problems of limited resolution and the impracticability of a single field ion source region by examining the focusing properties of an ion source with two accelerating regions (see Figure 4.1 (b)). The flight time of an ion in this case is the sum of the times spent in three regions, namely the source, acceleration and drift regions. By applying the equations of motion as in the previous analysis, the ion flight time can be shown to be:

$$T_f = T_s + T_d + T_D, \tag{4.5}$$

where

T_s = time in source region

T_d = time in acceleration region

T_D = time in drift region.

Explicitly,

$$T_s = (2m)^{1/2}/qE_s \left[(U_0 + qs_0E_s)^{1/2} + U_0^{1/2} \right], \tag{4.6}$$

$$T_d = (2m)^{1/2}/qE_d \left[U_{tot}^{1/2} - (U_0 + qsE_s)^{1/2} \right], \tag{4.7}$$

$$T_D = (2m)^{1/2} D/2U_{tot}^{1/2}, \tag{4.8}$$

where

$U_{tot} = U_0 + qs_0E_s + qdE_d$ = total ion kinetic energy

d = length of acceleration region

E_d = field strength in acceleration region

the other terms having been defined in Equation (4.3).

When deriving the space focusing condition for the double-field instrument, it is convenient to let $U_0 = 0$. Wiley and McLaren also introduced the parameter:

$$k_0 = (s_0E_s + dE_d)/s_0E_s. \tag{4.9}$$

The time of flight equation in terms of k_0 transforms to:

$$T(0,s_0) = (m/2U_{tot})^{1/2} (2k_0^{1/2}s_0 + 2k_0^{1/2}d(k_0^{1/2} + 1)^{-1} + D). \tag{4.10}$$

By setting $(dT/ds_0)_{U0=0} = 0$ we obtain the space focusing condition for ions formed at small displacements around s_0:

$$D = 2s_0k_0^{3/2}[1 - (d/s_0)(k_0 + k_0^{1/2})^{-1}], \tag{4.11}$$

D being the drift length from the flight grid to the spatial focus located in the detector plane. There are two crucial points to grasp here. Firstly, the space focusing condition now depends on the field ratio E_d/E_s, and is no longer purely geometric. If the position of ionisation changes, a simple adjustment of this ratio, which alters k_0 in the above equation, will re-focus the spectrometer. Secondly, the resolving power of this spectrometer in the case of a spatially-distributed

source of ions is improved compared to the single field instrument. A convenient way of expressing the resolving power is to obtain an expression for the maximum mass for which adjacent peaks are just separated: Using Equation (4.1) it can be shown that:

$$T_{m+1} - T_m = ((1 + 1/m)^{1/2} - 1)T_m, \tag{4.12}$$

which approximates to $T_m/2m$.

If the ions have initially zero kinetic energy and are formed over a range of positions, $s_0 \pm \Delta s/2$, the corresponding change in flight times is denoted by $\Delta T_{\Delta s}$, then the maximum resolvable mass M_s (considering spatial broadening contributions alone) can be calculated from:

$$\Delta T_{\Delta s} \leqq T_{Ms}/2M_s. \tag{4.13}$$

$\Delta T_{\Delta s}$ can be evaluated by expanding as a Taylor series in powers of (dT/ds_0) and Δs:

$$\Delta T_{\Delta s} = (dT/ds_0)(\Delta s/2) + 1/2!(d^2T/ds_0^2)(\Delta s/2)^2 + \text{higher terms.} \tag{4.14}$$

The first term is zero from the enforced space focusing condition. If we neglect the third and higher order terms in $\Delta s/2$, and evaluate (d^2T/ds_0^2), the following expression for M_s is obtained:

$$M_s = 16k_0(s_0/\Delta s)^2. \tag{4.15}$$

Clearly, since the maximum resolvable mass depends directly on k_0, the double field instrument ($k_0 > 1$) offers higher spatial resolution than the single field one ($k_0 = 1$, since d = zero). Increasing s_0 to improve the spatial resolution relies on increasing the length of the drift region in accordance with Equation (4.15). One should not overlook the fact that the above analysis concerned ions whose initial kinetic energy is zero. The position of this spatial focus has a small dependence on the initial energy, and no analytical solution exists for the equation $(dT/dU_0)_{s0} = 0$.

4.3.2 Energy resolution

A time spread in the ion packet is introduced by the distribution of initial ion velocities along the spectrometer axis. Unlike the spatial time spread, the first order effect of the initial energy distribution cannot be eliminated. No analogous solution for $(dT/dU_0)_{s0} = 0$ exists, so there is no "energy focusing" condition. A peak broadening contribution due to the initial kinetic energy distribution is always present. This effect is readily quantified by evaluating the difference in flight times between two ions which start at the same position in the source but with velocities equal and oppositely-directed along the flight-tube axis. The ion initially travelling away from the detector will "turn around" in a time ΔT_θ until it reaches its initial position again, with the same velocity towards the detector as the other ion. Thereafter its motion is identical to the other ion, except that it always lags behind it by a time:

$$\Delta T_\theta = 2(2mU_0)^{1/2}/qE_s. \qquad (4.16)$$

It is not possible to correct for this time spread, even in the more sophisticated reflecting field instruments described in Section 4.4 below. Applying the same criterion as in space resolution for calculating the maximum resolvable mass:

$$\Delta T_\theta = T_\theta / 2M_\theta, \tag{4.17}$$

Substituting for T_θ, ΔT_θ and D/s_0 from the space focusing condition, we obtain an equation for the maximum resolvable mass due to the initial kinetic energy distribution only:

$$M_\theta = 1/4(U_{tot}/U_0)^{1/2} K_0, \tag{4.18}$$

$$K_0 = k_0^{1/2} + k_0^{-1/2} - (d/s_0)(k_0^{1/2} - 1)/(k_0^{1/2} + k_0)$$

where

$U_{tot} = U_0 + qsE_s + qdE_d =$ total ion energy.

The above equation again demonstrates the advantages of the double field acceleration geometry over the single field geometry. The maximum resolvable mass increases with k_0, so that better energy resolution can be obtained with a double field instrument ($k_0 > 1$) than with a single field one where $k_0 = 1$.

4.3.3 Overall resolution: practical design considerations

In practice, ions are formed from finite initial spatial and velocity distributions over a range of times determined by the pulse width of the ionising laser. In order to calculate the resolution for a particular mass, an estimate must be made

of the overall ion packet width at the detector. If it is assumed that the variables s_0 and v_0 are Gaussian distributed about their mean values, with full widths Δs_0 and Δv_0 respectively, then the following expressions can be applied to calculate contributions to the peak width:

$$\Delta T_s = 1/2(d^2T/ds_0^2)(\Delta s_0^2), \tag{4.19}$$

$$\Delta T_\theta = (dT/dv_0)(\Delta v_0), \tag{4.20}$$

assuming that the instrument is spatially focused. The laser temporal profile can also be approximated by a Gaussian function, with full width at half maximum of ΔT_{laser}. An estimate for the overall peak width can be obtained by convoluting the three distributions and calculating the overall FWHM thus:

$$\Delta T_t = (\Delta T_s^2 + \Delta T_\theta^2 + \Delta T_{laser}^2)^{1/2}. \tag{4.21}$$

In designing an operational double field spectrometer, the system parameters must be chosen judiciously to give an optimum combination of high mass resolution and efficient ion transmission. How much importance is attached to each depends on the application envisaged.

Equation (4.15) indicated that the spatial resolution increased with s_0^2. In practice, s_0 will be limited by the physical dimensions of the ion source region itself, and a compromise solution must be sought. Accelerating the ions to a high total kinetic energy improves the energy resolution, since U_0 is then a smaller fraction of the total energy. An undesirable corollary is that the flight times may

become too short for adequate discrimination by the detector. M_θ can be increased by extending the drift length D, but such a modification must be traded off against the additional loss of ions which have velocity components perpendicular to the flight tube axis.

It might be thought that the spatial resolution could be further enhanced by operating under the additional constraint (d^2T/ds_0^2) to eliminate the second order terms from Equation (4.14). However, in order to satisfy this condition a short drift tube is required, which leads to unacceptably short flight times, negating the improvement in spatial resolution. Practical spectrometers operate with (d^2T/ds^2) = a maximum, a condition corresponding to a long drift tube.

A final practical consideration arises from the orientation of the spectrometer axis with respect to the molecular beam direction. (See Figures 3.1, 3.4 and 4.1 (b).) Ions extracted into the flight tube will retain the component of velocity parallel to the molecular beam direction. In order that they are steered on to the detector, and do not simply strike the walls of the flight tube before reaching it, they must be deflected back on to a trajectory parallel to the spectrometer axis. This is accomplished using a pair of biased parallel plates mounted above the extraction ion optics (see Figures 3.1 and 3.4). To compensate completely for the molecular beam velocity component v_b, requires the application of an electric field strength E_{def} across the plates, where:

$$E_{def} = (2mU_{tot})^{1/2} v_b / qL_{def}, \qquad (4.22)$$

in which

U_{tot} = the total kinetic energy of the ion entering the drift region

m = the ion mass

q = the ion charge

L_{def} = the axial length of the deflection plate.

Since all the cluster species in the beam are aerodynamically accelerated to approximately the same velocity v_b, irrespective of mass (see Section 2.3), the transmission function is clearly mass dependent. The deflection voltage must therefore be altered to optimise the transmission of different masses on to the detector. Curves showing the mass dependence of the transmission function of the MB2 linear TOF instrument are plotted in Figure 4.2. The data was obtained from experiments involving 266 nm photoionisation of niobium cluster distributions. As the relative concentrations and photoionisation efficiencies of the neutral precursors are not known, a mass versus voltage plot cannot be obtained directly. Instead, the intensities of specific masses were monitored as a function of the deflection plate voltage and plotted as a family of curves. It is evident that the mass transmission is not too sharp a function of voltage, and by judicious selection of the deflection plate voltage, appreciable transmission over a wide mass range can be achieved.

The experimental parameters for the operation of the MB1 and MB2 linear TOF spectrometers were chosen with all the above caveats in mind. Table 4.1 gives the operating parameters for the spatially-focused MB1 linear TOF instrument. Figures 4.3 and 4.4 show the dependence of ion flight time on s_0 and v_0

Figure 4.2 : Mass transmission function of the MB2 linear TOF mass spectrometer

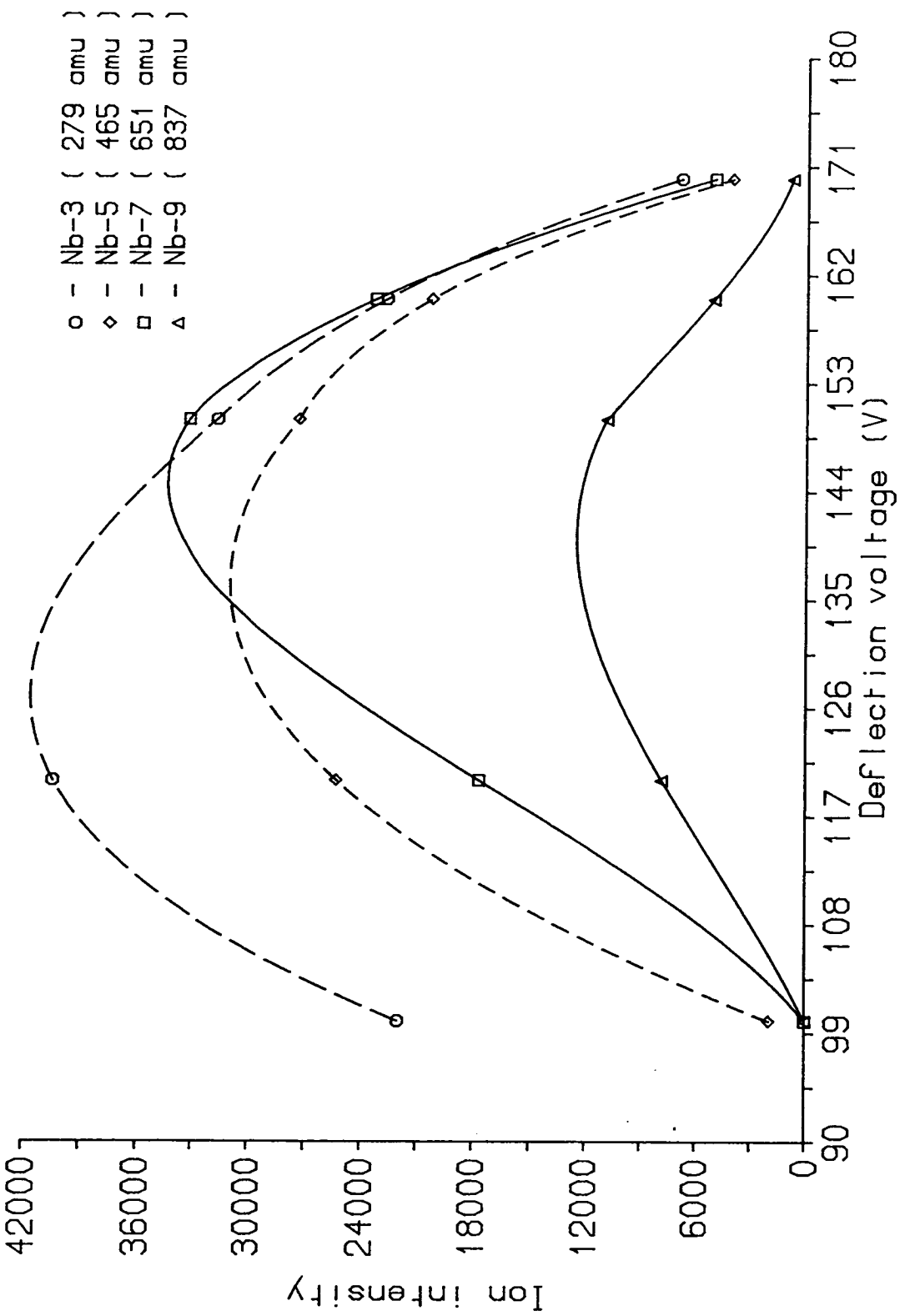

$(=(2U_0/m)^{1/2})$ for $^{98}Mo^+$. At a "worst case" translational temperature of 30 K, the full width at half maximum of the velocity distribution is approximately 120 ms^{-1}. The range of flight times corresponding to this range of velocities is 8.77 ns wide. In an idealised spatially-focused instrument, the main contributions to peak broadening come from the initial kinetic energy distribution of the neutral precursors and the ionising laser pulse width.

Figure 4.5 shows the atomic isotope distribution for molybdenum recorded with the MB1 linear TOF instrument, using an ArF excimer laser (193 nm) as the photoionisation source (see Section 4.7). Evidently, the individual mass peaks are significantly broader (typically 20-25 ns) than predicted by the model above (12.6 ns). The discrepancy is too large to be ascribed simply to the limited signal sampling rate (100 MHz ≡ 10 ns interval). To account for the discrepancy, some aspects of non-ideality in the experimental TOFMS must be recognised.

For example, the drift region is not truly field-free on account of the presence of the deflection field. Although this field is predominantly directed perpendicular to the spectrometer axis, there will be a component acting parallel to the axis due field penetration around the ends of the plates. Broadening of the peak could result from the fact that the ion formation region has a finite length along the molecular beam axis. Ions formed furthest upstream will pass closer to the grounded plate and suffer less of a retardation than those passing closer to the positively biased plate. Further non-ideality is introduced by field inhomogeneities in the source and acceleration regions themselves. Figure 4.6 shows a contour plot of the potentials in the source region generated by a

Figure 4.3 : Ion flight time vs. position of formation in the source of the MB1 linear TOF instrument

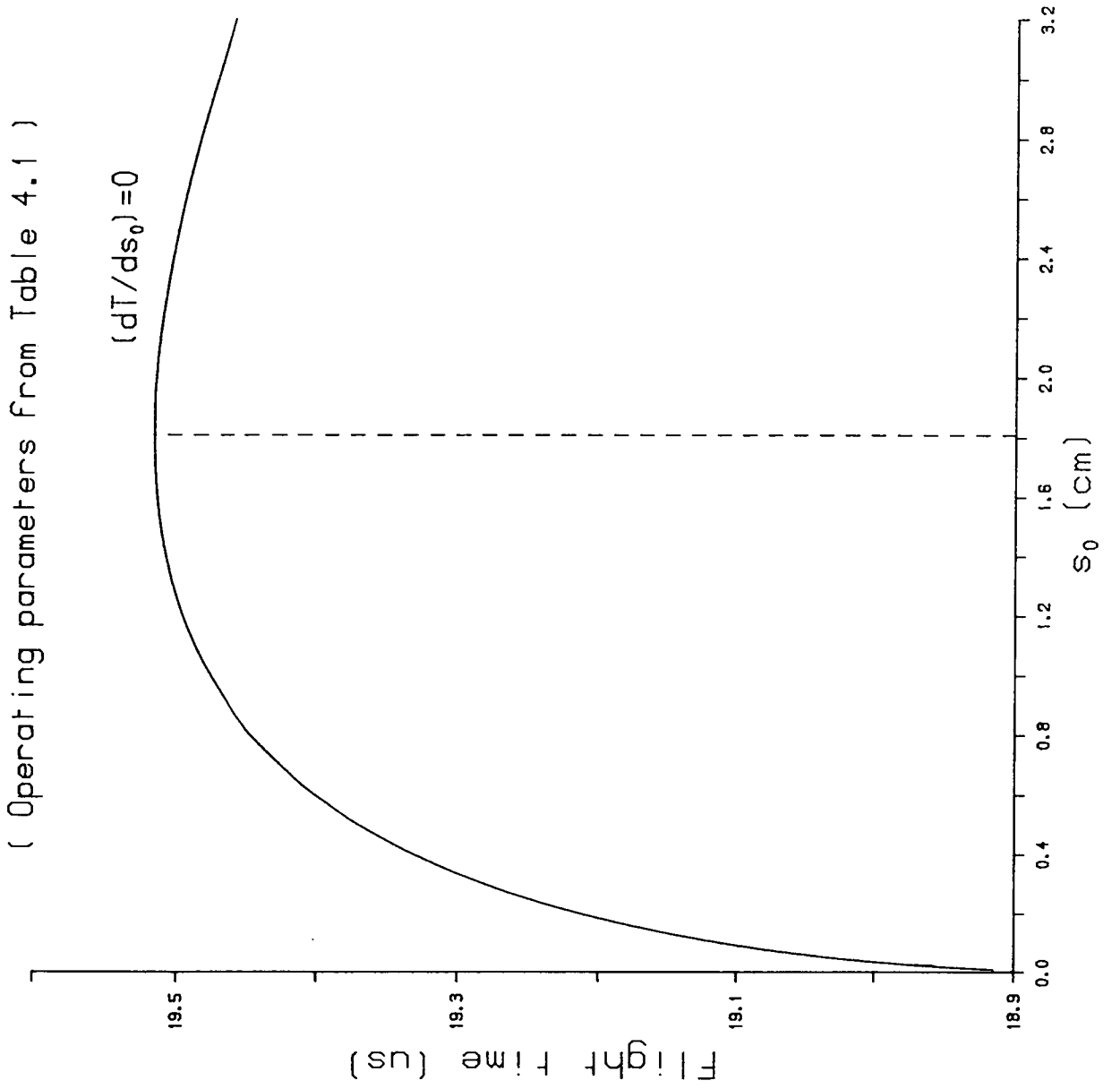

Figure 4.4 : Ion flight time vs. initial ion velocity for the MB1 linear TOF instrument

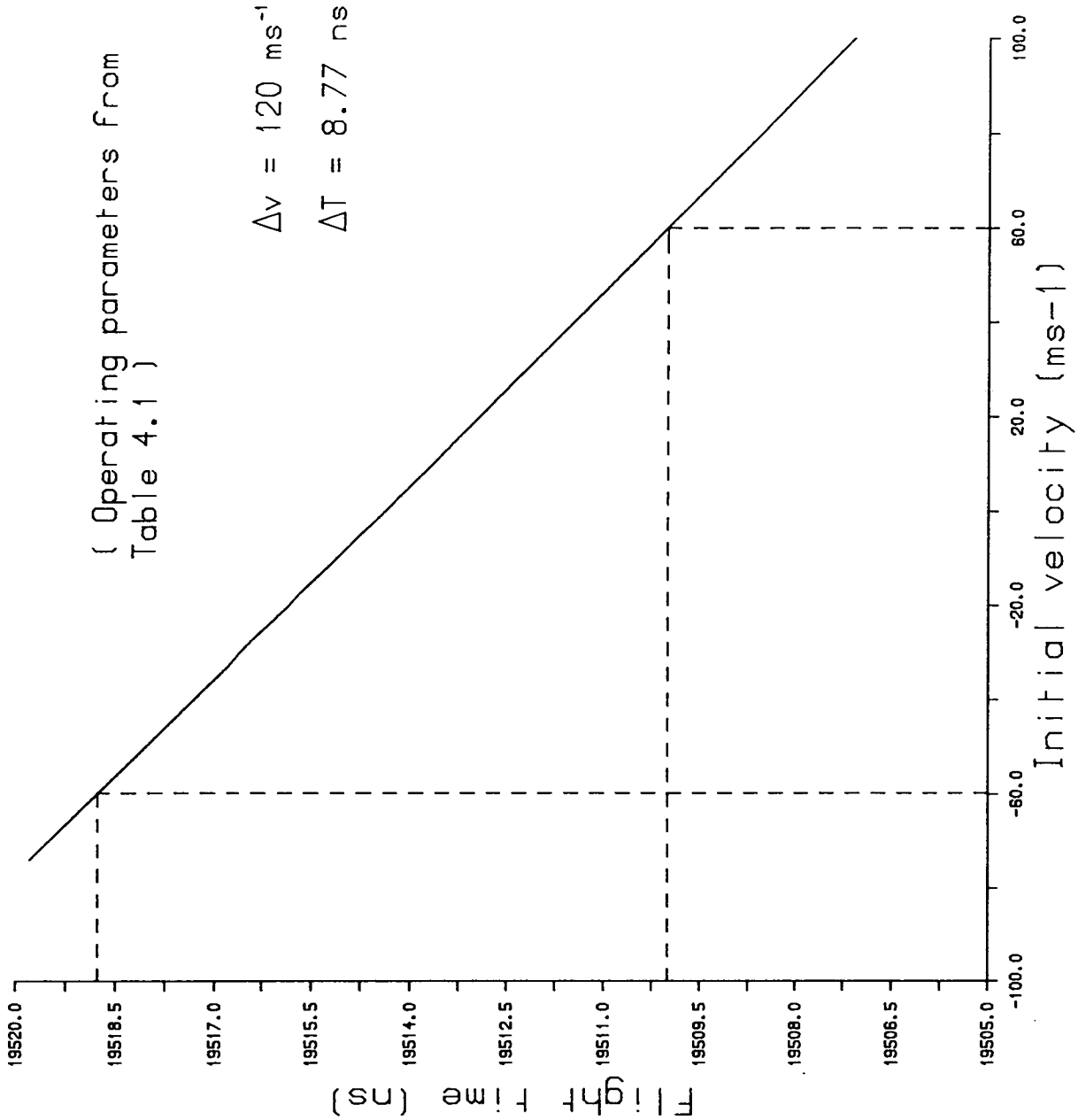

Figure 4.5 : TOF mass spectrum of molybdenum isotopes recorded on the MB1 linear instrument

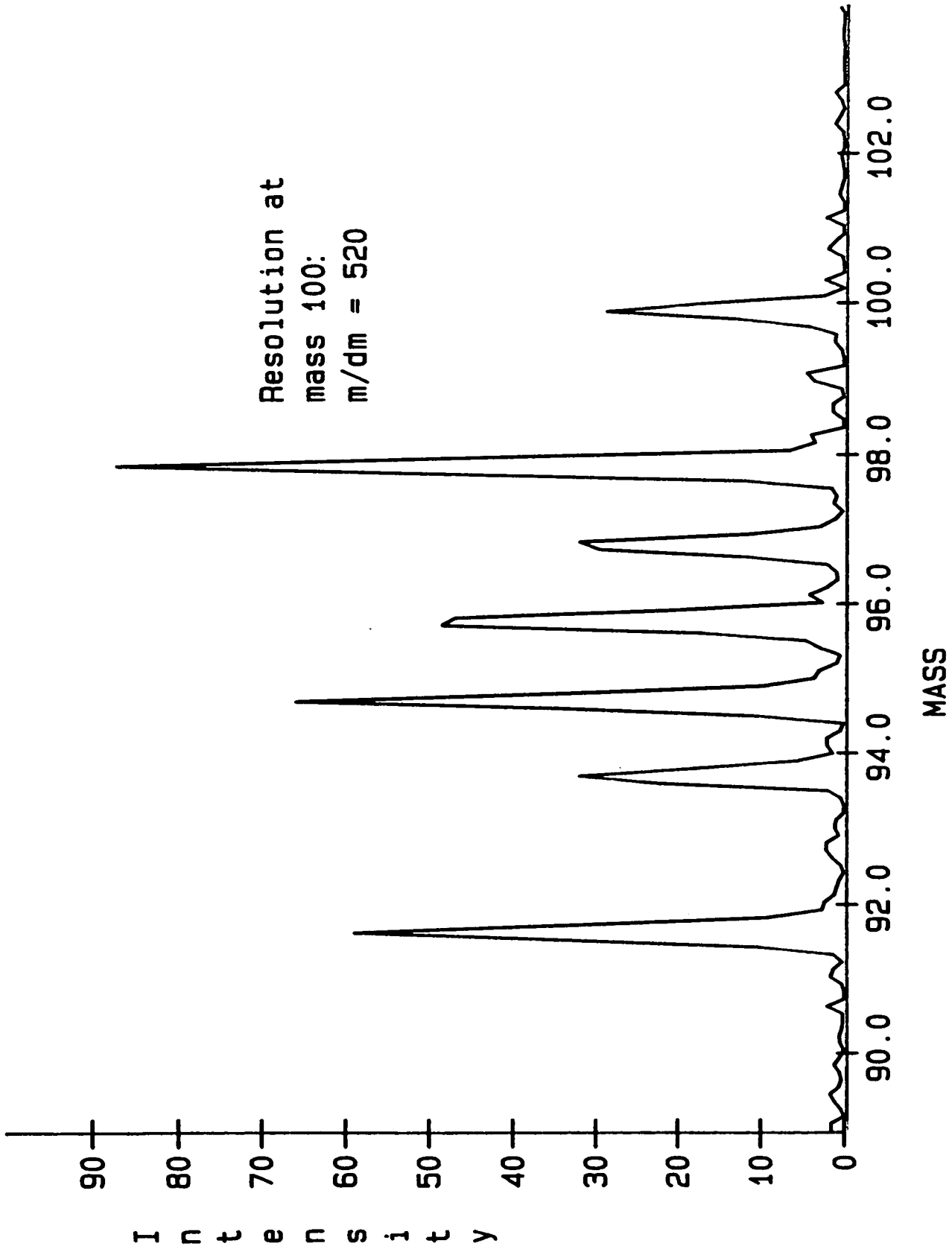

Table 4.1 : MB1 linear TOFMS performance

System parameters

Repeller to Drawout grid:	3.2 cm
Drawout grid to Flight grid:	0.6 cm
Drift length:	132.0 cm
Repeller plate voltage:	3000 V
Drawout grid voltage:	2555 V
Flight grid voltage:	0 V
E_s =	139.1 V/cm
E_d =	4258.3 V/cm
k_0 =	12.483

Calculated Performance (definitions in text)

Data for $^{98}Mo^+$, with initial maximum kinetic energy of 0.004 eV, spatially distributed (± 0.05 cm) about s_0 = 1.6 cm. Assumed that the signal sampling interval is small compared to the peak width.

ΔT_s =	0.63 ns
ΔT_θ =	8.77 ns
ΔT_{laser} =	9 ns (FWHM)
ΔT_t =	12.58 ns
Calculated resolution at mass 98:	776
Observed resolution at mass 98:	520
Calculated maximum resolvable mass:	915

Figure 4.6 : Contour plot of the potential distribution in the source region of the MB1 linear instrument

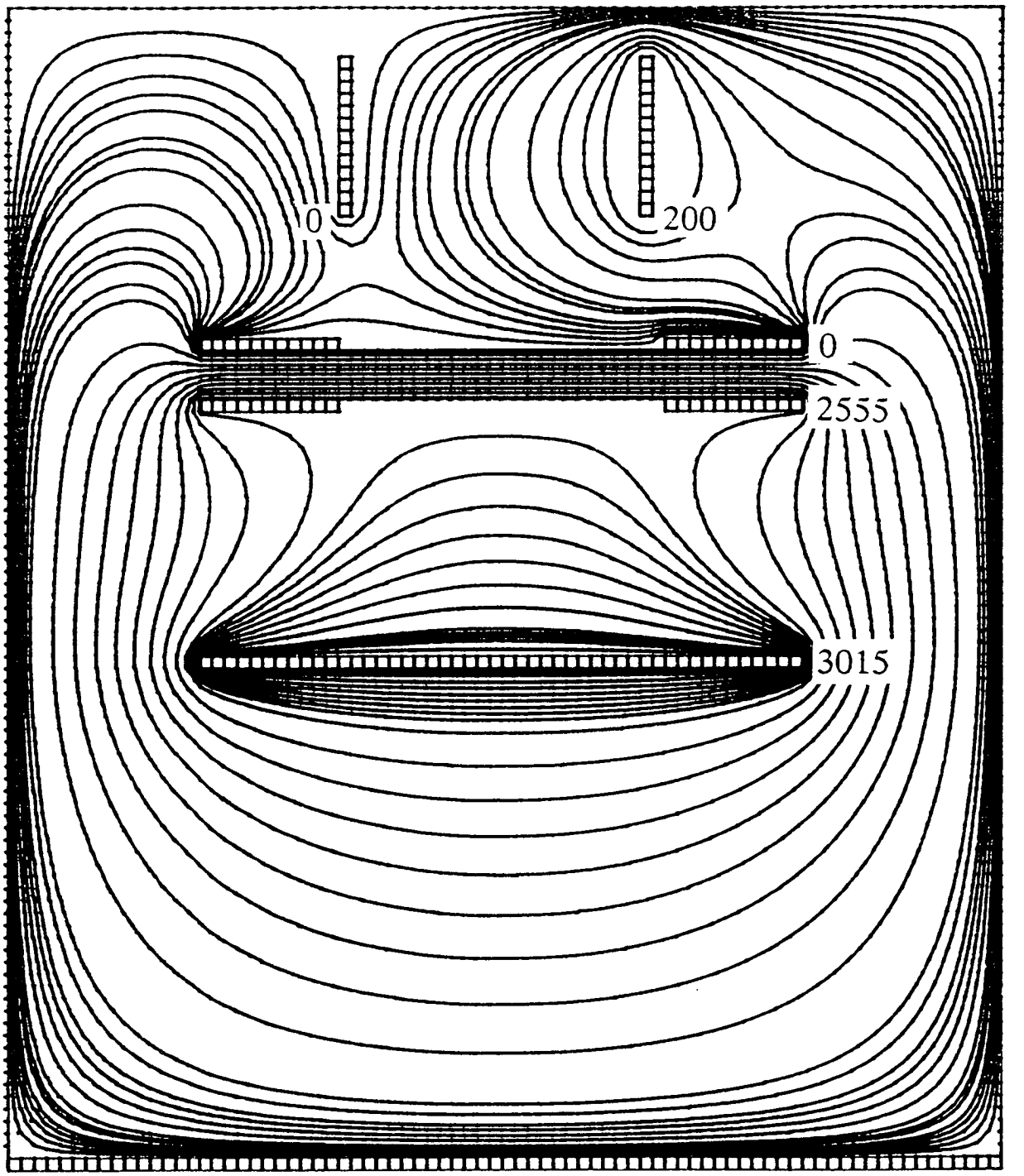

numerical solution of Laplace's equation in two dimensions (see Appendix B). There is obviously a certain amount of field penetration at the edges of the plates. Owing to this leakage, the fields in the source and acceleration regions will differ from the values set to satisfy the space focusing condition. Indeed, it may be no longer possible to satisfy this condition at all: the original equations of ion motion assumed constant field strengths in each region, which could only be realised by assuming infinitely large grid planes. The effects of field penetration around the source could be reduced by introducing guard rings between the plates to improve the field homogeneity in this region. This is not really practicable with perpendicular extraction of ions from a molecular beam since it is then more difficult to introduce the molecular beam and laser beams.

The overall effects on resolution of these inhomogeneities have been tackled with typical thoroughness by Cartwright. [5] He generated a two-dimensional potential map for the source and deflection plate region using the Laplace relaxation method described in Appendix B. Monte Carlo methods were employed to select initial values for the ion position (in two dimensions), its velocity and the time of its formation, simulating the creation of a large number of ions in the source. Ion trajectories were followed through the inhomogeneous potential, and the arrival times in the detector plane used to synthesise a mass spectral peak width. With an ionisation region measuring 10 x 1 mm, overall peak widths of 28 ns were calculated for ions of mass 98, in much closer agreement with the experimental value. It was found that the field in the region of the deflection plates had little effect on the peak width, but that the major effect was due to inhomogeneous fields in the source. In fact, the MB2 linear TOF instrument was

frequently operated well away from the supposed spatial focus to optimise the ion transmission, without any significant deterioration in resolution.

4.4 The Mamyrin reflecting field TOFMS

The Wiley-McLaren spatial focusing TOFMS represented a milestone in the quest for improved resolution in TOF mass spectrometers. However, the maximum resolvable mass that was attainable, several hundred at best, still lagged far behind the performance of sector instruments, where ions with masses of several tens of kiloDaltons could be resolved. There was clearly scope for the development of a higher resolution instrument, the impetus being provided by the wide range of potential applications in spectroscopy and analytical science.

In an ideal linear TOFMS instrument, the spatial and kinetic energy resolution are enhanced by increasing k_0. In practical terms, this requires the drift region to be lengthened, with a consequent loss in overall ion transmission. The compromise between resolution and instrumental sensitivity prevents the attainment of really high mass resolution. The novel solution developed by Mamyrin and co-workers [6] was to introduce a reflecting field in the drift region, as shown in Figure 4.7. This has a focusing action to compensate for the range of kinetic energies possessed by ions formed over a range of positions in the ion source.

4.4.1 Energy focusing in the RETOFMS

To analyse the operation of a reflecting geometry TOFMS, we consider only ions

Figure 4.7 : Schematic of reflecting field TOF mass spectrometer

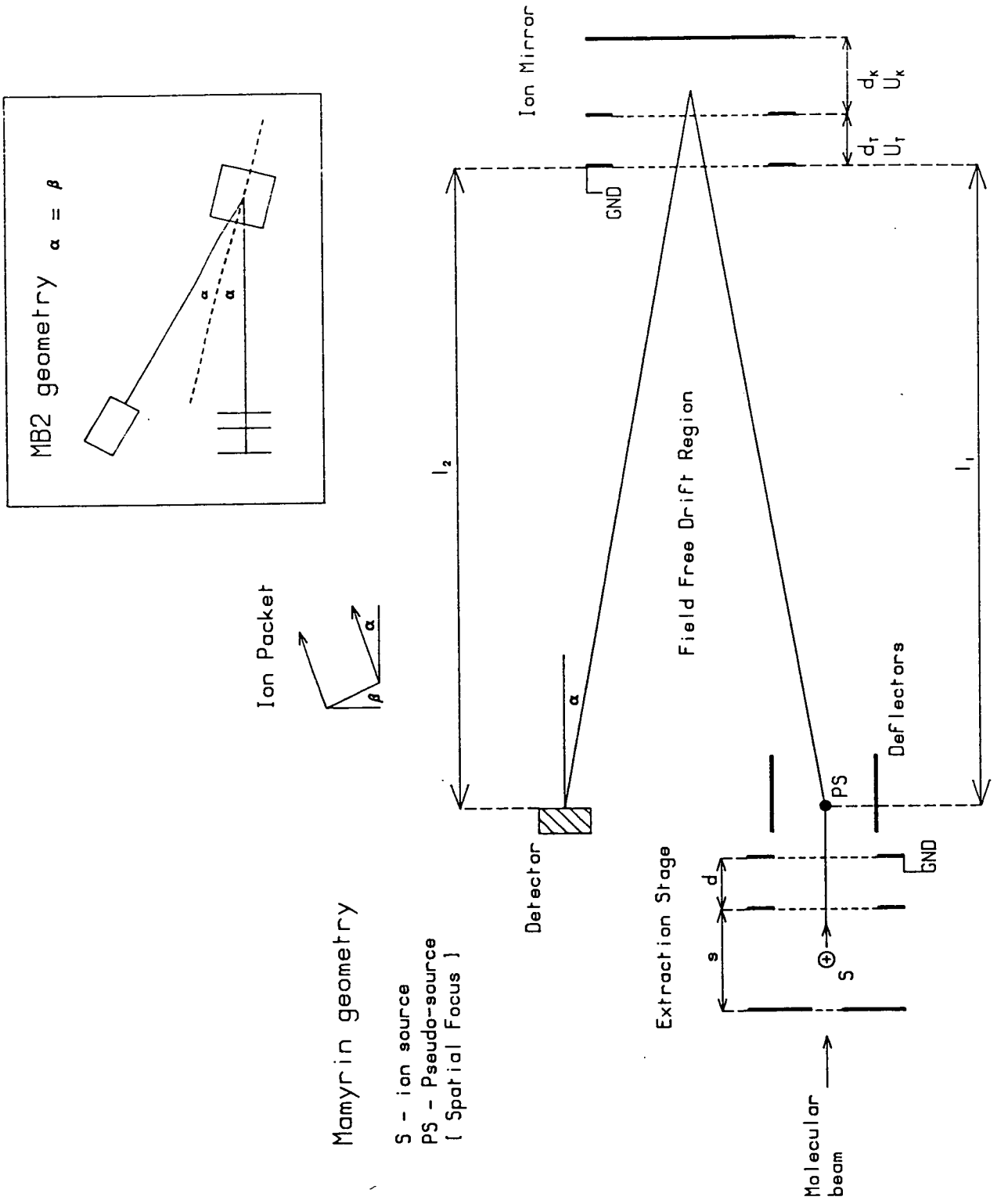

formed over a range of positions in the source which have zero initial kinetic energy. Fields in the extraction/acceleration stage are chosen so as to bring the ions to a Wiley-McLaren spatial focus part-way into the drift region. This point is reached by all ions at the same time, although they have a range of kinetic energies owing to the range of positions over which they were formed. If the ions now drift further before encountering a detector, the individual peaks become increasingly separated in time. However, because of the distribution in kinetic energies, the peaks broaden at points beyond the spatial focus position, and resolution is lost. The ions now encounter a two-stage reflecting field, held at a total potential higher than the potential used to extract the ions from the source. The ions are decelerated to rest by this electrostatic "mirror", and their directions are reversed. For a particular ion packet, the faster moving ions, which arrive at the reflector earlier, bury deeper into the reflecting field before coming to rest compared to the slower ones at the trailing edge of the ion packet. Parameters are chosen so that the extra time the fast ions spend in the reflector exactly compensates for their initial time lead. In this way, the ions may be brought to a focus in the plane of the detector placed at the end of a second drift region. The original narrow ion packet width at the Wiley-McLaren focus is preserved after a long drift period. Thus peak widths are kept narrow while the time interval between adjacent masses increases. The net result is that the overall resolution is increased significantly compared to the linear TOFMS.

The mathematical treatment to derive a focusing condition for the RETOFMS is fairly straightforward. The energy of an ion at the Wiley-McLaren space focus, or "pseudo-source", is conveniently written as kqU_0, where qU_0 is the average

kinetic energy of ions at this point, and k is a numerical factor, approximately equal to unity, specific to a particular ion. Ions formed at different positions in the source will have different values of k. qU_0 is simply determined by the total energy the ion acquires upon extraction from the source. With reference to Figure 4.7, and applying Newton's equations of motion, the total flight time of an ion of mass m from the "pseudo-source" to the detector is given by:

$$T_{tot} = T_L + T_T + T_K, \tag{4.23}$$

where

$$T_L = L(2qU_0/km)^{1/2} \tag{4.24}$$

is the flight time through the two drift regions

$(L = l_1 + l_2)$,

T_T is the total flight time through the retarding field region, and is given by the expression:

$$T_T = 4d_T(2qU_0/m)^{-1/2}(U_0/U_T)[k^{1/2} - (k - (U_T/U_0))^{1/2}], \tag{4.25}$$

where

d_T = the length of the retarding region

U_T = the voltage applied across it.

Finally, T_K is the time the ion spends in the second, reflecting stage of the

mirror:

$$T_K = 4d_K(2qU_0/m)^{-1/2}(U_0/U_K)[k - (U_T/U_0)]^{1/2}, \quad (4.26)$$

where

d_K = the length of reflecting region

U_k = the voltage applied across it.

It is useful to express the total flight time (T_{tot}) as a function of k thus:

$$T_{tot} = CF(k), \quad (4.27)$$

where C is a constant and

$$F(k) = A_1/k^{1/2} + nA_1(k^{1/2} - (k-p)^{1/2}) + (k-p)^{1/2}, \quad (4.28)$$

in which

$n = 4d_T U_0/LU_T$

$p = U_T/U_0$

$C = 4d_K(2qU_0/m)^{-1/2}U_0/U_K$

$A_1 = (L/4d_K)(U_K/U_0)$.

To derive the focusing conditions, we attempt to find the parameters for which the flight time is independent of the kinetic energy possessed by the ions at the "pseudo-source". In other words, for second order energy focusing of the reflectron, we require that:

$$(dT/dU)_{U=U0} = 0, \tag{4.29}$$

$$(d^2T/dU^2)_{U=U0} = 0. \tag{4.30}$$

These expressions can alternatively be couched in terms of F and k:

$$(dF/dk)_{k=1} = 0, \tag{4.31}$$

$$(d^2F/dk^2)_{k=1} = 0. \tag{4.32}$$

Since $n << 1$ normally, we obtain the following solution satisfying the above conditions:

$$A_1 \simeq \sqrt{3},\ p \simeq 2/3,\ (F)_{k=1} = 4/\sqrt{3}.$$

The reflectron is operated coupled to a double field Wiley-McLaren source, focusing in the first drift region. L, the total effective drift length, can then be evaluated and the voltages U_T and U_K set to satisfy the focusing relations. It is not necessary to use a double field extraction source, since the fully-geometric spatial focusing condition ($D = 2s_0$) gives a focal point just into the drift region. In the original Mamyrin design shown in Figure 4.7, a set of electrostatic deflectors are used to impart a transverse velocity component on the ions so that they follow the desired "V-shaped" trajectory.

With first- and second-order kinetic energy focusing conditions satisfied, only third-order and higher terms will contribute to the spread in the ion packet

width, which is traceable back to the original spatial distribution in the source. Of course, the problem of the initial kinetic energy distribution in the source region remains. The time lag between ions leaving the source "early" and those leaving "late" owing to their oppositely-directed velocities will be preserved throughout the reflectron to the detector. In other words, there is no solution to $(dT/dU)_{U=U0} = 0$, where T is the total flight time, including the source-to-pseudo-source flight time.

An additional contribution to the width of the ion packet arises from its deviation from a plane perpendicular to the axis of the TOFMS (angle β in Figure 4.7). The temporal broadening effects of this term have been investigated by Mamyrin and co-workers, [7] who found that it can be eliminated by ensuring that $\beta = 0$.

4.4.2 Overall resolution and system performance

The MB2 reflectron instrument was constructed broadly along the lines of the Mamyrin design, except that the ion mirror plane was angled with respect to the extraction optics (see Figure 4.7 inset). This geometry was chosen for ease of construction of the vacuum equipment, since the three MB2 chambers could then be mated on a common axis. The molecular beam and the ion extraction axis (first drift region) were aligned collinearly, with the core of the neutral beam admitted to the ion source through an aperture in the repeller plate. The second drift axis was angled at 8° with respect to the first, with the ion mirror axis bisecting this angle.

In this way, the deflecting force is provided by those components of the retarding

and reflecting fields in the mirror which act perpendicular to the axis (Esin4°). This should remove the need for electrostatic deflectors in the first drift region as employed in the Mamyrin design. However, accurate alignment of the mirror assembly at the required angle was not easily accomplished, and failure to do so could result in a loss of transmission and resolution. Thus it was felt prudent to include a set of XY deflection plates in the first drift region to increase the flexibility of beam steering. It should be noted that when the mirror is angled with respect to the extraction axis, the ion packet is no longer extracted at $\beta = 0$ (Figure 4.7), resulting in a small temporal broadening contribution to the ion packet width. Fortunately, its magnitude is negligible for the shallow angles used here.

The geometry adopted offers a number of advantages over a perpendicular extraction configuration. Photoions are extracted directly into the RETOFMS parallel to the direction of motion of their neutral precursors, without suffering a 90° change in trajectory as in the perpendicular TOFMS. This, in theory, gives a dramatic improvement in the ion intensity transmitted into the mass spectrometer, as the problems of compensating for the molecular beam velocity are largely eliminated. Maximum signal intensities recorded with the RETOF geometry were typically twice those recorded under the same conditions on the linear instrument. Also, the mass-dependence of the transmission function should be greatly reduced for the same reasons, as was confirmed by experiment. In an idealised situation, the transmission function of this reflectron geometry should be mass independent. Figure 4.8 (a) and 4.8 (b) show TOF mass spectra of niobium clusters recorded on the MB2 linear and RETOF instruments. The

Figure 4.8 (a) : TOF mass spectrum of niobium clusters recorded on the MB2 linear instrument

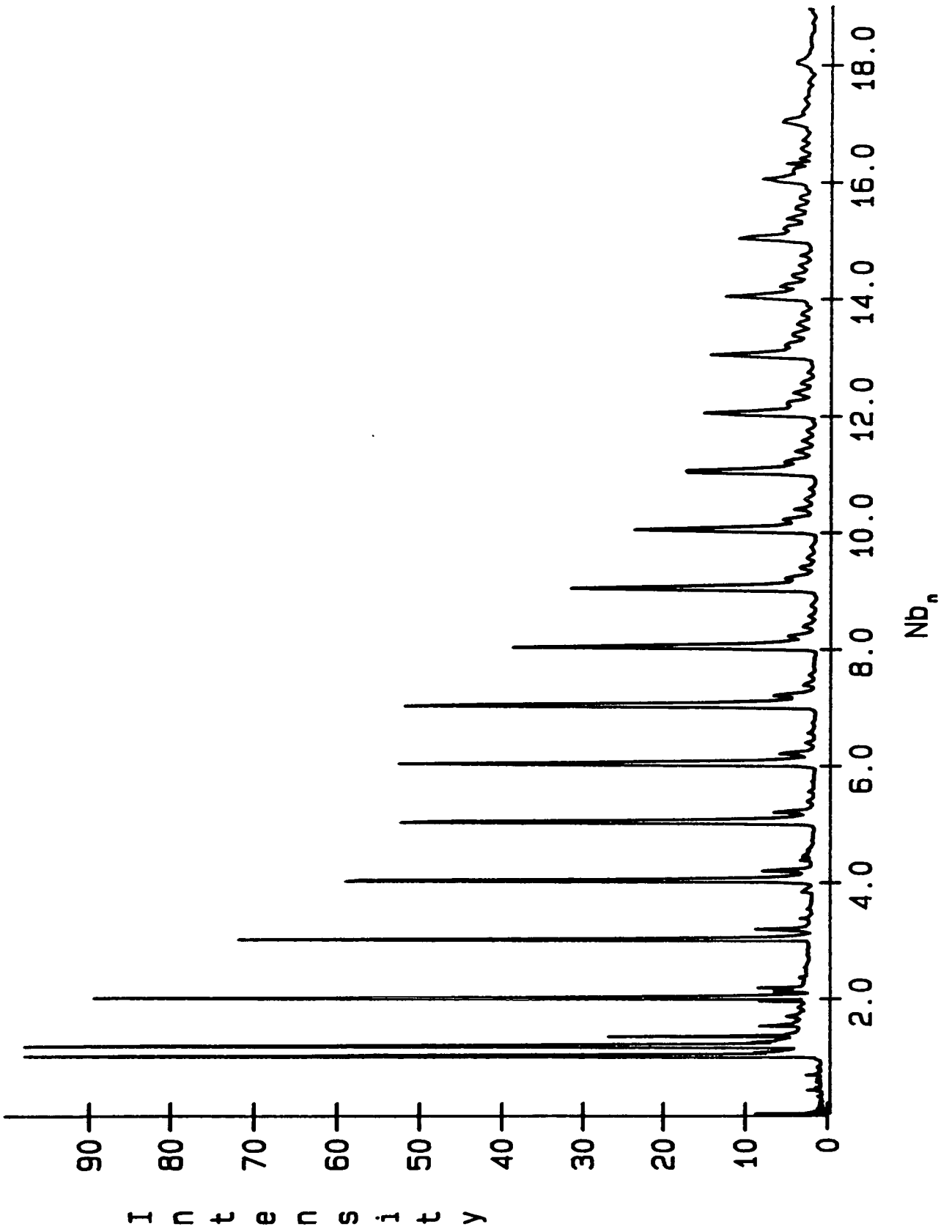

Figure 4.8 (b) : TOF mass spectrum of niobium clusters recorded on the MB2 reflectron instrument

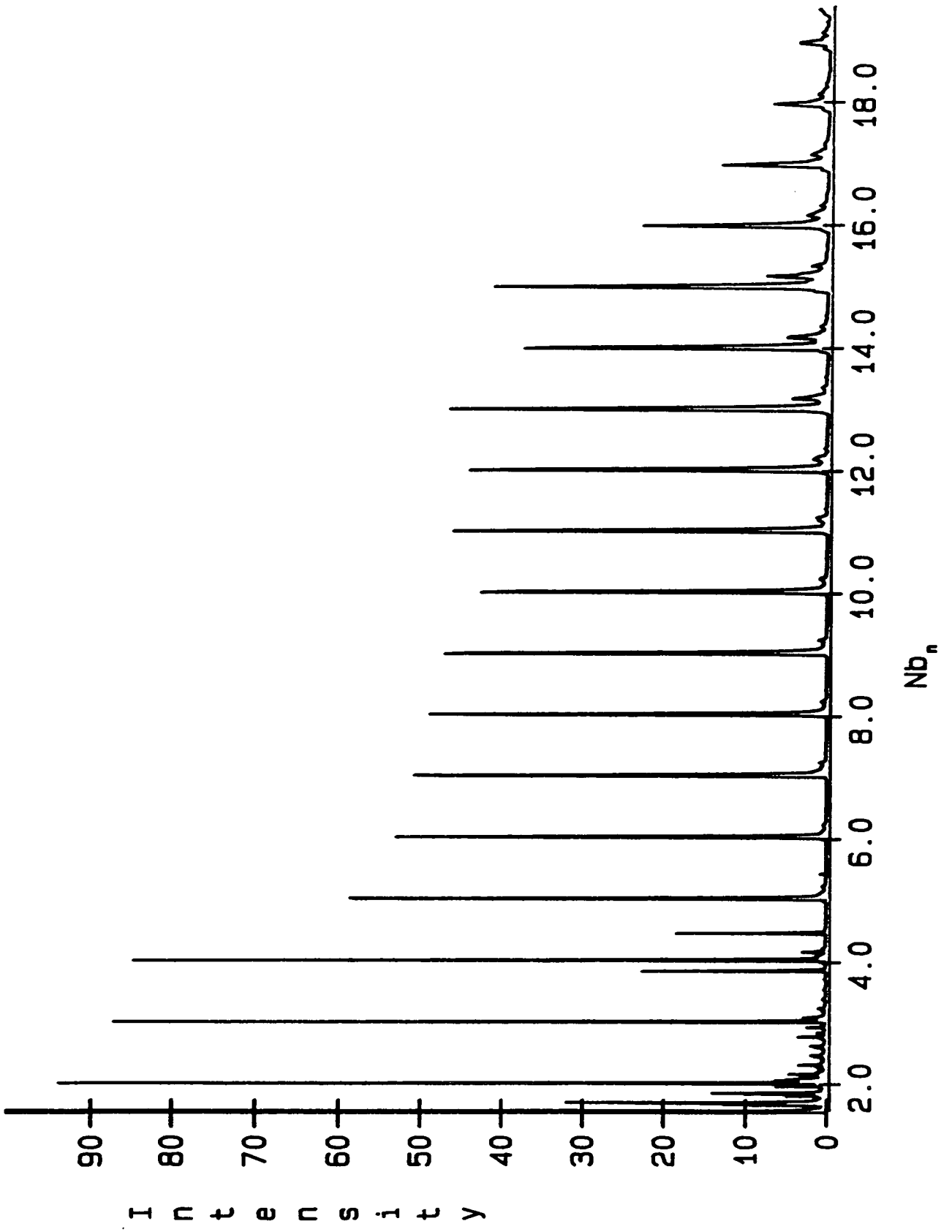

ionising wavelength was 266 nm in each case. The transmission profile of the RETOF is much flatter over a wider cluster size range. Its disturbingly sharp cut-off at high mass is probably a consequence of mirror misalignment.

The calculated resolution of this instrument should be $m/\Delta m = 1414$ at mass 98, and the maximum resolvable mass should be approximately 1365 amu (see Table 4.2). Experimental results obtained on niobium cluster mass spectra show these estimates to be a little over-optimistic. The molybdenum isotope distribution shown in Figure 4.9 was recorded using a tightly-apertured, focused, low power 266 nm beam from a quadrupled Nd:YAG laser. Under these conditions, the effects of any spatial defocusing should be minimal, and the peak width should be largely determined by the temporal profile of the ionisation source (9 ns FWHM), and the digitiser sampling rate (100 MHz ≡ 10 ns intervals). The observed peak width of the mass 98 isotope was 16 ns, corresponding to a resolution ($m/\Delta m$) of 1080, which is approximately twice as good as the linear instrument. Like the linear TOFMS, the discrepancy probably results from the limited sampling rate and the effects of field inhomgeneities in the source and mirror regions.

Figures 4.10 and 4.11 show contour plots for the reflectron ion extraction optics and ion mirror. It is clear that field penetration effects are substantial. Having an aperture in the repeller plate to admit the molecular beam leads to obvious field leakage problems. Attempts to eliminate this by placing a high-transmission grid over the aperture were not successful, as this was found to cut down the molecular beam transmission by an unacceptable amount. The lack of a

Table 4.2 : MB2 reflectron performance

System parameters

Repeller to Drawout grid:	3.0 cm
Drawout grid to Flight grid:	1.0 cm
Flight grid to Space focus:	25.9 cm
Space focus to Mirror:	72.1 cm
Mirror to Detector:	71.5 cm
Length of mirror retarding region:	1.4 cm
Length of reflecting region:	9.5 cm
Repeller to Drawout P.D.:	1107 V
Drawout to Flight P.D.:	1946 V
Flight and Mirror entrance grid voltage:	GND
Mirror retarding voltage (U_T):	-1667 V
Mirror reflecting voltage (U_K):	-1146 V
Ion energy at space focus:	2.5 keV
Wiley-McLaren k_0 parameter:	4.517

Calculated performance (Definitions in text)

Data for $^{98}Mo^+$, 30 K, spatially distributed (± 0.05 cm) about s_0 = 1.5 cm.

Assumed that the signal sampling interval is much smaller than the peak widths.

ΔT_s =	6.33 ns
ΔT_θ =	3.34 ns
ΔT_{laser} =	9.00 ns
ΔT_t =	11.50 ns
Calculated resolution at mass 98:	1414
Observed resolution at mass 98:	1080
Calculated maximum resolvable mass:	1365

Figure 4.9 : Time of flight mass spectrum of molybdenum isotopes recorded on the MB2 reflectron instrument

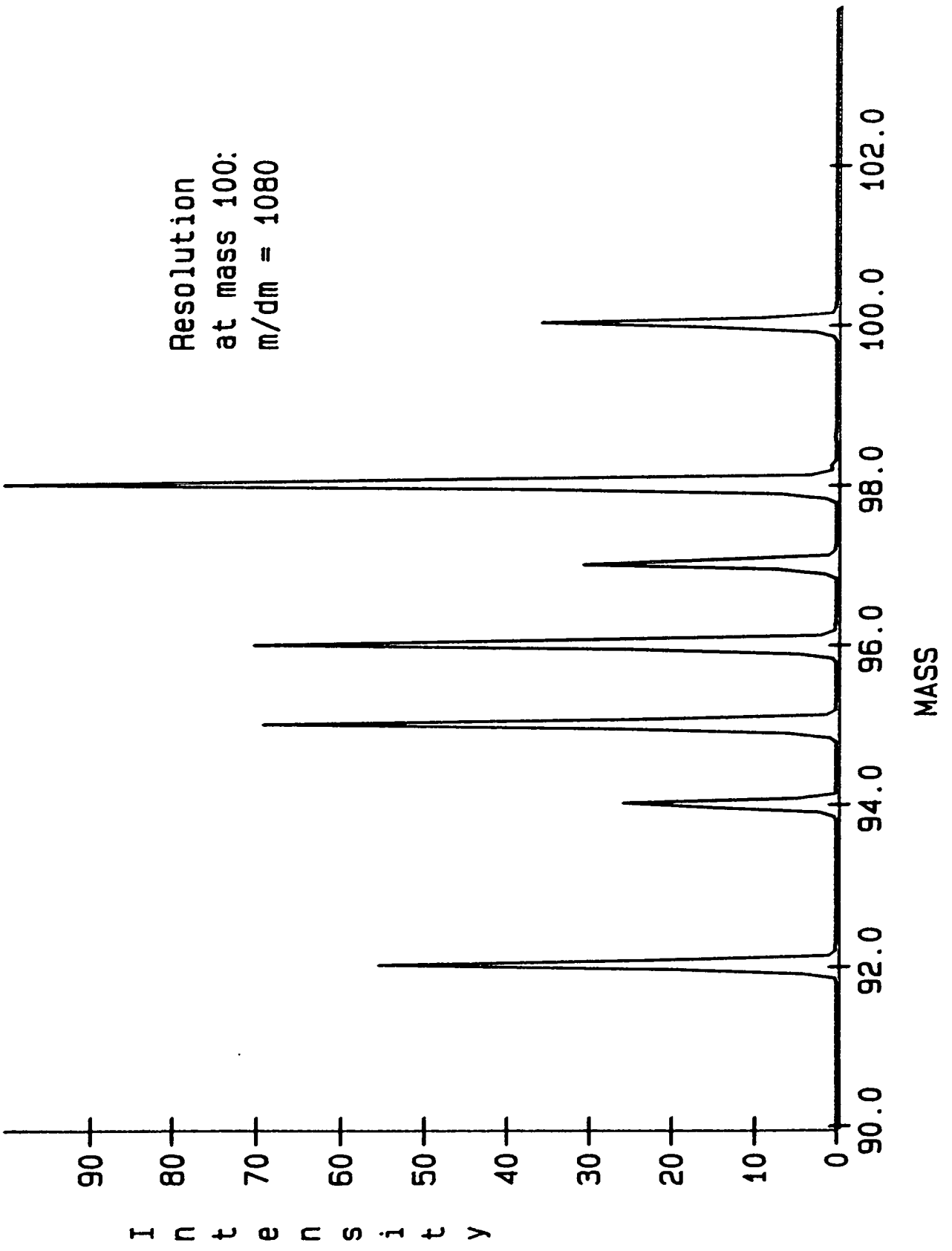

Figure 4.10 : Contour plot of the potential distribution in the source region of the MB2 reflectron instrument

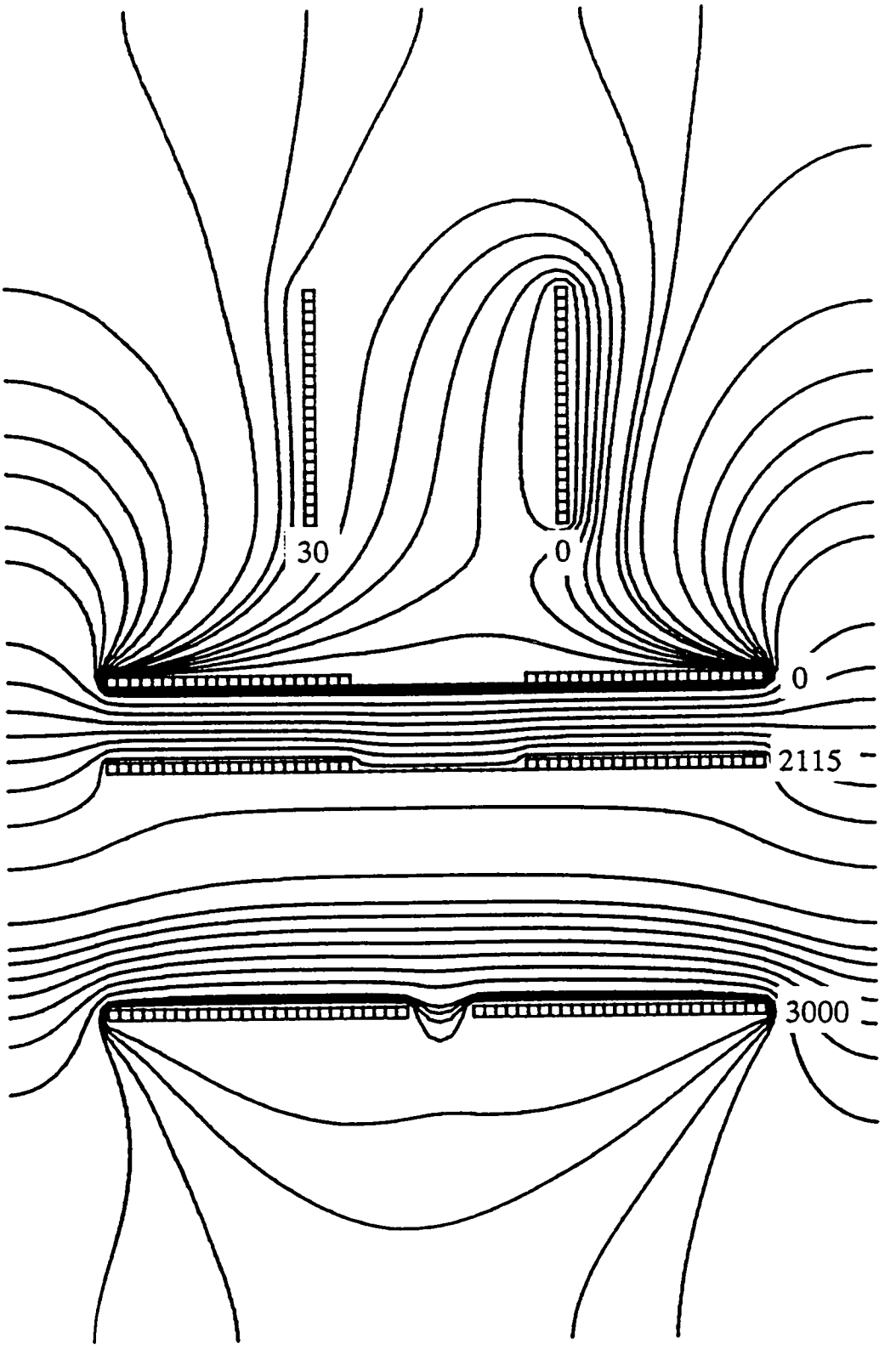

Figure 4.11 : Contour plot of the potential distribution in the source region of the MB2 reflectron ion mirror

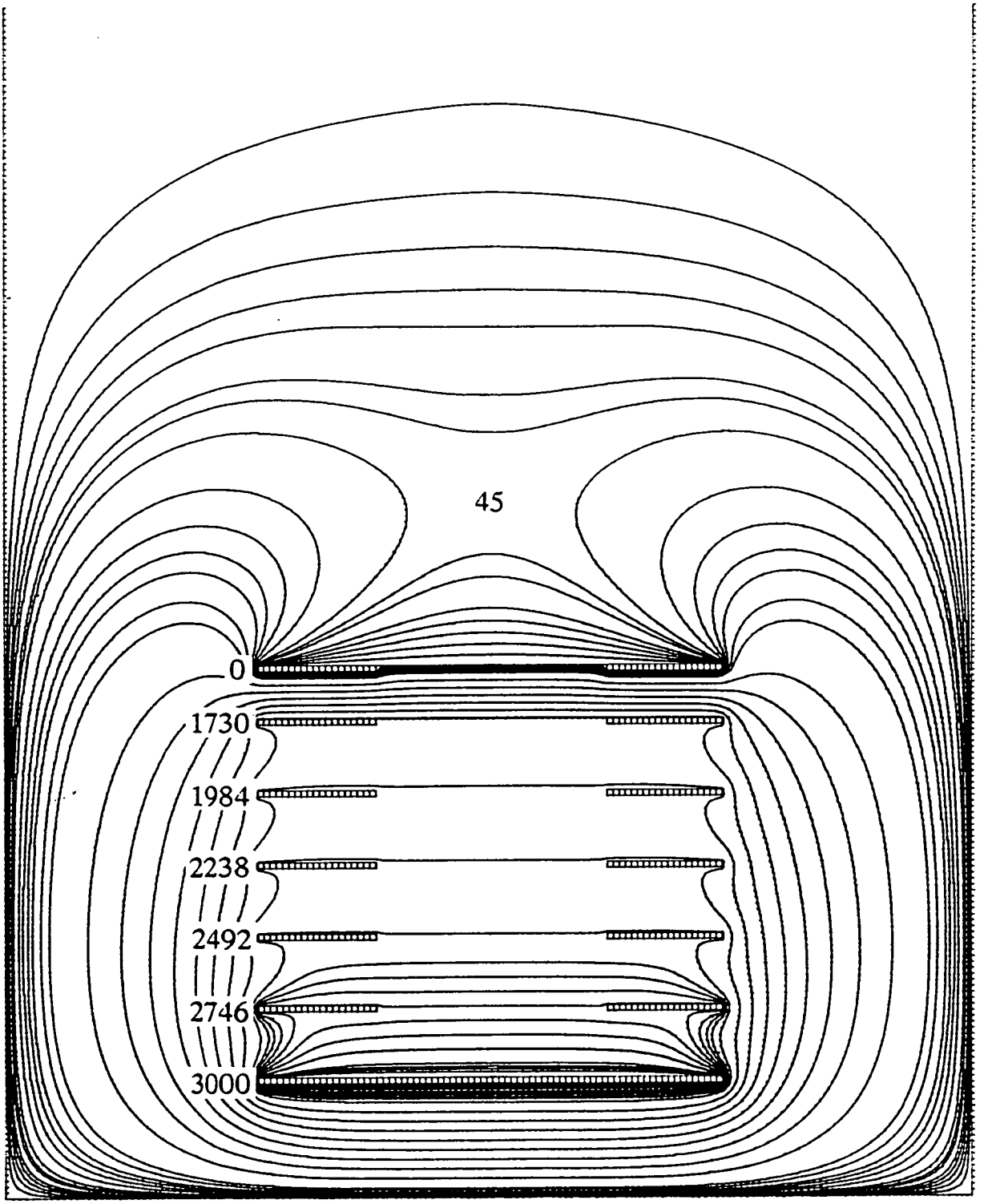

grounded cryoshield surrounding the extraction optics compounded the problem, since the field can spill out considerably to the nearest earthed surfaces: in this case the chamber walls. Also, the first drift region is not truly field free if any voltage is applied to the XY deflectors. For the purposes of potential mapping, the mirror axis in Figure 4.11 had to be coincident with the chamber axis, as the simulation program could not cater for the angled geometry (see Appendix B). As Figure 4.11 illustrates, extensive field penetration around the edges of the grounded entrance grid of the ion mirror posed a very serious problem. Voltages of up to 43 V were found on the mirror axis in the supposedly field-free drift region in front of the mirror entrance grid. Angling the mirror within the reflectron chamber will lead to even higher potentials being sampled by ions entering the mirror. These fringing fields destroy the focusing conditions derived for the RETOF geometry. The lack of grids on the guard rings in the ion mirror was essential to maintain a high ion transmission through the mirror. A design modification which would help to preserve ground potential in the drift region involves the mounting of a cylindrical, earthed "collar" around the mirror stack. This would help to trap the field and prevent leakage, particularly if it is mated with the grounded mirror entrance grid. Alternatively, the diameter of the grounded entrance element could be increased to block field penetration from the unguarded sides of the mirror. No trajectory calculations were performed for the RETOFMS, but it is likely that the effects of field penetration do have a significant effect on ion packet broadening. Despite these limitations, the overall resolution of the RETOFMS was substantially greater than that of the linear TOF instrument.

4.5 Ion transmission function

In an idealised TOF mass spectrometer, the transmission of ions formed at a point source on the spectrometer axis, with zero off-axis velocity component, will be limited only by the transmission of the grids intervening between the source and detector. With 90% transmitting mesh in the ion optic elements, and an 82% transmitting entrance grid on the detector, transmission functions of 66% (linear) and 43% (RETOF) are obtained. These figures represent gross overestimates, since a number of other factors must be taken into consideration to obtain realistic transmission functions.

If the ions being extracted in the idealised spectrometer have components of velocity perpendicular to the direction of extraction, those with the most divergent trajectories may miss the detector or strike the walls of the flight tube. Assuming a "worst case" translational temperature of 30 K, and assuming that the velocities perpendicular to the molecular beam axis are Maxwell-Boltzmann distributed about a mean of zero, it is easily shown that only a negligible fraction fail to strike the detector, even in the long-drift path reflectron.

Other effects are more difficult to quantify. The ions are not formed at a point source, but over a range of spatial positions, which may not be uniformly transmitted to the detector. Field inhomogeneities may alter ion trajectories to such an extent that the ions diverge strongly from the spectrometer axis. As has been discussed, in the linear geometry, the transmission function has a distinct mass dependence due to the velocity component of the ion in the molecular beam direction. In the RETOF instrument, the transmission function should not

exhibit any mass dependence, provided that the ion optical elements are properly aligned.

The effects of these factors can be treated using the numerical methods described by Cartwright for the synthesis of mass spectral peaks. [5] A more realistic overall transmission function of approximately 8% for the linear geometry has been calculated in this way. Space-charge effects and collisions with background gas molecules will reduce this further.

The overall transmission of the reflectron should be higher than this value, since there is no beam velocity component to eliminate. However, a reduction in transmission may result from misalignment of the molecular beam and ion extraction axes, which introduces some mass dependence. Also, field inhomgeneities may have more severe consequences in the RETOFMS since a longer drift region and a mirror stage must be negotiated by the ions.

Using the calculated transmission function, it is possible to estimate approximately the number of ions formed by a single laser pulse. Amplified signal intensities of 200 mV were readily obtained when niobium clusters in the range Nb_6-Nb_{10} were one-photon ionised at 193 nm in the linear TOF mass spectrometer. This ion signal is equivalent to a pulse of roughly 50 ions striking the first plate of the microchannel plate detector. With 8% ion transmission, approximately 625 ions are formed by the laser pulse. In recording these mass spectra, the laser power density was kept low, typically < 0.5 MW cm^{-2} to prevent saturation and fragmentation. Typical cross sections for a strong one photon ionisation process lie in the range 10^{-17}-10^{-18} cm^2. The probability of

ionisation (per pulse) is therefore < 0.05-0.005. Thus there are approximately 10^4-10^5 molecules in the ionisation volume, which is approximately 0.05 cm^3, giving cluster number densities in the range 2 x 10^5-2 x 10^6 cm^{-3}.

Since the number density of helium in the ion source region is around 10^{14} cm^{-3} (see Chapter 3), it appears that the seed ratio of cluster species in the beam is exceedingly small.

4.6 Photoionisation TOF mass spectra of Group 1b metal clusters

Time of flight mass spectra of copper, silver and mixed copper-silver clusters, obtained using 193 nm ArF laser photoionisation, are shown in Figures 4.12-4.14. These mass spectra, in common with all others presented in this thesis, are plotted with their abscissae linearised in mass units, in accordance with the equation $T = Km^{1/2}$. In each case, the clustering conditions and the mass spectrometer transmission function were optimised for high mass clusters. The Cu and Ag distributions were generated using the NRC BV-100 valve on the MB1 linear TOF rig. In the case of the mixed Cu-Ag distribution, the metal target was fabricated by melting a 1:1 mixture of copper and silver shot in a quartz tube under a stream of argon (see Chapter 5). Clusters in this case were generated using the General Valve pulsed nozzle source, and detected using the MB2 RETOFMS. Here, the rapid attenuation of the distribution with increasing cluster size may be explained by the low gas throughput of the General Valve nozzle, which inhibits efficient clustering.

In the pure metal TOF mass spectra, one feature is strikingly evident: namely a

Figure 4.12 (a) : TOF mass spectrum of copper clusters optimised for Cu_9^+

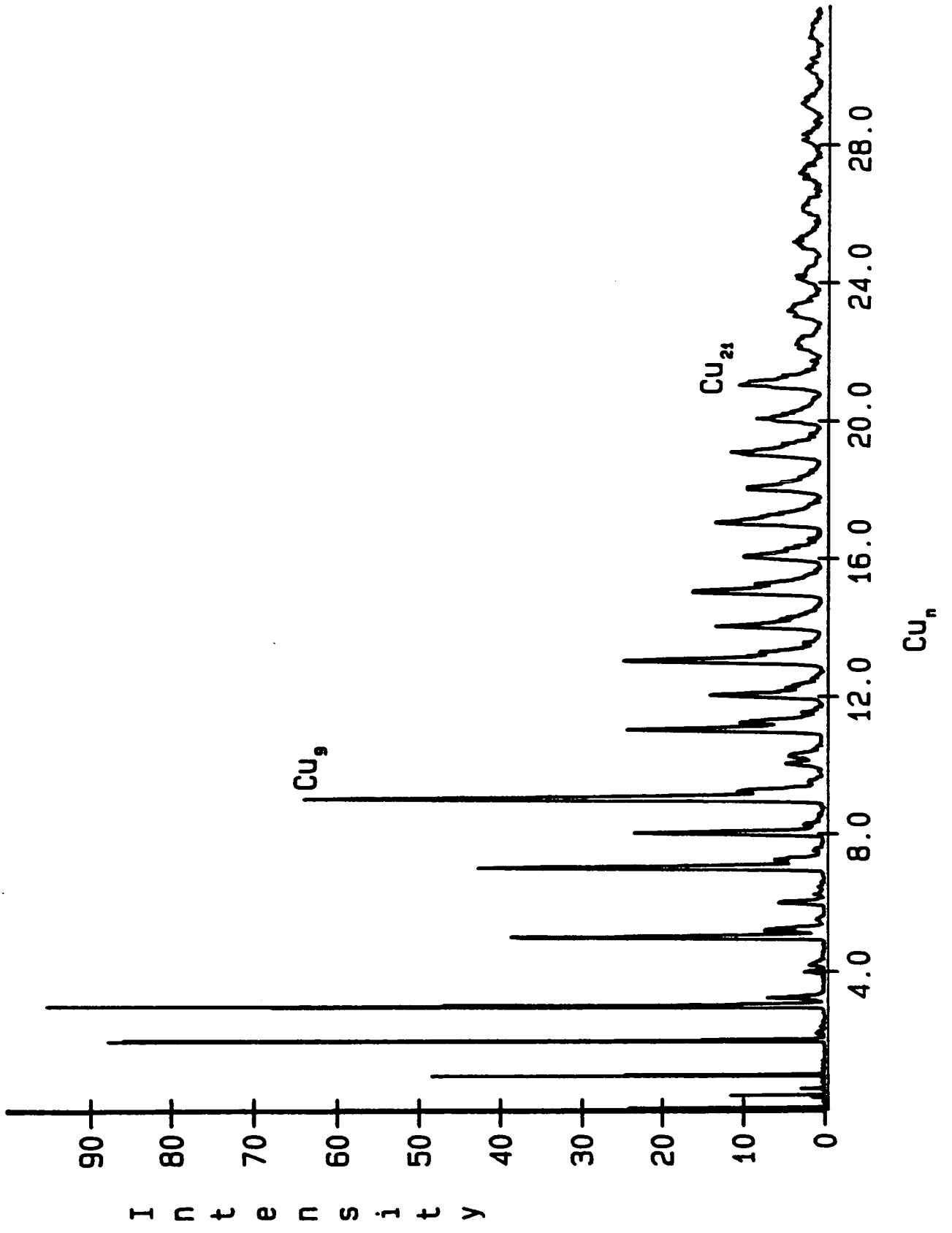

Figure 4.12 (b) : TOF mass spectrum of copper clusters optimised for high mass clusters

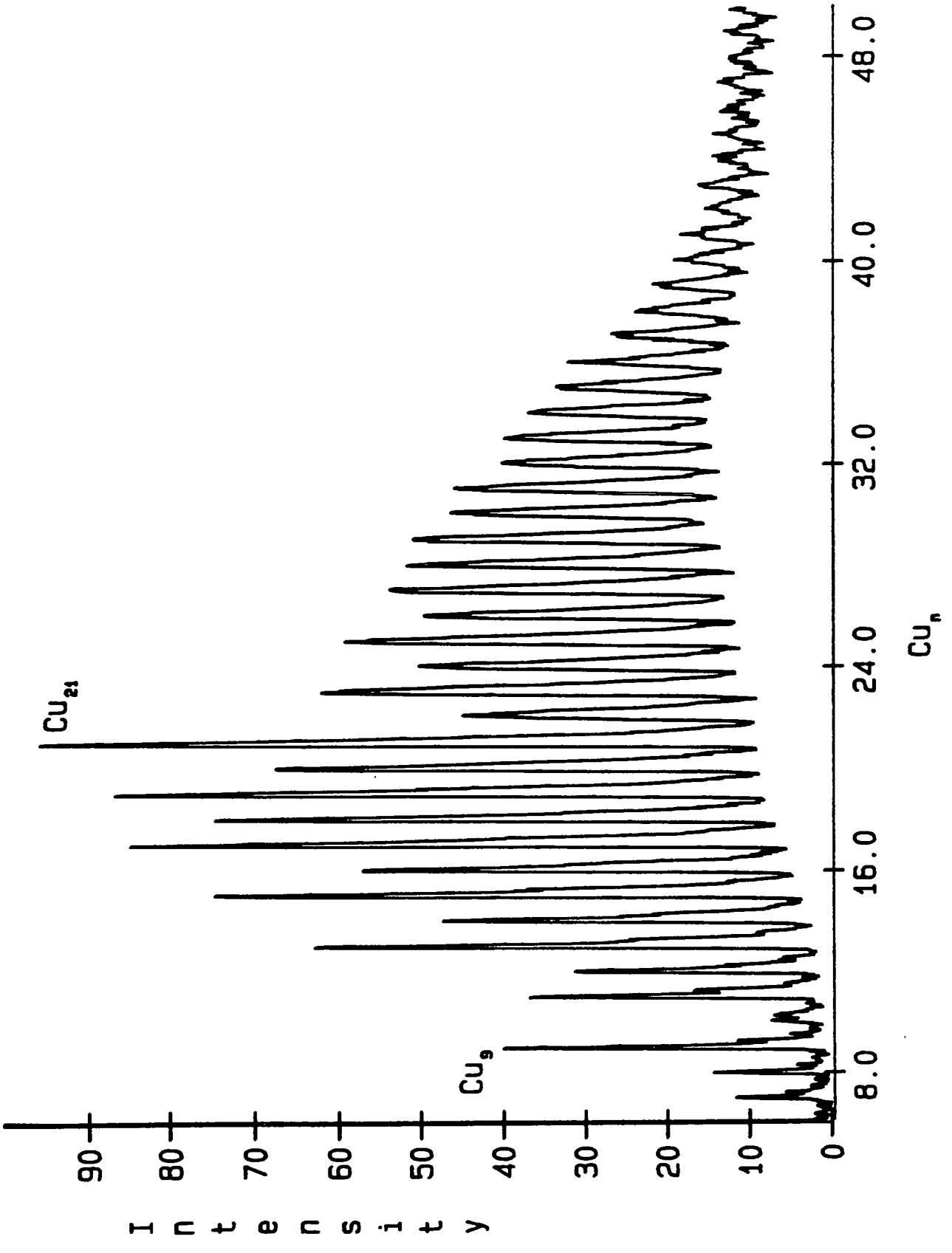

Figure 4.13 : TOF mass spectrum of silver clusters

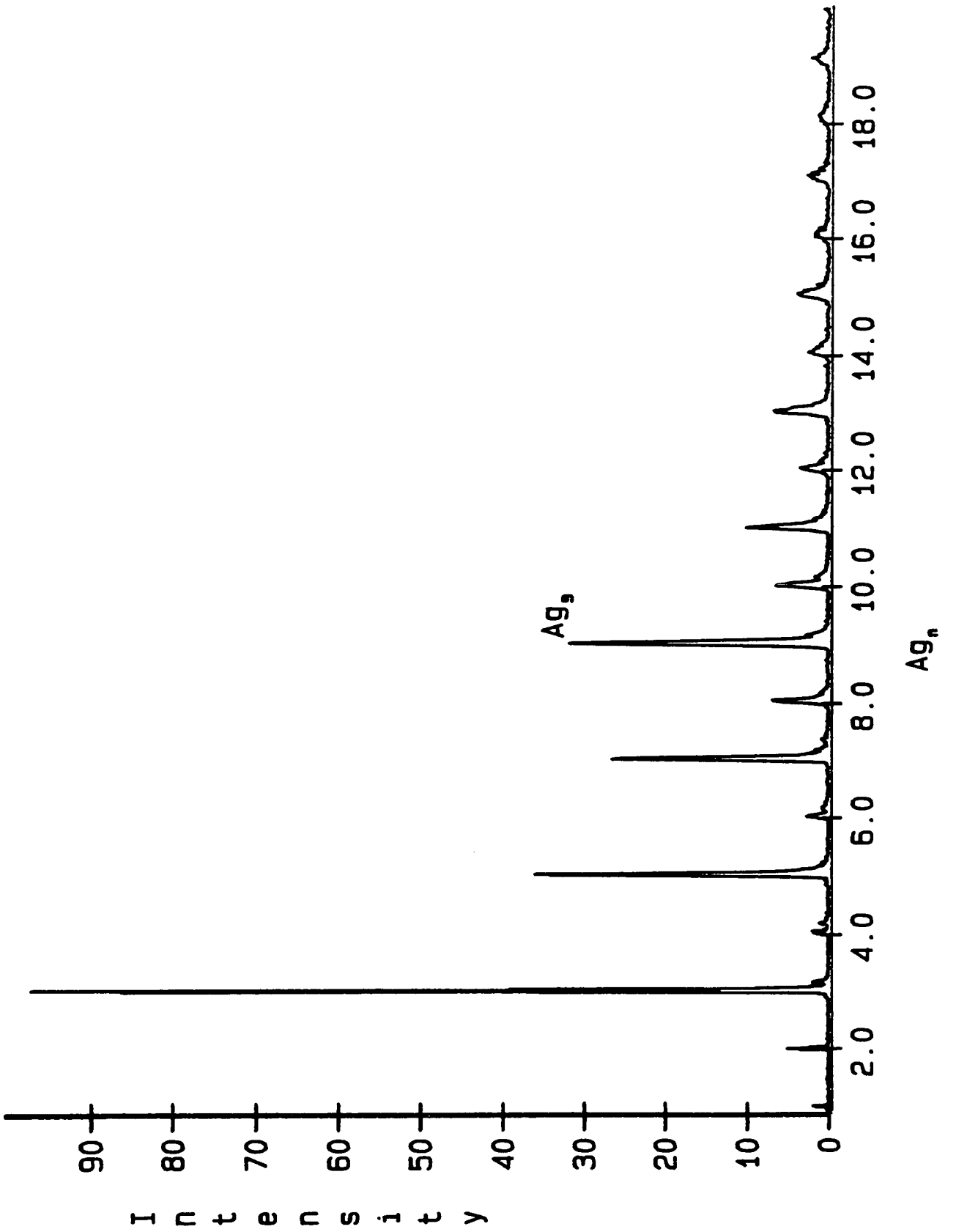

Figure 4.14 : TOF mass spectrum of copper- and silver-containing clusters

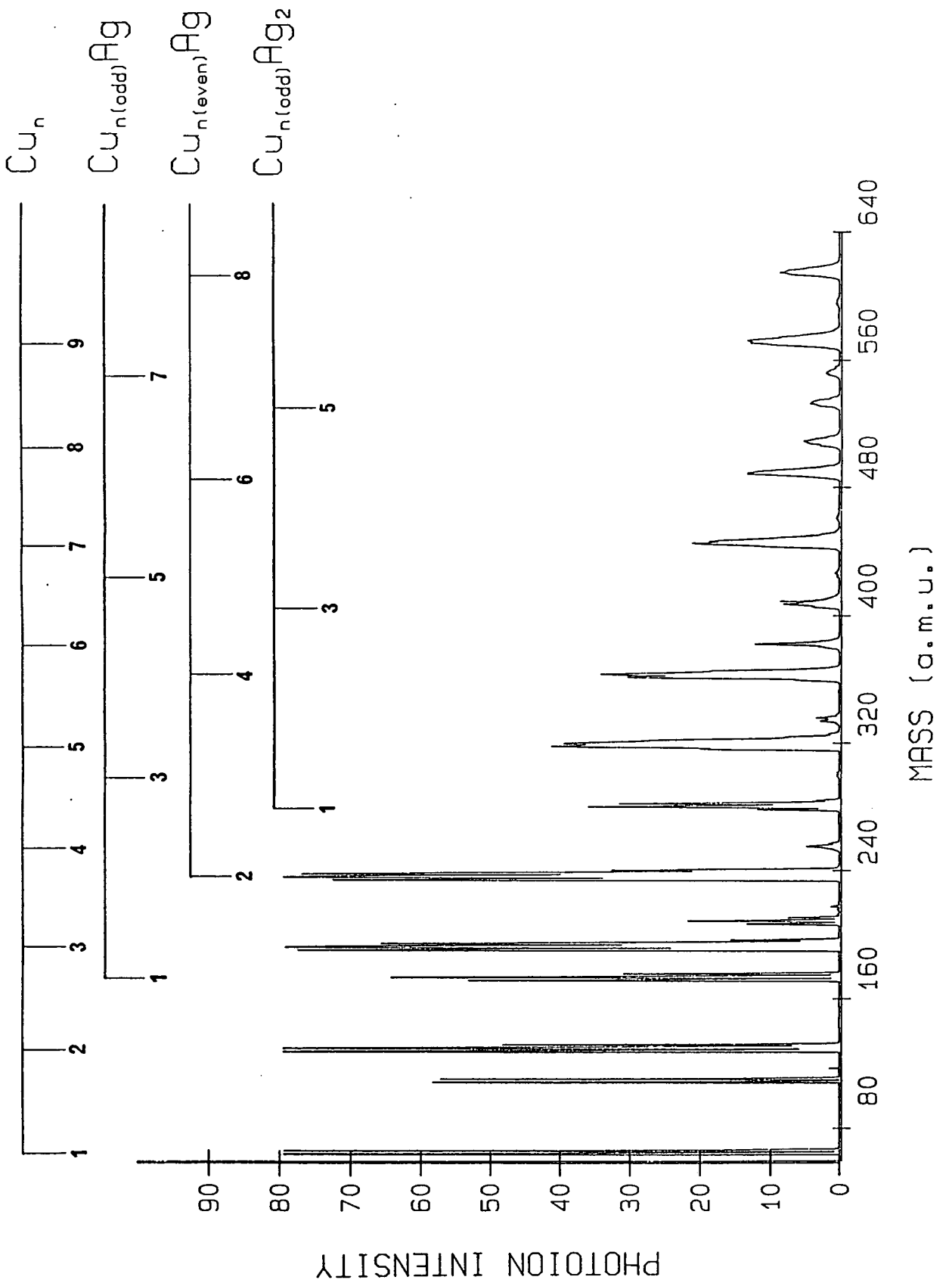

pronounced even/odd alternation in intensity with cluster size. The odd numbered copper and silver clusters are detected with significantly greater intensity than their neighbouring even numbered counterparts. This intensity alternation continues, with gradually diminishing contrast, out to approximately Cu_{27}. This phenomenon has also been observed by Powers *et al.*, [8] who determined copper cluster ionisation potentials by measuring the laser power dependence of the photoionisation signal (see Section 2.4). These IPs were observed to fall off with increasing cluster size, approaching the asymptotic limit of the the bulk work function, in accordance with theory. [9] [10] It was found that even numbered copper clusters in the size range Cu_n, n = 2-6, are two photon ionised with (193 nm) 6.4 eV photons, while the odd numbered clusters are one photon ionised at this wavelength. Beyond Cu_6, all clusters are one-photon ionised at 6.4 eV, although the even/odd intensity alternation continues out to Cu_{20} and beyond. When the ArF laser is replaced by a 157 nm F_2 laser, the intensity alternation vanishes. It would appear that the anomalous intensity distribution at 193 nm is an artifact of the photoionisation process itself, and not a reflection of the relative abundances of neutral species in the beam.

These observations have been rationalised by recourse to simple bonding theory. Copper and silver have the valence electronic configuration $(n-1)d^{10}ns^1$, and small clusters of these metals will be bonded primarily through s valence orbital interactions. The contribution of the fully-occupied and heavily contracted d orbitals is expected to be minimal, and these orbitals may be regarded to a first approximation as core orbitals outwith the valence space. We can thus view the clusters as being composed of atoms each contributing a single s valence electron

to intra-cluster bonding. Even numbered clusters of copper or silver are expected to have singlet ground states with a spin-paired, tightly-bound highest-occupied molecular orbital (HOMO). For example, bonding in the simplest "cluster" of copper, the dimer, is dominated by an $4s\sigma$ bond (see Chapters 5, 7 and 8). Conversely, odd numbered clusters will have doubly degenerate ground states, with a less stable, partially-occupied HOMO of less bonding character than that in the even numbered clusters. More elaborate *ab initio* and semiempirical calculations also show this simple result. [11]- [15]

Koopman's theorem [16] allows orbital energies to be related directly to ionisation potentials, through the equation:

$$IP_I = -\varepsilon_{HOMO}. \tag{4.33}$$

where IP_I is the (first) ionisation potential of the molecule, and ε_{HOMO} the SCF energy of the HOMO. The equation ignores relaxation effects and electron correlation in the ion, but these are not expected to be all that large for s orbital ionisation. Thus the HOMO energy may be related directly to the ionisation potential. Hence the ionisation potential for an odd numbered cluster will be less than that for the neighbouring even numbered cluster, due to the reduced bonding character of the odd numbered cluster HOMO. For the small copper and silver clusters, the ionisation potential oscillates above and below the 6.4 eV photoionisation energy. The resulting intensity alternation reflects the relative magnitudes of the one photon cross section for direct ionisation (odd numbered clusters) and the two photon nonresonant ionisation cross section (even numbered clusters).

The persistence of the intensity alternation beyond the point at which all clusters become one photon ionised is not explained by this model. It has been ascribed to the fact that one would expect the one photon ionisation cross section for removal of an electron from a weakly-bound HOMO to rise more rapidly near threshold than the corresponding cross section for removal of a more tightly-bound electron, as in the case of an even numbered cluster. As the cluster size increases, the intensity alternation gradually diminishes, since the clusters acquire more character of the bulk and the distinction between bonding and non-bonding orbitals becomes obscured.

Comparing the copper and silver cluster distributions, it is clear that the intensity alternation is more pronounced for silver than for copper. This may be related to the differing degree of d orbital participation in the bonding of the cluster. For example, comparative calculations on copper and silver dimer, by Shim and Gingerich [17] indicate that there is less d orbital hybridisation of the sσ bond in the case of silver dimer than in copper dimer. The "pure-s orbital" bonding model may therefore be more appropriate for silver clusters than for copper. Mixing of some d character into the valence orbitals in the copper clusters may reduce the sharp distinction between the even and odd numbered cluster HOMOs.

This model can be extended to the mixed CuAg cluster distributions. In Figure 4.14, intense cluster sequences may be picked out in which the total number of atoms is odd, irrespective of the composition of the cluster.

Supporting evidence for the model has come from a number of sources. The

systematic even/odd alternation in ionisation potential has also been observed for the Group 1(a) alkali metals lithium, sodium and potassium. [18] [19] Bonding in clusters of these univalent metals is also dominated by interactions between the s orbitals. The electron affinities of copper negative ion clusters were measured by Zheng *et al.*, [20] who found that the even clusters had a smaller electron affinity than their odd neighbours. Odd numbered negative ion clusters will have singlet ground states, with the extra electron spin-paired in the initially partially-occupied HOMO of the neutral cluster. The resulting configuration is more stable than that formed by electron attachment to an even numbered cluster, where the additional electron enters an unoccupied, less bonding orbital.

Meiwes-Broer and co-workers [21] have performed an elegant cluster fragmentation study, in which a beam of mass-selected copper cluster positive ions was fired at an argon target gas to induce collisional decomposition. In each case, the cross section for fragmentation of an odd numbered cluster ion (even number of electrons) was less than that for the nearest even neighbours. This is taken as evidence to reinforce the view that the spin-paired odd numbered cluster ions are more tightly-bound and less liable to fragment than the even numbered ones, which will have fewer fully-bonding MOs. Numerous *ab initio* and semiempirical calculations on the Group 1(a) and 1(b) metal clusters all agree that the highest occupied orbitals are dominated by sσ interactions, and predict an even/odd alternation in the HOMO energies. [11]- [15]

Further discontinuities in the TOF mass spectra become apparent upon close scrutiny. The Cu_9, Ag_9 and Cu_{21} peaks all show anomalously high intensity relative to the overall monotonically-decreasing trend in the intensity of the

cluster distribution. The Cu_9 and Cu_{21} peaks in particular are notably more intense than those due to Cu_{10} and Cu_{22}, which are in turn weaker than the general trend would predict. This behaviour is mirrored when Cu, Ag and Au clusters are produced by ion bombardment, a discontinuous drop in intensity being observed between n=3 to 4, n=9 to 10, n=21 to 22 etc. [22] This may be contrasted with the near threshold photoionisation mass spectra of alkali metal clusters, where intense peaks occur at M_2, M_8, M_{20} etc. [10] [23]

The stabilities of clusters derived from univalent atom precursors, particularly the alkalis, have been successfully modelled by the Spherical Jellium model, developed by analogy with the shell model for nuclear structure. [23] In this model, cluster energies are calculated by solving the Schrödinger wave equation for a simple, structureless, square well potential. The quantised energy level structure obtained predicts the existence of certain "magic numbers" of high stability in the size distribution. *Neutral* clusters M_n where n=2,8,18,20,34,40..... are particularly stable , since they have the requisite number of valence electrons (one per atom) for electronic shell closings with successive filling of the orbitals : $1s^2$; $1s^2 1p^6$; $1s^2 1p^6 1d^{10}$; $1s^2 1p^6 1d^{10} 2s^2$ etc. In the threshold photoionisation mass spectra of alkali clusters, anomalously intense peaks are observed for neutral clusters which have the required number of electrons for shell closing. The intensity maxima must therefore reflect the especially high concentration of M_8, M_{20} etc. neutrals in the beam, rather than any variation in ionisation cross section. These high abundances are in turn related to the high thermodynamic or kinetic stability of the closed shell clusters.

The parent *photoions* Cu_9^+, Ag_9^+ and Cu_{21}^+ are "magic" species possessing the

requisite number of electrons (8 and 20 respectively) for high stability. Their intense appearance in the TOF mass spectra is ascribed to another artifact which frequently complicates the interpretation of cluster intensity distributions, namely photofragmentation. Fragmentation of parent cluster photoions may be caused by (1) the ionising photon accessing dissociative states of the ion or (2) post-ionisation photoabsorption by the molecular ion populating such states. In these experiments, the photoionising power density was kept low to minimise the second factor, although the first cannot be controlled in the same way. If the ionising photon(s) carries the cluster well above its ionisation potential, there is a higher probability of accessing a repulsive state of the ion than if the ionising energy just exceeds the IP. As the cluster size increases, the IP falls off approximately with a 1/R dependence, where R is the effective cluster radius. [9] Therefore the difference between ionising photon energy and IP grows as the cluster size increases. Hence clusters, especially the larger ones, may exhibit photofragmentation even at low laser powers. In a fragmenting cluster distribution, the "magic" photoions $M^{+}_{9,21}$ are expected to represent islands of stability with respect to further unimolecular decomposition. Fragmentation channels involving single atom loss and cluster fission will lead to an accumulation in the intensity of these dissociation products. Fragmentation, if it occurs, is likely to enhance the even/odd intensity alternation. The even cluster ion population can be preferentially depleted by neutral atom loss to form stable odd daughter ion products. The Group 1b clusters formed by sputtering [22] not surprisingly show the same anomalies, since ionic fragmentation processes govern the observed intensity distribution.

Tentative evidence for the applicability of the Jellium model to clusters formed from polyvalent atoms comes from the observed aluminium cluster distribution, an example of which is shown in Figure 4.15. The MB1 linear TOF rig was used to record this mass spectrum, which was optimised for the transmission of higher mass clusters. Ultraviolet radiation (193 nm) from an ArF excimer laser was used as the photoionisation source. The Al_7^+ and Al_{14}^+ ion peaks appear with anomalously high intensity, while their neighbours to higher mass, Al_8^+ and Al_{15}^+ are weaker than would be predicted from the monotonically-decreasing intensity distribution. The observation of these "magic numbers" in the aluminium cluster distribution is perhaps surprising in light of the valence electronic structure of the Al atom: $[Ne]3s^2 3p^1$. The non-spherically symmetric character of the partially-occupied p orbitals will have a distinctive influence on the bonding in aluminium clusters. The Jellium model is not expected to be well suited to cases such as Al where charge is accumulated in directional bonds between atoms. Nevertheless, the observation of sharp intensity maxima in the distribution, for clusters with approximately the correct number of electrons for shell closing, suggests that the model has some validity for Al. The cluster ion Al_7^+ has the requisite number of valence electrons (20) for a stable, closed shell configuration $1s^2 1p^6 1d^{10} 2s^2$. Similarly, although the correspondence is less marked, Al_{14}^+ is the cluster closest in size to the 40 electron closed shell configuration $1s^2 1p^6 1d^{10} 2s^2 1f^{14} 2p^6$.

As with the Group 1(b) species, the high stability of these cluster ions towards photofragmentation may be responsible for their enhanced intensity in the TOF distribution. Given that the laser flux was similar to that in the experiments on

Figure 4.15 : TOF mass spectrum of aluminium clusters

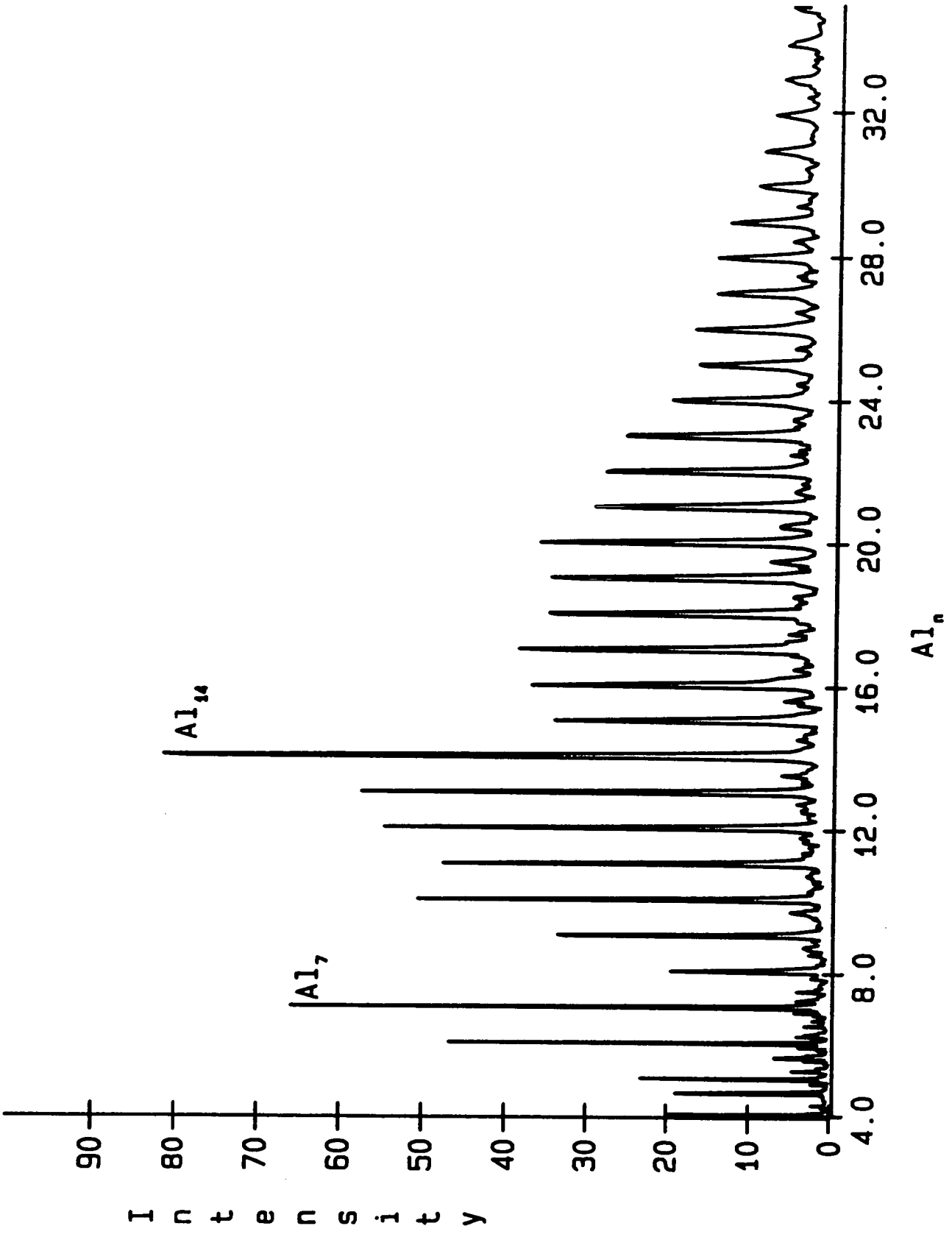

Cu,Ag clusters, fragmentation may be a more serious problem for aluminium clusters owing to their lower ionisation potential. The IP for Al is only 5.99 eV, whilst the IP for Cu is 7.73 eV, and that for Ag is 7.57 eV. [1] Thus the difference between the ionising energy (6.4 eV) and the IP is much larger for aluminium clusters. The relatively low intensity of Al_8^+ and Al_{15}^+ may indicate the operation of an efficient single-atom loss fragmentation channel, driven by the stability of the dissociation products, Al_7^+ and Al_{14}^+.

The foregoing discussion illustrates some of the pitfalls in the interpretation of cluster photoion distributions as being representative of the abundance of the neutral precursors. There is clearly much scope for a comprehensive investigation of Group 1(b) cluster dissociation channels and the islands of stability in the products. At the time of writing, some progress towards this end has been made by Smalley's group, [24] using a tandem-TOFMS apparatus to mass select specific negative cluster ions, photofragment them, and analyse the product species.

4.7 Photoionisation TOF mass spectra other transition metal clusters

The cluster generation experiments described here concentrated largely upon the Group 1(b) metals copper and silver, because of our spectroscopic interest in the dimers of these metals (see chapters 5-8). However, a number of other refractory metal cluster systems were investigated. Clusters of the following metals were generated with varying degrees of success: aluminium, iron, nickel, niobium and molybdenum.

Of the above, niobium clusters proved the easiest to generate and detect. The cluster distribution tolerated a wide range of vaporisation pulse energies and clustering conditions. Also, the relatively low ionisation potentials of niobium clusters, as determined by Whetten *et al.*, [25] meant that virtually all clusters could be one photon ionised at 6.4 eV. Niobium was used as the "standard cluster system" whenever a new TOF geometry was being tested. The fact that this metal has only a single naturally-occurring isotope was particularly convenient for the determination of the spectrometer resolution at high mass.

A persistent feature in the niobium cluster distributions, when photoionised with 193 nm radiation, was the presence of oxide satellites on the bare metal cluster peaks, corresponding to the molecular formula Nb_xO_y. Figure 4.16 (b) shows a TOF mass spectrum of niobium clusters recorded on the MB2 linear instrument using 193 nm ionisation. The number of oxide satellites on a particular cluster increased with the number of Nb atoms in the cluster, presumably reflecting the increasing number of available coordination sites. Oxide satellite peaks were also observed in the mass spectra for iron (Figure 4.17), nickel (Figure 4.18), copper (Figure 4.12) and silver clusters (Figure 4.13), which were all recorded on the MB1 linear instrument using 193 nm photoionisation. Rastering over the rod surface several times with the vaporisation laser would be expected to remove oxide layers and eventually expose the pure metal, but the oxide peaks in the mass spectrum proved in many cases to be very persistent. It thus appears likely that some of the oxygen uptake by clusters results from impurities in the helium stream.

The phenomenon of niobium cluster oxidation was investigated further by

Figure 4.16 (a) : TOF mass spectrum of niobium clusters recorded using 266 nm ionisation

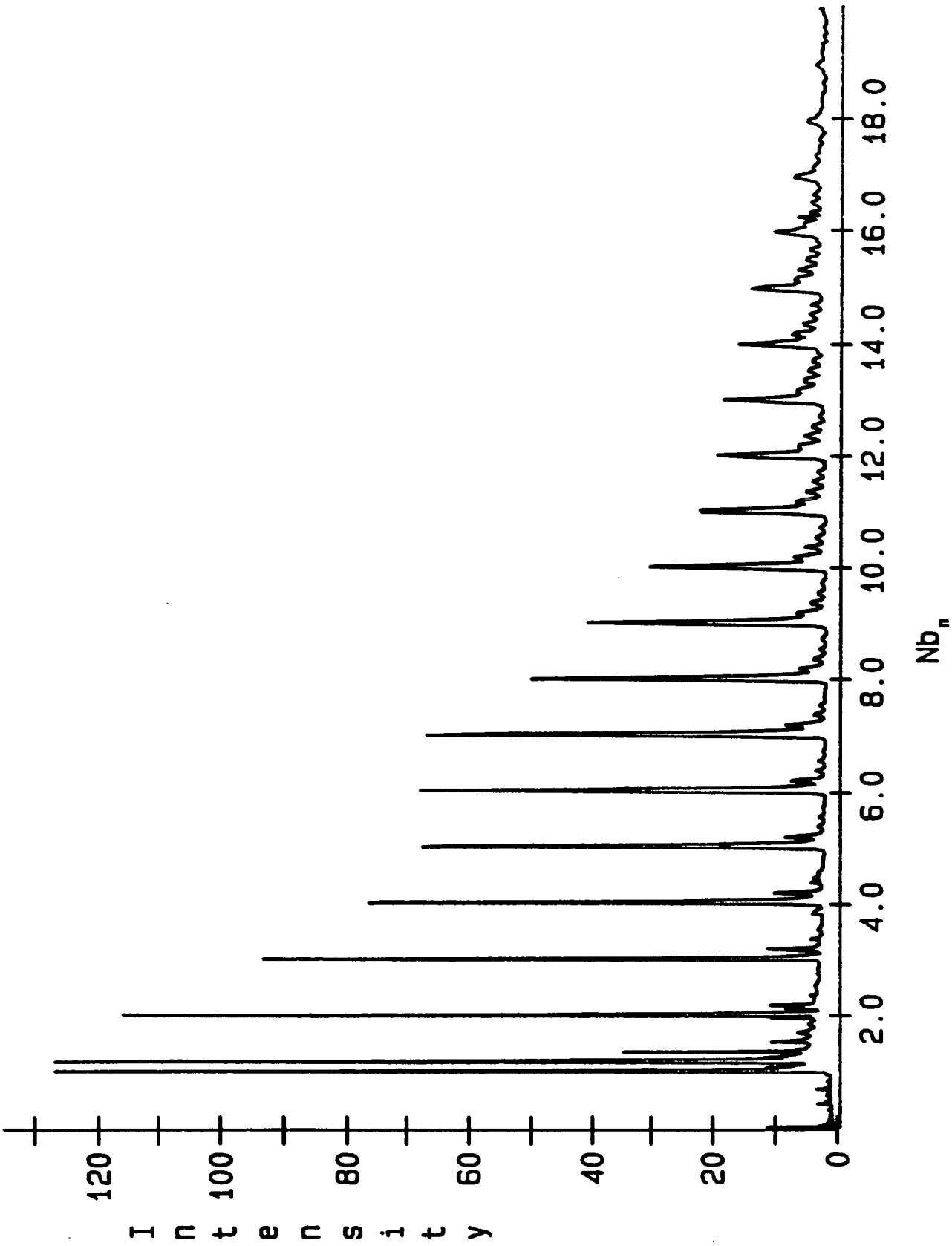

Figure 4.16 (b) : TOF mass spectrum of niobium clusters recorded using 193 nm ionisation

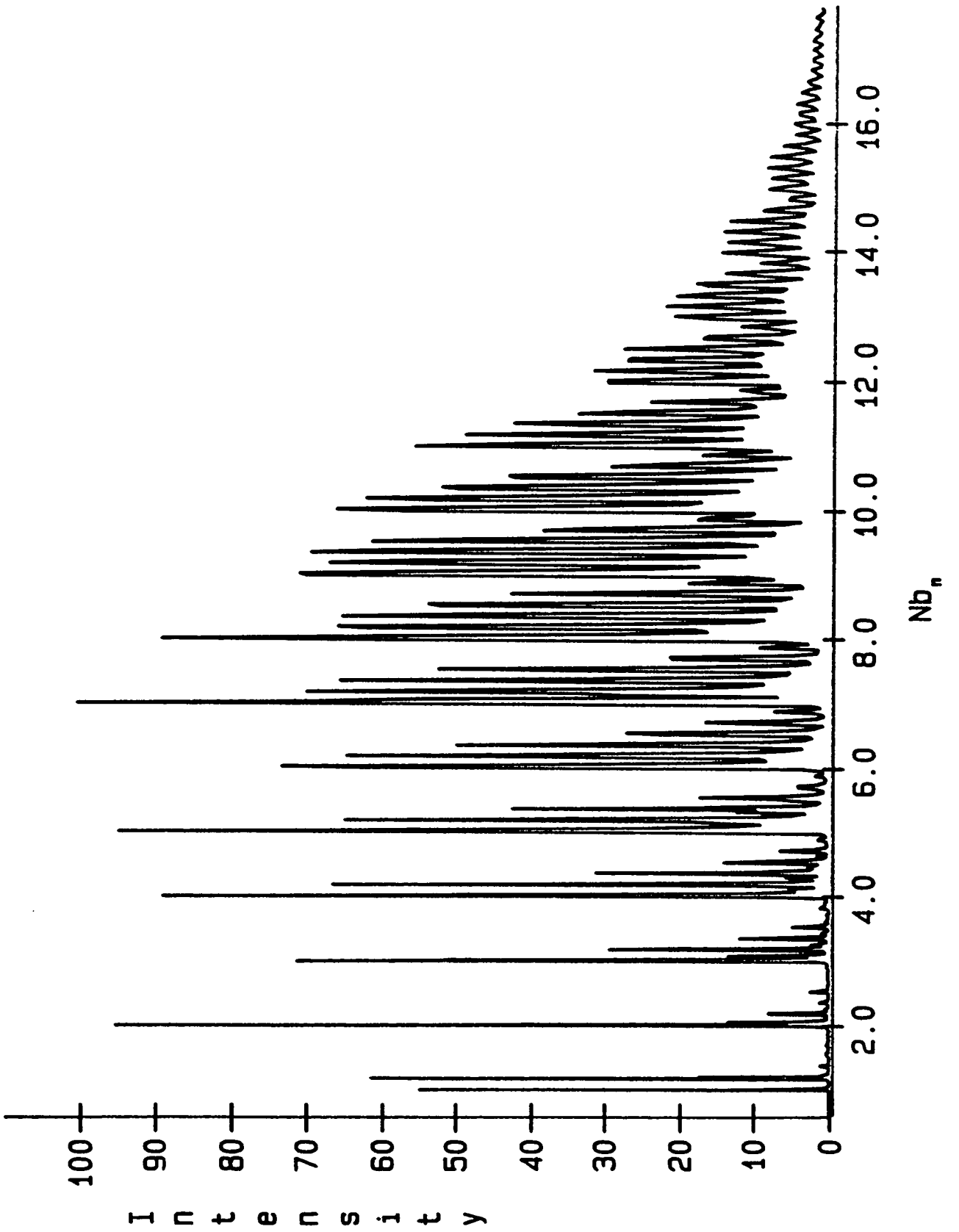

Figure 4.17 : TOF mass spectrum of iron clusters

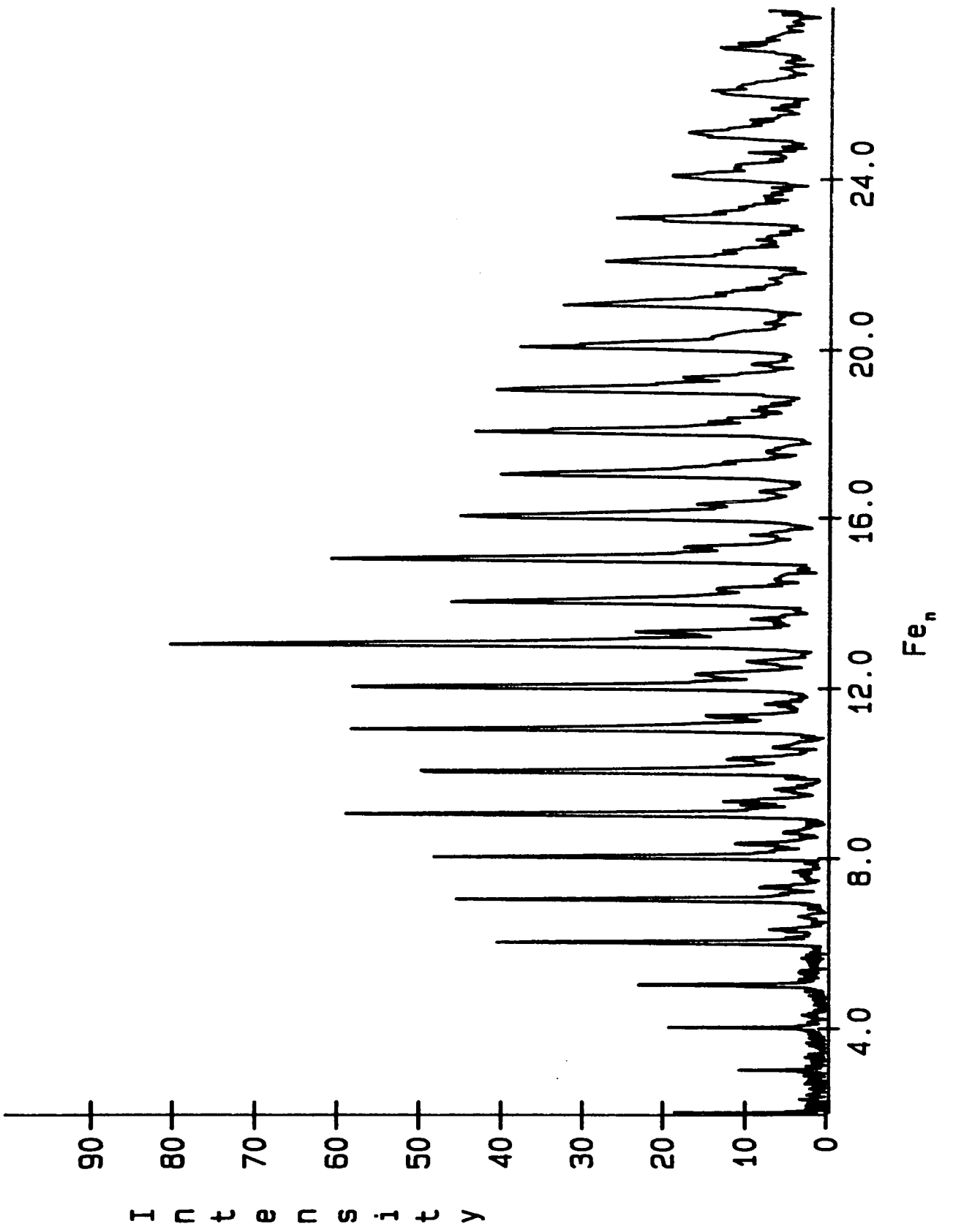

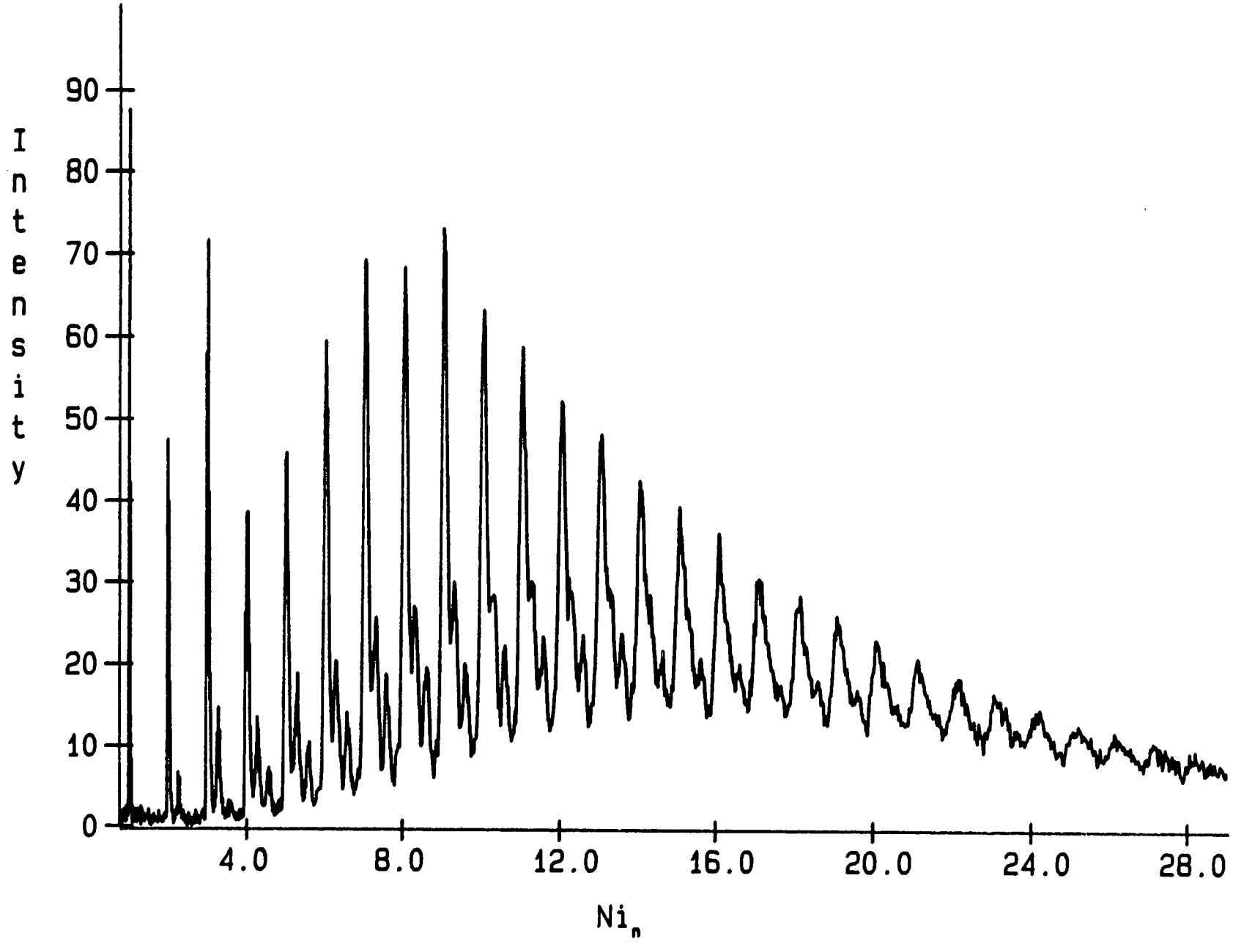

Figure 4.18 : TOF mass spectrum of nickel clusters

ionising the cluster distribution with both 266 nm (4th. harmonic Nd:YAG) and 193 nm (ArF excimer) radiation. The 266 nm radiation was generated by frequency doubling the 532 nm output of the HY750 Nd:YAG laser in a WEX-mounted KDP crystal. Figure 4.16 (a) shows the TOF mass spectrum obtained using the MB2 linear instrument (optimised for high mass clusters), when the distribution was photoionised at 266 nm (4.66 eV). The weakness of the oxide features suggests the possibility that they too, are two either two photon ionised (with lower efficiency) at this wavelength, or alternatively are present at low beam concentrations. A mass spectrum recorded immediately afterwards, with 193 nm radiation, under identical focusing conditions, was dramatically different, as Figure 4.16 (b) shows. All niobium clusters (apart from possibly the dimer and trimer, whose IPs have not been measured) are one photon ionised at this wavelength. [25] The intensity of the higher bare clusters (Nb_3-Nb_{15}) was markedly enhanced, reflecting the transition from a two to a one photon process. The second striking feature was the massive enhancement in the signal due to the higher cluster oxides relative to the bare clusters. This would appear to negate the argument that they are present in low concentrations in the beam, unless their one photon ionisation cross sections are unusually large compared to those of the bare clusters.

Making the reasonable assumption that the density of states is an increasing function of the electronic energy in the cluster, the increase in signal intensity for the oxides could point to an *increase* in cluster ionisation potential upon oxidation. For two photon ionisation at 266 nm, the first photon accesses a region of lower state density in the oxide than in the bare cluster. Thus there is

less chance of enhancement at the first photon energy since there are fewer real states nearby to contribute to the cross section (see Section 2.4). Thus the photoion intensity for the oxides using 266 nm excitation is lower than that for the unoxidised clusters. At 193 nm, all the larger cluster oxides are one-photon ionised directly into the dense continuum, as in the case for the bare metal clusters, and the corresponding smaller difference in the cross sections is reflected in the increasingly similar photoion intensity.

However, a perusal of related work urges a note of caution. Smalley and co-workers, [8] when recording photoionisation mass spectra of copper clusters, observed that when a KrCl excimer (5.58 eV) was used in place of ArF (6.4 eV) as the ionisation source, cluster oxide peaks dominated the mass spectrum. They concluded, fairly, that the bare clusters were two photon ionised at 5.58 eV, while the cluster oxides, with lower ionisation potentials, were one photon ionised at this energy. Compelling evidence to support this view comes from the surface science community. When oxygen is chemisorbed dissociatively on to a metal surface, the metal-oxygen bond is negatively polarised towards oxygen due to its considerably higher electronegativity. The work function of the surface is reduced as ejected electrons are repelled by the negative end of the metal-oxygen dipole. If our tentative interpretation has any validity, there must be substantial differences between the way in which oxygen bonds to copper and to niobium clusters. Possibly, oxygen may occupy "cage" sites in niobium clusters, partially invalidating the surface chemisorption model.

Alternative interpretations which do not rely on any energetic shift in ionisation potentials may be found. One such explanation would involve larger Nb_xO_y

clusters (outside the TOFMS mass range) being more efficiently photofragmented at 193 nm than at 266 nm, increasing both the oxide and bare cluster ion signals. Since the signal from the bare cluster ions is, in many cases, close to saturating the digitiser, a preferential enhancement in the initially-weaker cluster oxide mass channels would be seen. Alternatively, the two photon ionisation of niobium clusters at 266 nm may be resonance enhanced, with the first photon accessing a broad excitation band in a range of clusters. Oxygen chemisorption may alter the position of this absorption band to such an extent that the first photon moves well out of resonance. Thus a selective enhancement is seen for the bare clusters over the oxides at 266 nm.

In the absence of any additional data to confirm or refute any of these hypotheses, it would be unwise to speculate further on which, if any, are plausible. Clearly, there is a need to make accurate determinations of the ionisation potentials of the clusters and their oxides. Owing to the lack of a sufficiently sensitive and accurate power meter it was not possible to measure the power dependences of the photoion signal for any cluster in these experiments. Thus no crude "bracketing" of the ionisation potential between limits was possible. The ionisation thresholds of the niobium cluster oxides are sufficiently low to enable them to be accurately determined by scanning over the threshold with tunable laser radiation. The use of frequency doubled dye lasers coupled with Raman shifting should allow the thresholds of all but the smallest clusters to be measured. It is hoped that such studies would lead to an explanation of some of the peculiar features of niobium cluster oxidation.

References

[1] White F. A., Wood G. M., *Mass Spectrometry: Applications in Science and Engineering*, John Wiley, New York, 1986.

[2] Wiley W. C., McLaren I. H., Rev. Sci. Instr., **26**, p 1150, (1955)

[3] Wiza J. L., Nucl. Instr. and Methods, **162**, p 587, (1979)

[4] Parker D. H., *Ultrasensitive Laser Spectroscopy (ed. Kliger D. S.)*, Academic Press, New York, 1983.

[5] Cartwright P. C., *Ph. D. thesis*, University of Edinburgh, 1989.

[6] Karataev V. I., Mamyrin B. A., Shmikk D. V., Sov. Phys.- Tech. Phys., **16**, p 1177, (1972)

[7] Mamyrin B. A., Karataev V. I., Shmikk D. V., Zagulin V. A., Sov. Phys. JETP, **37**, p 45, (1973)

[8] Powers D. E., Hansen S. G., Geusic M. E., Michalopolous D. L., Smalley R. E., J. Chem. Phys., **78**, p 2366, (1983)

[9] Wood D.M., Phys. Rev. Lett., **46**, p 749, (1981)

[10] Kappes M. M., Schär M., Radi P., Schumacher E., J. Chem. Phys., **84**, p 1863, (1986)

[11] Tatewaki H., Miyoshi E., Nakamura T., J. Chem. Phys., **76**, p 5073, (1982)

[12] Post D., Baerends E. J., Chem. Phys. Lett., **86**, p 176, (1982)

[13] Cox P. A., Benard M., Veillard A., Chem. Phys. Lett., **87**, p 159, (1982)

[14] Richtsmeier S. C., Hendewerk M. L., Dixon D. A., Gole J. L., J. Phys. Chem., **86**, p 3932, (1982)

[15] Richtsmeier S. C., Dixon D. A., Gole J. L., J. Phys. Chem., **86**, p 3937, 3942, (1982)

[16] Hollas J. M., *High Resolution Spectroscopy*, Butterworths, London, 1982.

[17] Shim I. and Gingerich K. A., J. Chem. Phys., **79**, p 2903, (1983)

[18] Schumacher E., Gerber W. H., Harri H. P., Hoffmann M., Scholl E., *Metal bonding and interactions in high temperature systems*, ACS Symp. Ser. No.179, 1982.

[19] Hermann A., Schumacher E., Wöste L., Helv. Chim. Acta, **61**, p 453, (1978)

[20] Zheng L.-S., Karner C. M., Brucat P. J., Yang S. H., Pettiette C. L., Craycraft M. J., Smalley R. E., J. Chem. Phys., **85**, p 1681, (1986)

[21] Ganteför G., Siekmann H. R., Meiwes-Broer K. H., Lutz H. O., *XIth. Intl. Symp. on Molecular beams*, Edinburgh 1987,

[22] Katakuse I., Ichihara T., Fujita Y., Matsuo T., Sakurai T., Matsuda H., Int. Jnl. Mass Spec. Ion Proc., **67**, p 229, (1985)

[23] Cohen M. L., Chou M. Y., Knight W. D., de Heer W. A., J. Phys. Chem., **91**, p 3141, (1987)

[24] Brucat P. J., Zheng L.-S., Pettiette C. L., Yang S., Smalley R. E., J. Chem. Phys., **84**, p 3078, (1986)

[25] Whetten R. L., Zakin M. R., Cox D. M., Trevor D. J., Kaldor A., J. Chem. Phys., **85**, p 1697, (1986)

Chapter 5
Photoionisation Spectroscopy of the $A(0^+)$←$X(^1\Sigma^+)$ System of CuAg

5.1 Introduction

The mixed Group 1b dimers have received scant attention from both the experimental and theoretical communities. From the paucity of published work in this area, it should not be inferred that these systems are intrinsically lacking in interest. [1] To the contrary, they form an attractive and potentially very rewarding field of study. In general terms, information on the interaction potential between two unlike atoms can be of great utility in determining the properties of alloys. Focussing more specifically on the information of interest to quantum chemists, the validity of particular *ab initio* approaches can be assessed even more rigorously than usual when information on heteronuclear dimers as well as their homonuclear parents is available. This is particularly true in the case of the Group 1b transition metal triad.

Bonding in the homonuclear dimers of this triad is dominated by the interactions between the valence s shells, with a secondary contribution from the closed d shells which are fully occupied in the $^1\Sigma_g^+$ ground state. Extending this simple picture to the mixed dimers, we might expect to see similar trends, with the differences between the homonuclear and heteronuclear dimers being quite subtly expressed. The electronic simplicity of the closed d shell configuration should allow comparisons to be made without effects being masked by a high density of d core hole states, as is the case with the nickel-palladium-platinum

triad. [2] [3] This chapter is concerned mainly with high resolution electronic spectroscopy of the A←X system of the CuAg molecule, the simplest of these mixed dimers. Some preliminary work on ultraviolet systems of CuAg is also reported.

Early experimental investigations of the electronic spectroscopy of this molecule were limited to emission studies using high temperature (> 2000 K) King furnaces. [4] [5] Two emission systems terminating on a common lower state (presumed to be the ground state) were observed. While the spectra were characteristic of a diatomic molecule, they could not definitely be assigned to CuAg, as isotopic resolution was not achieved. However, there were pointers to support the assignment and make these systems desirable candidates for further investigation. The vibrational frequency measured for the common lower state (231.8 cm^{-1}) was roughly the arithmetic mean of the values known for the ground states of dicopper and disilver. [1] Furthermore, one of the emission systems appears in a region close to the dicopper B←X and disilver A←X systems, which are both $s\sigma^{*} \leftarrow s\sigma$ excitations. The CuAg A←X system may be their heterodimer analogue. (A summary of the known molecular constants for CuAg predating this work is given in Table 5.1.) The only other previous experimental study on CuAg was a determination of the ground state dissociation energy by Knudsen effusion mass spectrometry. [6]

Two theoretical studies of the ground $^{1}\Sigma^{+}$ state of CuAg have been carried out. In 1986 Walch *et al.* [7] performed calculations on CuAg, using a relativistic effective core potential (RECP) as part of an extensive study of the coinage metal dimers and trimers. Inclusion of f polarisation functions improved the

Table 5.1 : CuAg spectroscopic constants by thermal emission spectroscopy

State	T_e/cm^{-1}	ω_e/cm^{-1}	$\omega_e x_e/cm^{-1}$
B	25851.6	178.5	0.50
A	20836	171.5	0.50
X	0	231.8	0.80

Design.	ν_{00}	Reference
B→X	25825.0	[4] [5]
A→X	20807	[4]

Constants derived from isotopically-blended data.

calculated D_e value to within 0.08 eV of the experimental value, and the calculated ω_e to within 7 cm^{-1} of experiment. A more recent calculation by Bauschlicher *et al.* [8] yielded similar results, albeit in poorer agreement with experiment.

The apparent stagnation of experimental work in this field was largely due to the inadequacies of the King furnace method, which have been outlined in Chapter 2. With the development of the laser vaporisation-supersonic expansion technique for the preparation of cold cluster beams, and its successful interfacing to TOF mass spectrometry, refractory transition metal dimers and trimers could be studied in absorption with isotopomeric resolution (see Chapter 2).

However, there remained the problem of generating heteronuclear transition metal clusters in a controlled manner in a molecular beam environment. Several routes around this problem exist, including gas phase metal-metal reactions and the vaporisation of metal alloy targets. The former technique has been used to prepare mixed clusters of metals quite that are quite dissimilar in their physical properties, and which could not therefore be alloyed easily using thermal fusion methods. For example, this approach has been used by Duncan and co-workers [9] to prepare clusters containing bismuth (M.P. = 544 K) and chromium (M.P. = 2130 K). [10] A Bi target rod was vaporised in the conventional manner while helium doped with $Cr(CO)_6$ flowed over the target. The 308 nm vaporisation pulse photolytically strips the $Cr(CO)_6$ which reacts with Bi atoms in the plasma. This technique relies on there being a suitable volatile precursor capable of transporting one of the metals to the plasma zone.

Fabrication of metal alloy target rods by thermal fusion is well suited to mixtures of metals with similar melting points. For example, copper (M. P. = 1356 K) and silver (M. P. = 1235 K) can be readily alloyed in this way. [10] This approach has the added advantage that mixed metal targets compatible with the existing "rotating rod" cluster sources can be made. The thermal fusion method was employed in this work for these reasons. The technique clearly lacks versatility, as metals with substantially different melting points cannot be so easily mixed in the molten state.

A much more general approach which is beginning to find useful application is that of pressed metal target manufacture. The metals of interest are mixed in powdered form and compressed between two steel disks to form a thin wafer. (Sometimes it is necessary to add a binder to give the disk greater mechanical strength.) The disk is then used as a target in place of a rod in a modified metal cluster source. This "disk source" was first developed by Smalley's group [11] to mount semiconductor wafers as targets. Morse and co-workers have applied this method to the manufacture of mixed transition metal targets, and used them in elegant two colour R2PI experiments. For example, a copper-nickel disk was fabricated in this way (M.P.(Cu) = 1356 K, M.P.(Ni) = 1726 K [10]) and the electronic structure of the diatomic molecule CuNi probed using mass selective R2PI spectroscopy with rovibronic resolution. [12]

5.2 Experimental considerations

Some aspects of the experimental arrangement specific to the generation and spectroscopic characterisation of the CuAg molecule must now be considered.

The principles underlying the experiments were outlined in Chapter 2, whilst a description of the general experimental setup is to be found in Chapter 3.

5.2.1 Copper-silver alloy rod fabrication

Manufacture of the CuAg target rod followed a method communicated to us by Hackett and Simard. [13] Equimolar quantities of 5 mm diameter copper and silver rods were cut into short (3-5 mm) lengths and placed, in an alternating order, in a quartz tube (softening temperature = 1940 K [10]) of dimensions 100 x 6 mm. The tube was heated strongly with a blowtorch (acetylene flame) until the copper and silver slugs melted and became mixed. A stream of argon gas was flowed over the open end of the tube to prevent aerial oxidation of the exposed end of the rod. Heating was accompanied by vigorous agitation to drive off air bubbles trapped between the slug sections. Several melt-solidify cycles were usually needed to thoroughly mix the copper and silver. After the final solidification, the quartz tube was broken off and the rod turned down on a lathe until it fitted the cluster source fixture. The length of rod which could be fabricated was limited by the cost of silver and by the difficulty of maintaining a constant temperature over a long length of tube. A clear improvement in this respect would be the use of a furnace rather than a blowtorch as the heat source. To fit the dimensional requirements of the cluster source and rod rotation assembly, lengths of copper were brazed on to each end of the CuAg rod using a dovetail joint. From the observed long term stability of the cluster signal intensity in the TOF mass spectrum, it was concluded that copper and silver were distributed fairly homogeneously throughout the rod.

5.2.2 Experimental setup for R2PI spectroscopy

A beam of CuAg clusters was generated on the MB2 RETOFMS rig in the manner described in Chapter 3. The General Valve Series 9 pulsed nozzle was used as the source of quenching gas, operating at 10 Hz with 10 atmospheres of helium backing pressure. Vaporisation was accomplished by the Q-switched 532 nm second harmonic output of the DCR-2 Nd:YAG laser, focussed by a 100 cm BK7 plano-convex pyrex lens on to the target at a power density of ca. 180 MW cm^{-2}.

The cluster beam was first characterised by nonresonant photoionisation using the Lumonics TE-861-T excimer laser, operating on the ArF line (193 nm). The geometry of the laboratory necessitated siting the output coupler of the excimer laser all of 190 cm from the access window on the ion source chamber of the apparatus. Since the laser was not operated in an unstable resonator configuration, the considerable beam divergence (6 mrad) led to an unacceptably large expansion of the beam over this distance. A partial solution to this problem was obtained by irising the central portion of the beam and focusing the laser into the ion source chamber using a spherical biconvex quartz lens (30 cm focal length). The lens could be translated to move the position of the laser focus beyond the ion extraction region thus facilitating some degree of control on the laser power incident on the core of the molecular beam. This excimer laser was also used to provide the second ionising photon in the two colour photoionisation experiments. The power density required for a single photon ionisation step was much less than that required for two photon nonresonant ionisation. In this mode therefore, the beam was irised but not

focused, and the power density attenuated further (to < 0.05 MW cm^{-2}) using wire mesh gauzes inserted at an angle into the beam to cut down transmission.

The two colour R2PI experiments were performed using the Lambda Physik excimer pumped dye laser system as excitation source, and the ArF excimer laser to one photon ionise CuAg from the excited state. All the experiments reported here were carried out using the dye Coumarin 102 (Lambdachrome LC4800) which lases over the range 460-510 nm, peaking at 480 nm with 18 % efficiency. The two laser beams were overlapped spatially in the ion source of the RETOFMS. Optimum contrast between the resonant signal and nonresonant background was obtained when the narrow diameter ionisation beam ($\simeq$ 0.03 cm^2) was "buried" in a larger diameter beam ($\simeq$ 0.4 cm^2) from the dye laser. The output from the dye laser was attenuated to reduce saturation broadening using combinations of neutral density filters (Schott) placed in the beamline. Tunable ultraviolet radiation for one colour R2PI of the ultraviolet systems was obtained by frequency doubling the dye laser output in a β barium borate crystal (see Chapter 3). The resulting UV output (1 MW cm^{-2} maximum) was directed into the RETOFMS source without focusing.

In the two colour photoionisation experiments, accurate control of the time delay between the two excimer lasers was crucial to ensure that the two laser pulses were overlapped temporally during an experimental run. This was particularly important for the CuAg A$\leftarrow$X system where the excited state lifetime is short ($\simeq$ 30 ns), and excursions due to timing jitter destroy the signal stability. This was achieved by directing a small fraction of each beam on to fast photodiodes (Siemens BPY62 phototransistors, operated as simple emitter-collector junctions).

The light signals were monitored continuously on an oscilloscope (Tektronix 2445, 150 MHz) so that the relative timing of the lasers could be altered during the recording of R2PI spectra without having to halt execution and perform a "time scan" (see Section 3.7).

When digitising and averaging ion signals in the mass spectrum, it was desirable to maximise the number of points over which each peak was sampled. To achieve this, the RETOFMS was operated in a slightly out-of-focus mode. This broadened the ion peaks without degrading the resolution to the extent of blending neighbouring features. In this mode, ion peaks were typically 40 ns wide at mass 170 amu, so that 5 sampling points covered this range at 100 MHz sampling rate.

The vibronic spectra reported here were calibrated by simultaneous recording of transmission fringes from a fused silica monitor etalon (free spectral range = 3.333(2) cm^{-1} at 480 nm), and optogalvanically-recorded transitions in neon (Cathodeon hollow cathode lamp system). [14] These calibration signals were sampled and averaged by gated integrators (Stanford Research Systems SR250), prior to being fed to ADC input channels. The etalon free spectral range depends inversely on the refractive index of silica [15] and thus varies with wavelength. The wavelength-dependence of the FSR was established by measuring it at a range of wavelengths between 470 and 480 nm using neon optogalvanic transitions as reference. Band positions were measured from reference optogalvanic lines by counting and interpolation of etalon fringes, taking into account the variation of FSR with wavelength. The Lambda-Physik confocal monitor etalon accessory (air-spaced, FSR $\simeq$ 0.1 cm^{-1}) was used with a

gated integrator to calibrate the rotationally-resolved R2PI spectra.

5.3 R2PI spectroscopy of the A←X system in CuAg

5.3.1 Vibronic spectroscopy

Before performing any spectroscopy experiments, the concentration of CuAg dimers in the beam was optimised, monitoring the concentration by nonresonant photoionisation using 6.4 eV radiation from the Lumonics excimer laser. A typical distribution of copper-silver clusters was shown earlier in Figure 4.14. The adiabatic ionisation potential of CuAg has been determined to be 7.78058(54) eV (see Chapter 6), and thus the molecule is two photon ionised with ArF radiation. Despite this, the generation of strong nonresonant ionisation signals, comparable to those observed in earlier work on Cu_2, proved relatively easy. Facile two colour R2PI of the A←X system is viable, since CuAg can be one photon ionised from the lowest vibrational level of the A state with 6.4 eV radiation. Figure 5.1 shows a portion of the CuAg cluster TOF mass spectrum obtained by 6.4 eV photoionisation. The three CuAg mass peaks arise from the four different isotopic combinations of $^{63,65}Cu$ and $^{107,109}Ag$. An isobaric interference occurs at mass 172 between $^{63}Cu^{109}Ag$ and $^{65}Cu^{107}Ag$. The observed intensity ratios, 1.0 : 1.2 : 0.4, are in approximate agreement with those calculated assuming that equimolar concentrations of copper and silver are vaporised. The experimental resolution, with the spectrometer slightly defocused and a sampling rate of 100 MHz, was $t/2\delta t = 500$. Under these conditions, there is no risk of neighbouring peak interference when recording mass resolved R2PI

Figure 5.1 : TOF mass spectrum of CuAg isotopomers

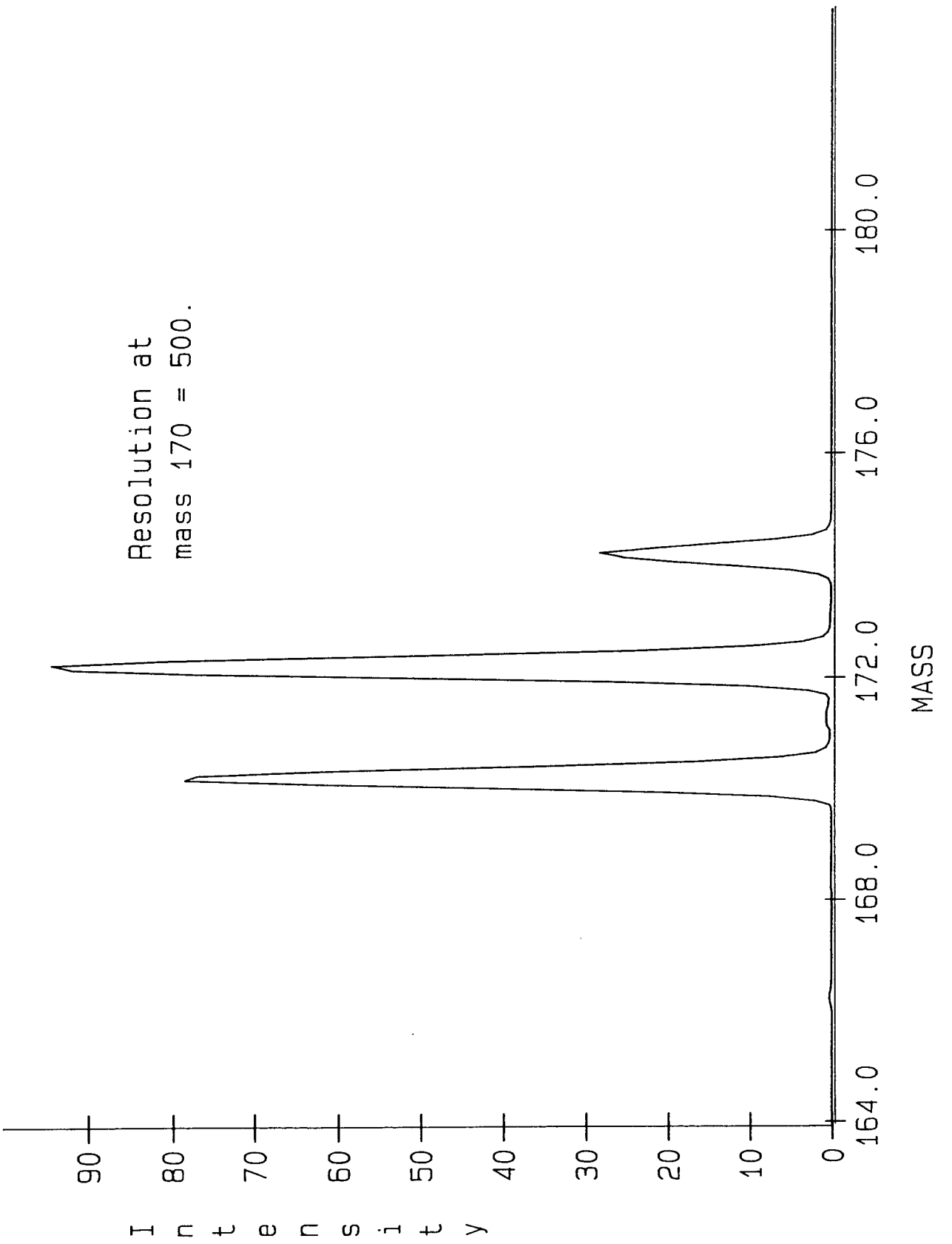

spectra.

Figure 5.2 shows the R2PI spectrum obtained by scanning the exciting dye laser (with a power density of 0.03-0.04 MW cm^{-2}), in the presence of the ArF excimer laser, through the region of the A←X system reported by Ruamps. [4] The ion signal was monitored in the mass 170 (Figure 5.2 (a)) and mass 172 (Figure 5.2 (b)) data channels. Recorded simultaneously with these spectra were monitor etalon fringes and optogalvanic lines for calibration purposes. The laser grating was stepped in 0.01 nm (0.43 cm^{-1}) increments, 35 experimental cycles being accumulated at each point in the scan. The step size was, by necessity, fairly large, as the long term cluster stability and ionisation laser pulse energy could not be guaranteed for more than a couple of hours.

Reasonably good agreement between the observed band positions and those calculated using the data of Ruamps was obtained. [4] The two main progressions observed were readily assigned to transitions originating from v" = 0 and v" = 1, terminating on a range of upper state vibrational levels. Observation of an appreciably intense (v',1) hot band progression suggests that vibrational cooling in the expansion may not be particularly efficient. From the observed intensity ratios of the (0-0), (2-1) and (3-2) bands (recorded in a region where the laser power was relatively constant), the vibrational temperature was estimated very crudely from a Boltzmann population analysis to be $\simeq$ 200 K. By contrast, T_{rot} was determined (see Section 5.3.3) to be < 20 K. This illustrates the severe disequilibrium between internal degrees of freedom which can occur during adiabatic expansion. For the spectrum recorded in the mass 172 data channels, bandheads due to the $^{63}Cu^{109}Ag$ isotopomer could just be distinguished from

Figure 5.2 (a) : Vibronic R2PI spectrum of the A←X system of $^{63}Cu^{107}Ag$

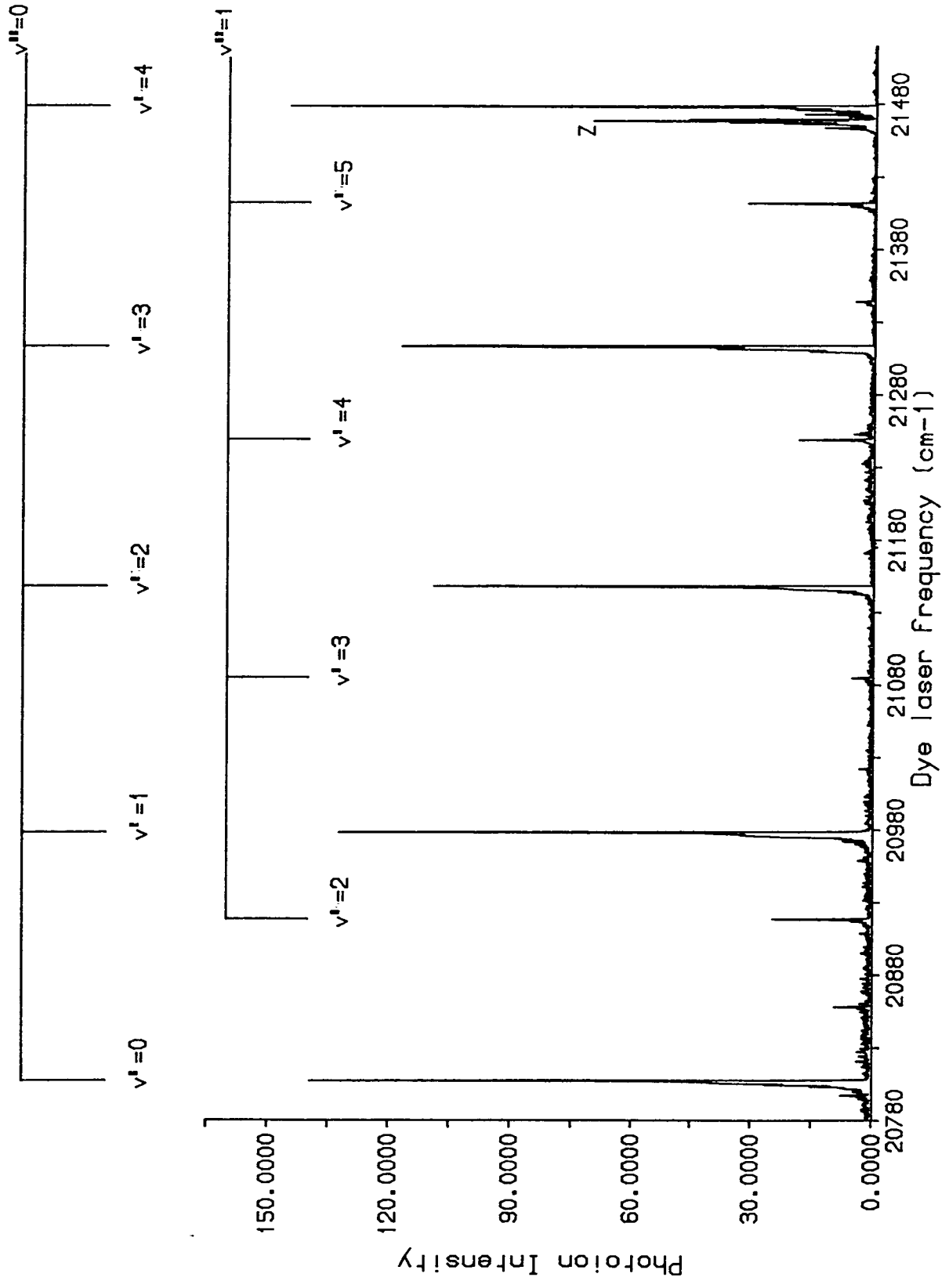

Figure 5.2 (b) : Vibronic R2PI spectrum of the A←X system of $^{63}Cu^{109}Ag$ and $^{65}Cu^{107}Ag$

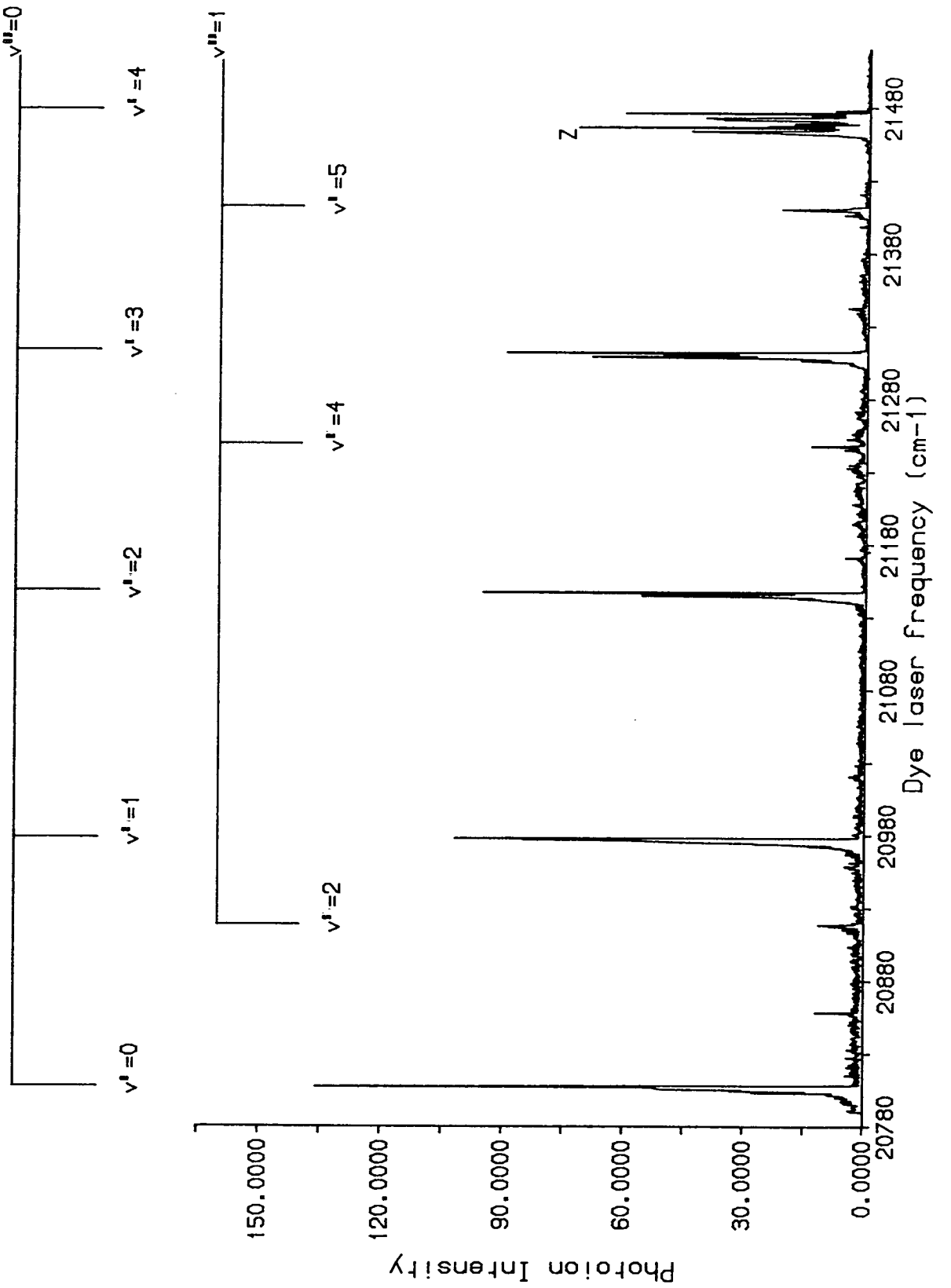

those due to $^{65}Cu^{107}Ag$. The former is more than twice as abundant than its isobaric companion. (The rotationally resolved spectra recorded in these mass channels, Figures 5.4 (b) and 5.5 (b), show this with much greater clarity.) The feature labelled "Z" lying just to the low wavenumber side of the (4-0) band is extraneous to the A←X system, and does not appear to perturb the position of the v_A = 4 vibrational level. Its origin is discussed in Section 5.5 below.

Due to blending in the mixed isotope mass channels and poor signal in the $^{65}Cu^{109}Ag$ channels, it was not possible to determine accurately the bandhead positions for this isotopomer. Thus to extract vibrational constants for the two states, the band positions for $^{63}Cu^{107}Ag$ alone were subjected to a linear least squares analysis. A program written in the FORTRAN 77 high level language, with algorithms developed by Bevington, [16] was used for this purpose. Band positions were assumed to be well represented by the expression: [17] [18]

$$\nu = T_e' + G(v') - [\, T_e'' + G(v'') \,] \qquad (5.1)$$

where

ν = the band position (transition energy)

$G(v) = \omega_e(v+1/2) - \omega_e x_e(v+1/2)^2$

T_e = the electronic term value.

Bandhead positions in these R2PI spectra were determined more accurately than those reported in the emission spectrum, since the latter were not isotopically resolved. However, a note of caution is sounded at this point. The positions of the relatively weak features in the (v',1) progression could not be determined

with the same precision as the members of the (v',0) progression. Furthermore, the range of vibrational levels spanned by the data set is somewhat limited: v" = 0,1 and v' = 0-5. This limits the effectiveness of the least squares treatment in producing reliable vibrational constants. These factors, coupled with some uncertainty in the absolute positions of the bandheads, due to the relatively large laser step size, led to rather imprecise determinations of the vibrational constants. The results of the least squares fitting procedure are presented in Table 5.2.

5.3.2 Lifetime measurements

Time-delayed R2PI spectroscopy was used to determine the lifetime of the v = 0 vibrational level of the A state. The dye laser was tuned to the R branch bandhead, and the time delay between the excitation laser and the ionisation laser scanned to map out the decay profile of the excited state. The ion signal was monitored at 1 ns intervals, and 15-20 timescans were averaged to generate the decay profile. Figure 5.3 shows the decay profile obtained for the $v_A = 0$ level of the $^{63}Cu^{107}Ag$ isotopomer. The decay profiles for the $v_A = 1$ and $v_A = 2$ levels were also recorded, but here it was not possible to extract sensible decay constants, owing to the interference of a fluctuating background ionisation signal. The cause of this was not apparent, although it may have derived from the one colour 1+2 ionisation mechanism described in Section 5.5.

The experimental decay profile represents a double convolution of the pure exponential decay function corresponding to the excited state lifetime, with the excitation and ionisation laser pulse profiles, which may be approximated by Gaussian functions. Since the pulse widths for the exciting and ionising lasers

Table 5.2 : Bandhead positions and vibrational constants for the A←X system of CuAg

Simultaneous fitting of both isotopes

Weighting = $1/(err^2)$

Isotopomer	Band	Obs./cm^{-1}	Err./cm^{-1}	Calc./cm^{-1}	Resid./cm^{-1}
63-107	(0-0)	20807.20	0.58	20807.24	-0.04
63-107	(1-0)	20978.27	0.68	20978.15	0.12
63-107	(2-0)	21146.79	0.78	21146.81	-0.02
63-107	(3-0)	21313.13	0.88	21313.23	-0.10
63-107	(4-0)	21477.42	0.98	21477.41	0.01
63-107	(3-2)	20857.86	1.03	20857.86	0.00
63-107	(2-1)	20918.27	0.57	20918.29	-0.02
63-107	(3-1)	21084.79	1.17	21084.72	0.07
63-107	(4-1)	21248.89	0.77	21248.90	-0.01
63-107	(5-1)	21410.86	0.86	21410.84	0.02

Reduced χ^2 = 0.0012

$^{63}Cu^{107}Ag$ constants:

State	T_e/cm^{-1}	ω_e/cm^{-1}	$\omega_e x_e/cm^{-1}$	ν_{00}/cm^{-1}
A	20835.8(10)	173.15(64)	1.12(11)	20807.20(58)
X	0.00	230.2(18)	0.83(69)	-

Errors quoted are ± 1σ

Figure 5.3 : Excitation decay profile for the $v_A = 0$ level of $^{63}Cu^{107}Ag$

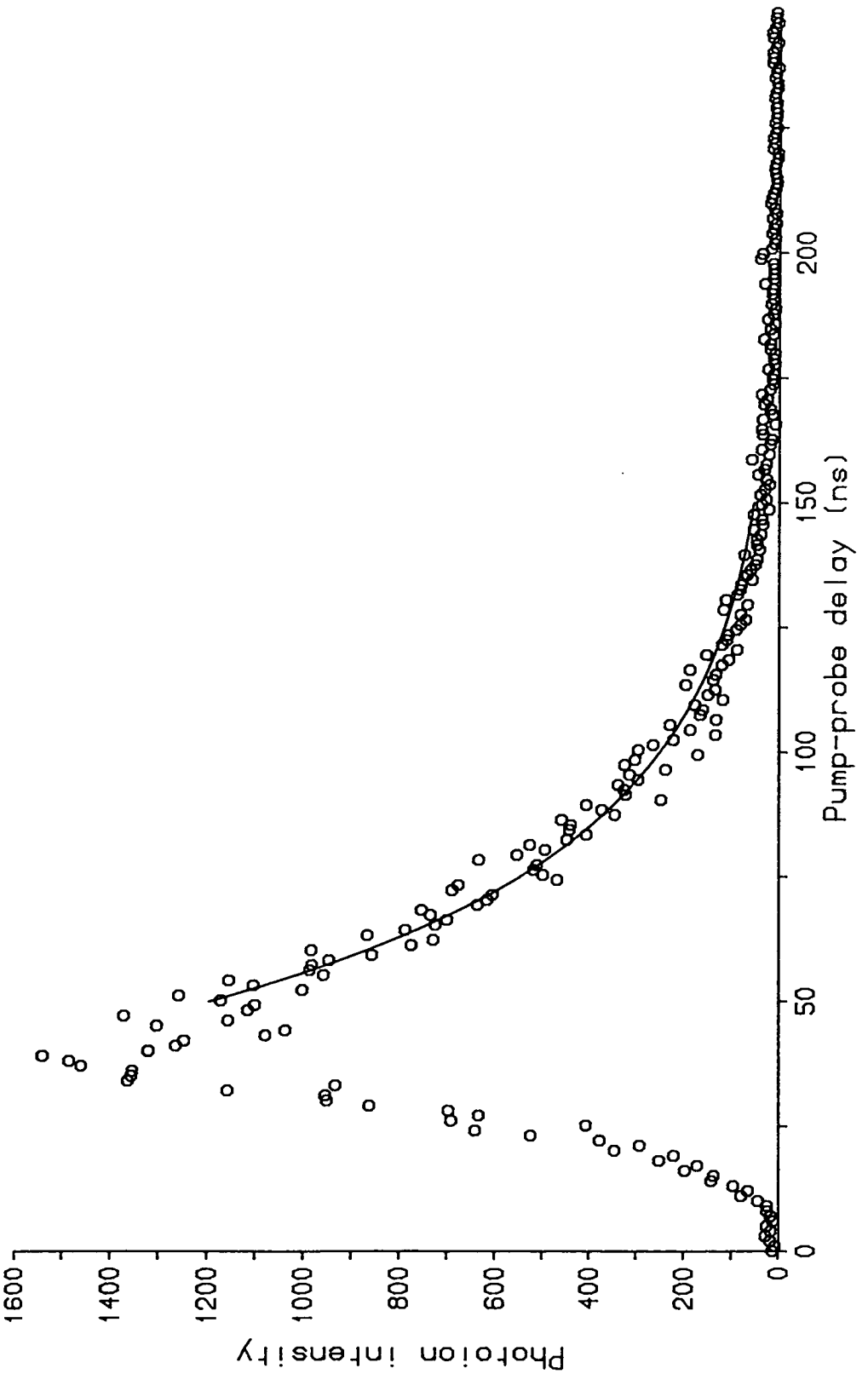

were $\simeq$ 20 ns and $\simeq$ 10 ns respectively, the lifetimes of short-lived excited states cannot be measured with any great accuracy. Double pulse deconvolution techniques could be applied to extract the true lifetime, but the quality of data obtained here hardly merited their application.

However, a crude upper-limit value for the lifetime may be extracted using a simplified analysis which ignores the broadening contributions of the two laser pulses. Assuming that the decay profile corresponds to a single exponential, the time variation of the R2PI signal will be given by the expression:

$$I_c(t) = I_{0,c}\exp(-t/\tau) \qquad (5.2)$$

where

the zero of time is a point on the decaying portion of the curve

t is the time elapsed from this point

$I_c(t)$ is the two colour resonant ionisation signal

at time t (background corrected)

$I_{0,c}$ is the resonant ionisation signal at the arbitrary zero of time

and τ is the experimental total decay lifetime.

A plot of $\ln I_c(t)$ versus t should yield a straight line of slope $1/\tau$. A point on the decaying portion of the curve near t = 60 ns, clear of the trace maximum, was selected as the zero of time. Following this procedure, data points for the v = 0 vibrational level of the A state were submitted to a least squares fit to determine τ. A value of 32 $\pm$ 2 ns was obtained.

$1/\tau$ represents the the A state lifetime for decay through all possible channels. The relatively short values confirm the experimental observation that the A←X transition is a strongly-allowed electronic promotion.

5.3.3 Rotationally-resolved spectroscopy

To obtain rotationally-resolved spectra of the A←X system required the use of etalon line-narrowed radiation from the dye laser ($\simeq$ 0.04 cm^{-1} bandwidth). The dye laser ($\simeq$ 0.01 MW cm^{-2} power density) was scanned with a stepping increment of $\simeq$ 0.038 cm^{-1}, accumulating 35 experimental cycles at each scan point. Ideally, a smaller wavelength step would have been preferred, but the stability of the cluster signal could not be guaranteed over a long period. Fortuitously, the vaporisation-expansion conditions which were found to optimise cluster intensity and stability also produced rotationally cold CuAg ($T_{rot} < 20$ K), as can be seen in Figure 5.4 (a). This depicts the origin band of the A←X system recorded in the $^{63}Cu^{107}Ag$ mass channels.

The spectrum clearly contains only P and R branches, indicating that a parallel transition is taking place with no change in overall angular momentum between the A and X states. [19] Thus the transition may be assigned as $A(0^+)\leftarrow X(0^+)$, where the lower 0^+ state is formally derived from $^1\Sigma^+$. The band is red-shaded with a rapidly-reversing R branch bandhead, indicating that substantial bond lengthening occurs upon electronic excitation. In general appearance, the spectrum is reminiscent of two systems of the homonuclear coinage dimers, namely the $B(0_u^+)\leftarrow X(^1\Sigma_g^+)$ [20] system of Cu_2 and the $A(0_u^+)\leftarrow X(^1\Sigma_g^+)$ system [21] of Ag_2. Spectra recorded for the origin band in the other mass channels are

Figure 5.4 (a) : Rotationally-resolved R2PI spectrum of the (0-0) band of the A←X system of $^{63}Cu^{107}Ag$

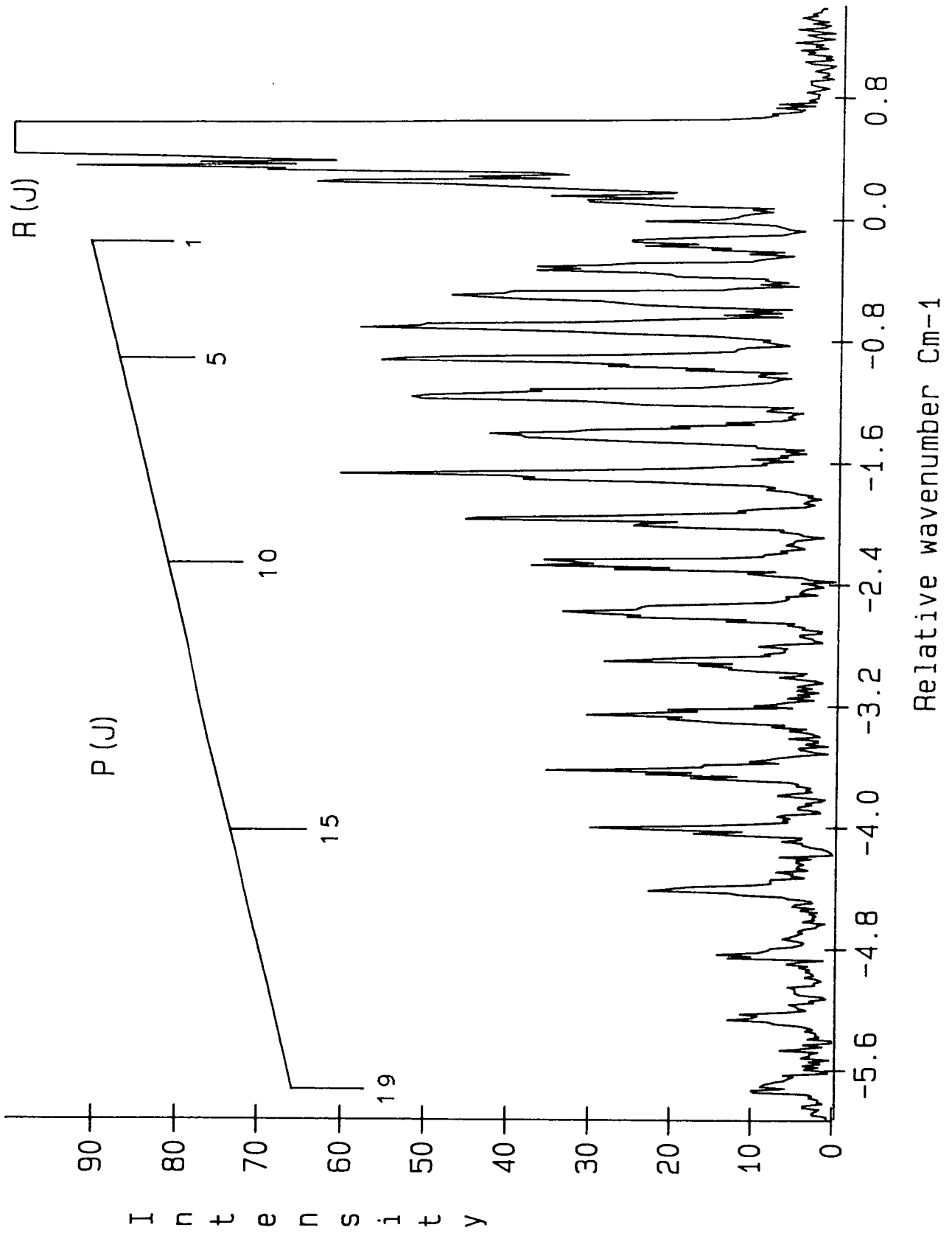

Figure 5.4 (b) : Rotationally-resolved R2PI spectrum of the (0-0) bands of the A←X system of $^{63}Cu^{109}Ag$ and $^{65}Cu^{107}Ag$

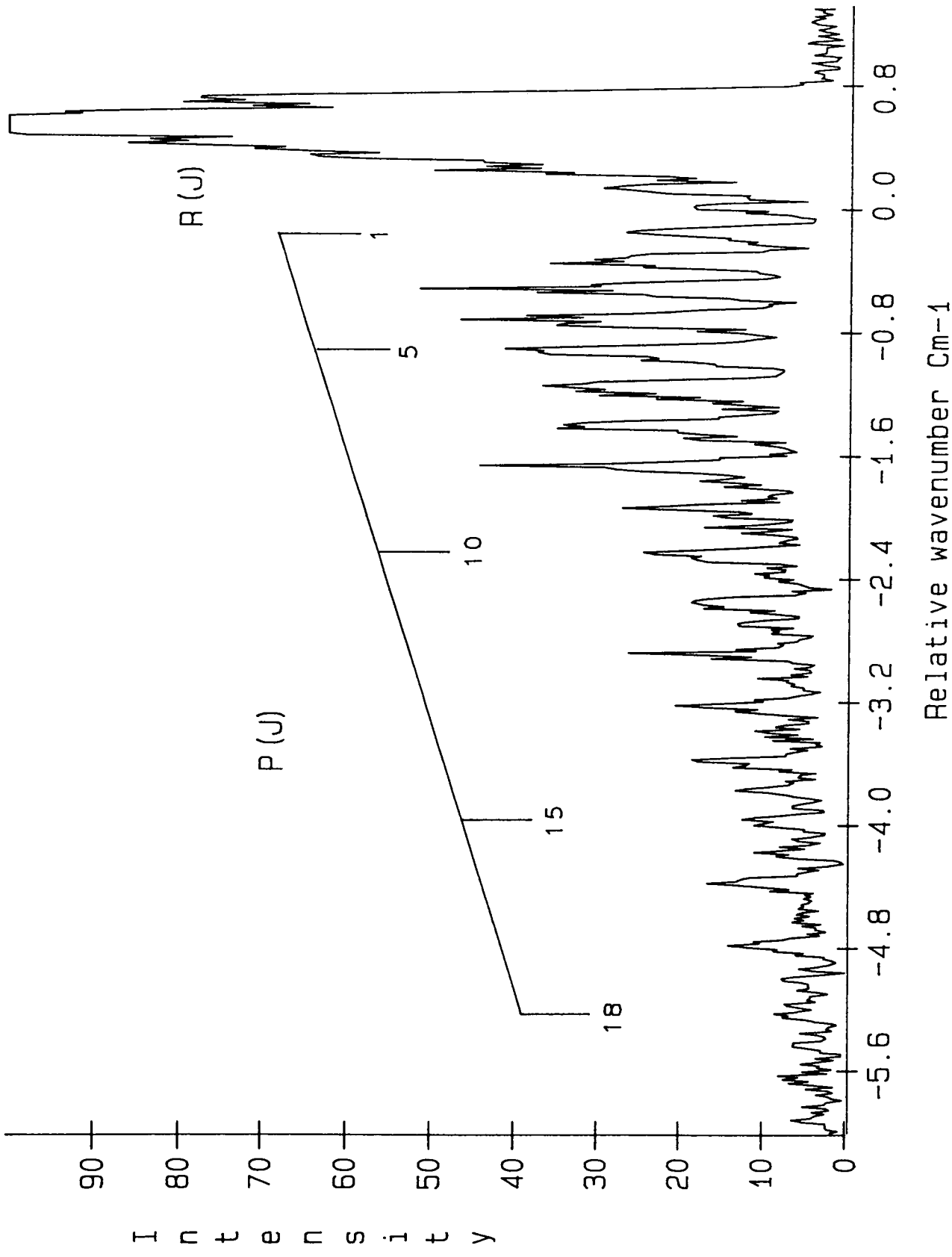

Figure 5.4 (c) : Rotationally-resolved R2PI spectrum of the (0-0) band of the A←X system of $^{65}Cu^{109}Ag$

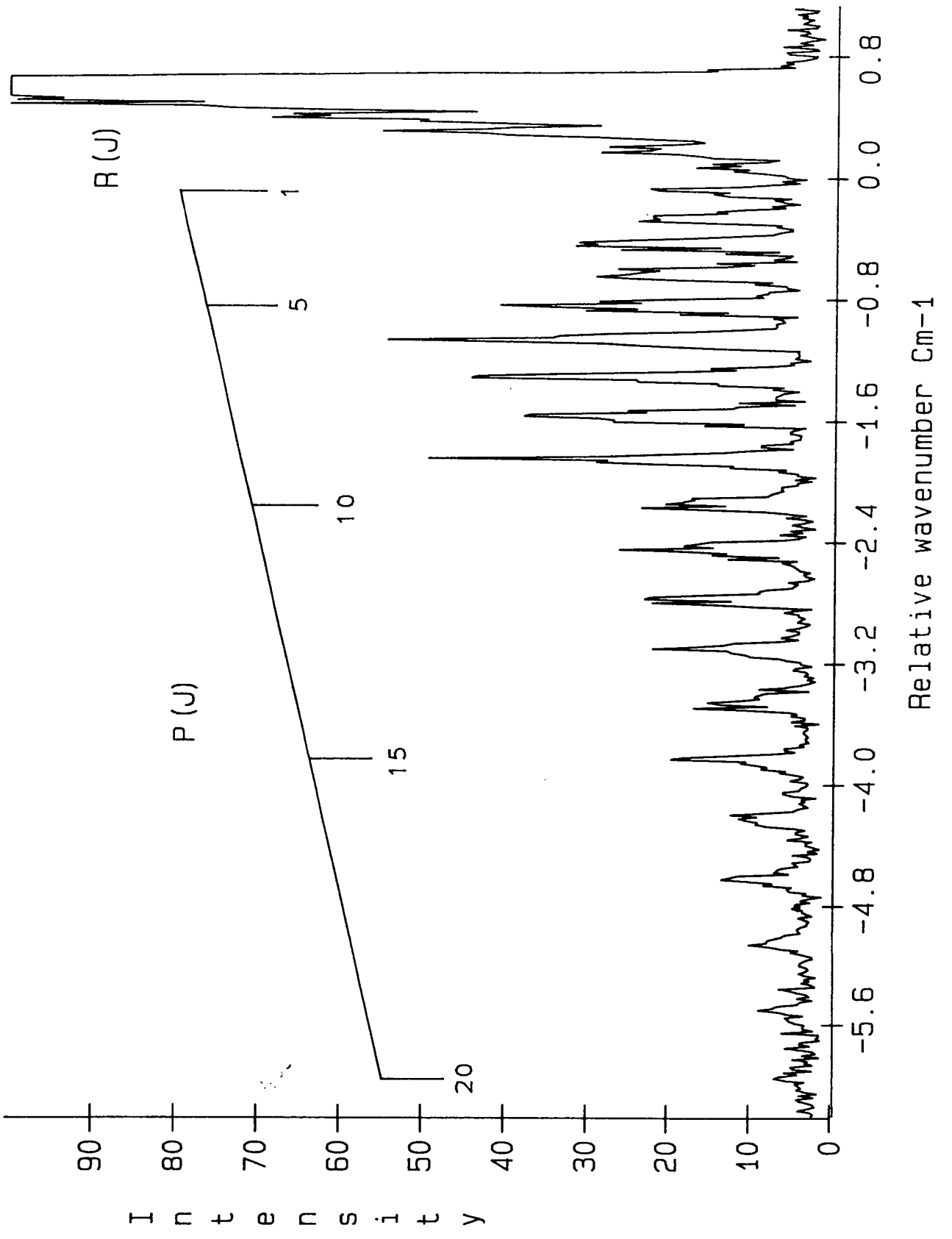

Figure 5.4 (d) : Experimental and simulated spectra of the (0-0) band of the A←X system of $^{63}Cu^{107}Ag$

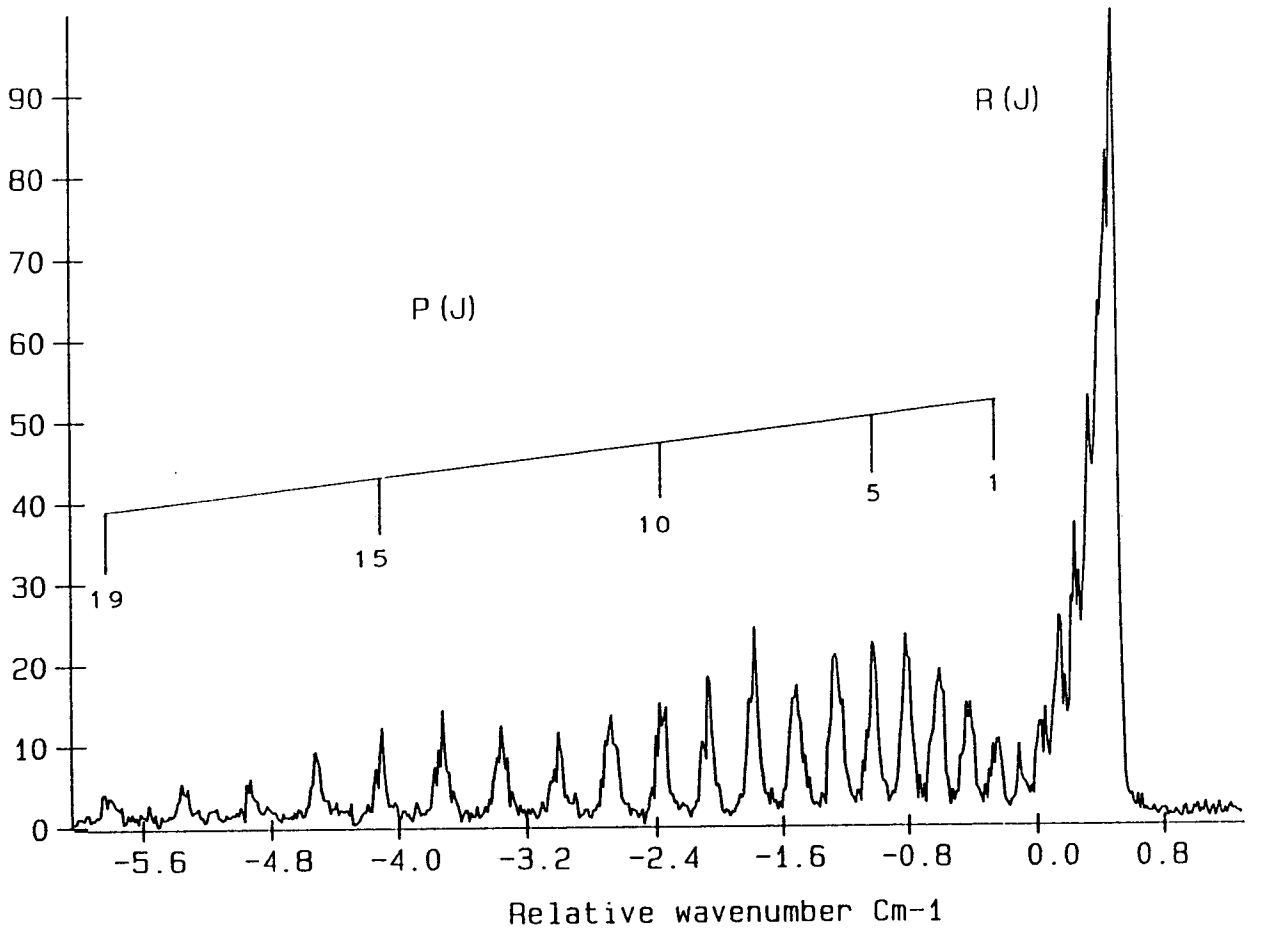

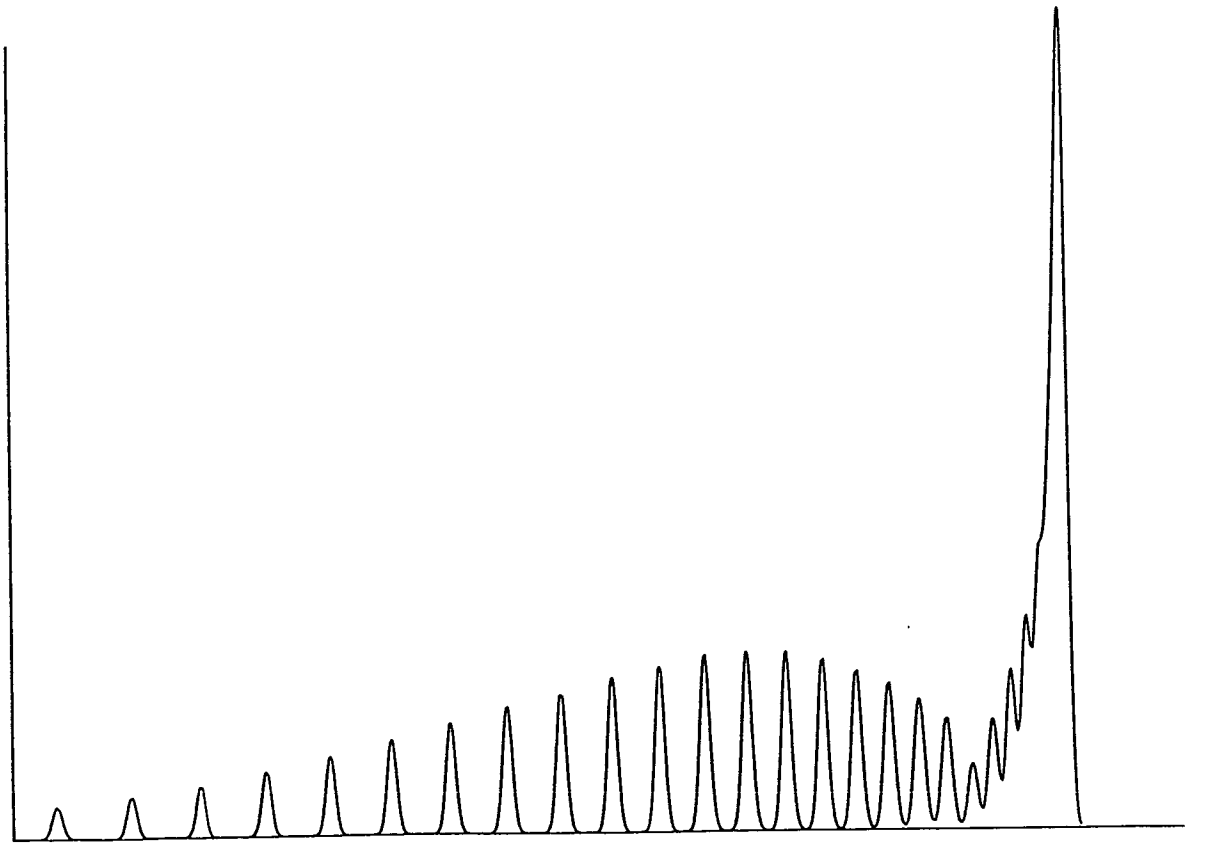

Figure 5.5 (a) : Rotationally-resolved R2PI spectrum of the (1-0) band of the A←X system of $^{63}Cu^{107}Ag$

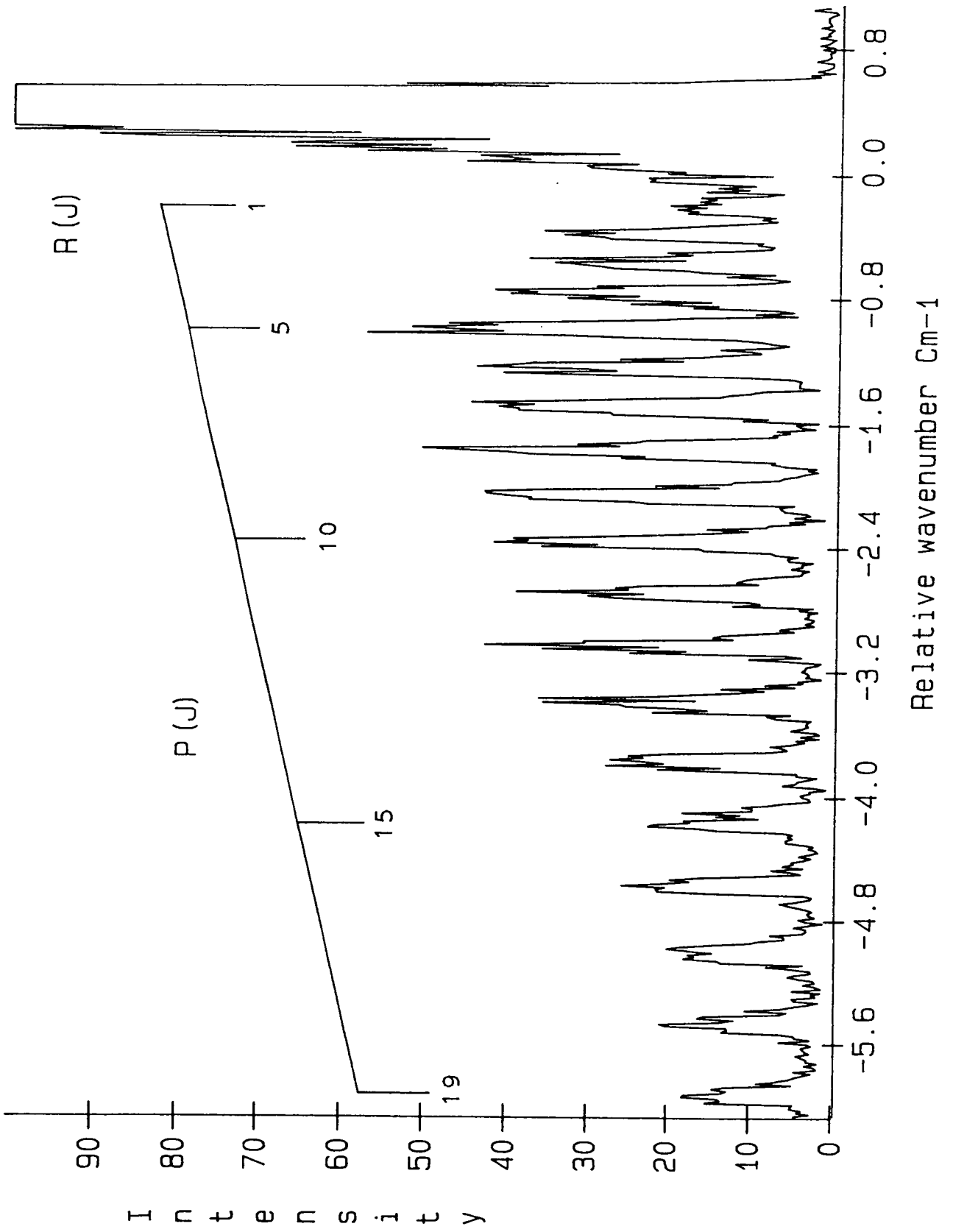

Figure 5.5 (b) : Rotationally-resolved R2PI spectrum of the (1-0) bands of the A←X system of $^{63}Cu^{109}Ag$ and $^{65}Cu^{107}Ag$

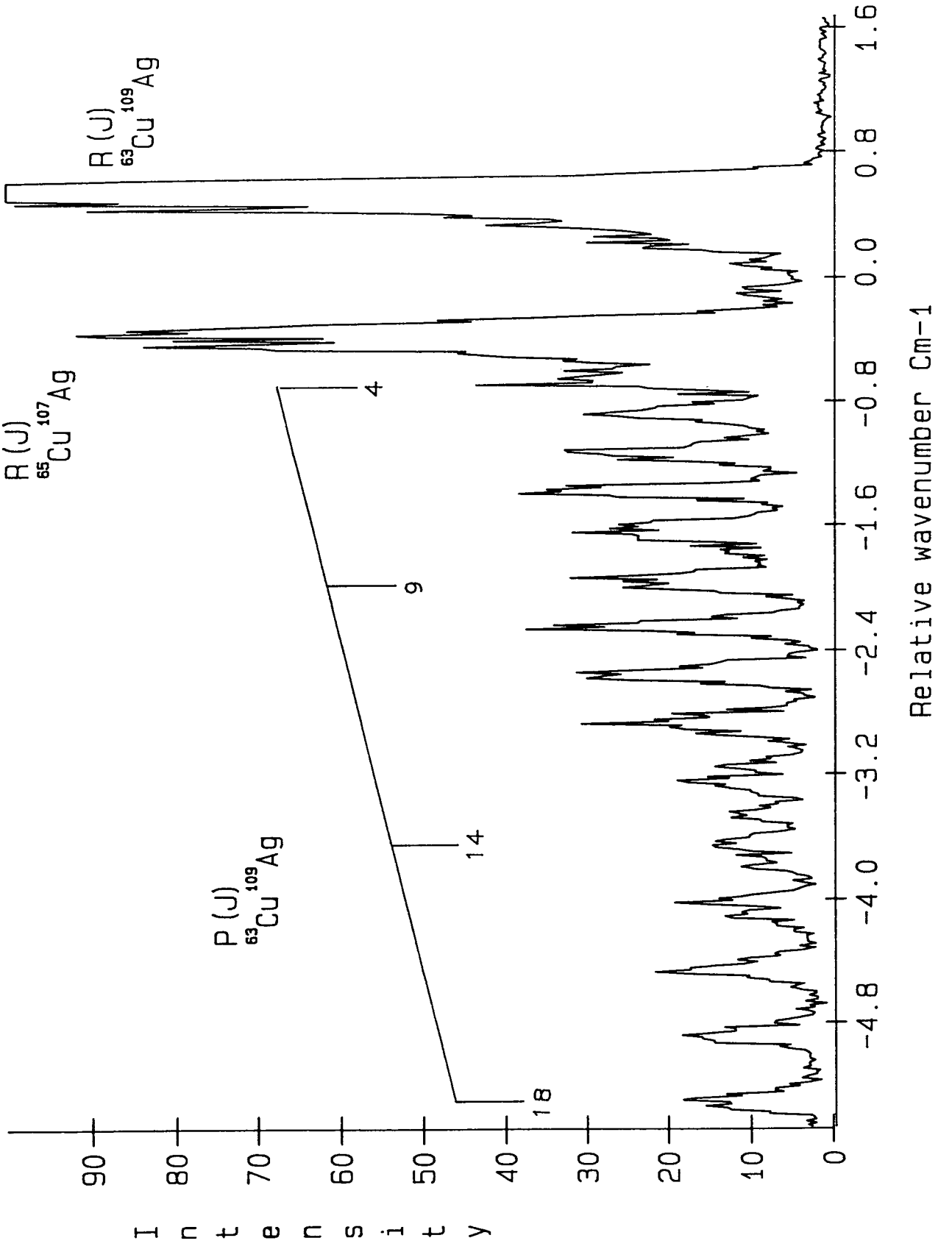

Figure 5.5 (c) : Rotationally-resolved R2PI spectrum of the (1-0) band of the A←X system of $^{65}Cu^{109}Ag$

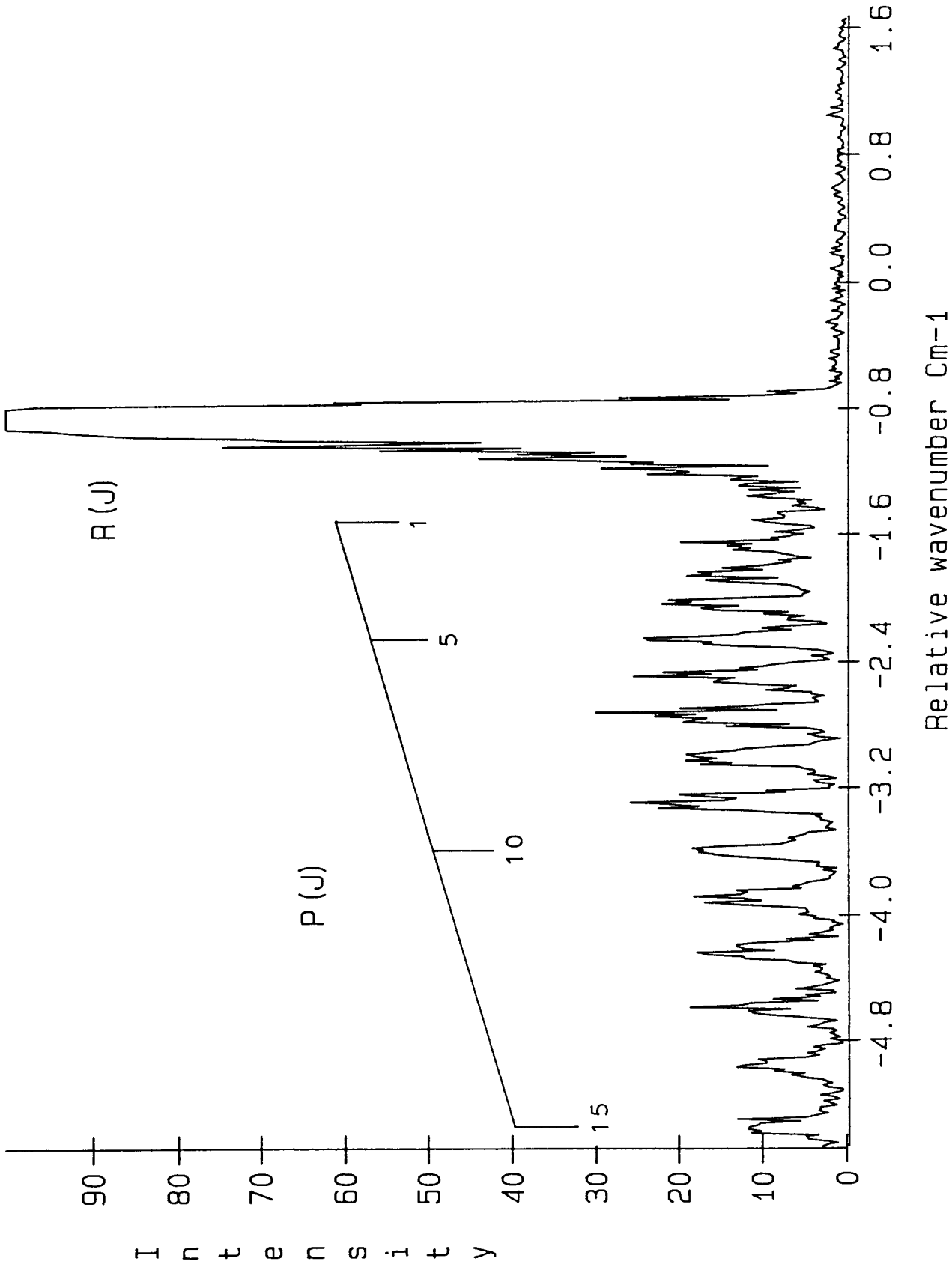

Figure 5.5 (d) : Experimental and simulated spectra of the (1-0) band of the A←X system of $^{63}Cu^{107}Ag$

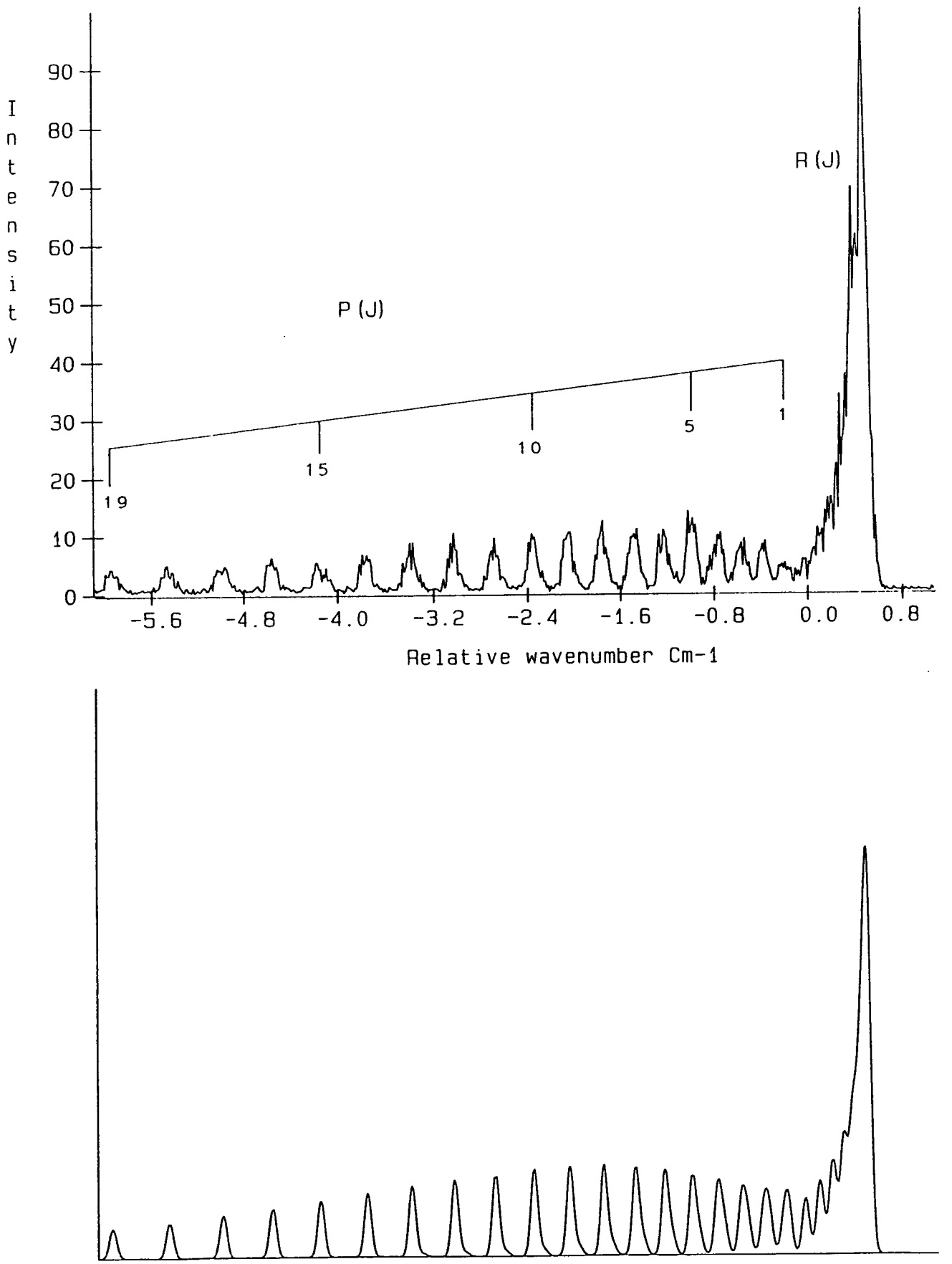

presented in Figures 5.4 (b) and (c), and those for the (1-0) band in Figure 5.5 (a)-(c). Simulations of the $^{63}Cu^{107}Ag$ rotational profiles are included for comparison as Figures 5.4 (d) and 5.5 (d). These best matched the experimental spectra when rotational temperatures of 13.5 K (0-0) and 17.5 K (1-0) were programmed. A description of the simulation procedure is the subject of Section 5.3.4. It is clear that less efficient rotational cooling would pose serious problems for spectroscopic interpretation. The higher members of the R branch would become blended with the P branch with the result that the null gap becomes completely obscured. Under the moderate laser resolution employed here, it was desirable to keep T_{rot} as low as possible, even if this entailed sacrificing higher J lines from the fit.

The experimental laser bandwidth was measured from the widths of the monitor etalon transmission fringes. A mean value of $\simeq$ 0.04 cm^{-1} (FWHM) was obtained, in agreement with the manufacturer's specification. However, the profiles of individual rotational lines were on average twice as broad. Since the Doppler linewidth ($<$ 0.003 cm^{-1}) is much smaller than the laser bandwidth, some residual power saturation broadening of the rovibronic lines must be present.

It was possible to assign nearly all P-branch members and some partially blended members of the R-branch for 3 of the 4 isotopomers. The relatively weak lines arising from $^{65}Cu^{107}Ag$ were in most cases completely obscured by those from $^{63}Cu^{109}Ag$, and only the bandheads were really discernible. Thus the fitting procedure was applied to $^{63}Cu^{107}Ag$, $^{63}Cu^{109}Ag$ and $^{65}Cu^{109}Ag$ only.

Line positions were measured relative to the first etalon fringe as an arbitrary reference marker. The etalon free spectral range (0.10008(57) cm^{-1}) [20] is itself subject to measurement uncertainty, and thus line positions were measured up in units of FSR before being fitted. Each line position was weighted by its measurement error as $1/(error^2)$. The fitted rotational constants and errors (in FSR units) were then multiplied by the etalon free spectral range, and the overall errors calculated.

For $0^+ \leftarrow 0^+$ transitions, the rovibronic selection rules are $\Delta J = -1$ (P branch) and $\Delta J = +1$ (R branch). The line positions therefore obey the simple expression: [19]

$$\nu(J) = \nu_0 + F'(J + i) - F''(J) \qquad (5.3)$$

where ν_0 is the rotationless band origin, i = -1 for the P-branch and +1 for the R-branch. The F(J)s are rotational term energy expressions of the form:

$$F(J) = B_v J(J + 1) - D_v J^2(J + 1)^2 + \ldots \qquad (5.4)$$

where B_v and D_v are the rotational and centrifugal distortion constants respectively. In the least squares fitting procedure, the D_v terms were dropped as the experimental precision was not sufficient to justify their inclusion.

A linear least squares fitting program, [16] written in FORTRAN 77, was employed to extract rotational constants and rotationless band origins from the measured line positions. A global fit on data from all three isotopes was performed, assuming that the rotational constant for the i th. isotopomer can be

written as: [19]

$$B^i = \rho_i^2 B \tag{5.5}$$

where B is the rotational constant for the lightest isotopomer ($^{63}Cu^{107}Ag$) and $\rho_i = (\mu/\mu_i)^{1/2}$. It should be noted that this is not strictly accurate, since B^i actually depends on ρ_i according to:

$$B_v^i = \rho_i^2 B_e - \rho_i^3 \alpha_e (v + 1/2) \tag{5.6}$$

where B_e is the equilibrium rotational constant and α_e the vibration-rotation coupling constant. In the approximation used here:

$$B_v^i = \rho_i^2 B_e - \rho_i^2 \alpha_e (v + 1/2). \tag{5.7}$$

Since α_e is very small ($< 1 \times 10^{-3}$ cm^{-1}) and $\rho_i \simeq 1$, the error introduced by making this approximation is found to be negligible at this level of precision.

The error in the free spectral range (0.57 %) was found to be significant when compared with the errors arising from the fits themselves. The FSR error does much to spoil the overall precision to which the constants may be quoted. This is a far from satisfactory situation, but represented the best which could be achieved under the circumstances. The FSR of the confocal monitor etalon was determined indirectly by Cartwright, [20] who normalised copper dimer spectral fits to literature values of the ground state constants. It was found to vary significantly over the range of determinations. An unambiguous *in situ* determination of the FSR could have been made in the course of recording the

CuAg spectra had there been a suitable set of optogalvanic lines nearby. Unfortunately, no such set of lines was present. Results of the fitting procedure are presented in Tables 5.3 and 5.4.

The vibronic isotope shifts were calculated from the differences between the rotationless band origins for the various isotopomers. These shifts can be expressed as the sum of an electronic and a vibrational isotope shift:

$$\Delta\nu^{i}_{vibel} = \Delta\nu^{i}_{el} + \Delta\nu^{i}_{vib} \tag{5.8}$$

where each $\Delta\nu^{i}$ is given by $\nu^{63-107} - \nu^{i}$. The vibrational isotope shift may be calculated explicitly from the vibrational constants of the lightest isotopomer: [22]

$$\Delta\nu^{i}_{vib} = \nu-\nu_i = (1-\rho_i)[\omega_e'(v'+1/2) - \omega_e''(v''+1/2)]$$
$$- (1-\rho_i^2)[\omega_e x_e'(v'+1/2)^2 - \omega_e x_e''(v''+1/2)^2] \tag{5.9}$$

where the terms have their usual definition. Using the vibrational constants for $^{63}Cu^{107}Ag$ from Table 5.2, $\Delta\nu^{i}_{vib}$ was calculated for each band. Had the vibrational constants been determined from a multi-isotope fit, it would have been necessary to treat the vibrationless origins as parameters to be fitted, rather than as a unique constant. (The electronic term values differ slightly between isotopomers: the molecular electronic isotope shift. [23] [24]) Table 5.5 contains the experimental vibronic and vibrational isotope shifts, and the electronic isotope shifts calculated from them.

For the A state, the equilibrium rotational constant (B_e) and the vibration-rotation coupling constant (α_e) were extracted from B_0 and B_1 using

Table 5.3 : Line positions and rotational constants for the CuAg A←X (0-0) band

Units of Free Spectral Range
Simultaneous fitting of all isotopes
Weighting = $1/(err^2)$

Isotopomer	Branch	J"	Calc.	Obs.	Error	Resid.
63-107	P	19	0.2323	0.3200	0.1850	0.0876
63-107	P	18	4.7420	4.8410	0.1850	0.0990
63-107	P	17	9.0850	8.9350	0.1850	-0.1500
63-107	P	16	13.2615	13.2500	0.1600	-0.0115
63-107	P	15	17.2714	17.1830	0.1850	-0.0884
63-107	P	14	21.1148	21.0720	0.1850	-0.0428
63-107	P	13	24.7916	24.7980	0.1480	0.0064
63-107	P	12	28.3018	28.3530	0.1600	0.0512
63-107	P	11	31.6454	31.6290	0.1480	-0.0164
63-107	P	10	34.8225	34.8540	0.1720	0.0315
63-107	P	9	37.8330	37.7270	0.1850	-0.1060
63-107	P	8	40.6769	40.6520	0.1850	-0.0249
63-107	P	7	43.3543	43.2940	0.1600	-0.0603
63-107	P	6	45.8651	45.7940	0.1850	-0.0711
63-107	P	5	48.2093	48.1860	0.1600	-0.0233
63-107	P	4	50.3870	50.3850	0.1480	-0.0020
63-107	P	3	52.3980	52.4680	0.1600	0.0700
63-107	P	2	54.2425	54.2830	0.1720	0.0405
63-107	P	1	55.9205	56.0600	0.1720	0.1395
63-107	R	0	58.7767	58.7830	0.1720	0.0064
63-107	R	16	57.6400	57.4810	0.1720	-0.1590
63-107	R	1	59.9549	60.0360	0.1850	0.0811
63-107	R	3	61.8123	61.9290	0.1850	0.1174
63-107	R	9	63.3842	63.3960	0.1720	0.0118
63-109	P	18	6.0276	5.8700	0.1970	-0.1576
63-109	P	17	10.3411	10.1800	0.1850	-0.1611
63-109	P	16	14.4892	14.5550	0.1850	0.0658
63-109	P	15	18.4719	18.6120	0.1970	0.1401
63-109	P	14	22.2891	22.4320	0.1850	0.1429
63-109	P	13	25.9409	25.9700	0.1850	0.0291
63-109	P	12	29.4272	29.4230	0.1850	-0.0042
63-109	P	11	32.7481	32.7910	0.1850	0.0429
63-109	P	10	35.9036	36.0200	0.1850	0.1164
63-109	P	9	38.8936	39.0130	0.1850	0.1194
63-109	P	8	41.7182	41.6900	0.1850	-0.0282
63-109	P	7	44.3774	44.3220	0.1850	-0.0554
63-109	P	6	46.8711	46.7230	0.1850	-0.1481
63-109	P	5	49.1994	49.1810	0.1850	-0.0184

63-109	P	4	51.3622	51.1800	0.1850	-0.1822
63-109	P	3	53.3596	53.2530	0.1850	-0.1066
63-109	P	2	55.1916	55.1320	0.1850	-0.0596
63-109	P	1	56.8581	56.9800	0.1850	0.1219
63-109	R	16	58.5659	58.6520	0.1850	0.0861
63-109	R	0	59.6949	59.8210	0.1850	0.1261
63-109	R	9	64.2711	64.1900	0.1970	-0.0811
65-109	P	20	0.5953	0.6420	0.1970	0.0467
65-109	P	19	5.1492	5.1990	0.1970	0.0499
65-109	P	18	9.5407	9.5880	0.1970	0.0473
65-109	P	17	13.7702	13.9270	0.1970	0.1568
65-109	P	16	17.8374	17.8610	0.1970	0.0236
65-109	P	15	21.7424	21.7790	0.1970	0.0366
65-109	P	14	25.4852	25.3920	0.1970	-0.0932
65-109	P	13	29.0657	29.1200	0.1970	0.0543
65-109	P	12	32.4841	32.3660	0.1970	-0.1181
65-109	P	11	35.7402	35.7500	0.1970	0.0098
65-109	P	10	38.8342	38.6960	0.1970	-0.1382
65-109	P	9	41.7659	41.7020	0.1970	-0.0639
65-109	P	8	44.5354	44.4650	0.1970	-0.0704
65-109	P	7	47.1427	47.0760	0.1970	-0.0667
65-109	P	6	49.5878	49.5820	0.1970	-0.0058
65-109	P	5	51.8707	51.8330	0.1970	-0.0377
65-109	P	4	53.9914	53.9390	0.1970	-0.0524
65-109	P	3	55.9498	55.9330	0.1970	-0.0168
65-109	P	2	57.7461	57.6770	0.1970	-0.0691
65-109	P	1	59.3801	59.5040	0.1970	0.1239
65-109	R	0	62.1616	62.2040	0.1970	0.0425
65-109	R	1	63.3090	63.3870	0.1970	0.0781
65-109	R	2	64.2941	64.3570	0.1970	0.0629

$B_0' = 0.67240 \pm 0.00171$ FSR

$B_0'' = 0.75568 \pm 0.00159$ FSR

Rotationless origins:

63-107 : 57.432 ± 0.042 FSR
63-109 : 58.359 ± 0.047 FSR
65-109 : 60.852 ± 0.049 FSR

Errors quoted are ± 1σ

χ-squared = 14.897
Degrees of freedom = 63
Reduced χ^2 = 0.236

Table 5.4 : Line positions and rotational constants for the CuAg A←X (1-0) band

Units of Free Spectral Range
Simultaneous fitting of all isotopes
Weighting = $1/(err^2)$

Isotopomer	Branch	J"	Calc.	Obs.	Error	Resid.
63-107	P	19	0.5611	0.5610	0.1850	-0.0001
63-107	P	18	5.2395	5.2710	0.1850	0.0315
63-107	P	17	9.7421	9.7390	0.1850	-0.0031
63-107	P	16	14.0691	14.0940	0.1850	0.0249
63-107	P	15	18.2203	18.2140	0.1850	-0.0064
63-107	P	14	22.1959	22.1940	0.1850	-0.0019
63-107	P	13	25.9958	26.0310	0.1850	0.0352
63-107	P	12	29.6200	29.5700	0.1850	-0.0500
63-107	P	11	33.0686	33.0710	0.1850	0.0025
63-107	P	10	36.3414	36.2900	0.1850	-0.0514
63-107	P	9	39.4385	39.4320	0.1850	-0.0065
63-107	P	8	42.3600	42.4060	0.1850	0.0461
63-107	P	7	45.1057	45.1270	0.1850	0.0213
63-107	P	6	47.6757	47.6320	0.1850	-0.0437
63-107	P	5	50.0701	50.0160	0.1850	-0.0541
63-107	P	4	52.2888	52.4230	0.1850	0.1342
63-107	P	3	54.3318	54.3510	0.1850	0.0192
63-107	P	2	56.1991	56.1910	0.1850	-0.0081
63-107	P	1	57.8907	57.8650	0.1850	-0.0257
63-107	R	5	64.8125	64.7400	0.1970	-0.0725
63-109	P	18	0.8271	0.8610	0.1850	0.0339
63-109	P	17	5.2991	5.2300	0.1850	-0.0691
63-109	P	16	9.5967	9.3530	0.1850	-0.2437
63-109	P	15	13.7197	13.7810	0.1970	0.0613
63-109	P	12	25.0419	25.3590	0.1970	0.3171
63-109	P	11	28.4669	28.4220	0.1850	-0.0449
63-109	P	10	31.7175	31.6200	0.1850	-0.0975
63-109	P	9	34.7936	34.6790	0.1850	-0.1146
63-109	P	8	37.6952	37.8300	0.1850	0.1349
63-109	P	7	40.4222	40.3900	0.1850	-0.0322
63-109	P	6	42.9748	42.9320	0.1850	-0.0428
63-109	P	5	45.3529	45.4420	0.1850	0.0891
63-109	P	4	47.5565	47.4810	0.1970	-0.0755
63-109	P	1	53.1203	53.2330	0.1850	0.1127
63-109	R	15	54.9840	54.9910	0.1850	0.0070
65-109	P	15	0.4902	0.5350	0.2100	0.0449
65-109	P	14	4.3617	4.5510	0.1850	0.1893

65-109	P	13	8.0622	8.0710	0.1850	0.0088
65-109	P	12	11.5916	11.5650	0.1980	-0.0266
65-109	P	11	14.9498	15.0400	0.1980	0.0902
65-109	P	10	18.1370	17.9770	0.1850	-0.1600
65-109	P	9	21.1531	21.1000	0.1970	-0.0531
65-109	P	8	23.9981	23.9700	0.1850	-0.0281
65-109	P	7	26.6720	26.6370	0.1980	-0.0350
65-109	P	6	29.1748	29.1000	0.1850	-0.0748
65-109	P	5	31.5065	31.5060	0.1850	-0.0005
65-109	P	4	33.6671	33.7170	0.1850	0.0499
65-109	P	3	35.6567	35.5820	0.1985	-0.0747
65-109	P	2	37.4751	37.4470	0.1980	-0.0281
65-109	P	1	39.1224	39.2280	0.1980	0.1056

$B_1' = 0.67011 \pm 0.00288$ FSR

$B_0'' = 0.75796 \pm 0.00264$ FSR

Rotationless origins:

63-107 : 59.407 ± 0.058 FSR
63-109 : 54.626 ± 0.061 FSR
65-109 : 40.599 ± 0.059 FSR

Errors quoted are ± 1σ

χ-squared = 10.708
Degrees of freedom = 45
Reduced χ^2 = 0.238

Table 5.5 : Isotope shifts in the A←X system of CuAg

Band/isotopomer	$\Delta\nu^i_{vibel}$	$\Delta\nu^i_{vib}$	$\Delta\nu^i_{el}$
(0-0) 63-109	-0.0928(89)	-0.0976(56)	+0.005(15)
(0-0) 65-109	-0.3423(92)	-0.377(22)	+0.035(31)
(1-0) 63-109	+0.478(12)	+0.4769(91)	+0.001(21)
(1-0) 65-109	+1.883(16)	+1.844(36)	+0.039(52)

See text for definitions.

the relation:

$$B_v = B_e - \alpha_e(v + 1/2). \tag{5.10}$$

For the ground state, only B_0 was known so it was not possible to solve linear equations for α_e. Instead, if it is assumed that the potential energy curve for the ground state can be well represented by a Morse function, [25] the following expression, due to Pekeris, may be used to estimate α_e: [26]

$$\alpha_e = 6(\omega_e x_e B_e^3)^{1/2}/\omega_e - 6B_e^2/\omega_e, \tag{5.11}$$

where B_0 ($\simeq B_e$) is the equilibrium rotational constant for the lowest vibrational level, and the other terms have their usual definitions. This relation gave a sensible value for α_e, although it should only be regarded as rough estimate.

The final molecular rotational constants for $^{63}Cu^{107}Ag$ are presented in Table 5.6. The experimental α_e value for the A state should be viewed with some caution owing to the large uncertainty associated with its determination.

5.3.4 Rovibronic spectral simulations

Providentially, the A←X system of CuAg was a simple $0^+ \leftarrow 0^+$ parallel transition, presenting few problems in the simulation of the rotational fine structure within the vibronic bands. A general purpose program, written in the FORTRAN 77 high level language, was developed to treat both $\Sigma \leftarrow \Sigma$ and $\Pi \leftarrow \Sigma$ transitions in both homonuclear and heteronuclear diatomic molecules. Simulation of rotational structure in a vibronic band requires a knowledge of the rotational energy

Table 5.6 : Rotational constants for the A and X states of $^{63}Cu^{107}Ag$

$B_1' = 0.06696(67)\ cm^{-1}$

$r_1' = 2.520(13)$ Å

$B_0' = 0.06739(60)\ cm^{-1}$

$r_0' = 2.512(11)$ Å

$B_0'' = 0.07574(45)\ cm^{-1}$ -a

$r_0'' = 2.3692(71)$ Å

$A(0^+)$ state :

$B_e' = 0.06761(75)\ cm^{-1}$

$\alpha_e' = 4.3(90) \times 10^{-4}\ cm^{-1}$

$r_e' = 2.508(14)$ Å

$X(^1\Sigma^+)$ state :

$B_e'' = 0.07592(46)\ cm^{-1}$

$\alpha_e'' = 3.6(20) \times 10^{-4}\ cm^{-1}$ -b

$r_e'' = 2.3664(71)$ Å

a - average of the two determinations
b - estimated from the Pekeris relation
Errors quoted are $\pm\ 1\sigma$

expressions and molecular constants for the upper and lower states, the selection rules for the transition, and several factors which modify the line intensities. The positions of individual lines were calculated using the fitted molecular constants, the transition energy expressions described above, and the selection rule $\Delta J = \pm 1$ appropriate for an $0^+ \leftarrow 0^+$ transition.

To obtain the correct distribution of line intensities, it is generally necessary to evaluate three factors which contribute to the strengths of individual rovibronic lines: (1) a population factor, (2) a line strength factor, and (3) a nuclear spin weighting factor.

(1) The intensity of a particular rovibronic transition $(v,J') \leftarrow (v,J'')$ is proportional to the population $N_{v\ J''}$ in the level (v,J''). Molecular populations are distributed among rotational levels of $^1\Sigma$ states according to the Boltzmann law: [17] [27]

$$N_{v\ J''} = (N_v/Q_{rot})(2J'' + 1)e^{-BvJ''(J'' + 1)/kTrot} \qquad (5.12)$$

where N_v is the total population in the level v, T_{rot} the rotational temperature, and Q_{rot} the rotational partition function.

(2) The observed line intensities are also affected by the intrinsic rotational line strengths. These were first derived by Hönl and London [28] for symmetric top molecules. For an $0^+ \leftarrow 0^+$ transition in a diatomic molecule their expressions reduce to:

$$S^R_{J''} = (J'' + 1)/(2J'' + 1) \qquad (5.13)$$

$$S^{P}_{J''} = J''/(2J'' + 1) \qquad (5.14)$$

for R- and P-branch transitions respectively.

(3) The rovibronic line intensities may also be modified by nuclear spin statistical weighting. This applies only to homonuclear diatomic molecules, and is not relevant to CuAg. Appendix E contains a brief description of the origin and consequences of this effect with regard to silver dimer.

The intensity of a rovibronic line in the CuAg A←X system is therefore proportional to the product of the population and line strength factors:

$$I = C \times S^{P/R}_{J''} \times N_{v\ J''}$$

where C is a collection of constants including the rotational partition function.

To simulate the rotational structure, the appropriate intensity factors were calculated for each line position using the above formulae. A Gaussian function representing the combined effects of the laser bandwidth and saturation broadening was run over the resulting "stick diagram" to obtain realistic blending of closely-spaced lines. The rotational temperature was varied until the best match of simulated and experimental spectra was obtained. A comparison of relative intensities among members of the P branch was adjudged to be the most reliable criterion for matching the simulated and experimental spectra. The overall intensity of the rapidly reversing R-branch bandhead, in which many lines overlap, is highly sensitive to the exact value of the laser bandwidth and to the the effects of power saturation broadening. Since these contributions were not

easily quantifiable, the relative intensity of the P-branch to the R-bandhead was not considered to be as reliable in matching the spectra.

5.4 Discussion

5.4.1 The X($^1\Sigma^+$) state

From a theoretician's standpoint, two of the most useful ground state spectroscopic parameters have been determined in this study, namely the vibrational frequency and the bondlength. Of these, a knowledge of the equilibrium internuclear separation is the more useful. The atomic orbital basis sets employed in calculations do not always provide an adequate representation of the electron distribution at large nucleus-electron distances, and tend to be optimised for interatomic separations closer to the equilibrium bondlength. Hence spectroscopic parameters which depend on the orbital overlap at long range will be highly sensitive to the exact formulation of the basis sets.

The *ab initio* potential curve is determined by first determining the total energy (E) at a range of internuclear separations, and subtracting the atomic energies at infinite separation. The bondlength and vibrational frequency are obtained by fitting a polynomial through a range of (E,R) data points. The value obtained for the bondlength is relatively insensitive to the behaviour of the wavefunction at long range, and reasonable agreement with experiment can be expected provided that the basis sets have been chosen with due care. Inadequacies in the basis sets may show up more sharply in the calculation of ω_e and D_e. Bearing in mind these caveats, *ab initio* data on the ground state of CuAg may be reviewed

critically in the light of this work.

Figure 5.6 shows non-relativistic Hartree-Fock orbital energies for the ground state ($^2S_{1/2}$) configurations of atomic copper and silver. [29] In molecular terms, the diagram shows the relative energies for copper and silver atomic orbitals when the two constituent atoms of CuAg are separated to infinity. Bonding in CuAg will arise primarily from overlap between the singly occupied Cu(4s) and Ag(5s) valence orbitals, which are separated in the nonrelativistic approximation by only 0.50 eV, the Cu(4s) orbital lying lower.

It is important not to overlook the effects of relativistic orbital stabilisation, which will be significant for the Ag(5s) orbital. The s orbital wavefunctions have nonzero amplitude at the nucleus. [30] If the nuclear charge is sufficiently high, the s electrons move in such a strong coulomb field in the vicinity of the nucleus that their velocities approach the speed of light. The relativistic mass of the electron increases with velocity, and thus a "mass-velocity" correction must be applied to the electron kinetic energy when solving the Schrödinger wave equation for the orbital energies. [31] Since the atomic scale of length varies inversely with the electron mass, the s orbitals become radially contracted and energetically stabilised. Electrons in orbitals with higher angular momentum, which do not penetrate the nuclear region, are uncontracted. In fact, the contraction of the s orbitals improves the shielding of these orbitals from the nuclear charge, and they expand. In diatomic molecules where the s orbitals are significantly involved in bonding, relativistic effects are manifested spectroscopically as a stiffening in the vibrational frequency, increase in the dissociation energy and a contraction in the bond length.

Figure 5.6 : Nonrelativistic Hartree-Fock orbital energies for the $^2S_{1/2}$ states of copper and silver

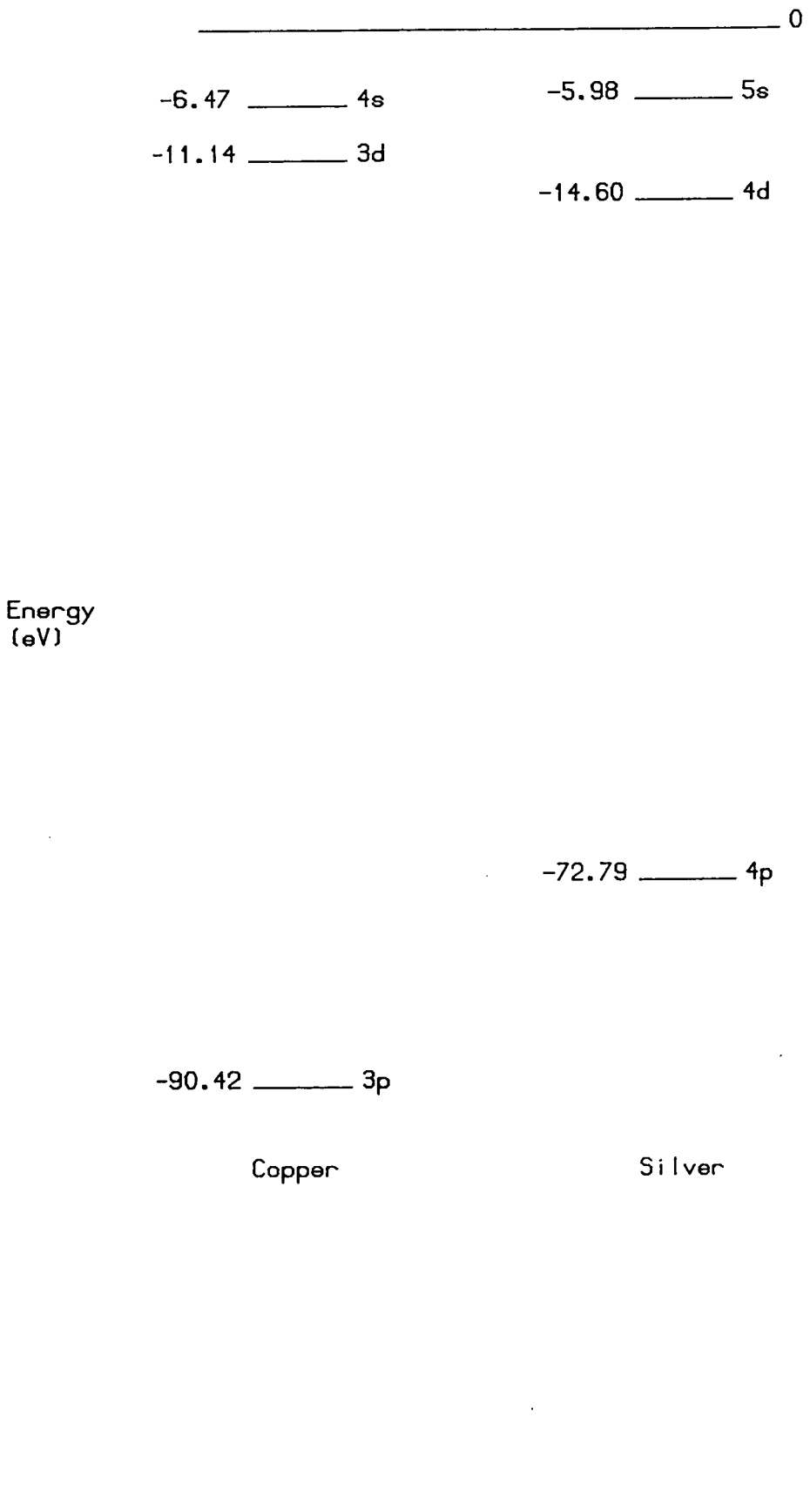

Relativistic effects start to become important in the late second transition period. Stabilisation of both the Cu(4s) and Ag(5s) orbitals occurs, but the effects are much greater for the Ag(5s) orbital. It may indeed lead to the Ag(5s) orbital descending below the Cu(4s) orbital on the energy scale, with the consequence that the sσ bonding molecular orbital has a larger contribution from silver than copper. A secondary interaction between the Cu(3d) and Ag(4d) orbitals of the appropriate symmetry will lead to a weakly antibonding, fully-occupied d^{20} "band". The d orbitals on both atoms are really too contracted to play any more than a subsidiary role in bonding. Thus on a very rudimentary level, the bond in CuAg is dominated by sσ interaction, just as in the parent dimers Cu_2 and Ag_2. The electronic configuration of the ground state is therefore:

$$X(^1\Sigma^+) \quad .....(d\sigma)^2(d\pi)^4(d\delta)^4(d\delta^*)^4(d\pi^*)^4(d\sigma^*)^2\ (s\sigma)^2,$$

where those orbitals lying below the d band have only a very minor interaction and retain much atomic character. In their *ab initio* treatment, Walch, Bauschlicher and Langhoff [7] replaced the deep core electrons in copper and silver by effective core potentials developed by Hay and Wadt. [32] The remaining 19 electrons in the valence space were distributed among the orbitals:

(n-1)s (n-1)p (n-1)d ns np,

where n = 4 for copper and n = 5 for silver. Relativistic corrections were included in the potential for silver, but not for copper. Functions describing the np orbitals, which are normally unoccupied in the atomic ground state, were included to allow for the effects of np←ns excitation. Polarisation functions [33] were added to the basis sets to describe the distortion in atomic electron densities

resultant upon molecule formation. Their calculations with the original basis set plus a diffuse d function on copper, predicted a weakly polarised $Cu^{-}Ag^{+}$ bond, and only moderate agreement with the experimental spectroscopic constants was obtained (see Table 5.7). The calculated direction of bond polarisation was at odds with the slightly larger electron affinity of silver. When f polarisation functions were added to the basis sets, better agreement with the experimental parameters was obtained. Additionally, the polarity of the bond was found to be reversed. Had the copper atom been treated relativistically in the atomic core potential calculation, even better agreement with experiment would have been obtained. The relativistic contraction in copper, while small ($\simeq$ 0.02-0.03 Å), is still significant. [34] [35]

A more recent study by Bauschlicher, Langhoff and Partridge [8] used the Hay-Wadt 19 electron RECP to describe the inner electrons on silver, and a non relativistic all-electron basis set for the copper atom, optimised for the ^{2}S state. [36] In this case, results were in rather poorer agreement with experiment, as Table 5.7 demonstrates. The failure of this calculation may be due partly to changes to the silver atom basis set, since parallel calculations on disilver were also in poorer agreement with experiment than those of WBL.

5.4.2 The A(0^{+}) excited state

The dearth of *ab initio* calculations on electronically-excited CuAg is hardly surprising in light of the absence to date of high resolution spectroscopic data. The scope of this section is therefore somewhat limited. Moreover, only the A excited state was investigated with rotational resolution, the symmetry and

Table 5.7 : Experimental and theoretical spectroscopic constants of the $X(^1\Sigma^+)$ state of $^{63}Cu^{107}Ag$

Ref.	r_e/Å	ω_e/cm^{-1}	D_e/eV
[8]	2.464	193	1.54
[7][v]	2.458	200	1.63
[7][w]	2.415	225	1.68
Expt.	2.3664(71)[x]	230.2(18)[x]	1.76[y]

v - d polarisation functions added to Cu basis set

w - d + f functions added to copper, f added to silver

x - this work

y - Reference [6]

bondlength of the B state having yet to be determined. Consequently, only tentative explanations for the experimental observations may be advanced.

With an *a priori* knowledge of the ground state symmetry ($^1\Sigma^+$), the observation of a parallel electronic transition limits the choice of candidates for the A state to be those of $\Omega = 0^+$ symmetry. CuAg contains one highly-charged nucleus (Ag, $Z = 47$), and therefore relativistic effects such as spin-orbit coupling are liable to be important in the molecule. A Hund's case (c) description of the coupling between orbital (**L**) and spin (**S**) angular momentum is probably most appropriate for this molecule. Here, **L** and **S** couple strongly, and the only good quantum number is Ω, the projection of the resultant of **L** + **S** along the internuclear axis. [30] Within the case (c) coupling formalism, 0^+ states may be derived from pure $^1\Sigma^+$ states, or as the $\Omega = 0^+$ spin-orbit component of states with non zero orbital and spin angular momentum. For 0^+ spin-orbit states, the strength of optical coupling to the ground state will depend on the magnitude of the **L-S** coupling term. The short A state lifetime is believed to be a manifestation of strong radiative coupling to the ground state. Predissociation effects are not thought to be in competition with radiative decay, since no 0^+ states arise from the $^2S + {}^2S$ ground state limits. This suggests that if the A state does arise through spin-orbit coupling, the strength of the interaction must be considerable.

Having examined the implications of the observed spectroscopy for the nature of the A state, it is now logical to determine which of the excited atomic dissociation asymptotes can give rise to 0^+ states. Any candidates must be tested for consistency with the experimental observations. Some dissociation limits of

CuAg are presented in Table 5.8, derived from the well-established atomic spectroscopy of Cu and Ag. [37] In selecting dissociation limits of perceived importance from the plethora of possible excitations, two guiding principles were applied. Firstly, limits containing excited atoms whose energy lies above those of of $Ag(^2D)$ and $Cu(^2P)$ were rejected as being too energetic. Molecular states derived from such limits would have to be inordinately deeply bound to exert much influence on any configurational description of the A state. A noteworthy exception to this rule is the inclusion of the lowest *ionic* asymptotes $Cu^+(^1S_0)$ + $Ag^-(^1S_0)$ and $Cu^-(^1S_0)$ + $Ag^+(^1S_0)$. As will be discussed below, the A state may possess some ion pair character. All double excitation limits (Cu^* + Ag^*) were discarded without qualms, since they are all much too high-lying to have an effect on the A state. Moreover, a molecular state involving double electronic excitation would be almost vanishingly inaccessible in one photon excitation from the ground state.

Figure 5.7 shows potential curves for the X and A states of CuAg calculated using the RKR method described in Appendix C. Also shown are the various excited atomic and ionic asymptotes of Table 5.8. On the evidence of the RKR curves alone, it would appear that the A state dissociates to the limits $Cu(^2D)$ + $Ag(^2S)$. If it is assumed that the experimental vibrational constants describe the potential right up to dissociation, then the following equation may be applied to obtain a crude estimate of the dissociation energy: [17]

$$D_e = \omega_e^2/4\omega_e x_e$$

where the terms have their usual definitions. Applying this equation to the A

Figure 5.7 : RKR potential curves for CuAg

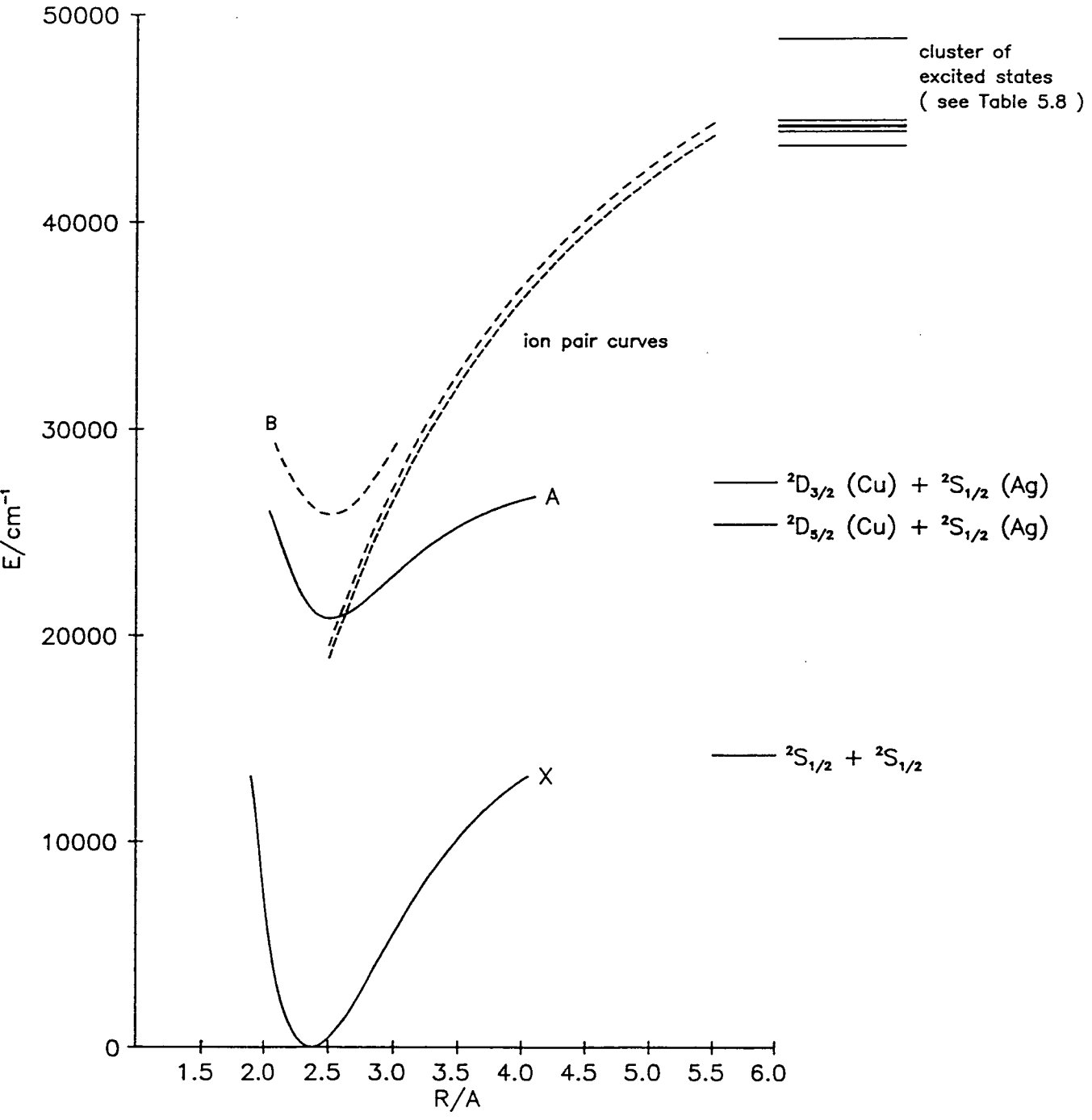

Table 5.8 : Atomic and ionic dissociation limits of Cu and Ag

Atomic/ionic states	Electron configuration	Energy/cm^{-1}
$^2S_{1/2}(Cu) + {}^2S_{1/2}(Ag)$	$3d^{10}4s^1 + 4d^{10}5s^1$	0.0
$^2D_{5/2}(Cu) + {}^2S_{1/2}(Ag)$	$3d^9 4s^2 + 4d^{10}5s^1$	11202.6
$^2D_{3/2}(Cu) + {}^2S_{1/2}(Ag)$	$3d^9 4s^2 + 4d^{10}5s^1$	13245.4
$^2S_{1/2}(Cu) + {}^2P_{1/2}(Ag)$	$3d^{10}4s^1 + 4d^{10}5p^1$	29552.1
$^2S_{1/2}(Cu) + {}^2D_{5/2}(Ag)$	$3d^{10}4s^1 + 4d^9 5s^2$	30242.3
$^2S_{1/2}(Cu) + {}^2P_{3/2}(Ag)$	$3d^{10}4s^1 + 4d^{10}5p^1$	30472.7
$^2P_{1/2}(Cu) + {}^2S_{1/2}(Ag)$	$3d^{10}4p^1 + 4d^{10}5s^1$	30535.3
$^2P_{3/2}(Cu) + {}^2S_{1/2}(Ag)$	$3d^{10}4p^1 + 4d^{10}5s^1$	30783.7
$^2S_{1/2}(Cu) + {}^2D_{3/2}(Ag)$	$3d^{10}4s^1 + 4d^9 5s^2$	34714.2
$^1S_0(Cu^-) + {}^1S_0(Ag^+)$	$3d^{10}4s^2 + 4d^{10}$	50583.7
$^1S_0(Cu^+) + {}^1S_0(Ag^-)$	$3d^{10} + 4d^{10}5s^2$	51793.4

Data from Reference [37]

state, a value of D_e = 6593 cm^{-1} is obtained, in good agreement with the energy of the excited limits. This further supports a simple picture of the A state dissociating to the first excited copper asymptotes. The large spin-orbit splitting in the $Cu(^2D)$ state (2043 cm^{-1}) indicates that case (c) coupling will prevail. Two states of 0^+ symmetry may be derived from these limits. One arises from the coupling of $Cu(^2D_{5/2})$, M_J = 1/2 with $Ag(^2S)$, M_J = -1/2, and the other correspondingly from $Cu(^2D_{3/2})$. The molecular orbital configurations of the states formed are:

$^1\Sigma^+(0^+) : d^{18}(d\sigma)^1\ (s\sigma)^2(s\sigma^*)^1$

$^3\pi(0^+) : d^{16}(d\pi)^3\ (s\sigma)^2(s\sigma^*)^1$

where the d and s notation refers to molecular orbitals with Cu(3d)/Ag(4d) and Cu(4s)/Ag(5s) parentage. Such excitations create a core vacancy on atomic copper, which may correlate with a corresponding core hole on copper in the molecule. Whether this hole resides in an orbital with more bonding or antibonding character will depend on the relative energies of the Cu(3d) and Ag(4d) atomic orbitals. The nonrelativistic Hartree-Fock calculations of Figure 5.6 placed the Ag(4d) orbitals lower in energy by $\simeq$ 3.46 eV. Assuming that relativistic effects do not re-order these orbital energies, a copper-localised d vacancy would reside in a molecular orbital with a slight excess of antibonding character.

This "single configuration" model of the A excited state is attractive in its simplicity but conflicts with certain of the other experimental observations. In the atomic limit, the $^2D \leftarrow ^2S$ transition is only allowed in Hund's case (c). In the

molecule, the corresponding transition is weakly allowed as an interatomic charge transfer. Although the atomic spin-orbit splitting is large, one would not expect the corresponding molecular transition to be quite so intense as was observed. This suggests that some other configurations arising from different asymptotes contribute to the A state near the potential minimum, augmenting the oscillator strength.

The involvement of particular configurations in the description of a state may be probed by examining the electronic isotope shifts. In heavy nuclei such as copper and silver, where the nucleus-electron reduced mass is almost independent of the nuclear charge, the electronic isotope shift arises partly from the isotopic variation in nuclear charge density, the so-called *normal mass shift.* There is an additional state-specific shift which results from coupling between different electronic angular momenta: the *specific mass shift*. [38]

McCaffrey *et al.* have performed an LIF investigation of the A←X and B←X systems of dicopper, focussing upon the determination of electronic isotope shifts from experimental spectra. [22] In this study, an atomic isotope shift of (ν^{63}-ν^{65}) $\simeq$ -0.07 cm^{-1} was obtained for the $^2P \leftarrow ^2D$ transition. They were unable to resolve any corresponding splitting in the $^2P \leftarrow ^2S$ transition, Previous observations [39] indicated that small isotope shifts occurred for transitions which do not involve a change in d orbital population. Thus a shift of $\simeq$ + 0.07 cm^{-1} might be expected for the $^2D \leftarrow ^2S$ transition itself. In the spectra of the A←X and B←X systems recorded by McCaffrey *et al.*, isotope shifts of similar magnitude and direction to the atomic isotope shifts were observed. It was argued that the molecular shifts directly reflected the amount of d core hole character in the

excited states, and concluded that admixture of $Cu(^2D)$ + $Ag(^2S)$ configurations in the A and B states must be substantial.

In CuAg, by way of contrast, the electronic isotope shifts in the A←X system were found to be much smaller (see Table 5.5). This suggests that configurations derived from $Cu(^2D)$ limits play a diminished role in the A state, at least near the potential minimum where the shifts were measured. The observed shifts are more consistent with those obtained by Butler [21] for the $A(0_u^+)$←$X(^1\Sigma_g^+)$ transition in disilver, where $Ag(^2D)$ limits are not thought to be significantly involved (see Chapter 7).

The electronic structure of the A state clearly cannot be rationalised without recourse to a more sophisticated model in which more than one configuration is involved in the description of this state. The question of which other excited configurations are involved is now addressed.

The general concensus of a wide body of theoretical and experimental work on the $B(0_u^+)$ state of Cu_2 [20] [40]- [42] and the $A(0_u^+)$ state of Ag_2 [21] [43] [44] is that the configuration derived from the excitation $s\sigma^*$←$s\sigma$ is an important component of the excited state. This is a relatively low energy promotion which avoids opening up the d shell or populating higher-lying np-derived molecular orbitals. The excitation is equivalent to a strongly-allowed electron transfer and will correlate formally with the asymptotic limit $M^+(^1S_0)\ d^{10}$ + $M^-(^1S_0)\ d^{10}s^2$. Given that the ns orbital energies in copper and silver are likely to be quite similar, it is not unreasonable to assume that the corresponding $s\sigma^*$←$s\sigma$ promotion in CuAg will lie fairly close to those in Cu_2 and Ag_2. On a cursory

examination of the spectroscopy of the A←X system of CuAg, one is immediately struck by the similarities with the Cu_2 B←X and Ag_2 A←X transitions. All three systems lie in a similar spectral region (20-23000 cm^{-1}), and involve a transition to the lowest (CuAg, Ag_2) or second-lowest observed singlet system (Cu_2) in these molecules. All are strongly allowed parallel transitions with a bond lengthening upon excitation of $\simeq$ 5 %. These similarities lend credence to the likelihood of an $s\sigma^*$←$s\sigma$ promotion contributing to the description of the A state.

To investigate this further, the interaction potential between the ionic cores in the lowest ion pair states of CuAg was constructed. The attractive limb of an ion pair potential can be represented to first order by a pure coulombic interaction. The potential energy of the interaction may be written as: [19]

$$E_c(R) = D_e(CuAg) + IP(M) - EA(M) - e^2/4\pi\varepsilon_0 R$$

where

$E_c(R)$ is the potential energy of the ionic state

measured with respect to the ground state potential minimum

$D_e(CuAg)$ is the ground state dissociation energy

IP(M) is the first ionisation potential of Cu (or Ag)

EA(M) is the electron affinity of Ag (or Cu)

e is the electronic charge

ε_0 is the vacuum permittivity

and R is the internuclear separation.

The possibility that dissociation of CuAg can produce two ionic product channels

$Cu^+ + Ag^-$ or $Cu^- + Ag^+$ is of course recognised. Figure 5.7 shows the two coulombic curves descending from their ionic dissociation limits. They differ only in their asymptotic energy because of differences in IP and EA between Cu and Ag. The true ion pair interaction potential will depart from these curves because of the action of the attractive polarisation term (α/R^4) which leads to further stabilisation. It is unlikely that the attractive limb of the ion pair state descends as far as the A state minimum before being intersected by its repulsive limb. The extent of ionic mixing in to the overall A state wavefunction will depend on the depth to which the ion pair state is bound. Ionic states are normally characterised by soft, albeit deeply-bound potentials with large equilibrium internuclear separations. The observed vibrational frequency, anharmonicity and bondlength of the A state are scarcely consistent with the values expected for an ion pair state, which are normally characterised by small $\omega_e, \omega_e x_e$ and large r_e values. This is further evidence to support the argument that the A state is most sensibly described as a multi- rather than single configuration. There remains the question as to which of the two possible ionic curves makes the greater contribution to the A state. The more accurate of the two *ab initio* calculations on the ground state [7] polarised the ground state bond in the sense Cu^+Ag^-, so that the $s\sigma$ bonding orbital has more silver than copper character. $s\sigma^* \leftarrow s\sigma$ excitation then involves a redistribution of electron density away from the silver atom. Under such circumstances, the ionic structure Cu^-Ag^+ would be expected to be more involved in the A state.

The remaining molecular states which can contribute are those of 0^+ symmetry derived from the atomic limits clustered 3.66-4.29 eV above the $^2S + {}^2S$ limits (

see Figure 5.7 and Table 5.8). The d core vacancy states which correlate with $Ag(^2D) + Cu(^2S)$ are unlikely to be sufficiently deeply bound to make much of an impression on the A state. Here, the excited electron leaves a d orbital and enters the $s\sigma^*$ orbital, with concomitant weakening of the bond. Involvement of configurations from the ^2P limits (excitation on either Cu or Ag) is desirable on the grounds of oscillator strength. In both atoms, the $(n-1)d^{10}np^1 \leftarrow (n-1)d^{10}ns^1$ transition which gives rise to the ^2P limits is intense. [45] Moreover, the lowest-lying excited states in the related alkali dimers are derived primarily from np + ns atomic states. [46] [47] The corresponding molecular excitations are expected to be similarly strong. These promotions produce states with the following configurations:

$^1\Sigma^+(0^+) : (d^{20})\ (s\sigma)^1\ (p\sigma)^1$

$^3\pi(0^+) : (d^{20})\ (s\sigma)^1\ (p\pi)^1$.

The latter configuration can only provide an 0^+ state through spin-orbit coupling. The multiplet splitting in these ^2P states is not particularly large for either copper or silver, and thus one would not expect the $p\pi$ excited configuration to make a major contribution to the A←X oscillator strength. Moreover, on energetic grounds, it is not easy to reconcile involvement of these molecular orbital configurations in a description of the A state. The A state lies $\simeq$ 2.84 eV below the lowest of these atomic asymptotes, and a configuration in which the $(s\sigma)^2$ configuration is disrupted is not likely to be so deeply bound unless there is significant sp hybridisation.

5.4.3 Conclusion

It is abundantly clear that whilst the ground state is dominated by the single configuration $d^{20}(s\sigma)^2$, the host of conflicting observations do not serve to clarify which, if any, is the dominant configuration of the A state near the potential minimum. Its chameleon-like spectroscopic properties can only be rationalised by recourse to a description in which there is a complex interaction of several configurations. Further speculation is unwarranted in the absence of any *ab initio* data on the excited states of CuAg. Threshold photoionisation spectroscopy, which gives a fresh insight into this problem, is described in Chapter 6. Further high resolution spectroscopy experiments should centre on the other system observed in emission (B→X), since the B state may well derive character from the same excited limits as the A state.

5.4.4 Results of Morse and co-workers

After performing this study, we learned of concurrent work by Morse's group in Utah. Bishea, Marak and Morse (BMM) [48] have also obtained rotationally-resolved spectra of the A←X system in CuAg. The molecular constants they derived for the X and A states are generally in good agreement with our own. For example, $r_0' = 2.512(11)$ Å, $r_0'' = 2.3692(71)$ Å (this work); and $r_0' = 2.521(3)$ Å, $r_0'' = 2.3728(12)$ Å (BMM). In addition to the A state, BMM observed two new states lying between the A state, and the former B state, now relabelled D. B←X and C←X spectra have been fully rotationally analysed, the symmetries of B and C being $\Omega = 1$ and 0^+ respectively.

Lifetime measurements on the four states yield values of 40 ns (A), 4 μs (B), 54 ns (C) and 12 ns (D). In terms of radiative lifetime, there is a clear parallel between the newly-discovered B state of CuAg, and the long-lived (1 μs) $C(^1\pi_u)$ state of Cu_2, which is believed to have an open d shell configuration. The short lifetimes of the A and C states of CuAg have a clear counterpart in the A and B states of Cu_2, which have been discussed at length by Morse (see Chapter 8) and Cartwright. [20] The symmetry of the D state remains indeterminate, but is likely to derive much character from the excited silver atomic limits, and possibly the ion pair limits.

5.5 Observation of new ultraviolet band systems in CuAg

As mentioned in Section 5.3.1 above, a distinct intruding feature, labelled Z, obviously unassignable to any transition in the A←X system, was observed approximately 10 cm^{-1} to the red of the (4-0) band. A cursory examination of the spectrum suggests a local perturbation in the vicinity of this band, although the band position was not displaced from its predicted position. The fact that this feature was not observed in the emission studies [4] [5] suggests that it is unlikely to be the origin of another band system.

With the timely intervention of serendipity, it was discovered that the A←X (3-0) and (4-0) bands, and the "Z" band, could all be observed strongly in ionisation using the unfocussed fundamental output (< 0.1 MW cm^{-2}) from the dye laser alone. There was some evidence to suggest that the (1-0) and (2-0) bands (but not the origin band) could also be observed in this way, although higher laser powers were required here. Ionisation by the dye laser in the absence of the

excimer entails the absorption of two photons from the A excited state, a three photon process overall. This intriguing phenomenon is illustrated in Figure 5.8. This figure shows the ionisation spectrum obtained for $^{63}Cu^{107}Ag$ when the dye laser was scanned over the region near the A←X (3-0) and (4-0) bands, using the same scan parameters as in Figure 5.2, at an unfocussed power density of 0.04 MW cm^{-2}. The absolute signal intensities of the (3-0) and (4-0) bands approached those obtained in the two colour R2PI spectra.

Intense 1+2 resonance enhanced multiphoton ionisation (REMPI) of the A←X (3-0) and (4-0) bands can only arise at such low laser powers if there is some resonant or near-resonant enhancement of the two photon ion←A transition. A possible explanation for these observations may reside in the existence of hitherto unobserved ultraviolet states of CuAg, of the appropriate symmetry, lying at twice the dye laser photon energy, which are capable of provided such an enhancement. A schematic energy level diagram of the near resonant enhancement of a 1+2 REMPI process is depicted in Figure 5.9 (b). It will be recalled from Section 2.4 that the expression for the two photon transition probability, calculated using perturbation theory, contains in its denominator terms of the form $(\omega_{ki} - \omega)^2$. Thus levels lying close in energy to twice the A←X excitation energy will be capable of producing significant enhancement of the two photon transition matrix element, provided that symmetry and Franck Condon requirements are fulfilled.

The inferred ultraviolet systems were probed directly by one colour R2PI, frequency doubling the dye laser output in a β barium borate crystal. Since the heteronuclear molecule CuAg lacks a centre of symmetry, there is no parity

Figure 5.8 : One colour, 3 photon ionisation spectrum of the A←X system of $^{63}Cu^{107}Ag$

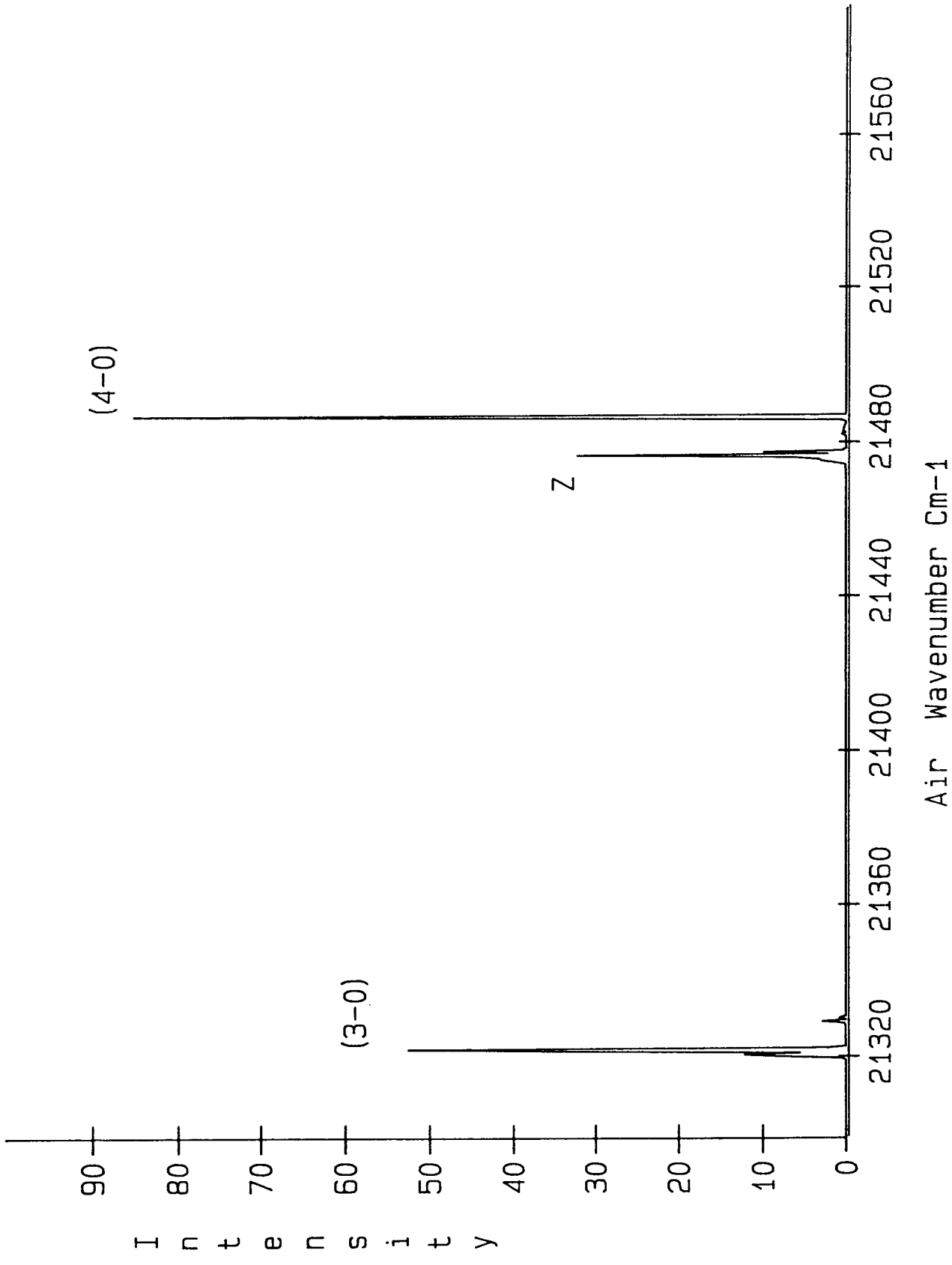

Figure 5.9 : REMPI processes in the 3 photon ionisation of CuAg

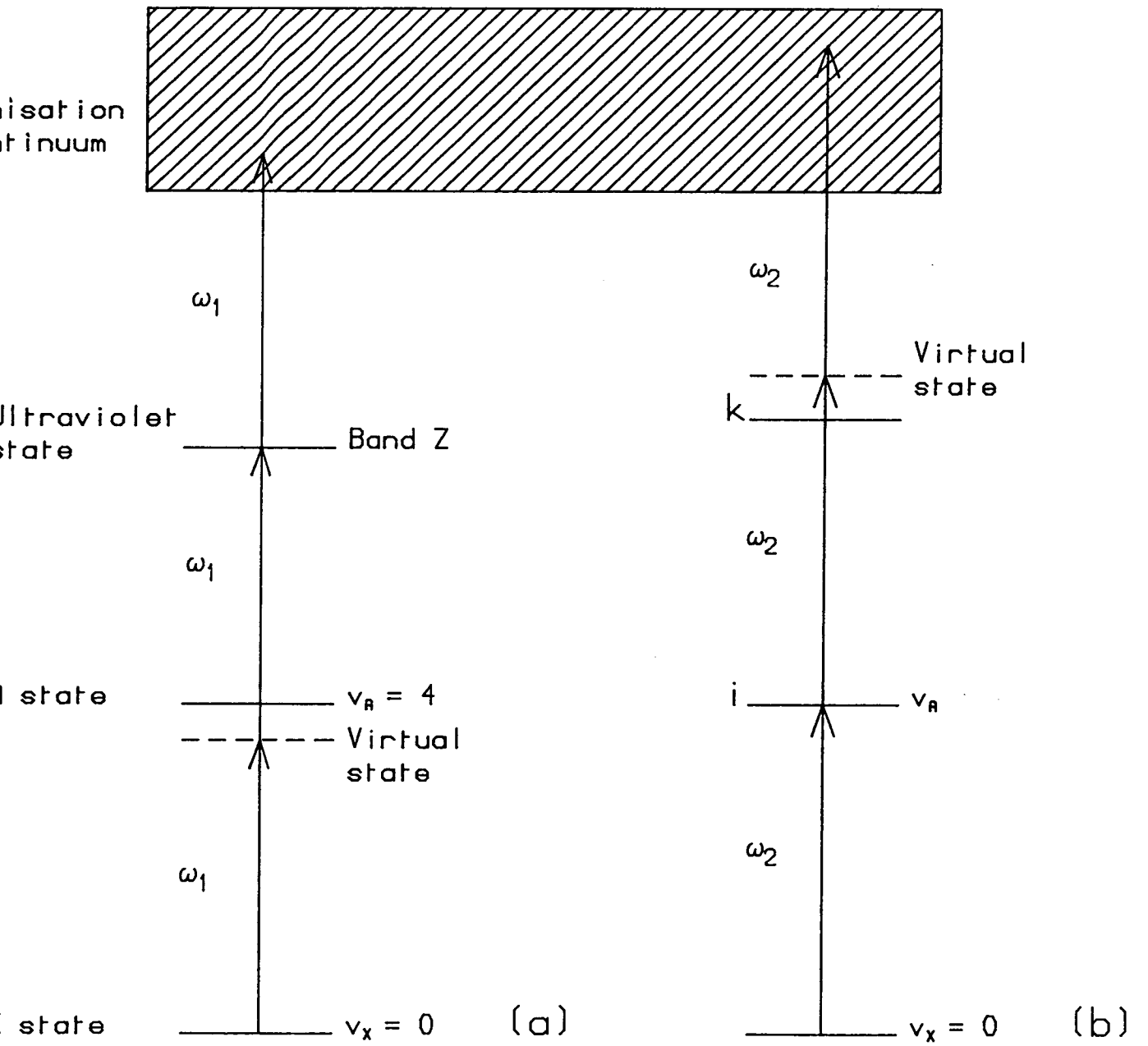

restriction preventing the single photon excitation of ultraviolet levels which were previously observed (by inference) in two photon absorption. The resulting one colour, two photon ionisation spectra are shown in Figures 5.10 (a) ($^{63}Cu^{107}Ag$) and 5.10 (b) ($^{63}Cu^{109}Ag$ + $^{65}Cu^{107}Ag$). Fairly rapid scanning of the laser was required (0.86 cm^{-1} step, 35 shots per step) to cover a wide spectral region while signal stability was maintained. Neon optogalvanic lines and etalon fringes were simultaneously recorded for calibration purposes. Owing to problems with the crystal tracking unit, the ultraviolet output fluctuated somewhat during the course of scanning. The spectra are presented without power normalisation because of problems with a drifting baseline on the sampled monitor photodiode output. Therefore the observed distribution of band intensities should not be regarded as a true reflection of their transition strength.

The highly congested vibronic spectra which were obtained may indicate that more than one ultraviolet state was being accessed in this spectral region. Attempts were made to pick out sequences of bands in the $^{63}Cu^{107}Ag$ mass channels, but to no avail. The measured principal band positions are presented in Tables 5.9 (a) and 5.9 (b). Also marked on Figures 5.10 (a) and 5.10 (b) are the ultraviolet energies corresponding to exactly twice the the A←X transition energies. The resonance enhancement of the (3-0) and (4-0) bands in three photon ionisation appears to stem from the proximity of ultraviolet states at twice the photon energy. Since both the X and A states have $\Omega = 0^+$ symmetry, ultraviolet states with $\Omega = 0$ or 1 are accessible in either a single or a two photon excitation scheme. On the grounds of electronic symmetry alone, there are no bands which, if two photon excited, cannot also be observed by single photon

Figure 5.10 (a) : One colour R2PI spectra of ultraviolet systems of $^{63}Cu^{107}Ag$

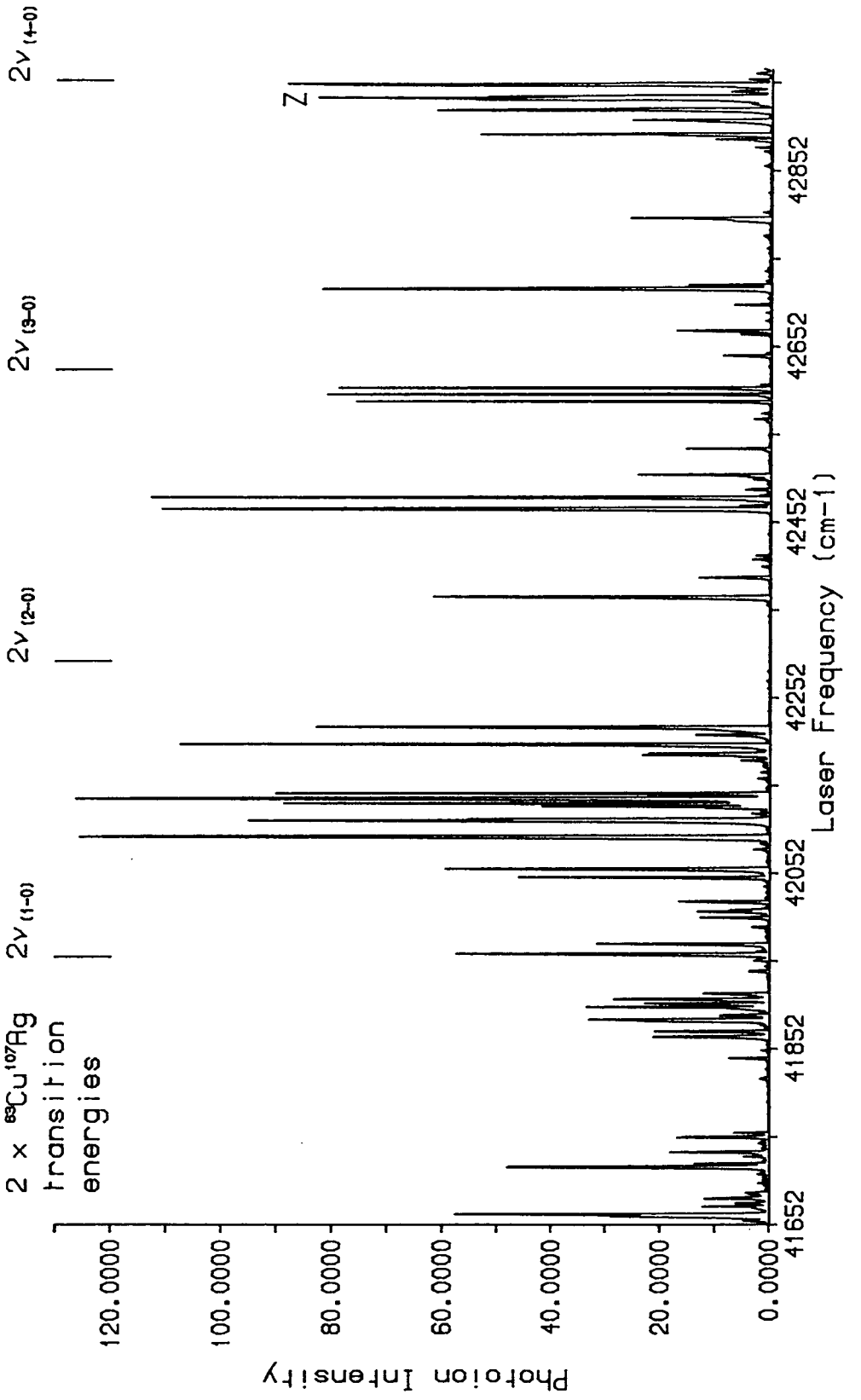

Figure 5.10 (b) : One colour R2PI spectra of ultraviolet systems of $^{63}Cu^{109}Ag$ and $^{65}Cu^{107}Ag$

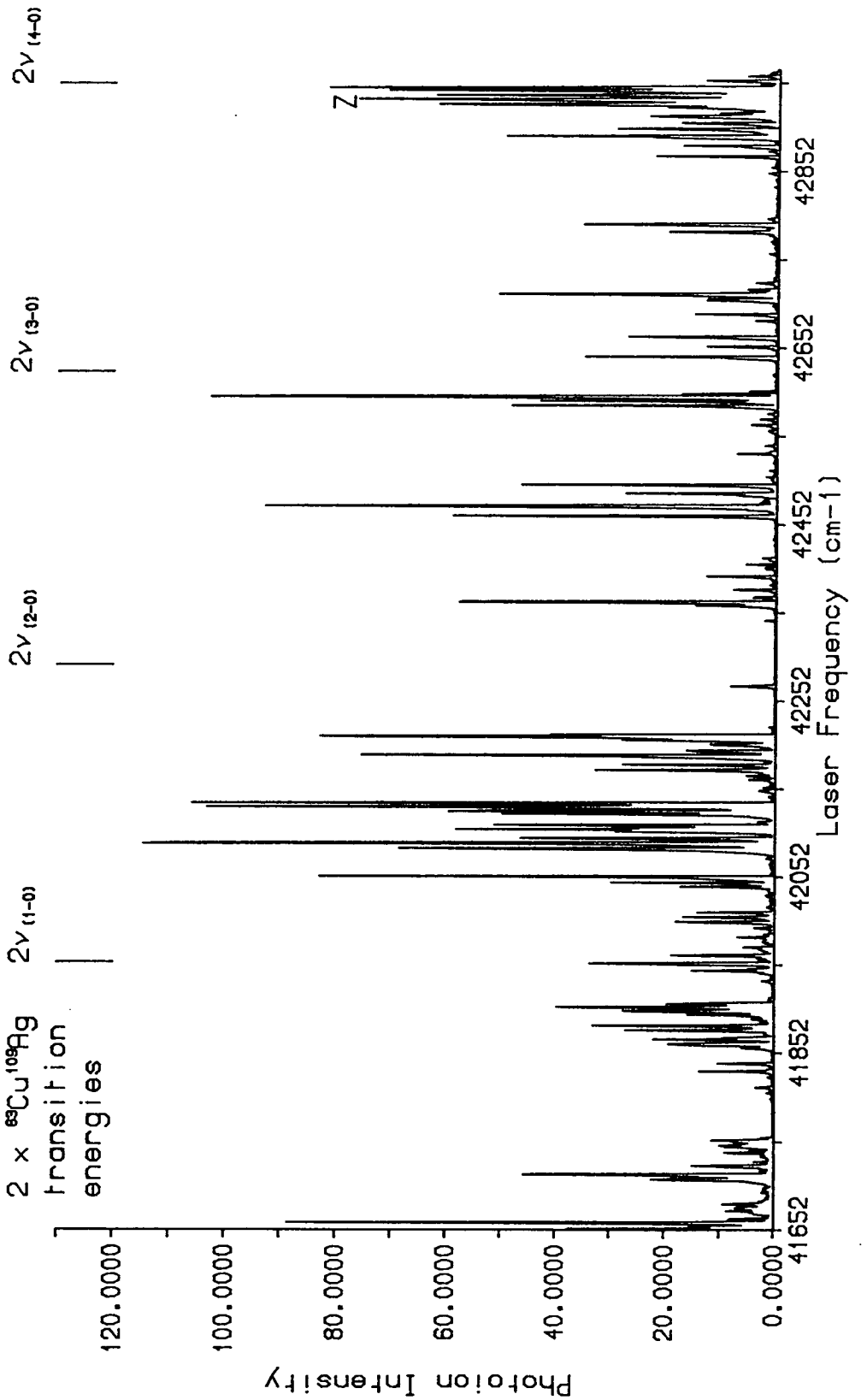

Table 5.9 (a) : $^{63}Cu^{107}Ag$ ultraviolet band positions

Band posn./cm^{-1}	2 x A←X trans. energy/cm^{-1}	A←X (v',v")
41657.28		
41663.06		
41665.74		
41674.74		
41678.34		
41683.60		
41690.26		
41719.12	41715.72	(3-2)
41723.13		
41730.72		
41735.50		
41752.30		
41757.24		
41842.66	41836.54	(2-1)
41866.44		
41872.78		
41886.34		
41891.34		
41900.88		
41905.48		
41910.40		
41916.80		
41941.90		
41961.30	41956.54	(1-0)
41972.36		
41991.34		
42002.60		
42010.12		
42022.04		
42049.16		
42058.88		
42094.20		
42113.06		
42129.52		
42133.30		
42138.96		
42145.02		
42182.32	42169.58	(3-1)
42188.44		
42190.04		
42200.10		
42210.46		
42219.78	42293.58	(2-0)

42368.64		
42390.48		
42410.66		
42415.18		
42467.82		
42471.82		
42481.88		
42490.78	42497.78	(4-1)
42501.36		
42507.42		
42536.38		
42568.30		
42575.22		
42588.74		
42597.60		
42605.32		
42608.64		
42630.88	42626.26	(3-0)
42642.76		
42645.44		
42666.06		
42670.52		
42699.26		
42718.36		
42722.96		
42798.00	42821.72	(5-1)
42888.22		
42894.54		
42909.68		
42921.66		
42935.10	42934.50	Band Z
42942.02		
42951.00		
42956.06	42954.84	(4-0)
42962.92		

Mean measurement error = 0.56 cm^{-1}

Table 5.9 (b) : $^{63}Cu^{109}Ag$ and $^{65}Cu^{107}Ag$ ultraviolet band positions

Band posn./cm^{-1}	2 x A←X trans. energy/cm^{-1}	A←X (v',v")
41654.08		
41656.08		
41661.40		
41669.60		
41675.06		
41679.04		
41682.94		
41710.60		
41716.12		
41725.86		
41739.72		
41747.90		
41754.04		
41814.66		
41832.80		
41841.26		
41858.04		
41862.44		
41867.92		
41878.82		
41884.16		
41896.68		
41900.94		
41905.48		
41909.48		
41934.80		
41947.06		
41954.64	41955.24	(1-0)
41963.96		
41972.48		
41983.88		
41994.48		
42001.86		
42007.72		
42013.24		
42042.50		
42047.02		
42053.96		
42085.04		
42090.64		
42096.24		
42103.70		
42106.16		

42108.02		
42111.76		
42124.48		
42127.48		
42132.94		
42137.54		
42164.10		
42168.62		
42174.88		
42181.08		
42181.44		
42191.96		
42196.04		
42230.28		
42207.94		
42212.00		
42214.12		
42270.74	42292.10	(2-0)
42361.12		
42365.32		
42370.90		
42379.56		
42394.94		
42403.00		
42408.06		
42415.18		
42462.16		
42473.36		
42488.34		
42498.42		
42532.78		
42564.30		
42570.56		
42578.96		
42586.48		
42592.14		
42596.80		
42600.66		
42603.52		
42615.64		
42622.88	42624.58	(3-0)
42641.10		
42654.56		
42664.14		
42682.72		
42689.78		
42705.88		
42707.66		
42713.52		

42718.84		
42726.82		
42784.24		
42792.56		
42869.98		
42881.82		
42892.72		
42900.70		
42907.10		
42914.28		
42914.74		
42927.72	42927.98	Band Z
42933.24		
42937.90		
42943.68		
42946.62		
42955.20	42951.10	(4-0)
42962.02		

Mean measurement error = 0.56 cm^{-1}

excitation. The smaller enhancement observed for the A←X (1-0) and (2-0) bands may be due to poorer Franck Condon factors for the virtual←A transition, which will attenuate the two photon transition matrix element.

In these experiments, an ultraviolet band was observed at exactly twice the photon energy of the "Z" band. This feature is thus ascribed to a two photon resonance with an ultraviolet state, which gains intensity through the proximity of the $v_A = 4$ level at the one photon energy (see Figure 5.9 (a)).

The power dependence of the three photon ionisation signal in Figure 5.8 was investigated using the method outlined in Section 2.4. Ion signal was accumulated for 500 experimental cycles for a range of laser powers spanning the range 0.03-0.2 MW cm^{-2}. The resulting plots of ln(ion signal) versus ln(laser intensity) are shown in Figures 5.11 (a) and 5.11 (b). Both plots give a slope of 2, within the error limits, indicating that saturation must be taking place at one of the single photon steps. In each case, the laser was resonant between real molecular eigenstates at the A←X step only, the other two-photon absorption involving a virtual state (see Figure 5.9 (b)). Virtual transitions will be weaker than the strongly optically-allowed A←X transition, and thus it is most likely that the three photon ionisation process is saturated at the A←X step. This is perhaps not surprising since the lowest laser powers employed in this study (0.03 MW cm^{-2}) were still greater than those used in the rotationally-resolved R2PI spectra of the A←X transition (0.01 MW cm^{-2}), where rovibronic lines were observed to be broadened due to power saturation.

It remains to consider the possible origins of the observed ultraviolet bands. In

Figure 5.11 (a) : Power dependence plot for the 3 photon ionisation of the $^{63}Cu^{107}Ag$ A←X (3-0) band

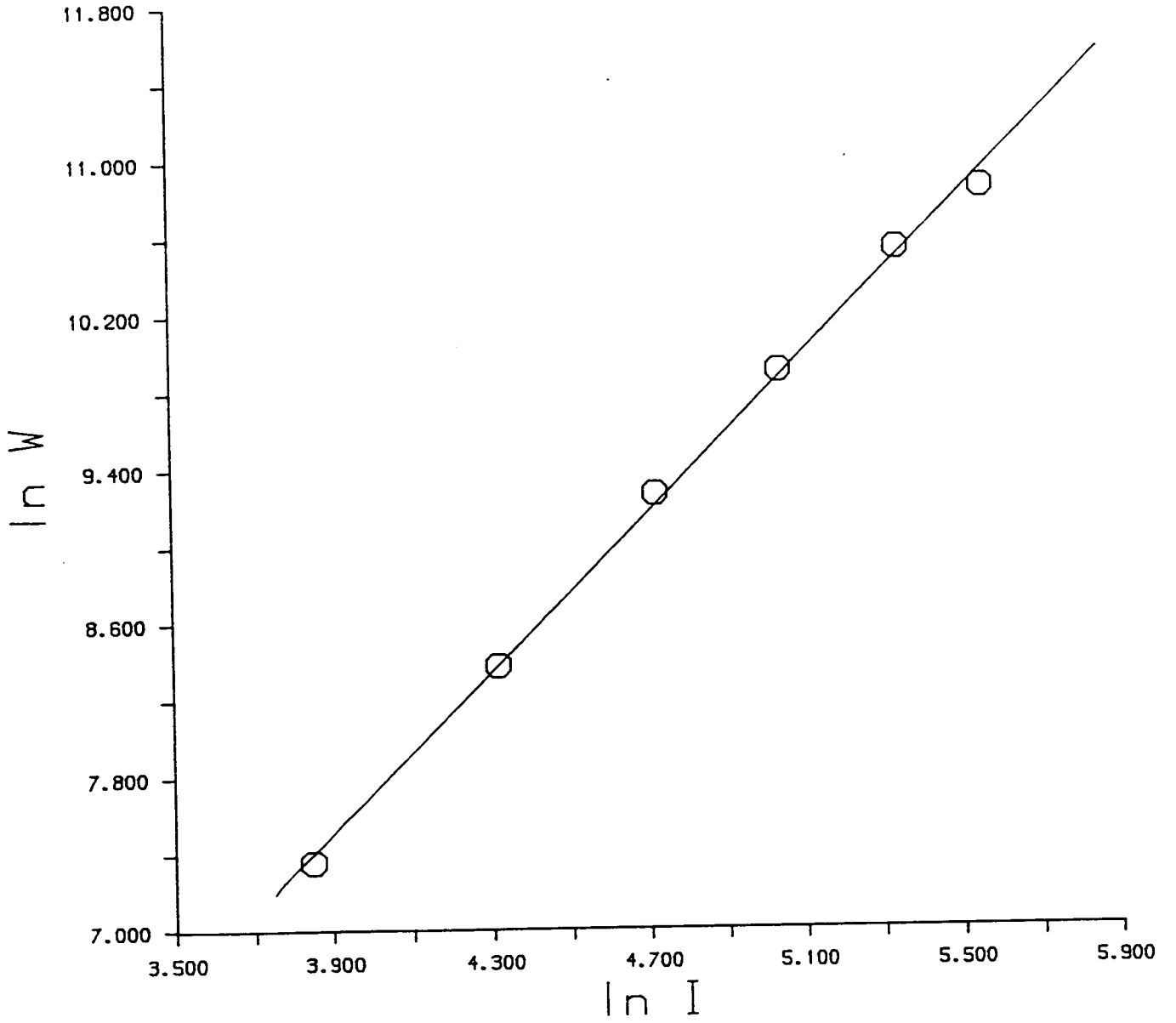

Figure 5.11 (b) : Power dependence plot for the 3 photon ionisation of the $^{63}Cu^{107}Ag$ A←X (4-0) band

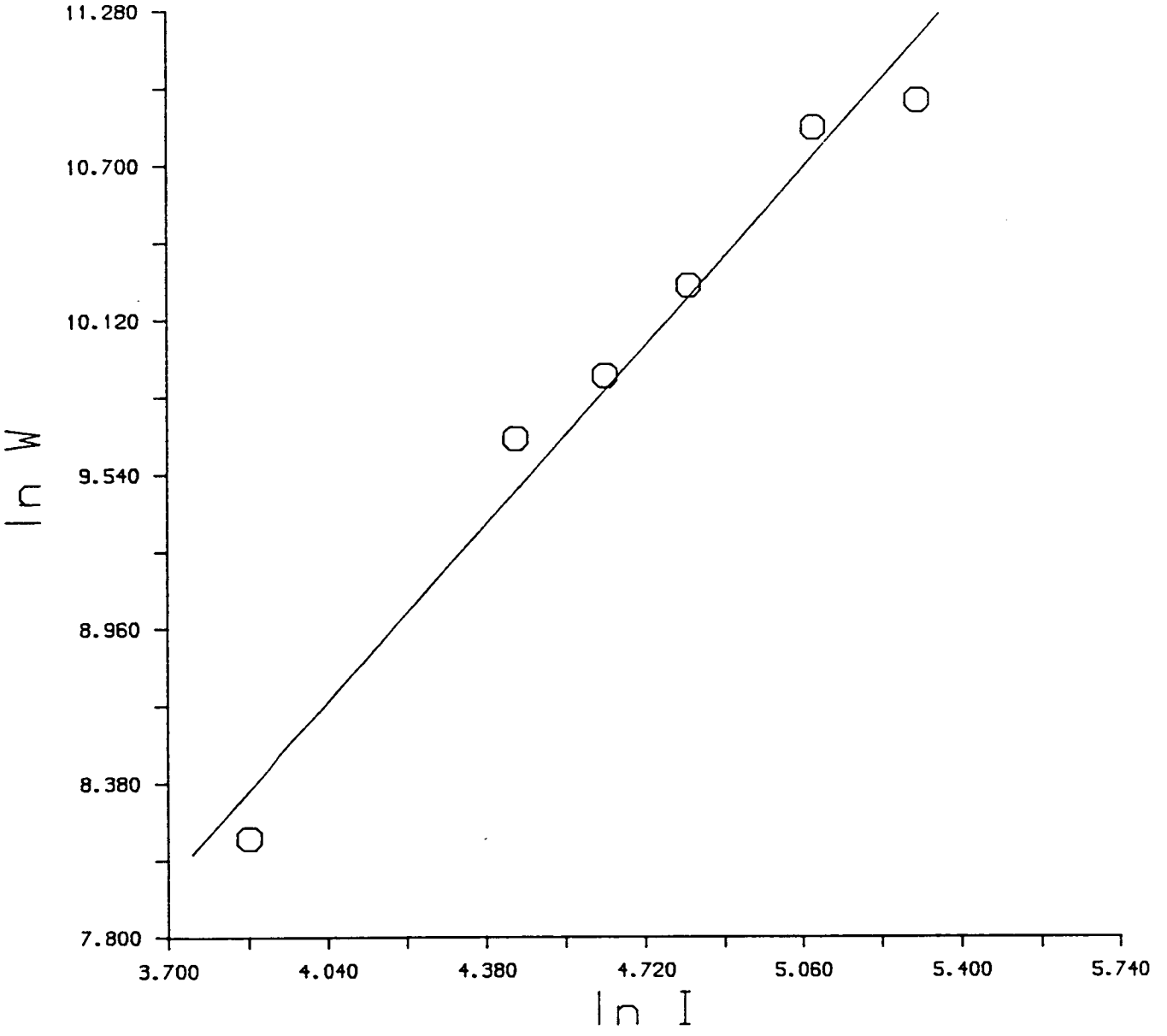

the case of copper dimer, five discrete band systems were observed in the corresponding spectral region. [18] Their vibrational numbering was easily established. In the case of CuAg, the much greater density of states observed may arise because, in the dissociation limit, excitation may be localised on either copper or silver. Overlapping systems are then observed in the molecule which correlate with either an excited copper or silver atom plus a ground state companion.

All excited states of atomic copper and silver, save for the $3d^9 4s^2\ ^2D$ state of copper, can conceivably give rise to ultraviolet states in the appropriate spectral region. Transitions which open up the 4d/5d band are particularly likely to lead to congestion since the different core hole states have similar energies.

References

[1] Morse M. D., Chem. Rev., **86**, p 1049, (1986)

[2] Morse M. D., Hansen G. P., Langridge-Smith P. R. R., Zheng L.-S., Geusic M. E., Michalopolous D. L., Smalley R. E., J. Chem. Phys., **80**, p 5400, (1984)

[3] Taylor S., Spain E. M., Morse M. D., J. Chem. Phys., **92**, p 2710, (1990)

[4] Ruamps J., Spectrochim. Acta Suppl., **11**, p 329, (1957)

[5] Joshi K. C., Majumdar K., Proc. Phys. Soc. London, **78**, p 197, (1961)

[6] Ackerman M., Stafford F. E., Drowart J., J. Chem. Phys., **33**, p 1784, (1960)

[7] Walch S. P., Bauschlicher C. W. Jr., Langhoff S. R., J. Chem. Phys., **85**, p 5900, (1986)

[8] Bauschlicher C. W. Jr., Langhoff S. R., Partridge H., J. Chem. Phys., **91**, p 2412, (1989)

[9] Laihing K., Cheng P. Y., Duncan M. A., J. Phys. Chem., **91**, p 6521, (1987)

[10] Weast R. C. (ed.), *Handbook of Chemistry and Physics*, 55th. edition, Chemical Rubber Company, 1974.

[11] Liu Y., Zhang Q.-L., Tittel F. K., Curl R. F., Smalley R. E., J. Chem. Phys., **85**, p 7434, (1986)

[12] Fu Z., Morse M. D., J. Chem. Phys., **90**, p 3417, (1989)

[13] Simard B., Hackett P. A., *private communication*, ,

[14] Paschen F., Ann. Phys., **60**, p 405, (1919)

[15] Demtröder W., *Laser Spectroscopy : Basic Concepts and Instrumentation*, Springer Verlag, Berlin, 1982.

[16] Bevington P. R., *Data Reduction and Error Analysis for the Physical Sciences*, McGraw Hill, New York, 1969.

[17] Hollas J. M., *High Resolution Spectroscopy*, Butterworths, London, 1982.

[18] Powers D. E., Hansen S. G., Geusic M. E., Michalopolous D. L., Smalley R. E., J. Chem. Phys., **78**, p 2866, (1983)

[19] Herzberg G., *Molecular Spectra and Molecular Structure. I: Spectra of diatomic molecules*, 2nd. edition, van Nostrand, Princeton, 1950.

[20] Cartwright P. C., *Ph. D. thesis*, Edinburgh University, 1989.

[21] Butler A. M., *Ph. D. thesis*, Edinburgh University, 1989.

[22] McCaffrey J. G., Bennett R. R., Morse M. D., Breckenridge W. H., J. Chem. Phys., **91**, p 92, (1989)

[23] Bunker P. R., J. Mol. Spectry., **42**, p 478, (1972)

[24] Watson J. K. G., J. Mol. Spectry., **80**, p 411, (1980)

[25] Morse P. M., Phys. Rev., **34**, p 57, (1929)

[26] Pekeris C. L., Phys. Rev., **45**, p 98, (1934)

[27] McQuarrie D. A., *Statistical Mechanics*, Harper and Row, New York, 1976.

[28] Hönl H., London F., Z. Phys., **33**, p 803, (1925)

[29] Clementi E., Roetti C., Atomic Data and Nucl. Data Tables, **14**, p 177, (1974)

[30] Atkins P. W., *Molecular Quantum Mechanics*, 2nd. edition, Oxford University Press, 1983.

[31] Balasubramanian K., J. Phys. Chem., **93**, p 6585, (1989)

[32] Hay P. J., Wadt W. R., J. Chem. Phys., **82**, p 299, (1985)
[33] Almlöf J., Helgaker T., Taylor P. R., J. Phys. Chem., p 3029, (1988)
[34] Werner H.-J., Martin R. L., Chem. Phys. Lett., **113**, p 451, (1985)
[35] Desclaux J. P., Atomic Data and Nuclear Data Tables, **12**, p 311, (1973)
[36] Wachters A. J. H., J. Chem. Phys., **52**, p 1033, (1970)
[37] Moore C. E., *Atomic Energy Levels*, NBS Circular 467, Vols. II and III, Washington D. C., 1971.
[38] Hughes D. S., Eckart C., Phys. Rev., **36**, p 694, (1930)
[39] Dabkiewicz P., Häncsh T. W., Opt. Commun., **38**, p 351, (1981)
[40] Ozin G. A., Huber H., McIntosh D., Mitchell S. A., Norman J. G., Noodleman L., J. Am. Chem. Soc., **101**, p 3504, (1979)
[41] Miyoshi E., Tatewaki H., Nakamura T., J. Chem. Phys., **78**, p 815, (1983)
[42] Witko M., Beckmann H. O., Mol. Phys., **47**, p 945, (1982)
[43] Basch H., J. Am. Chem. Soc., **103**, p 4657, (1981)
[44] Grinter R., Chem. Phys., **102**, p 187, (1986)
[45] Wiese W. L., Martin G. A., *Wavelengths and transition probabilities for atoms and atomic ions*, NBS Circular 68, Part II, Washington D.C., 1980.
[46] Konowalow D. D., Fish J. L., Chem. Phys., **77**, p 435, (1983)
[47] Konowalow D. D., Fish J. L., Chem. Phys., **84**, p 463, (1984)
[48] Bishea G. A., Marak N., Morse M. D., *in preparation*,

Chapter 6
Threshold Photoionisation Spectroscopy of CuAg and Cu_2

6.1 Introduction

One of the most fundamental properties of a molecule is its first ionisation potential (IP). The magnitude of the IP provides a direct measure of the strength with which the valence electrons are bound to the molecular core, and of the stability of the molecular ion. Ionisation potentials are consequently directly relevant to chemistry since they reflect the ability of a molecule to donate electrons in a chemical reaction. In metal clusters, the ionisation potential (IP) falls markedly by $\simeq$ 3 eV from the atom to the bulk. [1] A systematic investigation of the variation in ionisation potential with cluster size should shed some light on cluster valence bonding. Such measurements, in concert with analysis of the kinetic energy spectrum of the detached photoelectrons, make it possible to probe the gradual loss of discrete molecular orbital structure, and the evolution of bulk electronic structure as the cluster size increases.

The size-dependence of cluster ionisation potentials have been measured thoroughly for the alkali metals by Schumacher's group, [2] [3] and for some of the transition metals by a variety of other groups. [4]- [7] The results of all investigations conform broadly to trends predicted by simple electrostatics: a gradual decrease in IP with increasing cluster size, following an approximately 1/R dependence, and approaching the bulk work function asymptotically. [8] In

some cases, fine structure may be discerned in the size variation profiles. This is exemplified by the even/odd alternation in the ionisation potentials of copper and silver clusters, which was discussed in Chapter 4.

From painstaking experiments by the groups of Smalley [4] and Kaldor, [5]- [7] it has been possible to assemble a substantial database on the ionisation potentials of small transition metal clusters in the 1-20 atom size range. This begs the question as to why we have embarked on a systematic, high-accuracy redetermination of the ionisation potentials of the smallest Group 1b transition metal clusters, namely the dimers and trimers ?

The answer resides in the deficiencies of those techniques which were previously employed to measure cluster ionisation potentials. The ultimate objective of our programme of work is to probe differences in the electronic structure of the Group 1b clusters when stepwise replacement by other metal atoms of the triad occurs. For example, the difference in ionisation potential between Cu_3 and Cu_2Ag may be used as a handle on the electronic rearrangements which take place upon substitution of Cu by Ag. Such are the similarities in the valence electronic structure between members of the Group 1b triad, that only subtle changes in cluster ionisation potentials are expected to result upon atom replacement. Unless the ionisation potentials are determined with high precision, these effects may not be discernible. Most transition metal cluster IPs lie in the range 5-9 eV, [1] and are thus amenable to crude and imprecise determinations by measuring the fluence dependence of the photoionisation yield (see Section 2.4). Not surprisingly, uncertainties in ionisation potentials determined by this method are large, typically 0.3-0.7 eV. [4] [5] In the case of V_n, [1] Nb_n [7] and

Fe_n, [6] tunable laser sources were used to scan across the ionisation threshold region directly. Photoionisation efficiency (PIE) curves of ion intensity versus wavelength were obtained, from which the ionisation threshold was determined with higher precision. The ionisation potentials of the Group 1b clusters have eluded measurement by this technique, since their magnitudes (6-9 eV [1]) require efficient generation of tunable vacuum ultraviolet radiation. Whilst direct threshold measurements yield ionisation potentials with substantially more precision ($\simeq$ 0.05 eV [1]) than the fluence-dependence method, caution must be exercised when interpreting data. Removal of a valence electron upon single photon ionisation can result in a distinct change in molecular geometry. The Franck Condon overlap between the zero point vibrational level of the neutral cluster and that of the ion may therefore be small. Since the adiabatic ionisation potential is defined as the difference in energy between these levels, it may not be possible to measure the adiabatic IP by single photon ionisation out of the ground state. Instead, the technique measures a *vertical* ionisation potential, determined by the projection of the ground state vibrational wavefunction on to the ion potential surface. Moreover, even if the zero point level of the ion is accessible, the adiabatic IP may be obscured by photoionisation of vibrationally excited molecules, which can lead to a red "tailing" of the observed threshold. The cooling of molecules into the lowest ground vibronic state by supersonic expansion eliminates this red-shifting of the threshold, and additionally removes the risk of collisional ionisation. However, for trimeric and higher clusters, the neutral and ion potential surfaces may be quite corrugated, and consequently the threshold region can be difficult to interpret. Without an intimate knowledge of the electronic and geometric structure of the ground state molecule and

molecular ion, there would seem to be little point in pursuing these measurements beyond the levels of precision hitherto quoted.

Fortuitously, for many dimeric species, and some trimers, potential surfaces for at least the ground and excited states of the neutral have been determined by R2PI and LIF spectroscopy. An *a priori* knowledge of these states may be exploited to eliminate many of the ambiguities which arise when measuring ionisation thresholds. With this in mind, the various spectroscopy-based methods for measuring the ionisation potentials of small molecules are examined critically. In principle, these techniques are applicable to ionisation potential measurements on any size of cluster. In practice, they are limited to those cluster species for which vibronic spectra have been obtained. At the time of writing, only transition metal dimers and a few trimers fall into this category. [1] Thus, in the ensuing discussion, it is currently envisaged that the techniques can be applied to clusters no larger than the trimer. Furthermore, it should be stressed that, in all the approaches outlined below, the adiabatic IP can only be determined if the zero point vibrational level of the ion is somehow accessible, either through direct ionisation, or *via* an autoionisation mechanism.

Conventional photoelectron spectroscopy applied to pulsed cluster beams is not straightforward. It requires both a pulsed source of vacuum ultraviolet radiation, and the application of coincidence techniques for the identification of the cluster cation, because of the distribution of neutral clusters present. It suffers from the same deficiencies as the one photon threshold ionisation techniques in that the zero point vibrational level of the ionic ground state may not be Franck Condon accessible from that of the neutral molecule. The adiabatic ionisation potential,

if measurable, derives from the observation of a peak in the photoelectron spectrum due to transitions to the zero point level of the ion. The precision of the IP measurement is limited by the spectrometer resolution and calibration accuracy, typically 15 meV. [9]

Conspicuously more useful is the technique of multiphoton ionisation photoelectron spectroscopy (MPI-PES), also known as excited state photoelectron spectroscopy (ES-PES), [10]- [14] which employs well-established REMPI methodology (see Chapters 2 and 5). Molecules are pumped to some intermediate state by pulsed laser radiation, and subsequently ionised by absorption of another photon, a standard n+1 REMPI process. The ionising photon energy is chosen to drive the system well into the molecular ion-electron continuum. The kinetic energy of the photoelectrons produced is analysed to generate a conventional photoelectron spectrum for ejection of electrons from an excited state, rather than from the ground state. The use of multiphoton excitation removes the requirement for vacuum ultraviolet radiation sources, and higher kinetic energy resolution is attainable. Furthermore, the possibility of selecting different excitation routes confers great versatility on the technique: ionisation from a range of excited states with different equilibrium geometries allows wide portions of the potential energy surface of the ion to be sampled, increasing the likelihood of being able to access the zero point level of the ion. In addition, doubly excited states of the neutral molecule may be excited by the final photon, enabling the investigation of electronic autoionisation processes. Since the spectroscopy of the ground and intermediate state is usually first established by REMPI techniques, transitions originating from the zero point

vibrational level of the ground state may be used to prepare the excited state. Preparing molecules in a well-defined excited level completely eliminates the hot band congestion which besets direct, one photon IP measurements. An elegant example of the application of ES-PES to a system of relevance to this work is the study of copper dimer by Sappey, Harrington and Weisshaar (SHW). [15] The adiabatic IP of Cu_2 was determined with high (7 meV) precision, and electronic autoionisation processes were observed. ES-PES is a powerful and versatile technique, and is expected to be much applied to metal cluster dimers and trimers, where the electronic spectroscopy of the neutrals can usually be unravelled. The principal limitation of ES-PES is its limited resolution, typically no better than 10 meV. [16] Fine spectral detail may be obscured, particularly when attempting to resolve low frequency vibrational progressions in polyatomics.

A related photoelectron technique which offers even higher resolution, limited only by the laser bandwidth, is that of zero kinetic energy photoelectron spectroscopy (ZEKE-PES), developed recently by Schlag and co-workers. [16]-[18] Here, a combination of tunable laser sources is used to resonantly excite levels of the molecular ion, *via* an excited state of the neutral. When the total laser energy is truly in resonance with an eigenstate of the ion, photoelectrons are ejected with zero kinetic energy. Off-resonance, electrons are ejected with nonzero kinetic energy. Photoionisation is accomplished in the source of an electron time-of-flight spectrometer, a delayed, pulsed extraction field being used to extract the photoelectrons. The non-ZEKE photoelectrons drift away from the ionisation volume before the application of the pulsed field, and thus extract

different kinetic energies from this field relative to the ZEKE electrons which have only thermal drift velocities. The two types of photoelectrons may thus be discriminated by their differing flight times. Monitoring the electron signal at the ZEKE electron flight time while scanning the ionising laser maps out vibronic structure in the ion, the resolution being laser-limited. This is a substantial improvement over conventional PES or ES-PES. Rotationally-resolved photoelectron spectra of light molecules such as NO [18] and O_2 [19] have been obtained using ZEKE-PES. In these cases, the bond length in the ion ground state may be determined unequivocally. Here there is no the ambiguity regarding whether or not the adiabatic ionisation potential has been measured, since Franck Condon factors for the ion←molecule transition can be calculated directly. In the case of the transition metals, their larger masses will probably restrict ZEKE-PES to vibronic resolution. Nevertheless, ZEKE-PES is the photoelectron technique with the greatest potential for transition metal cluster applications. Recent results on the Au_2^- anion are eloquent testimony to its capabilities. [20]

In the present work, financial constraints and the limited time available for experimentation in this laboratory precluded the development of any photoelectron instrumentation. Instead, the "poor-man's" technique of threshold ionisation spectroscopy (TIS) was utilised, since this required no major modifications to the existing apparatus. TIS is simply a variant of the two colour R2PI technique described in Chapters 2 and 5, except that a tunable, instead of fixed-frequency, ionising photon is employed. The first laser is tuned into resonance to excite some specific intermediate state of the molecule, whilst the

second laser is scanned across the ionisation threshold, ionising molecules out of the excited state. By monitoring the photoion signal as a function of the wavelength of the ionising laser, a PIE curve may be generated. While outwardly similar to the one photon threshold ionisation method described earlier, TIS possesses all the advantages of ES-PES with regard to free choice of excited states and elimination of hot band complications. The technique has been applied to the study of the alkali dimers [21] [22] and to several polyatomic molecules. [23]-[25] It has proved more than simply a means of extracting ionisation potentials, as processes such as autoionisation may be probed by investigating the shape of the PIE curve in the post-threshold region. TIS is however, inferior to both ES-PES and ZEKE-PES in this respect, since autoionising structure is often swamped by the direct ionisation continua. The accuracy with which ionisation potentials may be measured by TIS is limited by the measured width of the threshold, which may be < 2 cm^{-1} when field ionisation effects have been completely eliminated. Hence measurements of the ionisation potentials of the Group 1b transition metal dimers may be undertaken, safe in the knowledge that the experimental precision is more than adequate to elucidate subtle bonding differences. The work described below is concerned with IP measurements and autoionisation in the molecules CuAg and Cu_2, the excited states of these molecules having been well-characterised (see Chapter 5). For this reason, Au_2, CuAu [26], and the trimers Cu_3 [27] and Ag_3 [28] are presently also amenable to study using this technique. Precise IP measurements on the other mixed Group 1b clusters must await the spectroscopic characterisation of their excited states.

6.2 Autoionisation processes

In the discussion of the TIS work which follows, much reference is made to autoionisation processes, which often give rise to rich post-threshold structure in PIE curves. These features may contain information of great relevance for an understanding of the electronic structure in both the neutral excited state and the ion. Therefore, a brief digression into the principles and consequences of molecular autoionisation processes is considered worthwhile.

Eigenstates of a neutral molecule which lie above particular ionisation thresholds may undergo a spontaneous ionisation process known as *autoionisation*. [29] Here, internal energy of the ion core is converted into kinetic energy of the ejected electron, by coupling of the neutral state wavefunctions with those in the continuum of electron-ion states. The core may be relaxed electronically, vibrationally or rotationally by the processes of *electronic*, *vibrational* or *rotational* autoionisation respectively. The physics of each of these processes is now considered.

6.2.1 Electronic autoionisation

Electronic autoionisation was first identified in atoms, where highly excited states, often those formed by a double electronic excitation, lie above the ionisation threshold. [30] The wavefunction for the discrete state is bathed in the continuum of states formed by M^+(ground state) + e^-, and ionisation of the molecule may occur. The radiationless autoionisation process for a state M^{**} involves ejection of one electron and de-excitation of the other to generate the

ground state configuration of the ion. The experimental evidence for atomic autoionisation comes from the observation of sharp resonances superimposed upon the smooth ionisation continuum absorption. Entirely analogous processes may occur in the case of molecules. For example, Guyon, Baer and Nenner [31] have ascribed features in the photoelectron spectrum of N_2O to the electronic autoionisation of a doubly excited state of the neutral molecule. Such states are often unstable with respect to dissociation into excited atoms, as well as to autoionisation. In such instances, where nuclear dissociative motion and electron ejection compete on similar time scales, highly non-Franck Condon distributions of peaks in the photoelectron spectra are obtained, as a wide range of internuclear separations are sampled when the molecule flies apart during the autoionisation process. A good example of this phenomenon, which will be discussed at length in due course, is the observation by SHW [15] of a highly extended vibrational progression in the ES-PES spectrum of the Cu_2^+ ground state. (See Section 6.5 below.)

Since it usually reasonably easy to ascertain the electronic configuration of the ion ground state, the observation of electronic autoionisation channels in ES-PES or TIS spectra provides some insight into the nature of the neutral excited state which was intermediate in the preparation of the autoionising state. This can be of considerable utility if there is any uncertainty surrounding the electronic configuration of these excited states.

6.2.2 Vibrational autoionisation

A molecular state capable of undergoing vibrational autoionisation comprises a

single highly-excited Rydberg electron orbiting a vibrationally excited molecular ion core. The autoionisation process involves some degree of vibrational relaxation with the energy released being transferred to the departing electron. In simple terms, the vibrating core interacts with the Rydberg electron, "spoiling" the stationary character of the Rydberg state. [29] The vibrational motion induces energy exchange between vibrational and electronic degrees of freedom. Failure of the slowly-orbiting Rydberg electron to keep pace with the vibrating nuclear framework forces the electron out to higher Rydberg states, as the core loses vibrational energy. Efficient vibrational autoionisation can take place when the Bohr period of the orbiting electron is closely matched to the vibrational period of the core. Under these conditions, there is a strong coupling between the two motions.

In homonuclear diatomic molecules, vibrational autoionisation is induced by an interaction between the vibrating quadrupole of the core and the Rydberg electron. For heteronuclear diatomics, the leading coupling term is the vibrating core dipole, so that both dipole- and quadrupole-induced vibrational autoionisation can take place. If the rate of change of the dipole with interatomic separation is small, the quadrupolar term may actually dominate in determining the autoionisation rate. [29] Berry has shown that for purely harmonic potentials of the core, the selection rule $\Delta v = -1$ is in strict operation. [29] Anharmonicity relaxes this rule so that higher vibrational transitions may be observed.

Vibrational autoionisation has been observed in the PIE spectra of the alkali dimers [22], and also in polyatomics. In an elegant study, Fujii *et al.* [32] identified vibrationally autoionising Rydberg states of diazobicyclooctane (

DABCO). These states converge to a series limit in the ion which is vibrationally excited by one quantum, and the states autoionise into the vibrationless continuum.

Vibrational autoionisation rates can sometimes be so high that it is no longer meaningful to speak of a discrete autoionising state with a finite lifetime towards ionisation. Here, the would-be autoionising Rydberg levels are lifetime-broadened to the extent that they overlap completely and form a quasi-continuum. The ionising process is then better envisaged as being direct, since no trapping in a discrete state can be identified.

6.2.3 Rotational autoionisation

This process is analogous to the vibrational case, except that it involves a rotational relaxation of the core during the autoionising step. [29] [33]- [37] In the absence of an external electric field, rotational autoionisation rates are mostly very small, as the transfer of many units of angular momentum from the core to the outgoing electron is not a favoured process. However, the application of even small (10-330 V cm^{-1}) static electric fields can facilitate efficient rotational autoionisation, with the angular momentum (and associated energy) being coupled out through the various multipole terms in the core. Mahon *et al.* [36] have observed strong rotationally-autoionising resonances in PIE spectra of Li_2, corresponding to loss of 10 units of core rotational angular momentum, when a field of only 10 V cm^{-1} was applied.

Most of the work described here was performed under zero static field conditions, where rotational autoionisation rates were negligible, so this process

concerns us less than does electronic or vibrational autoionisation.

6.3 Field ionisation

Atomic and molecular ionisation potentials are depressed in the presence of static electric fields due to the occurrence of field ionisation. The static field opposes the coulombic core-electron attraction and facilitates escape of the electron at a lower ionisation energy than in the zero-field case (see Figure 6.1). [38] The magnitude of the shift in ionisation potential, even at the relatively low field strengths encountered in the ion sources of our TOF instruments, can be quite significant. For example, a static field of 300 V cm^{-1} can red-shift an ionisation potential by as much as 100 cm^{-1}.

The classical treatment of this phenomenon is very simple. [30] The coulombic potential curve describing the attractive force between the core and the Rydberg electrons can be represented by the equation:

$$U(R) = -Ze^2/4\pi\varepsilon_0 R \qquad (6.1)$$

where

Z is the effective nuclear charge acting on the Rydberg electron

e is the electronic charge

ε_0 is the vacuum permittivity

and R is the nucleus-electron separation.

(see dashed curve in Figure 6.1)

Figure 6.1 : Ionisation threshold lowering by a static field

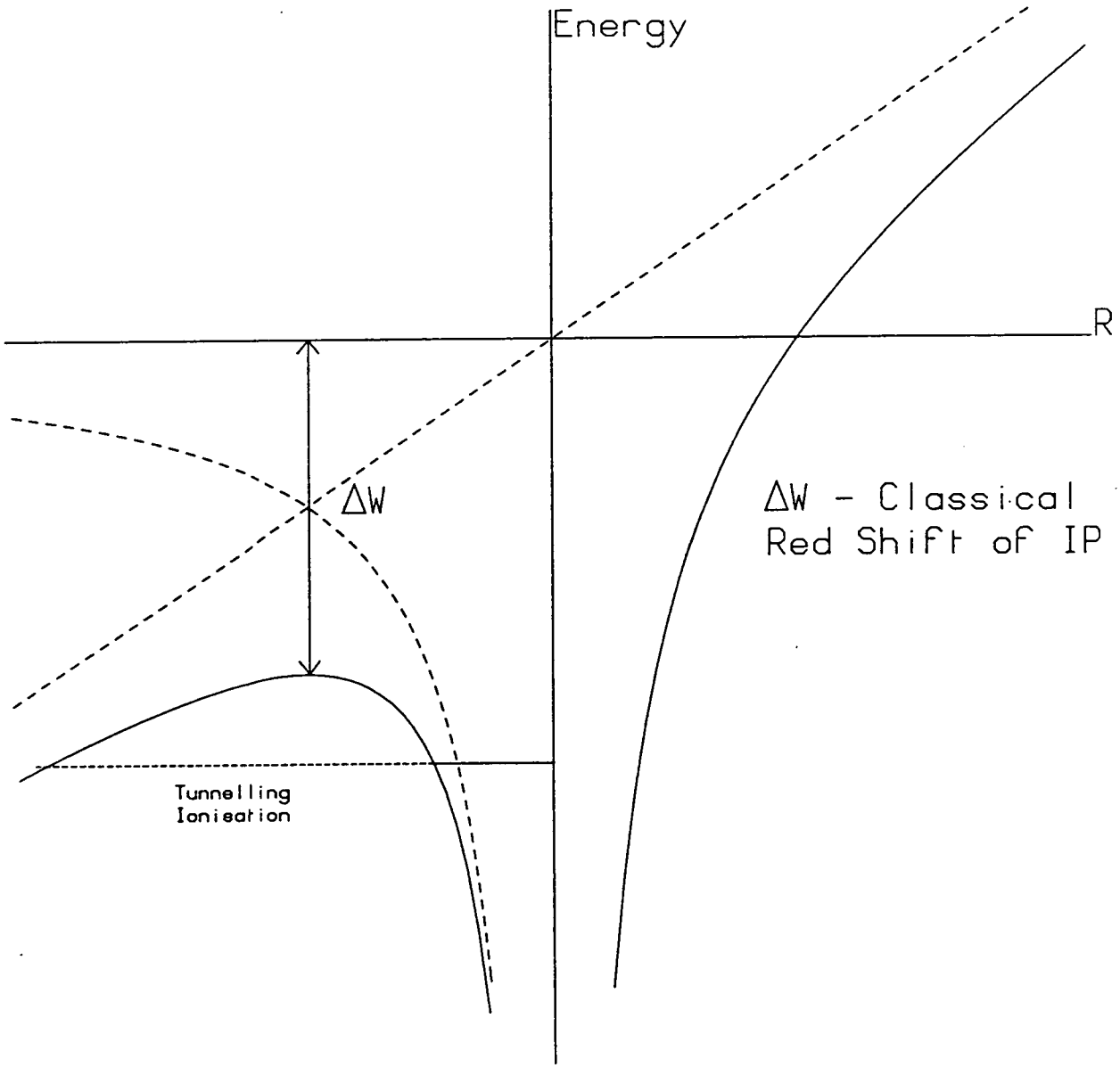

The potential energy is measured, of course, with respect to zero for infinite electron-core separation. When a static electric field of strength E is applied, the situation transforms to that shown by the solid curve in Figure 6.1. The potential energy is now described (for positive R values) by:

$$U(R) = EeR - Ze^2/4\pi\varepsilon_0 R, \tag{6.2}$$

The maximum turning point of this parabolic equation represents the situation where the attractive force is just balanced by the applied field. By differentiating Equation (6.2) with respect to R, it is easily shown that the shift in ionisation potential (δW) from the field-free value is given by:

$$\Delta W = -(Ze^3/4\pi\varepsilon_0)E^{1/2}. \tag{6.3}$$

Expressed in convenient units, with Z = 1, Equation (6.3) becomes:

$$\Delta W(cm^{-1}) = -6.13 \times [E(V\ cm^{-1})]^{1/2}. \tag{6.4}$$

The applied field balances the coulomb field at a distance R_c from the nucleus, where:

$$R_c = (Ze/4\pi\varepsilon_0 E)^{1/2}. \tag{6.5}$$

Rydberg states which lie on or above the field-depressed ionisation threshold are capable of spontaneous ionisation, although classically-quantised orbits may still exist above this energy. [39] Quantum mechanical treatments of the problem take into account the possibility of field ionisation by electron tunnelling through the

classically-forbidden potential barrier. [40] The wavefunctions for discrete Rydberg states just below the barrier penetrate through into the continuum, with the wavefunction amplitude progressively accumulating in the unbound region as the barrier extremum is approached. The quasi-bound Rydberg states may thus decay non-radiatively by tunnelling ionisation. Tunnelling therefore smears out the threshold region, and the effective appearance potential is lowered. In molecules, the true threshold may be further obscured by field-induced rotational autoionisation. In order to obtain accurate and precise ionisation potentials from threshold curves, the IP measurements really have to be performed under zero static field conditions to eliminate field ionisation effects.

Under certain circumstances, field ionisation may be exploited to the advantage of the spectroscopist wishing to measure ionisation potentials. Hackett and co-workers [41] [42] have made use of the long-lived nature of atomic Rydberg states to measure transition metal atom IPs. In a zero static field environment, Rydberg states lying close to the ionisation threshold are populated by double resonance laser excitation *via* some intermediate state. After a suitable time delay, the long-lived Rydberg states populated by the second laser are field-ionised by application of a pulsed d.c. field. The second laser is then scanned to excite complete Rydberg sequences right up to the convergence limit. Since the excitation takes place in the absence of an applied field, the true ionisation potential can be extracted by fitting the line positions to determine the series limit. This method offers greater precision than threshold estimations alone, provided that members of Rydberg series can be identified and assigned.

It remains to consider the other electric field present during these experiments,

namely the oscillating electric vector of the laser radiation field. The peak electric field intensity of an oscillating electromagnetic wave is given by the Poynting relation: [43]

$$E_0 = (\mu_0 c S)^{1/2}, \tag{6.6}$$

where

μ_0 is the vacuum permeability

c is the speed of light

and S is the power density of the radiation field

(in units of power per unit area).

For the laser sources used in these experiments, $S \simeq 5 \times 10^8$ W m^{-2}, so that $E_0 \simeq 4300$ V cm^{-1}, which is an order of magnitude larger than the fields encountered in the ion source ! One might envisage an ionisation potential which varies with time according to the instantaneous magnitude of the varying electric field. However, the E vector oscillates extremely rapidly, reversing direction on alternate phases. At a wavelength of 300 nm, a half-oscillation lasts only 5×10^{-16} s, which is much shorter than the timescale for electron ejection. Thus the effect of the time-varying electric field may be ignored.

6.4 Threshold photoionisation spectroscopy of CuAg

The logical starting point in attempting to determine the ionisation potential of CuAg is to scan, using TIS, over total energies between the known ionisation potentials of Cu_2 [4] [15] and Ag_2 [44]. The intermediate state selected was the

$A(0^+)$ state, whose spectroscopy was described in Chapter 5. When making threshold measurements using TIS, access to the ionic ground state through a direct ionisation channel is desirable, since it avoids the complications of electronic autoionisation. In Chapter 5 it was argued that there may be appreciable involvement of the excited configuration $(d^{20})(s\sigma)^1(s\sigma^*)^1$ in the description of the $A(0^+)$ state of CuAg. In the very simplest terms, direct ionisation from this state should be viable. Ejection of the most highly excited $s\sigma^*$ electron would produce the ionic ground state configuration, without any requirement for relaxation of the remaining electrons. The question of whether the zero point vibrational level of the ion is accessible is discussed in some detail in Section 6.4.5 below.

6.4.1 Experimental details

The basic experimental setup for the TIS experiment differed from that used in R2PI spectroscopy only in the choice of lasers used for each step (see Chapter 3). Vaporisation and clustering conditions were identical to those described in Chapter 5. The molecule was excited to the A state by a Nd:YAG pumped dye laser (JK HY750 pumping Quanta Ray PDL-2). The tunable ultraviolet radiation for the ionising step was generated by frequency doubling the output of the Lambda Physik excimer pumped dye laser system (EMG201MSC pumping FL3002EC) in a β barium borate crystal. Both dye lasers were operated on the dye Coumarin 102 (460-510 nm, 480 nm peak with 18 % efficiency). The exciting dye laser was tuned to the intense R-branch bandhead of the (0-0) or (1-0) band of the A←X system. The exciting laser bandwidth (0.4 cm^{-1}) was sufficient to overlap virtually all the observed lines in the R-head. Thus intense

resonant ionisation signals could be induced at the expense of slight, additional threshold broadening by excitation of multiple rovibronic transitions. The output power of each laser was kept low (< 0.5 MW cm^{-2}) to minimise the probability of three photon ionisation of Rydberg states lying below the ionisation threshold. Temporal overlap of the laser pulses was verified by monitoring with photodiodes and an oscilloscope (see Chapter 5). Since the molecular constants of the A and X states of CuAg had already been determined to high accuracy, there was no need to perform another calibration of the position of the A←X bandheads. It sufficed to perform a short R2PI scan before each threshold scan to ensure that the exciting laser was tuned correctly to the bandhead. Calibration of the photon energy in the second, ionising step was accomplished in the normal manner by recording monitor etalon fringes (3.333 cm^{-1} FSR) together with neon optogalvanic lines using the fundamental visible laser output. Laser powers were monitored using photodiodes in order to enable the PIE curves to be power-normalised. A more detailed description of the experimental setup can be found in Chapter 5.

6.4.2 Field dependence of the ionisation threshold

The initial TIS experiments were performed on the MB2 cluster rig, using the perpendicular ion extraction configuration. The application of $\simeq$ 3000 V to the repeller plate and $\simeq$ 2000 V to the draw out grid produced a static field in the ion source of approximately 180 V cm^{-1}. According to Equation (6.4), such a field should red-shift the ionisation potential by about 80 cm^{-1}. Figure 6.2 shows the PIE curve for $^{63}Cu^{107}Ag$ obtained in the threshold region when the ionisation

Figure 6.2 : PIE curve for $^{63}Cu^{107}Ag$, ionising from $v_A = 0$ in a static field of $\simeq$ 180 V cm^{-1}

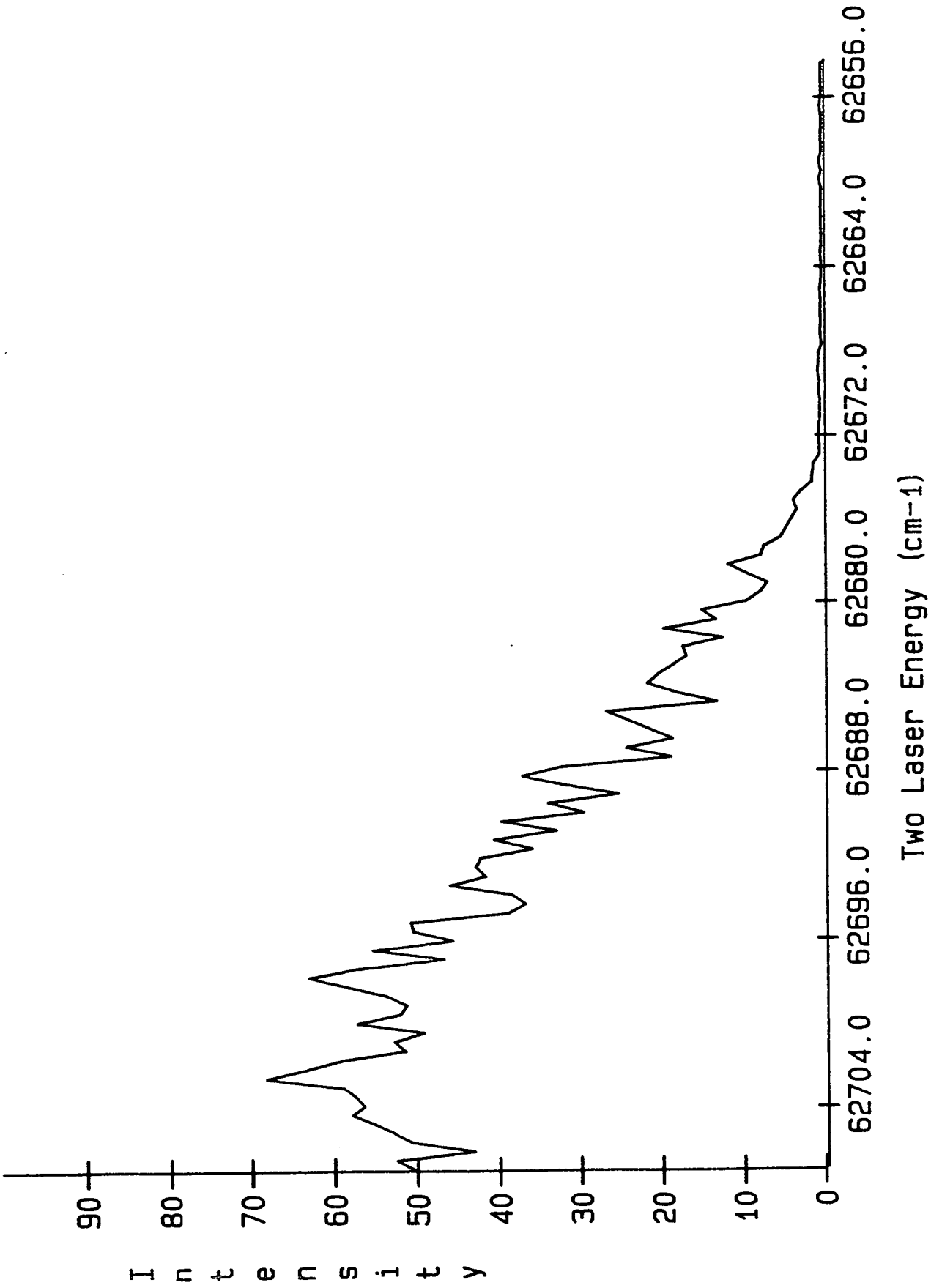

laser was scanned (0.42 cm^{-1} scanning step) with the exciting laser tuned to the A←X origin band. The horizontal scale in this, and all other threshold scans, is given as the sum of the laser photon energies. The red-shifted threshold was located at ≃ 62687 cm^{-1}. In common with several other molecular IP measurements in static fields, [24] [25] [45] the observed threshold is quite broad (≃ 30 cm^{-1}), and shows evidence of structure in the rising onset region. Laser timing jitter problems were encountered in this experiment, doubtless explaining some the observed oscillations. (This jitter was eliminated in all subsequent TIS scans.) Rydberg states which ionise by tunnelling through the potential barrier may also be responsible for such structure. Under even the modest fields applied here, efficient rotational autoionisation can occur. With the pump laser exciting the R-branch bandhead of the A←X system, the highest rotational quantum state accessed is J ≃ 10. The ion core should therefore contain 10ħ units of angular momentum, and the corresponding quantity of rotational energy. Rotational autoionisation induced by the applied field can transfer all this energy to the ejected electron. Assuming that the rotational constant of the Rydberg state is the same as that for the A state of CuAg, up to 7.5 cm^{-1} of rotational energy may be lost in autoionisation. This effect, coupled with the even greater contribution due to barrier tunnelling, broadens the threshold significantly, and makes assignment of its true position quite uncertain.

The variation of the threshold position with static field strength was investigated in an attempt to home in on the field-free value. This required an estimation of the static field present in the source region during ionisation. The repeller-draw out voltage difference was measured using a digital multimeter (Fluke 75),

floating the probe which was normally grounded to the draw out grid potential. The "idealised" static field strength was then obtained by dividing this voltage difference by the repeller-draw out plate separation.

It was found that as the extraction field was lowered, the post-threshold ionisation signal became progressively weaker. This was due to the increased time the ions spend in transit through the source and acceleration regions when they are extracted using a lower potential difference. Longer flight times lead to an increased displacement along the molecular beam axis, which could only be partially compensated by adjusting the voltage on the deflection plates (see Chapter 4). Therefore, for field strengths below 130 V cm^{-1}, it was necessary to switch to the RETOF configuration, where the ions are extracted collinearly with the molecular beam axis. Even using this geometry, the ion signal at extraction field strengths below $\simeq$ 40 V cm^{-1} was unacceptably low, necessitating an extrapolation to zero field to estimate the true IP. Figure 6.3 shows a plot of the observed ionisation threshold versus the applied field strength.

The threshold broadening introduced by tunnelling ionisation and field-induced rotational autoionisation creates an uncertainty in the classical threshold position. Since the classical model ignores tunnelling effects, one approximation was to place the threshold at the point where the onset region first levels off. However, this was often obscured by strong autoionisation features, and there was no reliable criterion for adjudging the classical threshold. A crude estimate was made by averaging the immediate post-threshold ion signal, and using this to determine the position of half-maximum signal intensity.

Figure 6.3 : CuAg ionisation threshold as a function of applied static field

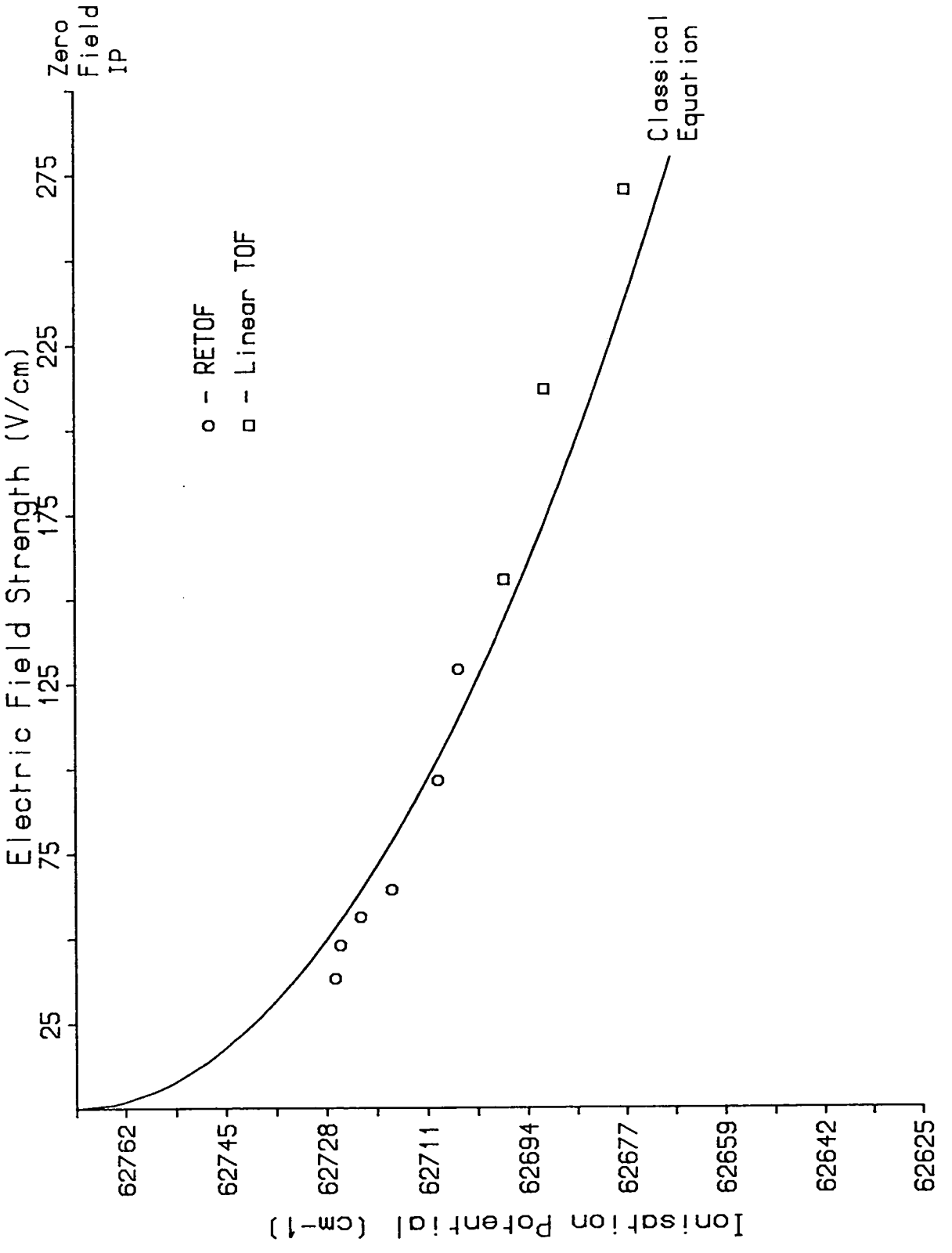

The field-free ionisation threshold was determined by extrapolating through the data points using a nonlinear fitting method. Equation (6.4) was used in a form where Z = 1 and E was set to the idealised value:

$$IP(E) = IP(E=0) - 6.13 \times E_{ideal}^{1/2}. \qquad (6.7)$$

The effective nuclear charge experienced by the Rydberg electron is unity because of the extremely diffuse nature of the Rydberg orbitals from which field ionisation occurs. A Rydberg state lying $\simeq$ 100 cm^{-1} below the convergence limit has an effective orbital radius of $\simeq$ 580 Å, and its electron grazes the barrier to field ionisation around 2300 Å from the core ! In such states, the orbiting electron is so remote from the nucleus that it cannot "see" core orbital structure, and can only "feel" an effective nuclear charge of 1.

The local field responsible for inducing ionisation is not homogeneous, and varies with position in the source region. However, the simulations of the potential in the source region of the RETOF shown in Chapter 4 indicated that the true field in the source is typically no less than 97 % of the idealised value. Hence the directly-measured field strengths were employed in the fitting procedure, introducing only a small error.

The field-free IP was determined in this way to be $\simeq$ 62771 cm^{-1}. (The abscissa intercepts the ordinate at this value in Figure 6.3.) However, it was felt that estimating the ionisation potential by an extrapolation to zero field was not sufficiently accurate, given the very obvious difficulty of locating the classical ionisation thresholds. Some independent corroboration was certainly required.

Hence it was decided to modify the experimental system in order that molecules could be ionised in a zero-field environment prior to detection in the TOFMS.

6.4.3 Experimental modifications for zero-field threshold ionisation studies

The use of pulsed, rather than static extraction fields enables the measurement of ionisation potentials under field-free conditions. Molecules are ionised with the ion extraction optics held at ground potential. After a short delay, the newly created ions are accelerated into the TOFMS by switching on the extraction voltages using a fast risetime high voltage pulse generator.

The fast-switching high voltage pulser used in these experiments was a prototype module obtained from Kentech Instruments, Didcot, Oxon. Since the complete circuit diagram for this device is proprietary information, only a simplified schematic is shown in Figure 6.4. (A high voltage pulser in the public domain has recently been described by Gandhi and Bernstein. [46]) The variable voltage from a stabilised d.c. supply (0.067 % ripple) is stepped up by a transformer (turns ratio = 1:300) to generate the high voltage to be switched (in this case $\simeq$ 3000 V). A spare channel on the LeCroy 4222 PDG was used to trigger the line driver, producing a TTL level pulse of 10 µs duration to drive the high voltage pulser. The trigger pulse is applied to a timing network which generates a square wave pulse to turn off current flow to the bases of a chain of field effect transistors (FETs). Since no current now flows down the arm AB, the potential V_S rises from -3000 → GND, and remains there until the square wave pulse terminates. The capacitive network which follows inverts the switching action from -3 kV → GND to GND → +3kV, and divides the output voltage between two

Figure 6.4 : High voltage pulser circuit schematic

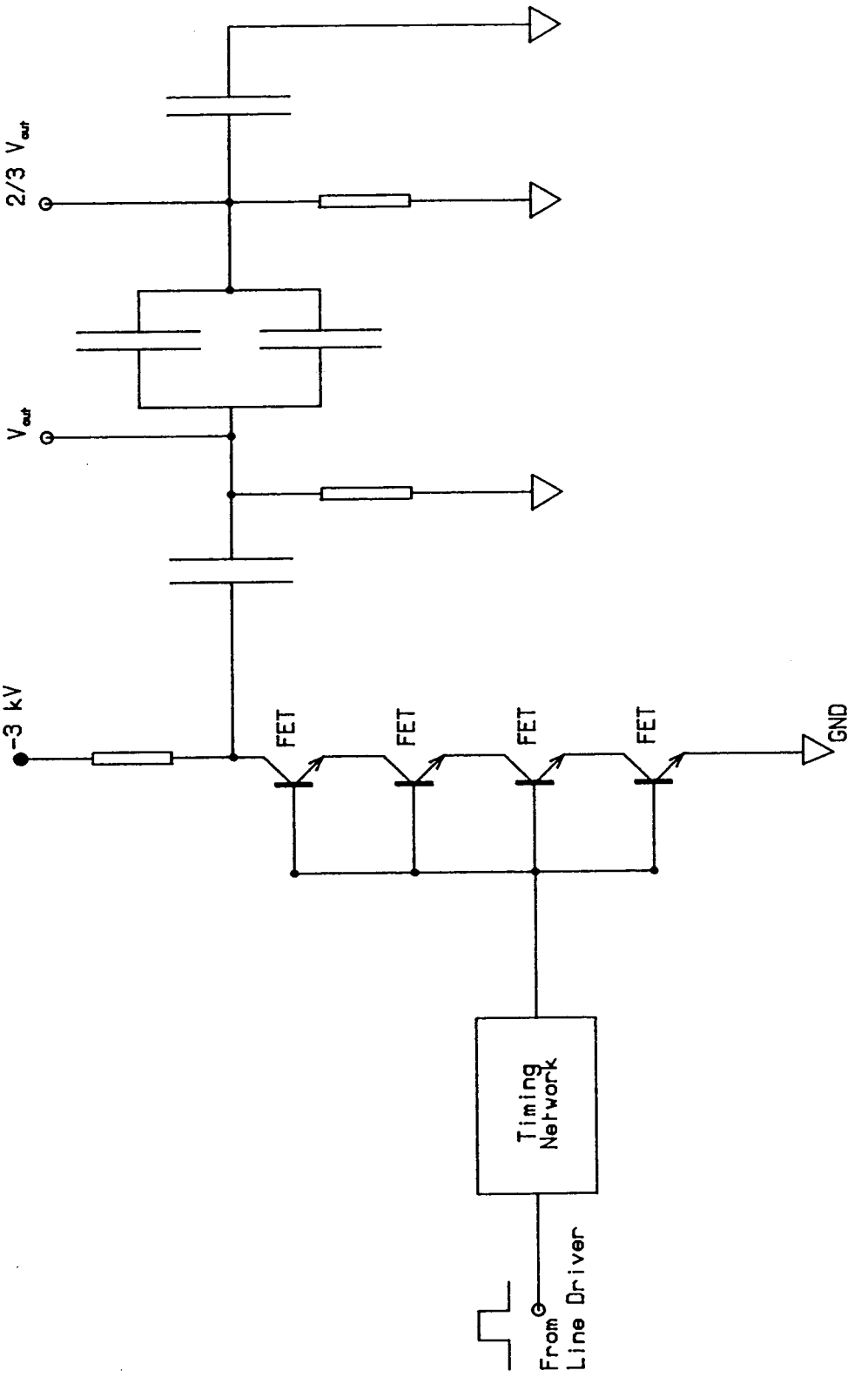

terminals in the ratio 3:2. These high voltage outputs were connected to the repeller plate and draw-out grid respectively. The temporal profile of the high voltage pulse applied to the repeller plate is shown in Figure 6.5. The rising edge of the pulse is only 25 ns wide, and the extent of overshoot is minimal. This high voltage pulse is held high for $\simeq$ 100 µs, which is ample time to accelerate all the ions out of the source region. When the driving pulse times out, the charge held on the capacitors gradually leaks away to ground in $\simeq$ 2 ms. Pulse-to-pulse amplitude reproducibility, as determined by the stability of the external supply, was found to be excellent over a long period. The finite risetime and "bounce" on the flat top of the pulse did not alter the ion flight times significantly. All the field-free threshold measurements discussed below were made using the RETOF geometry, with the voltage supply adjusted to provide a 3000 V pulse on the repeller and a 2000 V pulse on the draw out grid.

The only other modification required for field-free TIS work was purely precautionary. In normal, static field operation, the voltage applied to the RETOF repeller plate prevents any plasma-generated ions, carried along in the molecular beam, from entering the ion source. In the pulsed extraction mode, these ions could be admitted to the source region with the neutral beam, as there is no retarding field in the dead time between pulses. If present in high number density, these ions may swamp the MCP detector. To guard against this, a pair of Ni-Al ion scavenging plates, separated by 5.6 cm, were mounted immediately downstream of the extender channel of the cluster source. Their presence did not appear to disrupt formation of the cold molecular beam.

To investigate if any ions did survive collisional quenching prior to expansion, a

Figure 6.5 : Temporal profile of the high voltage pulse

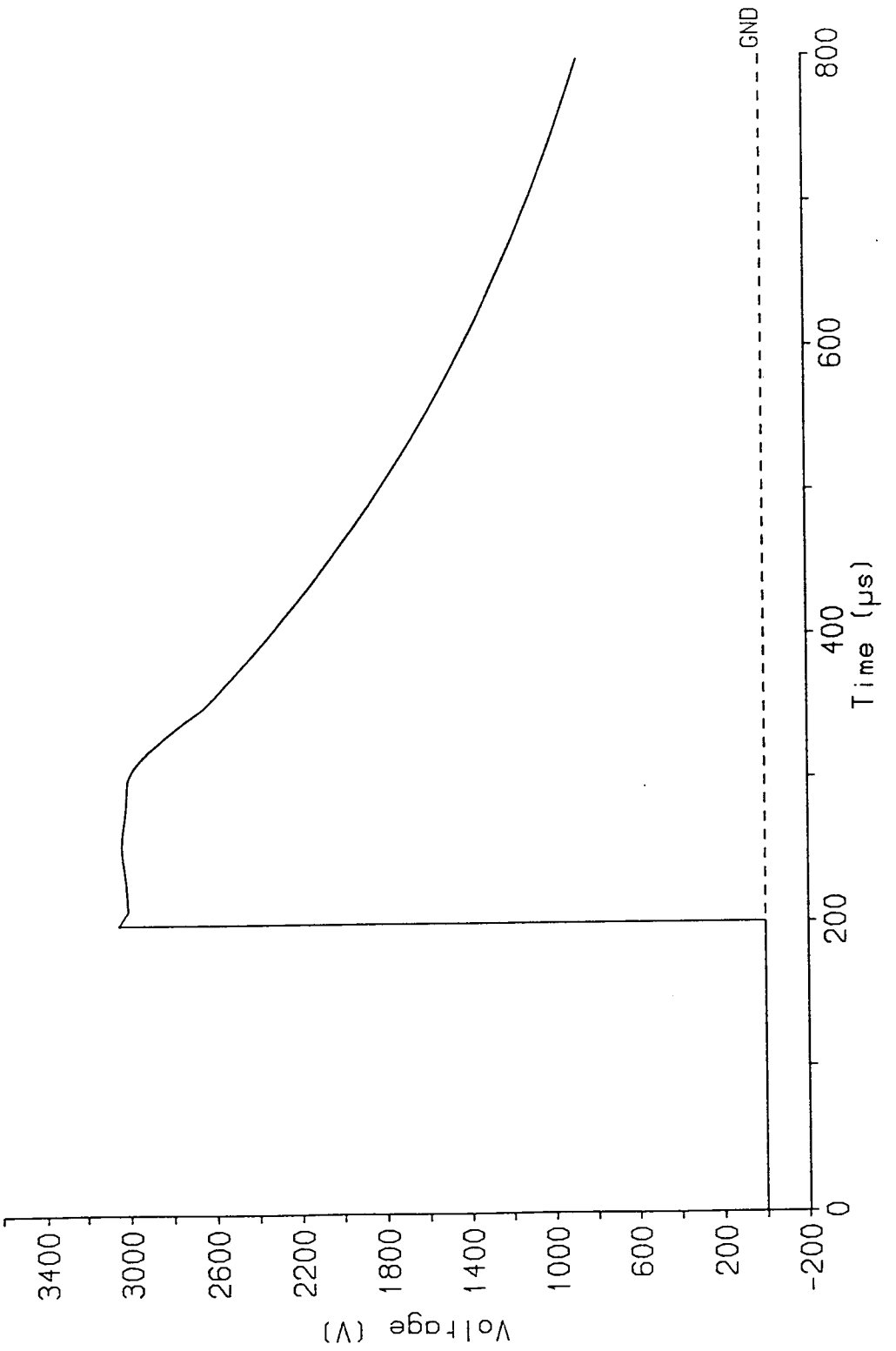

differential current operational amplifier [47] was connected across the scavenging plates. Even at the lowest gain setting of 10^3, a substantial ion signal was recorded, with a temporal distribution similar to that for the neutral species.

With a potential difference of 60 V (from dry cell batteries) across the plates, all ions up to mass 230 will be scavenged on to the plates, and the vast majority of the remainder deflected to the extent that they fail to negotiate the skimmer. Experimentally, no plasma ions could be detected in the TOFMS when the plates were biased in this manner.

6.4.4 Zero-field threshold ionisation measurements on CuAg

Figure 6.6 shows the PIE curve (0.87 cm^{-1} scan step) for two colour ionisation of $^{63}Cu^{107}Ag$ under zero-field conditions. Again, the exciting laser was tuned to the A←X origin band while the ionising laser was scanned over the threshold. The time delay between the synchronised laser pulses and application of the high voltage extraction pulse was ≃ 300 ns. During the delay period, the nascent ions drift along the molecular beam axis by only 0.5 mm, so that they are still well within the source when the accelerating pulse is applied.

The observed field-free threshold was noticeably sharper than before, with a width of 3.7 cm^{-1}. This enabled a much more accurate and precise determination of the ionisation potential to be made, by summing the laser photon energies at threshold (see Table 6.1). The residual threshold width was surprising, as tunnelling and rotational autoionisation should have been completely eliminated in zero field. It is conceivable that stray fields were present even when the high voltage pulser was grounded out. These fields may be partially responsible for the

Figure 6.6 : PIE curve for $^{63}Cu^{107}Ag$, ionising from $v_A = 0$ in zero static field (Δt = 300 ns)

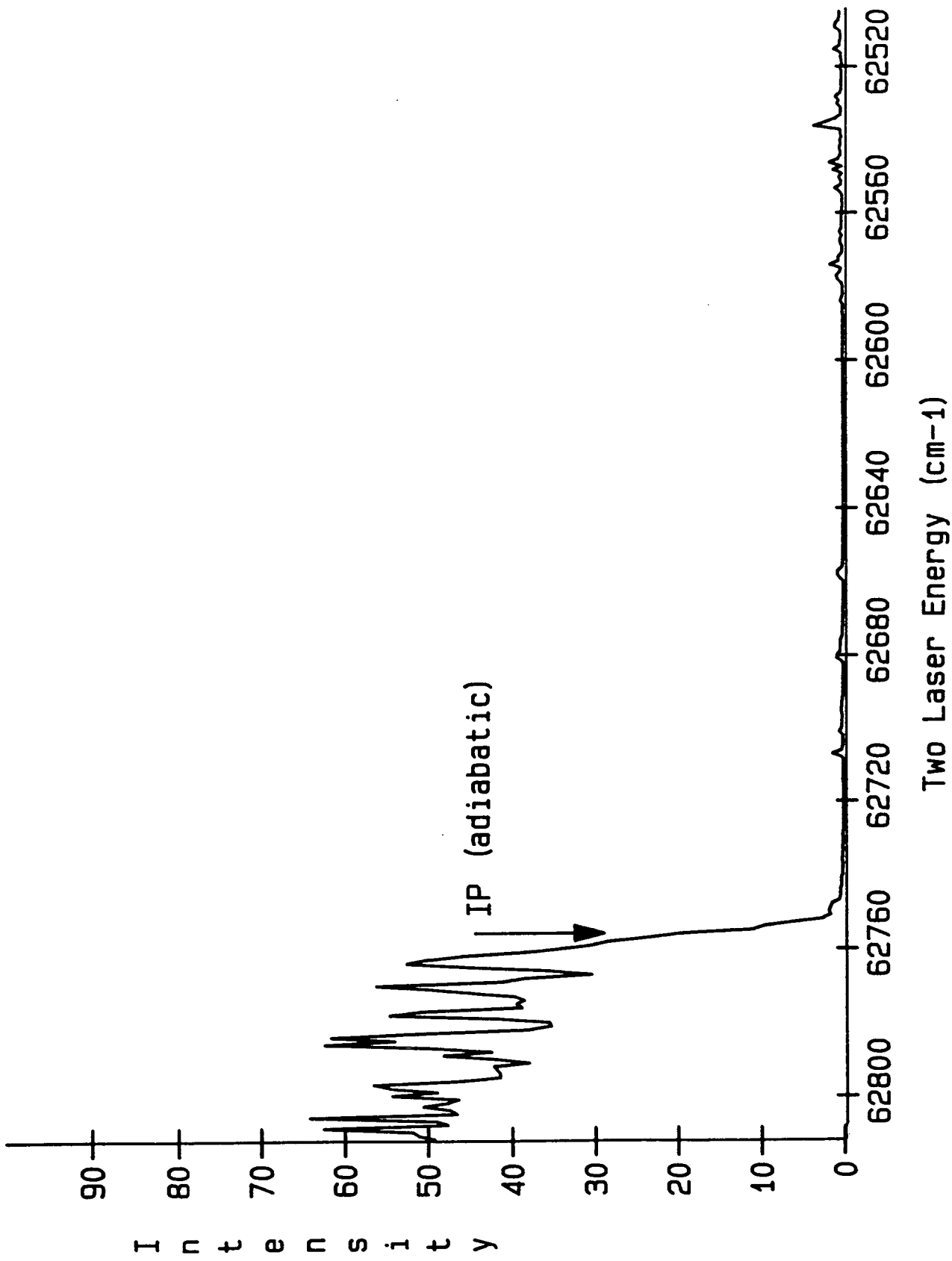

discrepancy ($\simeq$ 16 cm^{-1}) between the threshold measured here and that determined by extrapolation. The extrapolated static field result was felt to be too susceptible to errors in the estimation of the thresholds. Therefore the pulsed-field measurement is quoted alone in Table 6.1, with the proviso that it may lie slightly below the true field-free IP.

On examining the PIE spectrum, one is immediately struck by the almost complete absence of features lying to the red of the ionisation threshold. By analogy with atomic spectroscopy, one might have expected to see sharp features due to long-lived molecular Rydberg states being field-ionised by the pulsed extraction voltage before they decay. Longevity with respect to radiative decay is a well-documented feature of atomic Rydberg states. [48] Inter-Rydberg radiative transitions are very weak and slow ($>$ μs) processes because their transition frequencies are so small; the rate of spontaneous emission depending on the cube of the transition frequency. [38] Thus excited atoms trapped in long-lived Rydberg states can be detected easily by field ionisation, without the requirement for a particularly short delay between excitation and field ionisation. As related in Section 6.3, this property of Rydberg states has been exploited to obtain precise atomic IPs from an analysis of laser-excited, field-ionised Rydberg series. [41] [42] It had originally been hoped that the molecular Rydberg states of CuAg would be similarly long-lived, and that the ionisation potential could be determined in this way. Application of 1000 V across the repeller-draw out region creates an extraction field of $\simeq$ 330 V cm^{-1}. This permits the observation, by field ionisation, of all molecular Rydberg states as far as 110 cm^{-1} below threshold, provided that they do not decay during the time delay between laser

excitation and pulsed extraction. In Figure 6.6, there is only scant evidence for any states with lifetimes of 300 ns or greater: some very weak features are observed on the low wavenumber side of the threshold region. Whether these features are due to field ionisation or are simply the result of two-photon resonant, three-photon ionisation is a matter of conjecture. Figure 6.7 shows the corresponding $^{63}Cu^{107}Ag$ threshold spectrum (0.87 cm^{-1} scan step) when the ionisation-extraction delay was reduced to $\simeq$ 60 ns in an attempt to detect short-lived Rydberg states. (It was not convenient to work with shorter delays owing to the risk of pulse delay drift, which could have destroyed the field-free conditions due to overlapping of the laser and high voltage pulses.) Some weak features are discernible below threshold, but are hardly assignable. Additionally, the threshold region itself acquired a red "tail", suggesting that those Rydberg states within $\simeq$ 15 cm^{-1} of the convergence limit are longer-lived than those lower in energy.

The disquieting possibility that the "continuum" behaviour above the observed threshold is really due to field ionisation of a superdense manifold of long-lived Rydberg states, and that the true IP lies 110 cm^{-1} further blue, can be immediately ruled out. The measured field-free threshold lies to higher energy than any of the static field points in Figure 6.3. If the continuum had been due to field-ionised Rydberg states, the large (330 V cm^{-1}) pulsed field would give rise to a pseudo-threshold lying to lower energy than any of the data points in Figure 6.3. Therefore the observed onset may be confidently ascribed to the field free ionisation threshold of CuAg.

The unexpectedly short lifetimes of the molecular Rydberg states remains a

Figure 6.7 : PIE curve for $^{63}Cu^{107}Ag$, ionising from $v_A = 0$ in zero static field ($\Delta t = 60$ ns)

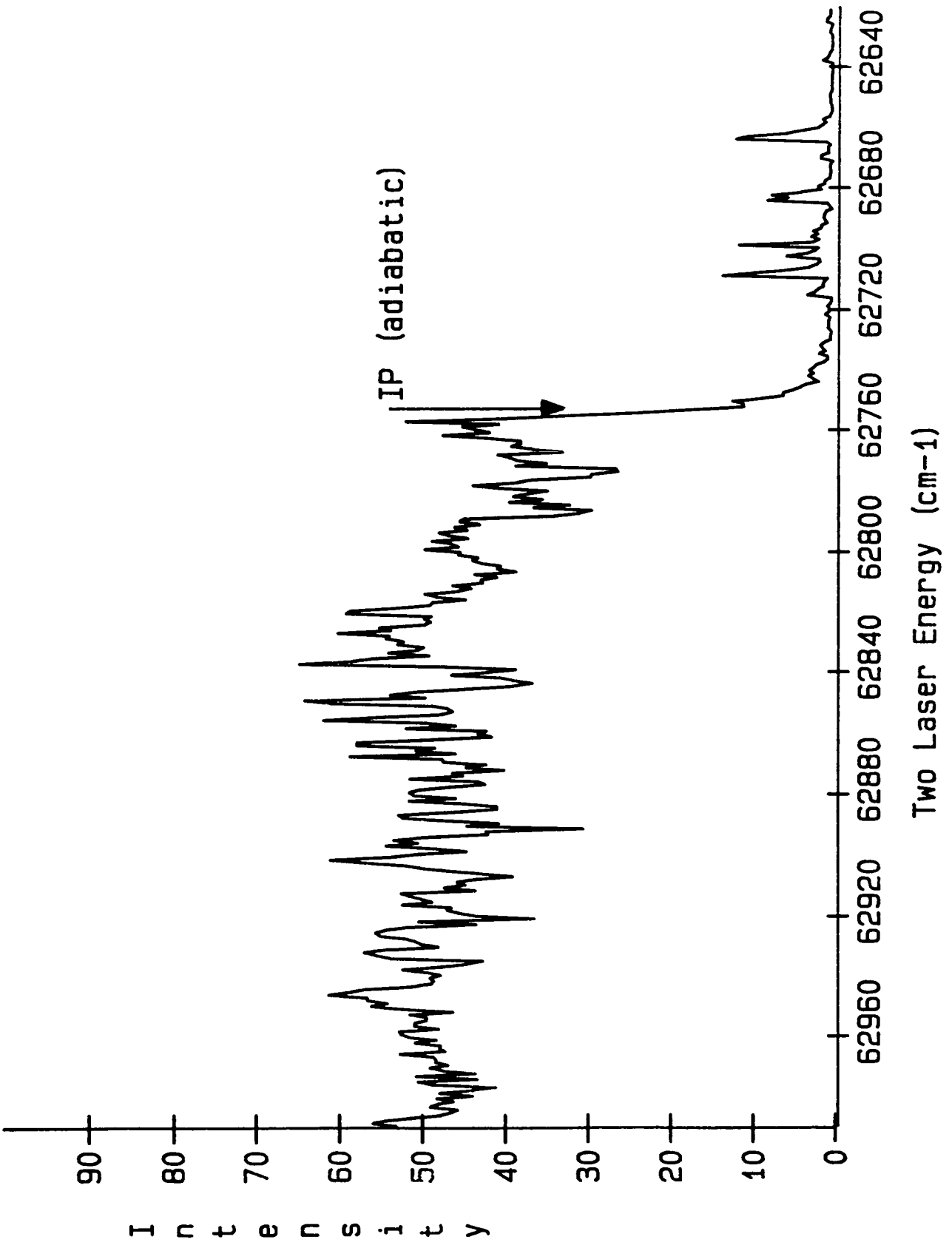

vexing problem. Reiser *et al.*, [18] using ZEKE-PES, have found Rydberg states of NO within 2.5 cm^{-1} of the ionisation threshold which have lifetimes of tens of μs. We have been unable to find a satisfactory explanation as to why the Rydberg states of CuAg are so short-lived. One possible explanation is that they may be heavily predissociated by repulsive states correlating with excited neutral atomic limits. Their lifetimes would then be dramatically foreshortened relative to unperturbed atomic Rydberg states. When the ionisation limit is reached, a rapid and efficient direct ionisation channel opens up, competing efficiently with the predissociation channel, and producing the molecular ion in high yield. There is clearly scope for future experimentation here, with efforts directed towards elucidating the dynamical processes responsible for the early demise of the neutral Rydberg states of CuAg.

An independent determination of the ionisation potential of CuAg was made by exciting the (1-0) band of the A←X system and recording the $^{63}Cu^{107}Ag$ PIE curve, with a 0.26 cm^{-1} scan step (see Figure 6.8). The ionisation threshold was found at exactly the same two-laser energy as in the (0-0) determination, within the limits of experimental error (see Table 6.1). Qualitatively, the PIE curve in the post-threshold region was very different to that obtained when the vibrationless level of the A state was excited. The initial rise in ion signal as the first threshold is crossed was substantially diminished compared to that observed for the (0-0) excitation PIE curve. On scanning to higher energy, a second, considerably more intense threshold was encountered, displaced by $\simeq$ 162 cm^{-1} to the blue of the first one. In the intervening region between the two thresholds, strong and completely reproducible discrete resonances were observed. This

Table 6.1 : Threshold ionisation measurements on $^{63}Cu^{107}Ag$

A←X Band	$\hbar\omega_1$ /cm^{-1}	$\hbar\omega_2$ /cm^{-1}	$\hbar(\omega_1 + \omega_2)$ /cm^{-1}
(0-0)	20807.20(58)	41947.2(38)	62754.4(44)
(1-0)	20978.27(68)	41776.6(37)	62754.8(44)

IP(CuAg) = 62754.6(44) cm^{-1} ≡ 7.78058(54) eV

$D_0(CuAg^+)^a$ = 1.56(10) eV

a - using $D_0(CuAg)$ = 1.76(10) eV from Ref. [61] and IP(Ag) from Ref. [60]

Errors quoted are ± 1σ

Figure 6.8 : PIE curve for $^{63}Cu^{107}Ag$, ionising from $v_A = 1$ in zero static field (Δt = 300 ns)

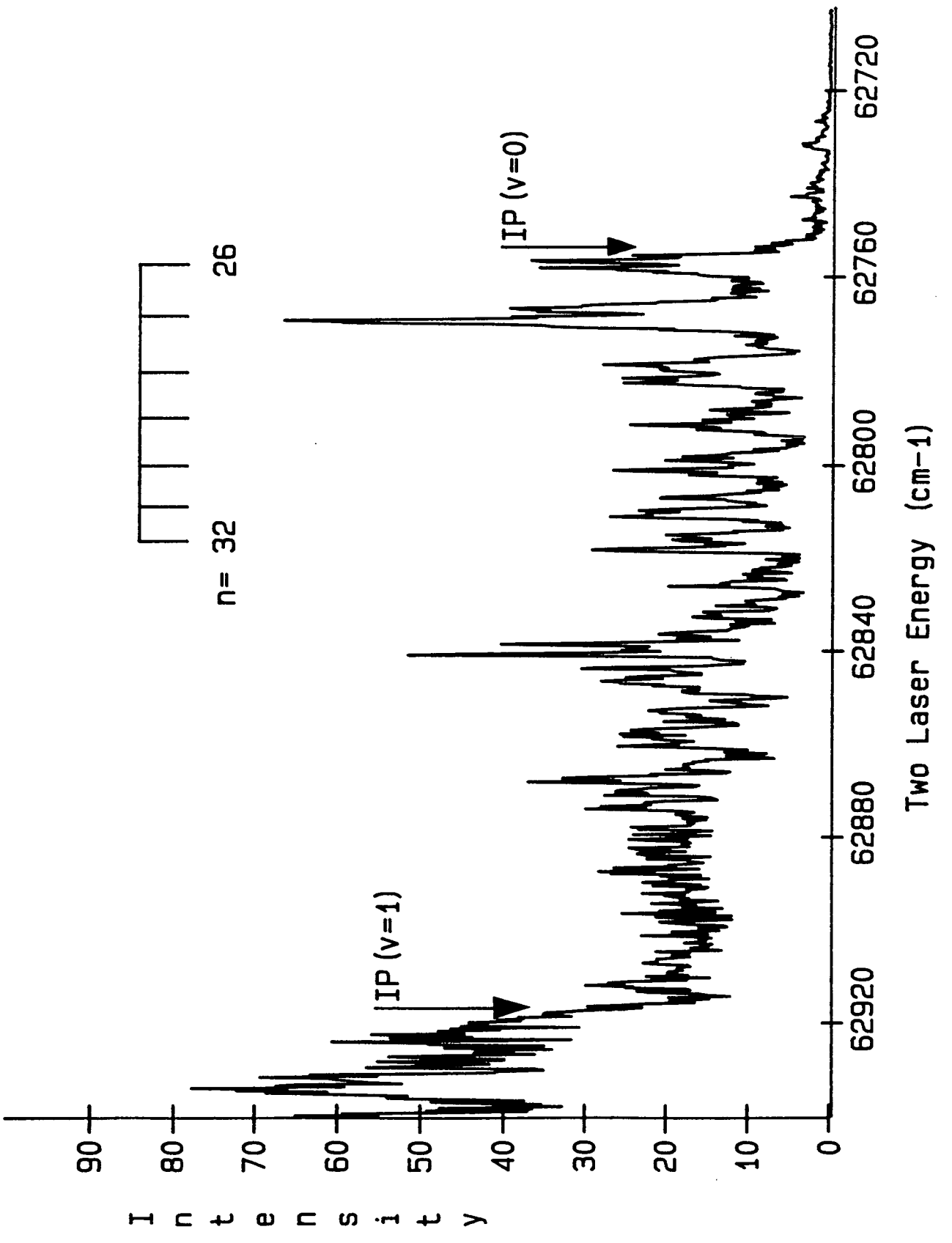

structure is assigned to vibrationally excited states which autoionise into the first continuum (see Section 6.4.5.).

6.4.5 Assignment of the adiabatic ionisation threshold in CuAg

The observation of "staircase" structure in the post-threshold region is a well-documented phenomenon previously observed in the two colour ionisation of certain aromatic molecules. [49] The "steps" are generated as the ionising dye laser energy is scanned across successive vibrationally-excited ion thresholds. The energy differences between successive steps can be equated to the magnitudes of vibrational quanta in the ion. The relative intensities of the steps reflect the Franck Condon factors for transitions leading to direct ionisation from the pumped intermediate level to the various vibrational levels of the ion.

Such behaviour has been observed in the case of ionisation from the S_1 states of benzene, [24] [50] naphthalene [24] [51] and toluene. [52] Here, a $\Delta v = 0$ vibrational propensity rule governs the threshold intensities, the degree of vibrational excitation in the ion core being conserved upon electron ejection. This behaviour may be rationalised by examining the electronic configuration of the S_1 excited state. [53]- [55] It is formed in each case by a $\pi^* \leftarrow \pi$ promotion, and ionisation of an electron from the π^* HOMO produces the ground state ion configuration π^1. The out-of-plane π^* orbital is effectively non-bonding. Ionisation of a non-bonding electron has little effect on the molecular geometry, and the potential surface of the ion ground state lies almost directly above that of the S_1 π^* state. Consequently only those transitions which preserve the vibrational excitation of the core have appreciable Franck Condon factors: the

equivalent in photoionisation of sequence bands in diatomic absorption spectroscopy. Thus excitation of a particular vibration in the S_1 state leads to the observation of a strong threshold, displaced to the high energy side of the adiabatic IP by an amount equal to the wavenumber of this vibration in the ion. Under these circumstances, the transition to the ionic zero point level may be suppressed to the extent that it is difficult to observe.

At first glance, it would appear that we could press the analogy with the aromatic series completely to the PIE curves in CuAg, assigning the first observed ionisation thresholds in Figures 6.6-6.8 as corresponding to the vibrationless level of the ionic ground state, with a $\Delta v = 0$ propensity rule in operation. However, such an assignment ignores two crucial differences between the photoionisation of these aromatic molecules and CuAg. Firstly, the electronic structure in the intermediate excited state and the ionic ground state of CuAg are considerably more complex than that in the aromatics. Secondly, and related to this point, the electron removed from the CuAg A state is liable to be much more involved in bonding than the aromatic π^* electron. Its removal is liable to cause a substantial change in molecular geometry, with the result that the ionic zero point vibrational level may be inaccessible, and the adiabatic IP unmeasureable. These two points are now examined in detail to test the validity of our assignment of the adiabatic IP to the first observed ionisation threshold.

The S_1 state and ionic ground states for the aromatic systems are dominated by the valence configurations $\pi^1\pi^{*1}$ and π^1 respectively. A simple, direct ionisation mechanism can be envisaged involving ejection of the π^* electron, and minimal disruption of the σ-bonding framework. In CuAg, matters are complicated by the

involvement of low-lying d core hole excited states. In Chapter 5, it was argued that the $A(0^+)$ state of CuAg is a complex admixture of several configurations, with the $d^{20}(s\sigma)^1(s\sigma^*)^1$ and $d^{19}(s\sigma)^2(s\sigma^*)^1$ configurations believed to play a central role. In the absence of any *ab initio* calculations on electronically excited states of CuAg to determine the mixing coefficients, it is not clear which of the configurations, if any, is dominant near the potential minimum. Similarly, we lack any theoretical work on the molecular ion $CuAg^+$. Some indication of the likely involvement of d hole configurations in the ionic ground state comes from the ES-PES work of SHW on copper dimer. [15] The two spin-orbit components of a $^2\Pi$ state were observed to lie only 1.14 eV above the ground ($^2\Sigma_g^+$) state of the ion. These results are in qualitative agreement with all electron *single* configuration SCF calculations by Miyoshi *et al.*, [56] who found $^2\Sigma$, $^2\Pi$ and $^2\Delta$ d vacancy states lying 0.6-0.7 eV above the $d^{20}(s\sigma)^1$ ion ground state. Given the similarities in electronic structure between Cu_2 and CuAg, it is likely that corresponding d hole states lie close to the ground state of $CuAg^+$. The $X(^2\Sigma^+)$ state of $CuAg^+$ may therefore involve considerable contributions from $d\sigma$ vacancy states, as in the $A(0^+)$ state of the neutral.

It is thus difficult to establish with certainty the nature of the molecular orbital from which the electron is removed in these photoionisation experiments. However, with the expectation of significant involvement of the d and s hole configurations in both the neutral A state and ion ground state, it seems reasonable to assign the observation of a strongly direct ionisation channel to the production of ground state $CuAg^+$. If, on the other hand, the A state and ionic ground state were dominated by completely dissimilar configurations, we would

not expect to observe a strong direct ionisation channel.

While it appears likely that the ionic ground state is electronically accessible using the chosen ionisation route, it remains to establish if the zero point vibrational level of this state is Franck Condon accessible from the A state. Unlike the aromatic S_1 systems, the electron removed does not reside in a non-bonding orbital, so we cannot invoke the $\Delta v = 0$ propensity rule without supporting evidence. Indeed, the possibility exists that the potential energy curve of the ionic ground state is displaced from the $A(0^+)$ curve to the extent that the observed first ionisation threshold is a transition to a vibrationally-excited level of the ion. The crux of the argument centres on the equilibrium bondlength in the $X(^2\Sigma^+)$ state of the ion. If this could be measured, Franck Condon factors for the (ion, $v_+ = 0$)$\leftarrow$A transition could be calculated, their magnitude indicating the likelihood of observing the zero point threshold. We lack a direct spectroscopic determination of either this bondlength, or that of closely-related neutral Rydberg states lying near threshold. It is therefore necessary to resort to a combination of common sense and semiempirical methods to validate our assignment of the first threshold.

Initial evidence in support of our assignment comes from the intensity of the observed first threshold, as shown in Figures 6.6 and 6.7, where $v_A = 0$ in the intermediate A state was excited. The marked rise in ion signal at the onset, and the relatively structureless post-threshold region, indicates the sudden opening of a strong and direct ionisation channel. The ion signal rises from a negligible background level to to an absolute level commensurate with the two colour R2PI signal obtained when 193 nm ionising radiation was used, the excitation laser

power levels being similar.

The vibrational wavefunction for the zero point level of the A state is smooth and nodeless. Projection of this bell-shaped wavefunction on to the potential surface of the ion is unlikely to produce the observed sharp threshold behaviour, unless the $v_+=0$ level is being accessed. In the case of large geometry changes between the A state and the ionic ground state, a "staircase" PIE curve would result, with the $v_+=0$ threshold only weakly detected. Subsequent thresholds would grow in intensity in a smooth manner, until the ion vibrational level which had maximum Franck Condon overlap with $v_A=0$ was attained. In this case, there would be no sudden "switching on" of a strong ionisation channel, just a gradual series of successively more intense threshold steps. Our observation of an intense onset strongly suggests that the $v_+=0$ direct ionisation channel is being accessed, and that the Franck Condon factor for the (ion, $v_+=0$) $\leftarrow$ (A,$v_A=0$) transition is favourable. Strong Franck Condon overlap of this type can arise when the equilibrium bondlengths in both states are similar, the origin of the $\Delta v = 0$ propensity rule. Evidence in support of the operation of a propensity rule which conserves vibrational energy comes from the PIE curve obtained when $v_A=1$ was excited, Figure 6.8. The $v_+=0 \leftarrow v_A=1$ channel is relatively weak due to poorer Franck Condon overlap, and a strong threshold is obtained for the $v_+=1 \leftarrow v_A=1$ transition, which obeys the propensity rule. It is less easy to explain the absence of the expected second threshold in Figure 6.7, corresponding to the transition $v_+=1 \leftarrow v_A=0$. This may be due to inadvertent saturation of the digitiser by the $v_+=0 \leftarrow v_A=0$ ionisation channel, preventing the observation of the weaker second step superimposed on an intense continuum.

In order to place the analysis on a more quantitative footing, an estimation of the bondlength in the ground state of the molecular ion is required. Its approximate magnitude may be obtained by applying the semiempirical relation known as Badger's rule. [57] [58] This relates the force constant (k_e) to the equilibrium bondlength (r_e) for a diatomic molecule through the equation:

$$k_e(r_e - d)^3 = C, \tag{6.8}$$

where C is a general constant, and d a constant specific to the molecular system under consideration.

The spectroscopic constants for the X and A states of CuAg, which were determined in Chapter 5, were used to estimate d. Assuming that our assignment of the adiabatic ionisation threshold is valid, the energy difference between the two thresholds in Figure 6.8 (162.5(60) cm^{-1}) is equal to $\Delta\tilde{G}_{3/2}(ion)$ (= ω_e - $2\omega_e x_e$). With an approximate anharmonicity of 0.5 cm^{-1}, $\omega_e(ion)$ is calculated to be 163.5(60) cm^{-1}. Inserting this value in to Equation (6.8) yields an equilibrium bondlength for the ground state of the ion of 2.62(07) Å. The relative difference in bondlengths between the neutral and ion ground states of CuAg is therefore $\simeq$ 10 %. The corresponding value for Cu_2, again employing Badger's rule, is $\simeq$ 6 %. [59] If this value was directly transferable to CuAg, the bondlength in the ion would be $\simeq$ 2.51 Å.

Franck Condon factors for the transition from the A state to the ground state of the ion were calculated using the methods described in Appendices D and E. The RKR-generated A state potential curve of Chapter 5 was used, along with an

approximate curve for the ionic ground state, assuming that ω_e = 163.5 cm^{-1} and $\omega_e x_e$ = 0.5 cm^{-1}. Franck Condon factors were evaluated for transitions originating from $v_A = 0$ to the zero point level of the ion, for a range of ion equilibrium bondlengths. Results are shown in Figure 6.9. Marked on this figure is the range of ionic bondlengths spanned by the Badger's rule calculation.

The pure electronic transition moment for ionisation from the A state is manifestly large. A corresponding Franck Condon calculation on the A←X system revealed that the Franck Condon factor for the intense (0-0) band was ≃ 0.1. We can therefore expect vibronic transitions with Franck Condon factors > 0.1 to give rise to strong ionising transitions. For most of the range of bondlengths spanned by the estimations, Franck Condon factors for the $v_+ = 0 \leftarrow v_A = 0$ transition fall into the "strong" category. Only when r_{ion} > 2.66 Å does the zero point Franck Condon factor become weak by our classification. However, the ionic bondlength is unlikely to be so long. With such large values of r_{ion}, it is not possible to reproduce the approximate intensity ratio of the two direct channels observed in Figure 6.8, whatever vibrational quantum numbers are assigned to the two thresholds. Hence the hypothesis that $v_+ = 0$ should be observable from the zero point vibrational level of the A state appears to be valid.

A more precise estimate of the ion bondlength could be made by measuring the relative intensities of the $v_+ = 0 \leftarrow v_A = 1$ and $v_+ = 1 \leftarrow v_A = 1$ direct ionisation channels from Figure 6.8. Unfortunately, the rich autoionising structure obscures the true magnitude of the former channel. However, there does appear to be a strong propensity for $\Delta v = 0$ ionisation, suggesting that the bondlengths in the A

Figure 6.9 : Franck Condon factors for the CuAg $v_+ = 0 \leftarrow v_A = 0$ transition

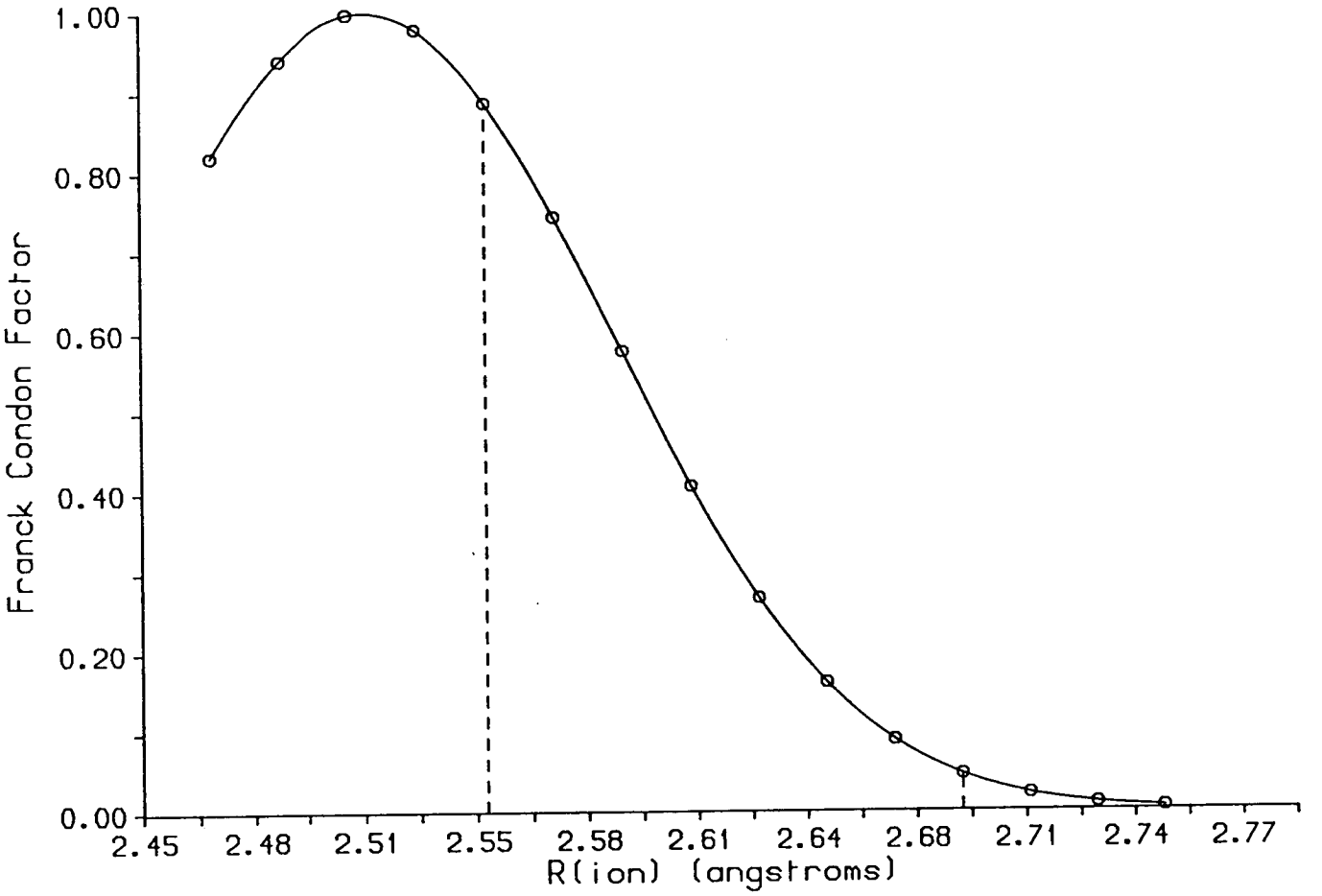

state and ion ground state may be quite similar.

It remains to explain the rather perplexing autoionisation structure lying between the two direct thresholds in Figure 6.8. A regular progression of apparent doublets may be picked out, beginning just above the $v_+ = 0$ threshold. These become hard to discern from the direct channel at higher wavenumber. It should be noted that the discontinuity in signal midway between the two thresholds was an artifact of the frequency doubling efficiency, and was not observed in other scans of the same region. The discrete resonances are due to vibrationally-excited Rydberg states converging to $v_+ = 1$, which autoionise into the $v_+ = 0$ electron ion continuum. There are close parallels between the structure observed in Figure 6.8 and observations of vibrational autoionisation in the two colour ionisation of the DABCO molecule. [32] Some of the autoionising resonances are so strong that they dominate the direct ionisation channel. This might be expected from the favourable Franck Condon factors for the transition $v_+ = 1 \leftarrow v_A = 1$. Efficient vibrational autoionisation occurs with the loss of one quantum of vibrational energy to the outgoing electron. An energy level schematic of the process taking place is shown in Figure 6.10. Autoionising transitions involving the loss of more than one vibrational quantum can, in principle, occur. However, the relatively poor Franck Condon factors for excitation of ion vibrational states higher than $v_+ = 1$ from $v_A = 1$, coupled with their lower efficiency of autoionisation into the $v_+ = 0$ continuum, make these channels less favoured.

Autoionising molecular Rydberg states should exhibit rotational structure, provided that the autoionising lifetime is not so short that features are excessively broadened. Where the direct channel is reasonably weak, it should be possible to

Figure 6.10 : Vibrational autoionisation schematic

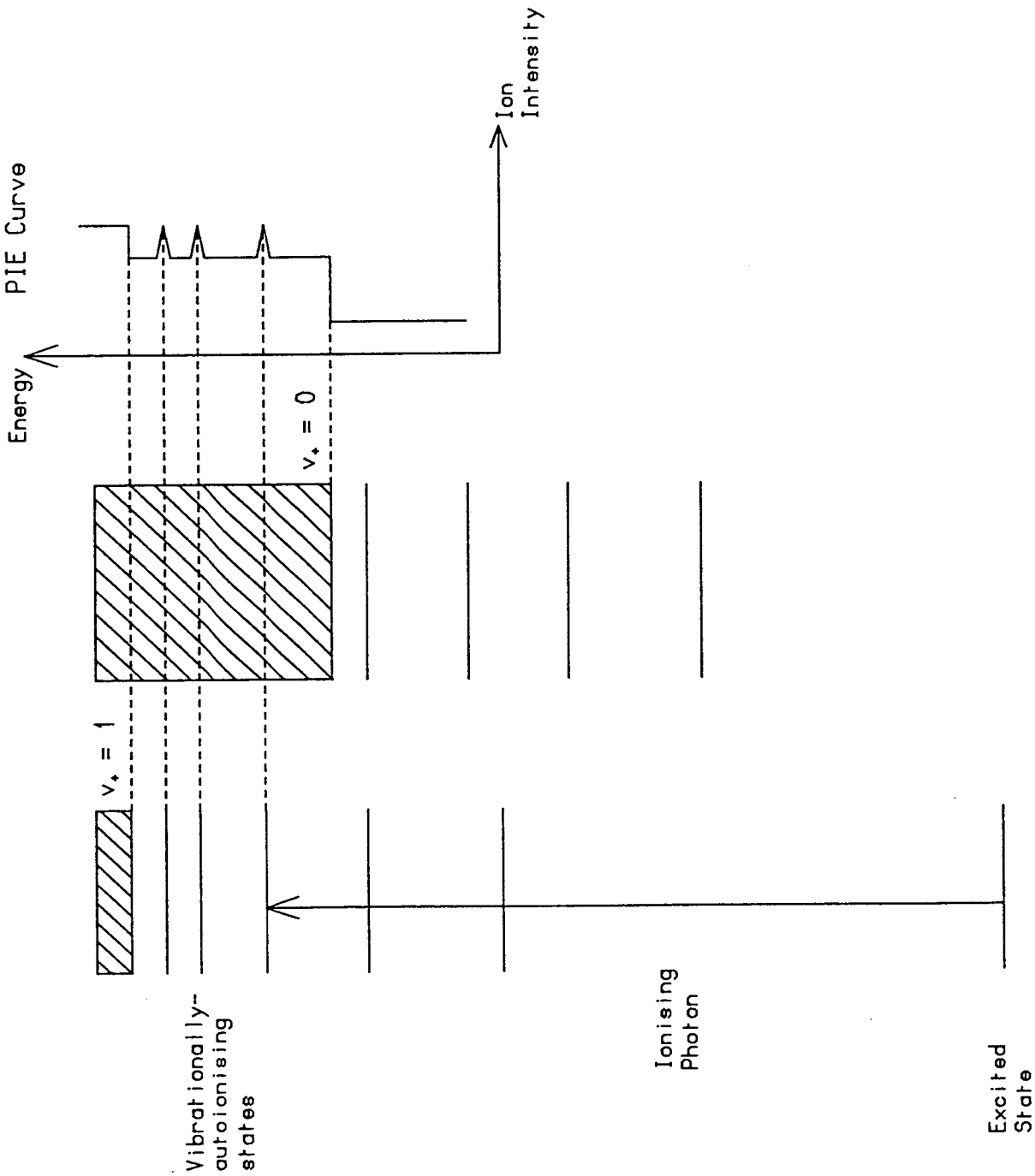

discern this structure. In these experiments, neither laser had a sufficiently narrow bandwidth to afford rotational resolution. The exciting laser (0.4 cm^{-1} bandwidth) overlapped several (J = 4-10) rovibronic transitions in the R bandhead of the A←X system. The observed doublets could arise from the operation of the $\Delta J = \pm 1$ selection rule for transitions from the levels J_A = 4-10 to an autoionising state with $\Omega = 0$. Alternatively, they may arise from two distinct and nearly-overlapping Rydberg series. However, in this case the individual components of the doublets would be rather too narrow to be complete rotational profiles.

Attempts were made to fit the observed band positions to a standard term value expression for Rydberg series, assuming that each doublet was a P-R rotational profile. The electronic term value $T_e(n,\delta)$, for a Rydberg state of principal quantum number n and quantum defect δ, joining on to the $v_+ = 1$ series limit $T_e(v_+ = 1)$ is given by the expression: [21]

$$T_e(n,\delta) = T_e(v_+ = 1) - R_H/(n - \delta)^2, \qquad (6.9)$$

where R_H is the Rydberg constant for $^{63}Cu^{107}Ag$ (= 109737.3 cm^{-1}). The $v_+ = 1$ threshold was equated to $T_e(v_+ = 1)$, and the effective quantum number n^* (= n - δ) calculated for each state. The exact location of the series limit was subject to some uncertainty ($\simeq$ 6 cm^{-1}), owing to the broadening of the threshold. Because this was a significant fraction of the difference in term values ($T_e(n,\delta) - T_e(v_+ = 1)$), the error bounds on n^* were substantial. This precluded a meaningful measurement of δ. At the very least, it was possible to determine n^* for some Rydberg orbitals, the results being presented in Table 6.2.

Table 6.2 : Autoionising Rydberg states of $^{63}Cu^{107}Ag$

Band Design.	T_e/cm^{-1}	n^* a
1	62756.70(50)	26.15(30)
2	62767.76(50)	27.10(34)
3	62779.97(50)	28.28(40)
4	62789.35(50)	29.30(44)
5	62799.58(50)	30.54(49)
6	62803.48(50)	31.06(53)
7	62815.87(50)	32.91(59)

a - using $T_e(v_+ = 1) = 62917.2(37)\ cm^{-1}$

Errors quoted are ± 1σ

6.4.6 The dissociation energy of $CuAg^+$

Having determined what is believed to be the adiabatic ionisation potential of CuAg, it is possible to calculate the dissociation energy of the ionic ground state using a thermochemical cycle method. It must be recognised that there are two distinct and nondegenerate dissociation limits for $CuAg^+$: $Cu^+(^1S_0)$ + $Ag(^2S_{1/2})$ and $Cu(^2S_{1/2})$ + $Ag^+(^1S_0)$ (see Table 6.1). The former limit lies higher in energy by $\simeq$ 0.15 eV, on account of the larger IP of atomic copper. [60]

In the simplest model, and ignoring interactions with d vacancy states, each limit formally gives rise to a $^2\Sigma^+$ state. As the two nuclei are brought together to form the molecular ion, the two states interact through exchange terms. The state derived from the lower limit descends to give the stable ionic ground state, while its higher energy companion becomes the repulsive $s\sigma^*$ state. The interaction between these configurations, and the additional interaction with $d\sigma$ core hole states will be appreciable, so that only a complex multiconfiguration description of the ionic ground state will suffice. Our observation of vibrational structure in the PIE curve is a clear indication that the lower, bonding $^2\Sigma^+$ state is being accessed in the ionisation step. The energy of the $Cu(^2S_{1/2})$ + $Ag^+(^1S_0)$ dissociation limits (relative to $Cu(^2S_{1/2})$ + $Ag(^2S_{1/2})$) was therefore employed in calculating the dissociation energy, in the equation:

$$D_0(CuAg^+) = IP(Ag) + D_0(CuAg) - IP(CuAg), \qquad (6.10)$$

where D_0 refers to dissociation energies measured with respect to zero point levels.

A value of $D_0(CuAg^+)$ = 1.56(10) eV was obtained in this way (see Table 6.1). The principal source of error rests with the relatively imprecise determination of the ground state dissociation energy using effusion mass spectrometry. [61] The dissociation energy of the ion is ≃ 88 % of that of the neutral ground state, a quite substantial fraction. This lends support to the argument that the ionic ground state is a mixture of several configurations, with important contributions from $d^{19}(s\sigma)^2$. Were it dominated by the configuration $d^{20}(s\sigma)^1$, one would expect the ion to be quite weakly bound, as the bond order would be halved upon ionisation. That $CuAg^+$ is bound by more than 1.5 eV demonstrates that $d^{19}(s\sigma)^2$ "$d\sigma$ hole" configurations, which preserve the integrity of the $(s\sigma)^2$ bond, play a major role in determining the bond strength. The large dissociation energy ties in with the observation of a fairly large value of $\Delta G_{3/2}$, indicating that the force constant in the ground state of the ion is moderately strong.

The observation of intense, direct ionisation to a state of mixed $d^{19}(s\sigma)^2$ + $d^{20}(s\sigma)^1$ parentage reinforces the view that the A state is also a mixed state. Direct ionisation proceeds with ejection of a largely $s\sigma^*$ electron, with preservation of the d hole character.

6.5 Threshold photoionisation spectroscopy of Cu_2

The low-lying electronically-excited (A, B and C) states of the dicopper molecule have been the subject of extensive spectroscopic investigations in recent years. [1] In that respect, they are suitable candidates as the intermediate states in TIS measurements of the ionisation potential of Cu_2. However, spectral interpretation has been beset by conflicting evidence over the electronic

configurations which contribute to the A, B and C excited states. The ion ground state may not be accessible in single photon excitation from some of these states, and the adiabatic IP not amenable to measurement. In such cases, TIS has greater utility in elucidating electronic autoionisation processes which occur in the region beyond threshold.

A series of TIS experiments on copper dimer was planned with twofold aims. Firstly, to extract the adiabatic IP of Cu_2 as part of the ongoing study of Group 1b clusters. Secondly, to probe electronic autoionisation in the post-threshold region, with a view to revealing the configurations in the neutral excited states. The remainder of Section 6.5 is concerned with the very first of these experiments, namely threshold ionisation spectroscopy on copper dimer *via* the lowest-lying singlet excited state, $A(0_u^+)$. Before examining the results, some background preamble on the nature of the A state and ionic ground state, as well as independent measurements of the IP is deemed appropriate.

Several groups have examined the low-lying $A(0_u^+)$, $B(0_u^+)$ and $C(1_u)$ states of the dicopper molecule in the gas phase. [62]- [68] Foremost amongst these is a mass-resolved R2PI study of all three systems by Cartwright. [62] His analysis remains the most complete and wide-ranging of all work in this field.

The $A(0_u^+)$ state is envisaged as being the $\Omega = 0$ component of a $^3\pi_u$ state correlating with $^2D + {}^2S$ limits. A pure $^3\pi_u \leftarrow {}^1\Sigma_g^+$ transition is only allowed in Hund's case (c), and would not give rise to the observed short radiative lifetime for the A state of $\simeq$ 115 ns ($v_A = 0$). [67] Configuration mixing with a deeply-descending "intruder" state is believed to be mainly responsible for the

rapid decay. The origins of the $\Omega = 0$ intruder state are not clear. It is possibly derived from the higher-lying ^2P (4p) + ^2S limits, or alternatively from the ion pair limits $Cu^+(^1S_0)$ + $Cu^-(^1S_0)$. In molecular orbital terms, the A state possesses character from the d vacancy configuration:

$$3d^{16}(3d\pi_g^*)^3\ (4s\sigma_g)^2(4s\sigma_u^*)^1,$$

with some extraneous character mixed in from the intruding state. If the d hole configuration dominates the A state, one would not expect to see a strong direct ionisation channel to the ground state of the ion, unless it too has appreciable contributions from d hole configurations.

The first accurate measurement of the ionisation potential of Cu_2 was made by Powers *et al.* in 1983. [4] The fluence-dependence method was initially employed to bracket the copper dimer IP in the range 7.74-7.90 eV. However, in the course of their studies on several ultraviolet band systems using one colour R2PI spectroscopy, a sharp cut-off was observed at the red end of the lowest-lying vibronic progressions. Since the excitation energy of this lowest observed band was known accurately, the ionisation potential could be calculated as lying between twice the photon energies required to excite the "cut-off" band and that lying immediately below it (observed independently by two colour R2PI). After correcting for the static field in the TOFMS ion source, an ionisation potential of 7.894(15) eV was obtained. The abrupt termination of the progression in the one colour R2PI spectrum suggests that the measured IP was the adiabatic value, and not a vertical ionisation threshold.

Our attempts to verify and refine this measurement have been somewhat

overshadowed by the pre-emptive publication of some highly elegant and convincing ES-PES work by SHW. [15] Using the $J(0_u^+)$ state of Cu_2 as the resonant intermediate state, ES-PE spectra were recorded which showed an extensive and entirely non-Franck Condon progression spanning 80 vibrational levels. In addition, two much sharper sets of peaks were observed about 1.1-1.2 eV above the origin of this progression. The long progression is assigned to vibrational structure in the $^2\Sigma_g^+$ ion ground state, terminating abruptly on the $v_+=0$ level. From this, a refined adiabatic IP of 7.899(7) eV was obtained. The observed non-Franck Condon behaviour arises from the excitation of a dissociative autoionising state from the J state.

In a one colour R2PI study using line-narrowed radiation, Butler [69] obtained rotationally-resolved spectra of the J←X transition and found the upper state bondlength to be contracted somewhat with respect to the ground state. This observation, coupled with the large vibrational frequency of the J state (ω_e = 288.4 cm^{-1}), suggested that excitation of a non-bonding or antibonding electron to a bonding orbital was taking place. Butler has argued that the electronic configuration of the J state is:

$$3d^{16}(3d\pi_g^*)^3\ (4s\sigma_g)^2\ (4p\pi_u)^1$$

and SHW concur with this assignment. In the ES-PES study, a second electronic promotion takes place from the J state, exciting the dissociative autoionising state, which lies in the ionisation continuum and is therefore unstable with respect to both dissociation and autoionisation. The most obvious candidate for the autoionising state is that formed by $4s\sigma^*$←$4s\sigma$ promotion from the J state,

since this avoids the creation of two d holes and disrupts the sσ bond. Excitation thus creates the following configuration:

$d^{16}(d\pi_g^*)^3\ (s\sigma_g)^1(s\sigma_u^*)^1\ (4p\pi_u)^1$.

Autoionisation takes place by ejection of one of the highest-lying electrons accompanied by relaxation of the other into the core to generate the ionic ground state configuration $d^{20}\ (s\sigma_g)^1$. Had the doubly excited state been created by a second promotion out of the d cores, the relaxation of a single electron would be incapable of generating the ion ground state. The doubly excited repulsive Cu_2^{**} state undergoes dissociative motion on a timescale comparable to that of electron ejection. Thus a very wide portion of the $^2\Sigma_g^+$ ion potential surface is sampled during autoionisation, leading to a highly extended vibrational progression in the photoelectron spectrum. There is tentative evidence in the ES-PE spectrum for the formation of excited copper atoms ($3d^9 4s^1 4p^1$) from the dissociation of the doubly excited state.

The two sharp sets of peaks observed in the ES-PE spectra at higher ion energy are due to direct ionisation involving the ejection of the $4p\pi_u$ electron, leaving an excited core configuration $d^{19}\ (s\sigma_g)^2$. The proximity of d vacancy excited states to the ionic ground state points to an appreciable admixture of d core hole character into the ground state wavefunction.

Having examined the existing experimental evidence for dicopper autoionisation and IP measurements, the two colour TIS work is now addressed.

6.5.1 Zero-field threshold ionisation measurements on Cu_2

Prior to recording a PIE curve, the A←X system was examined under rovibronic resolution using a line-narrowed dye laser for excitation and 193 nm radiation for ionisation (see Chapter 5). This enabled the R-branch bandheads to be located for excitation in the TIS work. A typical R2PI spectrum of the (1-0) band is shown in Figure 6.11.

The experimental arrangement for the TIS work on Cu_2 was identical to that used for CuAg. The exciting dye laser (PDL-2, Coumarin 102) was tuned to an R-branch bandhead, overlapping several rovibronic lines, and the ionising laser scanned to generate the PIE curve. Figure 6.12 shows the threshold curve obtained when the (1-0) band was excited, with a delay of $\simeq$ 60ns between the ionising laser and high voltage pulses.

A weak threshold was observed, from which the ionisation potential was determined to be 7.90426(42) eV, in excellent agreement with the result of SHW (see Table 6.3). The shape of the PIE curve in the immediate post-threshold region was markedly different from that observed for CuAg. The sharp rise in signal just beyond threshold appears to be due to autoionisation, as the signal dropped down again almost to the baseline within 100 cm^{-1} of the threshold. Power normalisation procedures were checked, and it was verified that the shape of the curve was not an artifact of the laser power.

Although this result represents only the first experiment in what will hopefully be an extensive study, some useful information can be extracted. Firstly, the dissociation energy of the ion may be estimated using the thermochemical cycle:

Figure 6.11 : Rotationally-resolved R2PI spectrum of the (1-0) band of the A←X system of $^{63}Cu^{63}Cu$

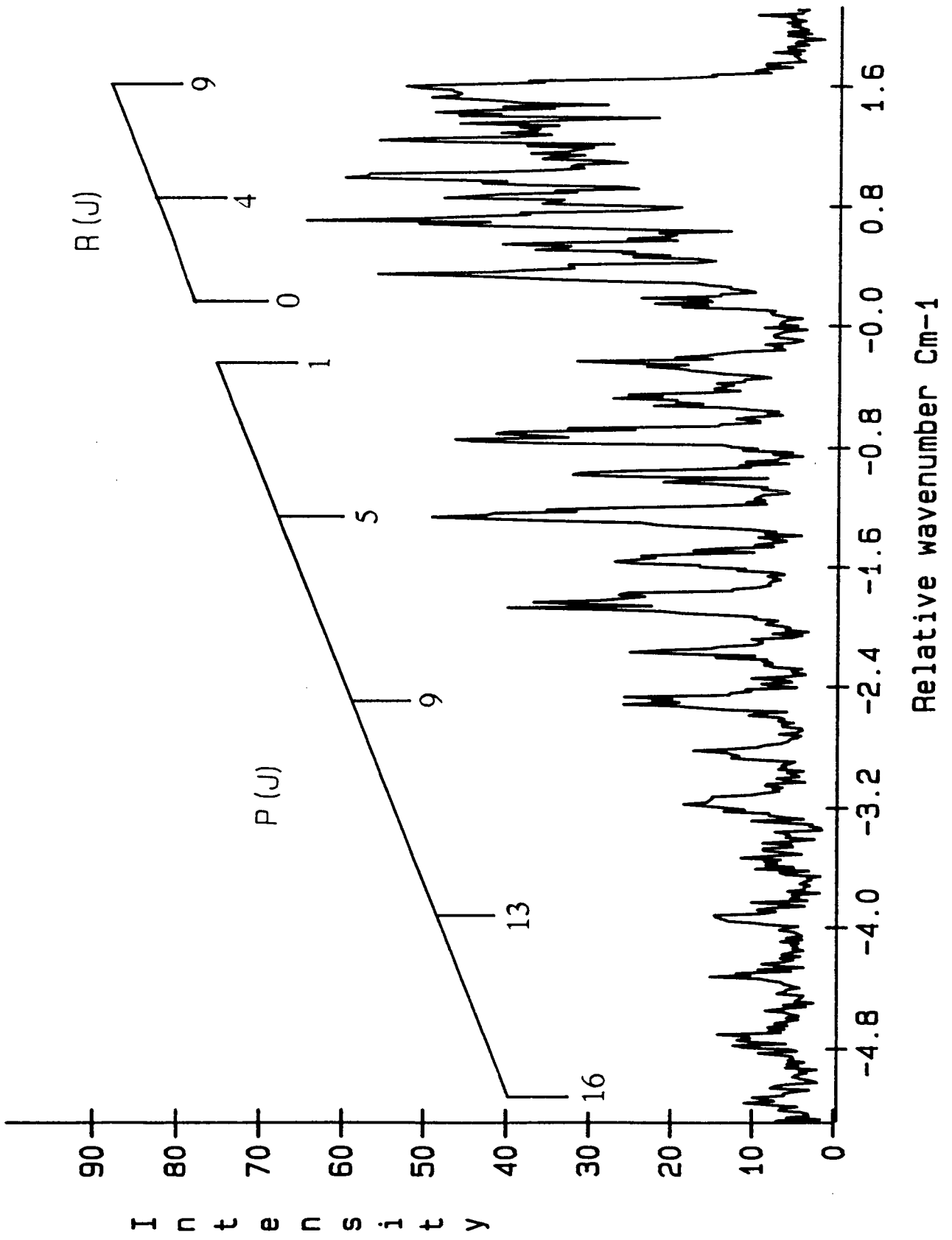

Figure 6.12 : PIE curve for $^{63}Cu^{63}Cu$, ionising from $v_A = 1$ in zero static field ($\Delta t = 60$ ns)

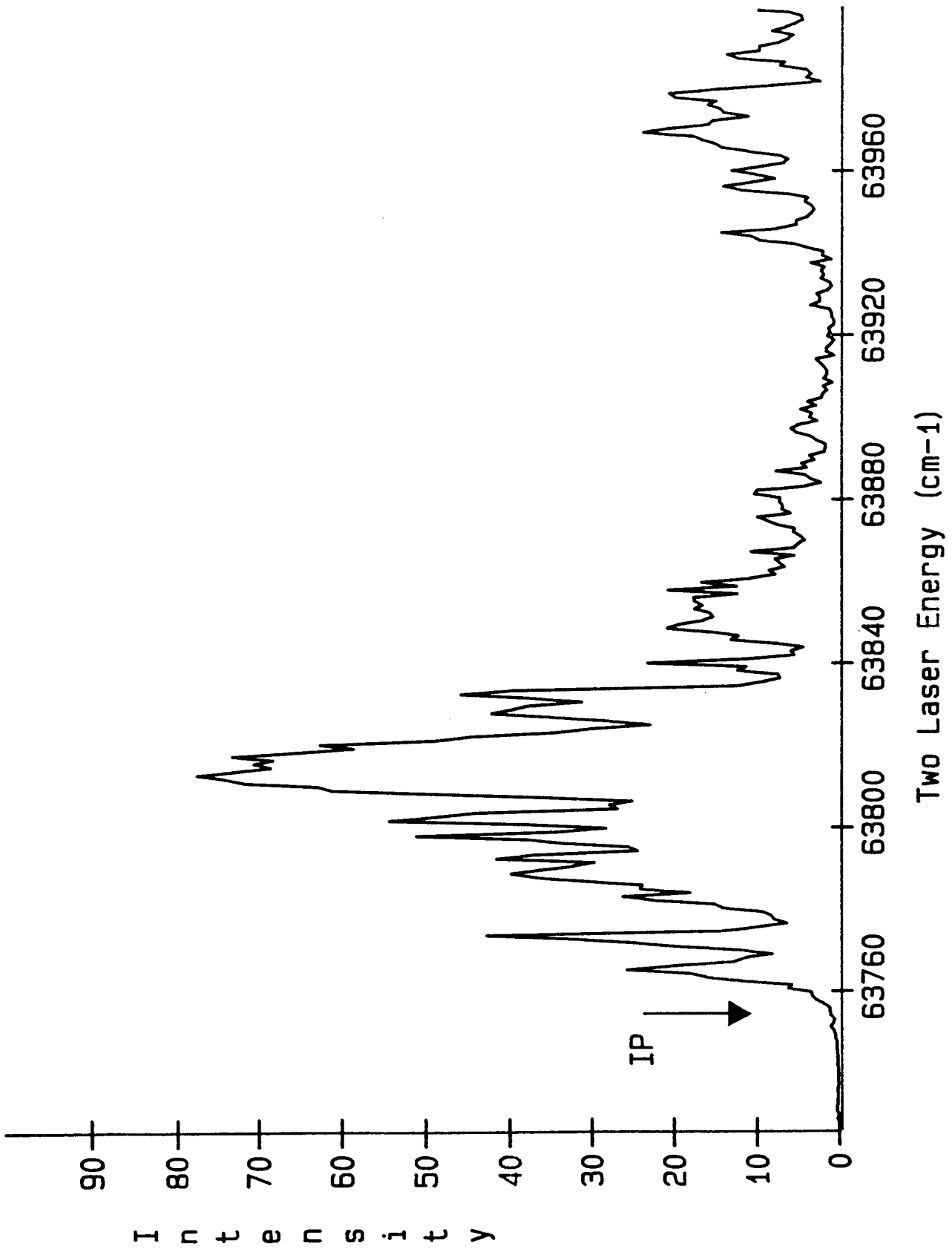

$$D_0(Cu_2^+) = IP(Cu) + D_0(Cu_2) - IP(Cu_2).$$

Dispersed fluorescence studies on Cu_2 [63] have yielded an accurate and precise measurement of $D_0(Cu_2)$, enabling the dissociation energy of the ion to be calculated with similar small error. A value of $D_0(Cu_2^+) = 1.83(08)$ eV is obtained, which is $\simeq$ 91 % of the corresponding value for the neutral ground state (see Table 6.3). As in the case of CuAg, the substantial binding energy suggests that $d^{19}(s\sigma)^2$ configurations, which are strongly bonding, are intimately involved in a description of the ionic ground state. In the ES-PES study, the observation of low-lying $d\pi$ core hole states further reinforces the view that $d\sigma$ states with intact $(s\sigma)^2$ orbitals are heavily involved.

Initially striking in the PIE curve shown in Figure 6.12 is the low intensity of the direct ionisation channel. Two possible explanations may be advanced. Firstly, an electronically-efficient direct channel exists, but the $v_+=0$ continuum is suppressed because of poor Franck Condon factors for the $v_+=0 \leftarrow v_A=1$ transition. Alternatively, the channel may be weak because the configurations which are mixed to form the ionic ground state are dissimilar to those which give rise to the A state. We examine each of these hypotheses in turn.

Franck Condon factors for the $v_+=0 \leftarrow v_A=1$ transition were calculated using the well-established spectroscopic constants of the A state and those of the ion ground state from the ES-PES study. Results for a variety of ionic bondlengths are presented in Figure 6.13. Using Badger's rule, SHW estimated the bondlength in the ionic ground state to lie in the range 2.25-2.45 Å. These limits are plotted as dashed lines in Figure 6.13. Where the A state and ionic ground

Table 6.3 : Threshold ionisation measurements on $^{63}Cu^{63}Cu$

A←X Band	$\hbar\omega_1$ cm^{-1}	$\hbar\omega_2$ cm^{-1}	$\hbar(\omega_1 + \omega_2)$ cm^{-1}
(1-0)	20587.76(50)	43164.3(34)	63752.1(34)

$IP(Cu_2) = 63752.1(34)\ cm^{-1} \equiv 7.90426(42)\ eV$

$D_0(Cu_2^+)^a = 1.83(08)\ eV$

a - using $D_0(Cu_2) = 2.01(08)$ eV from Ref. [63] and IP(Cu) from Ref. [60]

Errors quoted are ± 1σ

Figure 6.13 : Franck Condon factors for the Cu_2 $v_+ = 0,1 \leftarrow v_A = 1$ transitions

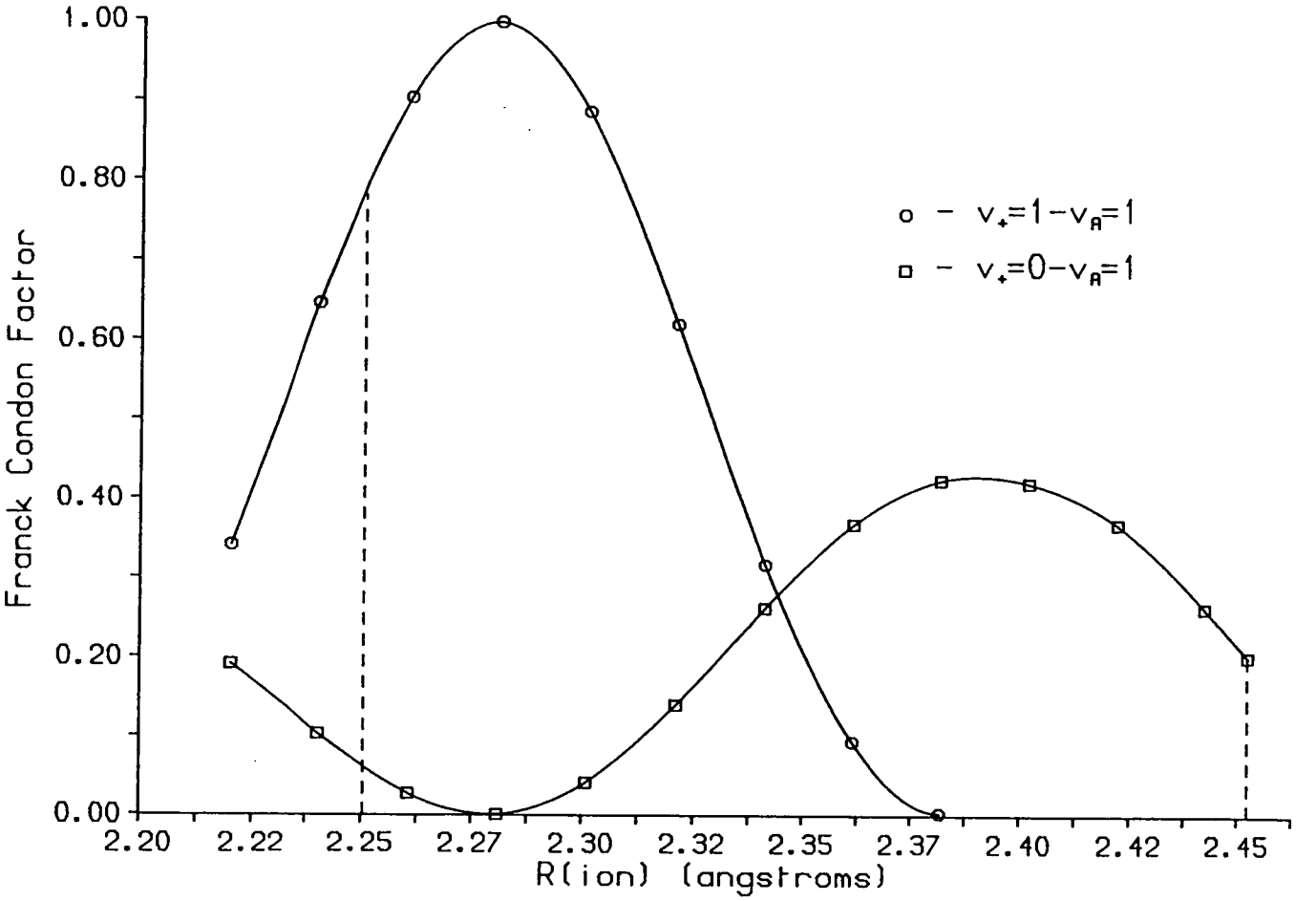

state bondlengths are similar, the $v_+=0$ channel is certainly suppressed in accordance with the $\Delta v = 0$ propensity rule. However, in such cases the $v_+=1$ channel would be very strong, and there is no evidence in the PIE curve for the opening of such an intense channel at $T_e(v_+=1), \simeq 190\ cm^{-1}$ beyond threshold. From the Franck Condon analysis, there do not appear to be any ion bondlengths, within a reasonable range dictated by Badger's rule, which would lead to very weak thresholds for both $v_+=0$ and $v_+=1$. Thus it seems fair to conclude that the low intensity of the direct ionisation channel has its origins in electronic, as opposed to Franck Condon effects.

We now turn to the possible electronic origin for the weak direct channel, and how this may validate Cartwright's model of the A state. If this state is indeed formed largely by admixture of an intruder state into the configuration:

$$3d^{16}(3d\pi_g^*)^3\ (4s\sigma_g)^2(4s\sigma_u^*)^1,$$

it will possess little $d\sigma$ hole character. Conversely, the ionic ground state appears to have large contributions from $d\sigma$ vacancy configurations, as described above. Direct ionisation from the A state, involving ejection of an electron from the σ^* orbital, will leave an ion with a $d\pi$,as opposed to $d\sigma$ hole. We might therefore expect a weak direct ionisation mechanism to prevail for post-threshold energies up to 1.1-1.2 eV, where the $d\pi$ hole states are known to lie.

The origin of the broad and partially-structured autoionisation resonances in the post-threshold region is not clear. Dissociative autoionising states of the type invoked by SHW may be partly responsible, a schematic of this process being shown in Figure 6.14. The unstable autoionising state, accessed from the A state

Figure 6.14 : Electronic autoionisation schematic

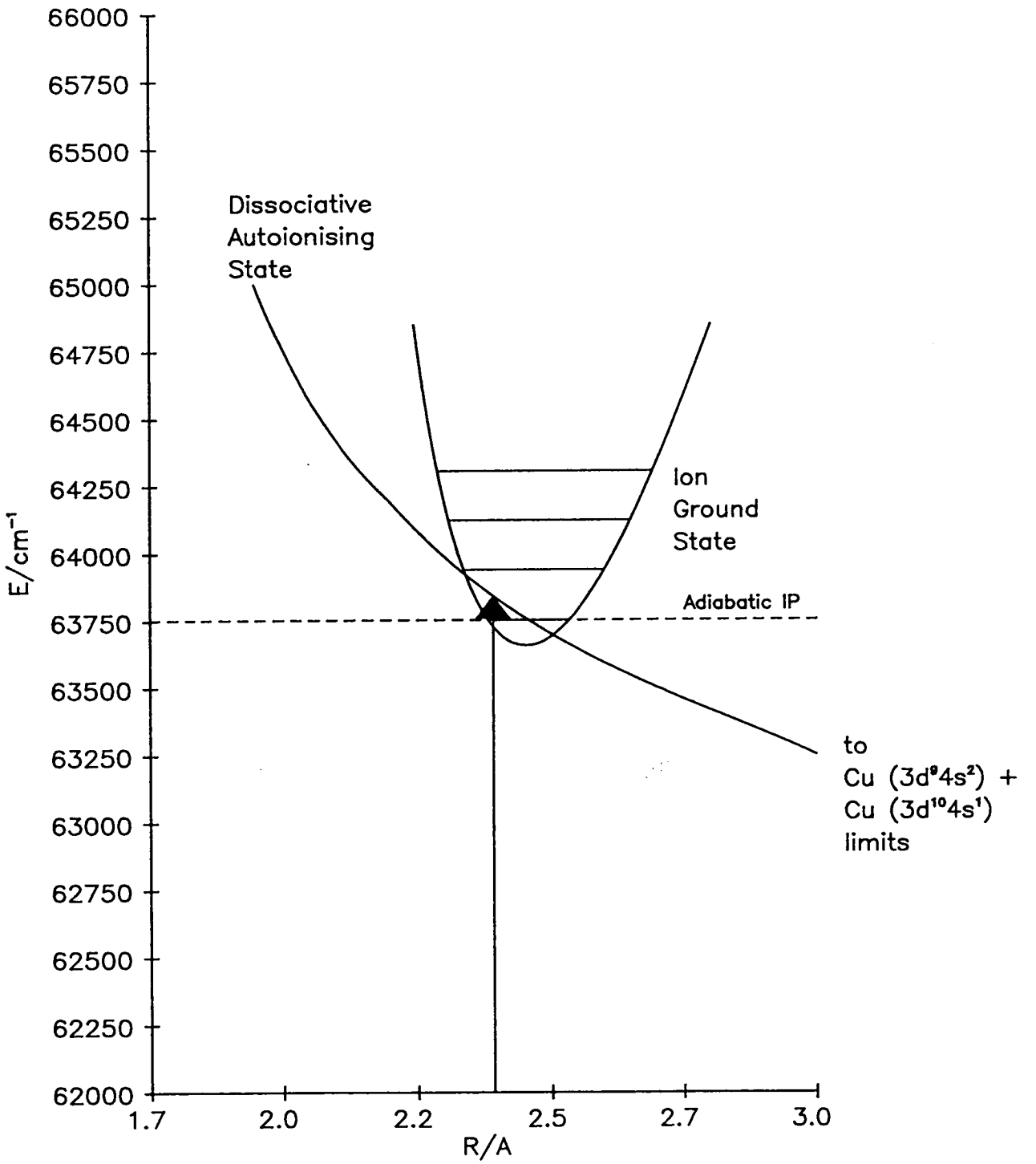

by a $4p\pi \leftarrow 4p\sigma$ promotion, cuts through the vicinity of the ionic zero point vibrational level on its way to dissociation to excited atomic limits. The shape of the PIE curve will be determined by the overlap of wavefunctions for the autoionising state and those for vibrational levels of the ion ground state. This is only one example of an autoionisation process, and there are numerous other doubly-excited states which might be involved. Some may be bound, and are responsible for the sharp features. With the very limited data available, continued speculation on these phenomena is not warranted. We may at least conclude that the adiabatic IP of dicopper has been measured, and in doing so some electronic autoionisation observed. To what extent the suppression of the direct channel reflects the differences between d hole configurations in the A state and the ion is a moot point at present. The resolution of this matter must await future TIS experiments, using other possible intermediate states.

References

[1] Morse M. D., Chem. Rev., **86**, p 1049, (1986)

[2] Schumacher E., Kappes M., Marti K., Radi P., Schär M., Schmidhalter B., Ber. Buns. Phys. Chem., **88**, p 220, (1984)

[3] Kappes M. M., Schär M., Radi P., Schumacher E., J. Chem. Phys., **84**, p 1863, (1986)

[4] Powers D. E., Hansen S. G., Geusic M. E., Michalopolous D. L., Smalley R. E., J. Chem. Phys., **78**, p 2866, (1983)

[5] Rohlfing E. A., Cox D. M., Kaldor A., J. Phys. Chem., **88**, p 4497, (1984)

[6] Rohlfing E. A., Cox D. M., Kaldor A., Johnson K. H., J. Chem. Phys., **81**, p 3846, (1984)

[7] Whetten R. L., Zakin M. R., Cox D. M., Trevor D. J., Kaldor A., J. Chem. Phys., **85**, p 1697, (1986)

[8] Wood D. M., Phys. Rev. Lett., **46**, p 749, (1981)

[9] Reisler H., Wittig C., Adv. Chem. Phys., **60**, p 1, (1985)

[10] Kimura K., Adv. Chem. Phys., **60**, p 161, (1985)

[11] Meek J. T., Jones R. K., Reilly J. P., J. Chem. Phys., **73**, p 3503, (1980)

[12] Compton R. N., Miller J. C., Carter A. E., Kruit P., Chem. Phys. Lett., **71**, p 87, (1980)

[13] Achiba Y., Hiraya A., Kimura K., J. Chem. Phys., **80**, p 6047, (1984)

[14] O'Halloran M. A., Pratt S. T., Dehmer P. M., Dehmer J. L., J. Chem. Phys., **87**, p 3288, (1987)

[15] Sappey A. D., Harrington J. E., Weisshaar J. C., J. Chem. Phys., **91**, p 3854, (1989)

[16] Chewter L. A., Sander M., Muller-Dethlefs K., Schlag E. W., J. Chem. Phys., **86**, p 4737, (1984)

[17] Muller-Dethlefs K., Sander M., Schlag E. W., Z. Naturforsch Teil A, **39**, p 1089, (1984)

[18] Reiser G., Habenicht W., Muller-Dethlefs K., Schlag E. W., Chem. Phys. Lett., **152**, p 119, (1988)

[19] Tonkyn R. G., Winniczek J. W., White M. G., Chem. Phys. Lett., **164**, p 137, (1989)

[20] Gantefor G. F., Cox D. M., Kaldor A., *5th. Intl. Symp. on small particles and inorganic clusters*, Konstanz, 1990.

[21] Broyer M., Chevaleyre J., Delacretaz G., Martin S., Wöste L., Chem. Phys. Lett., **99**, p 206, (1983)

[22] Leutwyler S., Herrmann A., Wöste L., Schumacher E., Chem. Phys., **48**, p 253, (1980)

[23] Smith M. A., Hager J. W., Wallace S. C., J. Chem. Phys., **80**, p 3097, (1984)

[24] Duncan M. A., Dietz T. G., Smalley R. E., J. Chem. Phys., **75**, p 2118, (1981)

[25] Lemaire J., Dimicoli I., Piuzzi F., Botter R., Chem. Phys., **115**, p 119, (1987)

[26] Morse M. D., *Adv. Metal and Semiconductor Clusters. Vol. I :Spectry. and Dynamics*, (to be published), .

[27] Morse M. D., Hopkins J. B., Langridge-Smith P. R. R., Smalley R. E., J. Chem. Phys., **79**, p 5316, (1983)

[28] Cheng P. Y., Duncan M. A., Chem. Phys. Lett., **152**, p 341, (1988)
[29] Berry R. S., J. Chem. Phys., **45**, p 1228, (1966)
[30] Brandsen B. H., Joachain C. J., *Physics of Atoms and Molecules*, Longman, London, 1983.
[31] Guyon P. M., Baer T., Nenner I., J. Chem. Phys., **78**, p 3665, (1983)
[32] Fujii M., Ebata T., Mikami N., Ito M., Chem. Phys. Lett., **101**, p 578, (1983)
[33] Eyler E. E., Pipkin F. M., Phys. Rev. A, **27**, p 2462, (1983)
[34] Jaffe S. M., Kachru R., van Linden van den Heuvell H. B., Gallagher T. F., Phys. Rev. A, **32**, p 1480, (1985)
[35] Bordas C., Brevet P., Broyer M., Chevaleyre J., Labastie P., Europhys. Lett., **3**, p 789, (1987)
[36] Mahon C. R., Janik G. R., Gallagher T. F., *private Communication*, ,
[37] Berkowitz J., Ruscic B., J. Chem. Phys., **93**, p 1741, (1990)
[38] Atkins P. W., *Molecular Quantum Mechanics*, 2nd. edition, Oxford University Press, Oxford, 1983.
[39] Robertson H. P., Dewey J. M., Phys. Rev., **31**, p 973, (1928)
[40] Lanczos C., Z. Physik, **62**, p 518, (1930)
[41] Callender C. L., Hackett P. A., Rayner D. M., J. Opt. Soc. Am. B, **5**, p 614, (1988)
[42] Rayner D. M., Mitchell S. A., Bourne O. L., Hackett P. A., J. Opt. Soc. Am. B, **4**, p 900, (1987)
[43] Halliday D., Resnick R., *Physics*, 3rd. edition, John Wiley, New York, 1978.
[44] Hopkins J. B., Langridge-Smith P. R. R., Morse M. D., Smalley R. E., *unpublished results*, ,
[45] Lipert R. J., Colson S. D., J. Chem. Phys., **92**, p 3240, (1990)
[46] Gandhi S. R., Bernstein R. B., J. Chem. Phys., **93**, p 4024, (1990)
[47] Adams T. E., Morrison R. J. S., Grant E. R., Rev. Sci. Instr., **51**, p 141, (1980)
[48] Metcalf H., Nature, **284**, p 127, (1980)
[49] Antonov V. S., Letokhov V. S., *Laser Analytical Spectrochemistry (ed. Letokhov V. S.)*, Adam Hilger, Bristol, 1986.
[50] Long S. R., Meek J. T., Reilly J. P., J. Chem. Phys., **79**, p 3206, (1983)
[51] Cooper D. E., Frueholz R. P., Klimcak C. M., Wessel J. E., J. Phys. Chem., **86**, p 4892, (1982)
[52] Meek J. T., Long S. R., Reilly J. P., J. Phys. Chem., **86**, p 2809, (1982)
[53] Parmenter C. S., Adv. Chem. Phys., **22**, p 365, (1972)
[54] Beck S. M., Powers D. E., Hopkins J. B., Smalley R. E., J. Chem. Phys., **73**, p 2019, (1980)
[55] Hopkins J. B., Powers D. E. Smalley R. E., J. Chem. Phys., **72**, p 5039, (1980)
[56] Miyoshi E., Tatewaki H., Nakamura T., J. Chem. Phys., **78**, p 815, (1983)
[57] Badger R. M., J. Chem. Phys., **2**, p 128, (1934)
[58] Badger R. M., J. Chem. Phys., **3**, p 710, (1935)
[59] Weisshaar J. C., J. Chem. Phys., **90**, p 1429, (1989)
[60] Moore C. E., *Atomic Energy Levels*, NBS Circular 467. Vols. II and III, Washington D. C., 1971.
[61] Ackerman M., Stafford F. E., Drowart J., J. Chem. Phys., **33**, p 1784,

(1960)
[62] Cartwright P. C., *Ph. D. thesis*, University of Edinburgh, 1989.
[63] Rohlfing E. A., Valentini J. J., J. Chem. Phys., **84**, p 6560, (1986)
[64] Lochet J., J. Phys. B, **11**, p L55, (1978)
[65] Gole J. L., English J. H., Bondybey, J. Phys. Chem., **86**, p 2560, (1982)
[66] Powers D. E., Hansen S. G., Geusic M. E., Puiu A. C.,Hopkins J. B., Dietz T. G., Duncan M. A., Langridge-Smith P. R. R., Smalley R. E., J. Phys. Chem., **86**, p 2556, (1982)
[67] Bondybey V. E., Schwartz G. P., English J. H., J. Chem. Phys., **78**, p 11, (1983)
[68] McCaffrey J. G., Bennett R. R., Morse M. D., Breckenridge W. H., J. Chem. Phys., **91**, p 92, (1989)
[69] Butler A. M., *Ph. D. thesis*, University of Edinburgh, 1989.

Chapter 7
Laser Induced Fluorescence Spectroscopy of the $A(0_u^+) \leftarrow X(^1\Sigma_g^+)$ System in Ag_2

7.1 Introduction

Interest in the spectroscopy and electronic structure of the silver dimer molecule stems from a number of sources. Enhanced catalytic activity is a well-known property of small metal particles and is is exemplified in the role played by silver atom clusters in the development of photographic latent images. [1] [2] One can argue that silver dimer represents the simplest, as well as the smallest, cluster of silver, with properties resembling those of dicopper. Like dicopper, the bonding in the ground state of silver dimer is expected to be dominated by overlap of the s atomic orbitals, with the filled d orbitals playing a subordinate role. Atomic silver has the electronic configuration [Kr] $4d^{10}$ $5s^1$. The $4d^9 5s^2 \leftarrow 4d^{10} 5s^1$ promotion energy is 3.97 eV [3], a clear illustration of the high stability of a fully-occupied d shell. There thus appears to be some justification in describing atomic silver as a "pseudo-alkali", since it possesses a stable, fully-occupied core with a single s valence electron. As one would therefore expect, theory predicts a closed shell ground state for silver dimer. [4]- [21] Two fully-occupied $4d^{10}$ cores interact repulsively, slightly weakening the $5s\sigma_g^2$ bond formed by overlap of the 5s atomic orbitals. This state dissociates to two ground state ($^2S_{1/2}$) silver atoms. This closed shell ground electronic configuration, lacking the complications of non-zero electronic and spin degeneracies ($^1\Sigma_g^+$ term), makes disilver an attractive candidate for *ab initio* studies. Furthermore, since the d

cores have only a limited influence on bonding, they can be treated outside the valence space, a valuable simplification.

Interest in Ag_2 is heightened by the significance of relativistic effects in the molecule. In highly-charged atoms, s orbital wavefunctions which penetrate the region of the nucleus become energetically stabilised and radially contracted (see Chapter 5). These effects are reflected in a reduction in bond length and a stiffening in the force constant in those diatomic molecules where $s\sigma$ bonding contributes appreciably. Late second row transition metals such as silver ($Z=47$) are sufficiently highly charged to exhibit these effects to a marked degree. Such effects will be particularly noticeable when the diatomic bond is formed primarily from contracted s orbitals, as is the case with disilver. Thus a comparison of experimental bond lengths with those calculated using a non relativistic theoretical framework should yield an indication of the extent of the relativistic contribution to bonding. In a similar fashion, the accuracy of the relativistic theoretical treatments themselves can be assessed.

Some experimental work on silver dimer has been reported, although its bearing on the nature of the bonding in the molecule is somewhat limited. The first electronic spectrum of Ag_2 was obtained by Ruamps [23] in 1954, who recorded dispersed emission spectra from silver dimers generated in a King furnace. The observed band system, with origin at 435 nm, was denoted $A\leftarrow X$. Shortly afterwards, Kleman and Lindqvist [24] photographed this system in both absorption and emission, improving the vibrational constants for both the A and X states. A number of other investigators, using King furnace [25]- [28] and electric discharge [29] techniques have extended knowledge of the $A\leftarrow X$ and

ultraviolet band systems of the molecule. Results of the previous studies are summarised in Table 7.1. The vibronic analysis by Kleman and Lindqvist remains the most complete for the A←X system.

All the emission and absorption studies were greatly hampered by isotopic interferences. Silver atom has two isotopes, 107 (51.35 %) and 109 (48.65 %), giving approximate dimer abundance ratios of 1:2:1. The large relative abundance of all these isotopic combinations, the high rotational temperatures of molecules emanating unrelaxed from furnace or discharge sources, and the small rotational constant (ca. 0.05 cm^{-1}) for a heavy second row diatomic such as disilver, all created severe spectral congestion. This confounded any attempts at rotational analysis. Srdanov and Pesic [28] eliminated the isotopic blending problem by using silver enriched with the 107 isotope to greater than 90 %. Some attempt was then made to extract rotational constants from an analysis of the ultraviolet C←X system. However, their results should be treated with extreme caution: the analysis was based on a ground state rotational constant which had been calculated semi-empirically by Brown and Ginter. [26] The known B_e values for the Cu_2 and Au_2 ground states, along with the Morse-Clark formula, [30] [31] were employed to calculate a corresponding value for Ag_2 by interpolation. Since this crude method takes no account of the differing extents of relativistic contraction for the three dimers, nor the differing bonding contributions of core orbitals, its reliability is highly questionable.

Extensive spectroscopic studies of silver dimer isolated in rare gas matrices have been carried out. [3] [32]- [35] Common to all investigations was the observation

Table 7.1 : Spectroscopic constants of the Ag_2 molecule

State	T_e/cm^{-1}	ω_e/cm^{-1}	$\omega_e x_e/cm^{-1}$
$H(0_u^+)$	58273.1	166.7	2.48
$E(0_u^+)$	40159.4	146.2	1.55
$D\ 0_u^+$	39014.5	169.0	1.21
$C\ 1_u\ ^1\Pi_u$	37631.3	171.4	0.91
$B(0_u^+)$	35835.6	152.5	0.88
$A\ 0_u^+$	22996.4	155.3	0.59
$X\ ^1\Sigma_g^+$	0	192.4	0.60

Data from reference [3]
Uncertain assignments in brackets.

of a band system with origin near 390 nm, the blue-shifted matrix analogue of the gas phase A←X system. A magnetic circular dichroism (MCD) study [39] revealed that both states in this system were orbitally non-degenerate. This confirms the ground state assignment as $^1\Sigma_g^+$, and suggests that the A state symmetry is 0_u^+.

While these wide-ranging studies provided some food for thought in the theoretical community, they posed more questions than they answered. Firstly, there was still no unequivocal proof that the carrier of the excitation was actually Ag_2, although the general structure of the electronic spectrum appeared highly characteristic of a diatomic molecule. Secondly, while useful information on transition energies and vibrational constants was obtained, no fully isotopically and rotationally resolved spectroscopy had been performed. Thus no definite assignment of spin multiplicity or state symmetry was possible. Furthermore, lack of knowledge of any bondlengths in silver dimer left theoreticians with little at which to aim.

The advent of the laser vaporisation-supersonic expansion technique opened up new avenues to the experimentalist and revived a somewhat moribund field. In an unpublished study, Hopkins *et al.* [36] used two colour photoionisation spectroscopy with mass resolved photoion detection to confirm that the A←X transition did indeed belong to silver dimer. Unfortunately, the bandwidth of their exciting dye laser was incapable of resolving rotational structure within the vibronic bands. There remained to be performed a definitive rotationally-resolved experiment, enabling a precise determination of the ground state bond length in Ag_2. A recent R2PI study on the A←X system of silver

dimer, similar to the Morse experiment, was performed in our laboratory. [37] A tunable pulsed dye laser excited the (0-0) and (1-0) bands of this system, one photon ionisation from the excited state being accomplished by an ArF excimer laser (193 nm). Analysis of the rotationally-resolved, single isotopomer spectra obtained was limited by the dye laser bandwidth (0.04 cm^{-1}), which was only just adequate for the purpose. This, not surprisingly had a detrimental effect on the precision to which rotational constants could be determined. A further complication arose from an experimental artifact: the effects of timing jitter between the excimer and dye laser output pulses. Since the excited state lifetime, as measured by time-resolved R2PI spectroscopy, appeared short (< 40 ns), the effects of time excursions between the lasers of as much as 15 ns played havoc with signal stability. It was not possible to cure this problem for the duration of these onerous experiments, and the poor signal quality of the spectra had to be accepted. Despite this, some useful information was obtained. At the very least, it was clear that the silver dimer molecule had a $^1\Sigma_g^+$ ground state, as was expected from theory. The A←X transition was confirmed to be a parallel electronic transition ($\Delta\Omega = 0$), since the spectrum showed only P- and R-branches. Also, the rapid reversal of the R-branch bandhead indicated that the bond lengthened substantially upon excitation. Moderately accurate values for the rotational constants in both states were extracted, along with reasonable values for the isotope shifts between each isotopomer.

The purpose of the ring laser LIF study described in this chapter was to obtain a Doppler-limited fluorescence excitation spectrum of jet-cooled silver dimer. Although such a spectrum necessarily contains lines from all three isotopomers,

the rotational constants and isotope shifts from the photoionisation study could be employed to assist in assignment. Since the ring laser LIF system can offer an order of magnitude higher resolution, congestion should be greatly reduced. The accurate rotational constants obtained could then be compared with the many studies reported in the literature.

Most of the recent theoretical studies on disilver have concentrated on providing an accurate description of the ground state. [4]- [21] Several investigators have used effective core potentials (ECPs) or pseudopotentials to reduce the number of electrons in the valence space and thus simplify the calculation. While there may be clear differences in the magnitudes of the molecular parameters calculated, there are no departures from the concensus concerning contributions to bonding in the ground state. The 5s-5s orbital overlap dominates in bond formation, with the fully-occupied 4d cores interacting more weakly and repulsively. The contraction of the nd orbitals as the nuclear charge increases across a period is more pronounced for the 3d than for the 4d series. As Morse observes: [3] $< r_{4s} >/< r_{3d} > = 3.36$ for copper, while $< r_{5s} >/< r_{4d} > = 2.67$ for silver. Relativistic effects, which become important in the late second transition period, lead to a contraction of the ns orbitals, and an expansion of the (n-1)d orbitals (see Chapter 5). The appreciable spatial extension of the 4d orbitals dictates that they should interact more strongly in disilver than do the 3d orbitals in dicopper, although they are too low-lying to influence the valence $s\sigma$ bond appreciably.

Few excited state calculations on disilver have been performed, due to the computational complexity, particularly if the d shell is opened up. Basch [38]

has calculated a bound excited state (T_e = 2.59 eV) consistent with the experimentally observed $A(0_u^+)$ state. This state, which dissociates to $^2P + {}^2S$ excited atom limits, involves the promotion of a $5s\sigma_g$ bonding electron to the corresponding $5s\sigma_u^*$ antibonding orbital. It is expected to have significant contributions from the first ion pair limit. This excitation energy agrees with the results of a semi-empirical spin-orbit study [39], and also with extended Hückel [40] and SCF-Xα [33] calculations. It would appear that the A state is the silver analogue of the well-characterised B state of copper dimer, which involves a $4s\sigma^* \leftarrow 4s\sigma$ promotion, correlating with $^2D + {}^2S$ limits. [41]

7.2 Experimental setup

The molecular beam containing Ag_2 was generated by pulsed laser vaporisation of a silver target rod situated in the flowstream from a pulsed molecular beam valve. The principles of laser vaporisation, plasma quenching and cluster entrainment have been covered in detail in Chapter 2. The molecular beam, upon expansion into vacuum, was interrogated by the output of a cw ring dye laser, crossing the expansion perpendicular to the beam direction. Fluorescence was collected at right angles to the plane of intersection of these beams by an imaging lens-monochromator arrangement, and detected by a photomultiplier tube. Operation of the vaporisation laser, molecular beam valve and detection electronics was in pulsed mode (10 Hz), while the ring dye laser excited the beam continuously. A schematic of the complete experimental setup is shown in Figure 7.1.

Figure 7.1 : Schematic of the molecular beam-ring dye laser apparatus

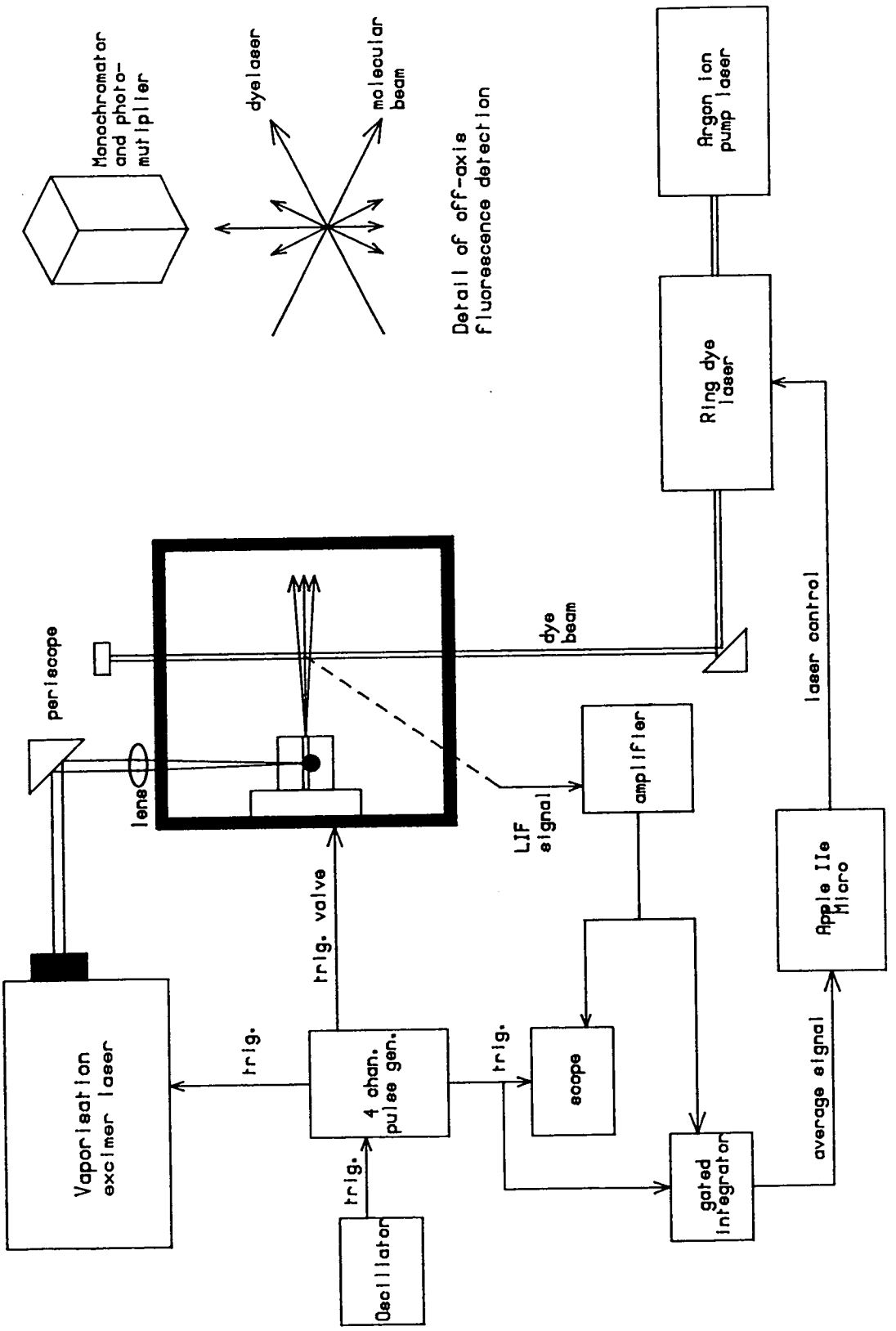

7.2.1 Vacuum system

The vacuum system consisted of a single stainless steel chamber in a six way cross configuration with 8" conflat flanges. The chamber was pumped by a 6" diffusion pump (Varian VHS-6) backed by a two-stage rotary pump (Varian CD-700). The background pressure was typically 10^{-6} mbar, as measured by a Bayard-Alpert type ionisation gauge. The cluster source assembly, comprising the molecular beam valve and faceplate fixture was mounted on a conflat flange which bolted to one of the horizontal arms of the chamber. On the arm directly opposite this one, a perspex flange permitted viewing of the source and target when the vaporisation beam was directed on to it. The vaporisation and dye laser beams were admitted through quartz windows on the other horizontal ports. Atop the chamber, facing the throat of the diffusion pump, was mounted a tube containing the fluorescence collection optical system, mounted on an XY translator.

7.2.2 Cluster source

The cluster source followed the standard Smalley design described in Chapter 3. Three channels were drilled in mutually perpendicular directions into the faceplate which fitted over the molecular beam valve. The rod (nominal 6 mm diameter) was mounted in the vertical off-axis channel. It was rotated and translated during operation by direct shaft coupling to a MicroMo micrometer driven by a d.c. motor. Limit switches were used to restrict the screw travel. A commercial valve (Newport BV100, 500 μm orifice) was used in these experiments. This valve, although of the same type as one employed at

Edinburgh which was frequently defective; proved reliable in operation with the 6 bar helium backing pressure used in this experiment. The typical operating pressure in the chamber, as measured by the Bayard-Alpert gauge was 10^{-4} mbar.

The vaporisation source was an excimer laser (Lumonics model 430) operating on the XeCl line (308 nm). This laser operates in a superradiant mode, and the broad rectangular spatial output profile (20 x 5 mm) was exploited to preserve signal stability. The beam was passed through a quartz periscope with the second prism rotated 90° about the vertical with respect to the first. The beam profile, originally lying in the horizontal plane, undergoes a rotation into the vertical plane. When focussed by a 20 cm quartz lens on to the target rod, also aligned vertically, the excimer beam vaporises evenly over the target surface presented to it. Had the beam struck the target while lying in a horizontal plane, a "thread" marking the path of the laser would tend to be cut in the rod surface, since the beam covers only a small region vertically. This thread cutting effect is even more pronounced with Nd:YAG vaporisation sources, where the focal spot is smaller. The laser output (15-20 mJ , 10 ns pulse) was focused to typical power densities of 180 MW cm^{-2} (1 mm^2 spot). Clustering took place in a channel 1.5 mm diameter by 25 mm long, with each molecule undergoing about 10^5 collisions prior to adiabatic expansion into vacuum.

7.2.3 Ring dye laser system

The ring dye laser system consisted of a Coherent Innova 100 argon ion laser pumping a Coherent CR-699-29 ring dye laser. For these experiments, the

multiline ultraviolet output of the argon ion laser (351-364 nm, 3.2 W) was used to pump the dye Stilbene 3 (415 - 479 nm range), producing 200 mW of single mode radiation at 435 nm. The ring dye laser is a considerably more complex instrument than the pulsed dye lasers described in Chapter 3, and the principles of its narrow-bandwidth operation merit some discussion. A schematic of the ring laser optical layout is shown in Figure 7.2.

The argon ion pump beam intercepts the flowing dye jet at Brewster's angle to minimise reflection losses from the jet surface. A fast flowing dye jet is essential to minimise intersystem crossing with respect to $S_1 \rightarrow S_0$ emission, and ensure efficient lasing operation. The fluorescent radiation is constrained to travel within the ring by spherical mirrors as shown. Operation of these mirrors in an off-axis mode results in an astigmatism, which is corrected by the compensation rhomb. One of the mirrors is mounted on a piezo translator slaved to the reference cavity (see below).

A ring laser cavity will support either of two counter-propagating travelling waves. Without any means of selecting one direction in preference to the other, lasing will switch rapidly between the two, and the resulting laser output is unstable. One of the travelling waves must be suppressed if stable single frequency operation is to be achieved. In the CR-699, unidirectional operation was enforced by means of an "optical diode" device. This comprises a Faraday glass rhomb, placed in a strong permanent magnetic field, and a plate of crystalline quartz cut for optical activity at Brewster's angle. Plane polarised light passing through the rhomb experiences a rotation in polarisation according to the Faraday effect. [42] The sense of rotation is independent of the direction

Figure 7.2 : Ring dye laser optical layout

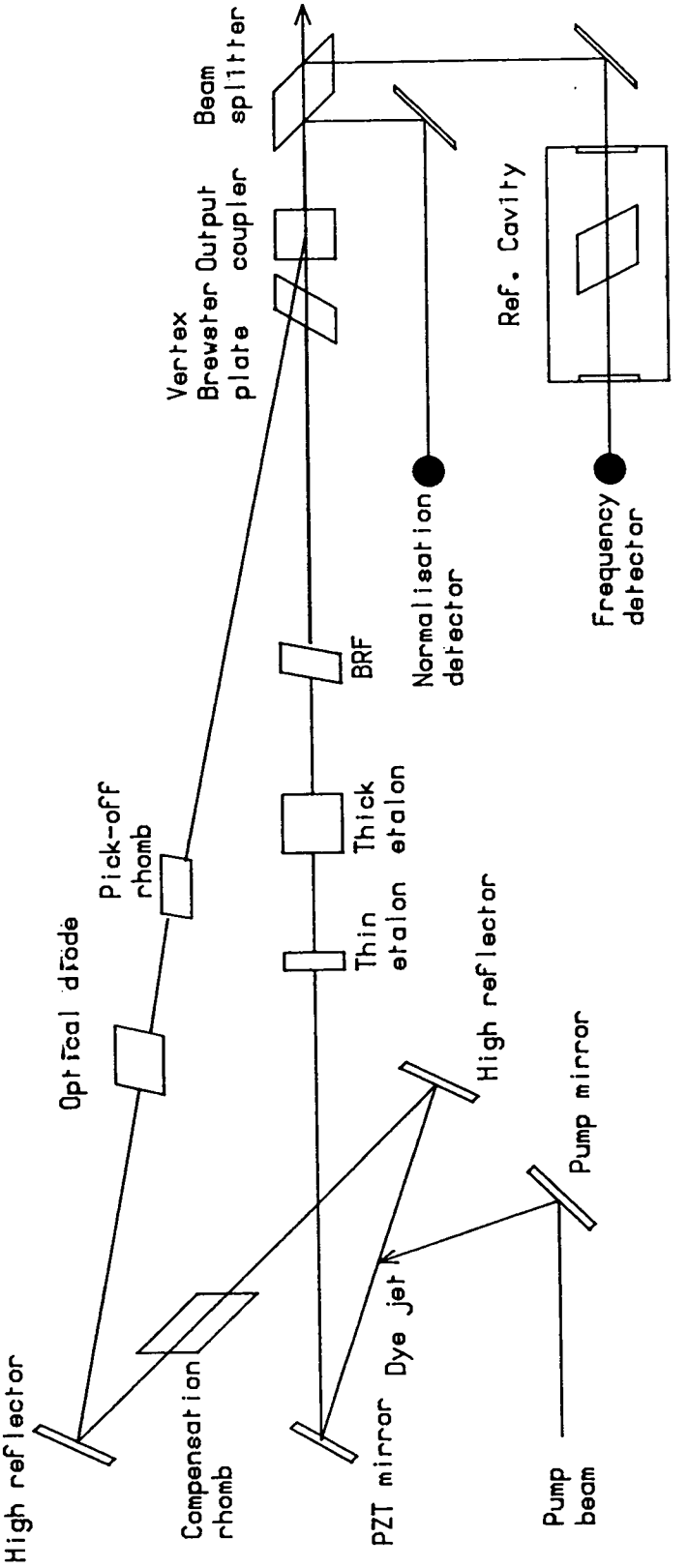

of propagation, being governed by the direction of the magnetic field. The quartz plate is aligned so that it rotates the plane of polarisation of one of the waves back into the original plane, cancelling the Faraday rotation. The other wave experiences a net polarisation rotation, with the Faraday- and quartz-induced rotations adding. The latter wave, having been rotated out of the plane for transmission by Brewster-angled surfaces in the cavity, is soon extinguished by reflection losses.

Wavelength selection within the dye profile is accomplished by a combination of a birefringent filter (BRF) stack and two etalons. The birefringent (Lyot) filter selects a wavelength passband by exploiting the birefringence properties of a biaxial crystal. A typical filter consists of a biaxial crystal placed between two linear polarisers aligned parallel to the electric vector of an incoming plane-polarised wave. The wave can be considered to be split into two components, one parallel (ordinary wave) and one perpendicular (extraordinary wave) to the optical axis of the crystal. Because of the different refractive indices of the ordinary and extraordinary waves in the crystal, superposition of the two waves emerging generally results in elliptical polarisation. It can easily be shown that the overall transmission function of the dual polariser-crystal combination is a function of the phase retardation, and is repetitive in frequency in the manner of an etalon. The free spectral range of a birefringent filter is given by: [43]

$$FSR = c/\Delta nL \tag{7.1}$$

where

c = the speed of light

L = the crystal length

Δn = the difference between ordinary and extraordinary refractive indices.

The free spectral range depends on the crystal thickness, and multiple stacking of several such filters of different thicknesses facilitates considerable narrowing of the lasing passband. If the tilting angle is chosen to equal Brewster's angle, the plates themselves act as both retarding and polarising elements, without any need for additional polarisers. In the CR-699 three such plates are stacked in the thickness ratio 1:4:16, suppressing all oscillation outside a 57 cm^{-1} passband. The BRF plates are rotated by a micrometer to tune the dye laser over the dye gain range.

Single longitudinal mode selection is achieved by two low finesse, low loss solid etalons. A "thin" etalon (0.5 mm, FSR = 225 GHz , finesse = 2) selects a single ring cavity mode, suppressing oscillation in neighbouring modes. This etalon is mounted on a galvanometer drive for the purposes of angle tuning to maintain the alignment of the etalon transmission maximum while the lasing wavelength is scanned. A "thick" etalon (10 mm, FSR = 10 GHz, finesse = 2), constructed from two Littrow prisms, prevents the laser mode hopping by complete free spectral ranges of the thin etalon. These prisms are mounted on piezoelectric translators for tuning purposes.

The lasing wavelength in a ring cavity is normally altered by changing the cavity

length, the wavelength varying according to:

$$L = m\lambda, \tag{7.2}$$

where L is the cavity length and m the mode number. The wavelength changes continuously with L, provided that there are no mode hops. In the CR-699-29 system, an etalon quality plate is mounted at near Brewster's angle next to the output coupler vertex for continuous scanning of the cavity length. Changing the angle between the plate and the reflected beams alters the total optical path length of the cavity, since the beams are refracted between the two surfaces of the plate. Rotation of the plate is controlled by a galvanometer slaved to the reference cavity (see below).

The CR-699-29 is equipped with a complete electronic control system to ensure stable, single frequency scanning operation, based on a stable external reference cavity. A fraction of the ring beam is split off and run into this cavity, a pressure- and temperature-stabilised confocal Fabry-Perot interferometer. [43] The laser wavelength is locked to an interferometer transmission peak electronically. Any jitter in the laser wavelength due to jet turbulence or mechanical disturbances is detected as an excursion from the lock point. Correction is achieved by moving the vertex mounted Brewster plate (low frequency jitter) or the piezo-driven mirror (high frequency jitter). To scan the laser wavelength, the reference cavity length is altered by rotating a galvanometer-driven Brewster plate mounted between the Fabry-Perot mirrors. This changes the wavelength of the Fabry-Perot transmission peak, and with it the position of the lock point. As the wavelength of the lock point alters, single

mode oscillation is maintained by slaved tracking of the vertex Brewster plate and the two etalons.

Accurate wavelength calibration is effected by an integral wavemeter device. The Coherent wavemeter consists of an optical activity meter (OAM) for coarse wavelength measurement, and a Vernier etalon assembly (VET) for fine determinations. The OAM utilises the optical activity of crystalline quartz to make a wavelength measurement. A fraction of the ring laser beam is split off and run into a beamsplitter which generates two parallel beams with a precisely defined polarisation relationship. These beams are passed through two crystalline quartz bars of differing lengths, where their polarisation vectors are rotated according to the optical rotatory power of the quartz. The different phase shifts created by the differing bar lengths are detected and serves as a guide to the wavelength. For example, a 10 cm piece of quartz produces 2170° rotation at 600 nm. [44] The extra shift generated by the additional length of the second permits an unambiguous determination of the wavelength, albeit with limited precision (ca. 2 cm^{-1} uncertainty).

The VET assembly establishes the laser operating wavelength to high accuracy. The VET comprises two vacuum-spaced low finesse Fabry-Perot etalons differing in length by approximately 5%, with free spectral ranges of approximately 6.8 and 6.5 GHz. One of two parallel beams from the laser output passes through each etalon. At some laser frequency, the transmission peaks of each of the etalons coincide. They next coincide after a frequency change equal to the overall FSR of the Vernier combination, which in this case was approximately 150 GHz. This interval defines the order of operation of the VET. Coarse wavelength

determination using the OAM permits this order to be determined. A short (15 GHz) scan of the laser located the laser position by measuring the frequency interval between a transmission peak from each etalon. The recorded fringes of the Fabry-Perot pair form a "vernier" pattern, from which the wavelength at each point may determined by measuring the separation of adjacent transmission peaks. A coarse calibration of the integral wavemeter was achieved using an external wavemeter (Burleigh WA-20). This instrument, a scanning Michelson interferometer, [43] employs a He-Ne laser as the reference line and had a specified accuracy of 0.02 cm^{-1}. The overall calibration procedure led to a combined absolute wavenumber accuracy of 200 MHz. While scanning the laser frequency, the laser wavemeter was checked against the external wavemeter so that proper functioning of the auto-scanning system could always be ascertained. The effective laser linewidth was approximately 1 MHz, and a scanning rate of 300 s per 10 GHz was normally employed. With a stepping increment of 20 MHz and a pulse repetition rate of 10 cycles per second, six cycles were completed at each wavelength position in the scan.

The CR-699 was fully controlled by a dedicated Apple IIe microcomputer equipped with a 6522 VIA interface adaptor for the input and output functions. Data was logged by the computer while scanning by 12 bit fast A/D conversion.

7.2.4 Fluorescence detection and experimental control

The narrow bandwidth afforded by a ring dye laser presents an ideal opportunity to perform Doppler-limited rotationally-resolved electronic spectroscopy. Clearly, there would be little point investing in such a laser system if the Doppler

width of the rovibronic lines themselves is so large that it leads to spectral congestion. According to Equation 2.5, the Doppler halfwidth of a spectral line varies as $T^{1/2}$, where T is the translational temperature. High temperature sources, such as effusive beam ovens, are thus to be avoided in Doppler-limited spectroscopy experiments. For example, at a typical oven temperature of 2000 K, the Doppler width of a rovibronic line in the disilver A←X system at 435 nm would be in excess of 1500 MHz. Such a linewidth is comparable to the resolution of an etalon-narrowed pulsed dye laser, so no advantage would be gained in using the ring laser.

To fully utilise the narrow bandwidth of the ring dye laser, the system must be coupled to a free jet expansion source. The laser vaporisation-supersonic nozzle source described here can be expected to produce translational temperatures of < 5 K about 20 nozzle diameters from the source using helium as the carrier gas. [45] Estimating the translational temperature of silver dimers formed by plasma quenching is a more difficult task. The principal unknown is the translational temperature of clusters immediately prior to expansion. This so-called "source" temperature could be significantly greater than the helium reservoir temperature (300 K). Such a situation would arise if the initially-hot Ag_2 molecules are incompletely quenched prior to expansion. It is simpler to determine the rotational temperature experimentally and infer that the translational temperature will not exceed this value on the grounds of greater cooling efficiency.

Previous work on ZrO by Simard *et al.*, [46] using the same molecular beam source, suggests that the rotational temperature of dimers produced may be as

high as 45 K. Under these conditions, assuming in the worst case equality of translational and rotational temperatures, the Doppler width of a rotational line in the A←X system would be greater than 220 MHz. Clearly, to best exploit the narrow linewidth of the ring laser and remove congestion, some means of selecting molecules with a narrower velocity distribution than the molecular Doppler width is desirable.

A simple but effective solution is to use a fluorescence collection system which will image a portion of the supersonic jet onto the entrance slits of a monochromator. If the laser beam propagates at right angles to the molecular beam axis, molecules on a streamline at an angle θ to the axis will be Doppler shifted by an amount $v_b\omega_0\sin\theta/c$, where v_b is the beam velocity, c the speed of light and ω_0 the unshifted transition frequency. [45] [47] Molecules whose transverse velocity in the laser propagation direction exceeds $v_b\sin\theta$ will not be imaged, since they travel on streamlines which do not cut through the detection zone. Since the molecular beam source has a finite width, defined in this case by the clustering channel diameter, the maximum value of $\sin\theta$ is given by:

$$\sin\theta = d_t/d_a, \tag{7.3}$$

$$d_t = (W_s/M + d_c)/2, \tag{7.4}$$

where

d_a = the nozzle-imaging region axial distance

W_s = the monochromator slit width

M = the optical system magnification

d_c = the clustering channel diameter.

The effective resolution is therefore: [43] [47]

$$\Delta\omega_d = 2(\ln 2)^{1/2}\omega_0 v_b \sin\theta/c, \tag{7.5}$$

where all terms have previously been defined.

Clearly, moving further downstream from the point of expansion will increase the resolution, although this must be weighed against the concomitant loss of signal due to reduced axial number density.

In the present experiments, sample emission at d_a = 2.5 cm was collected by means of a biconvex 5 cm f/1 quartz lens, and imaged at the entrance slits of a monochromator (Bausch and Lomb, 15 cm focal length, 1200 grooves/mm). The lens was located to give a magnification of 5 on to the slits, which were set at 1000 μm aperture. The resolution of this system was calculated to be approximately 220 MHz. This was far from the best resolution of the system, but at least preserved signal intensity while ensuring that high translational temperatures (>45 K) could not have a deleterious effect on the experiment.

Imaging fluorescence from a small zone centred on the molecular beam axis had

the added advantage of reducing the background signal due to scattered light. To further minimise scattered light collection, a black anodised aluminium cone with a 3 mm opening at the apex was placed over the collection lens. The lens was located in a tube which fitted into the XY translator flange on top of the chamber.

Coaxial alignment of the projection of the monochromator slit with the molecular beam axis was crucial to ensure that only the high density core of the jet was sampled. To assist while aligning, a rigid wire was inserted in the clustering channel to simulate the molecular beam core, and light from a He-Ne laser was directed along the ring laser propagation axis. Light scattered vertically from this rod simulated fluorescence, and was imaged in the exit plane of the monochromator. In this way light collection from the excitation zone could be optimised by XY translation of the optical system. The LIF signal was detected by a water-cooled photomultiplier tube (Hamamatsu R943-02). It was subsequently amplified by a Keithly 427 current amplifier before being averaged by a homebuilt gated integrator (10 V maximum input). The averaged signal was read directly by the 12 bit A/D interface of the controlling microcomputer.

Relative timing of the opening of the pulsed valve, the timing of the vaporisation laser and the triggering of the gated integrator was controlled using a 4-channel digital pulse delay generator (Stanford DG435). An external homebuilt master oscillator generated a 10 Hz clock cycle to trigger this device. The fluorescence decay trace and sampling gate were viewed on a 2-channel oscilloscope (Telequipment D1011) for synchronisation. Owing to the continuous nature of the exciting source, the experimental decay trace represented a convolution of

the time of arrival profile of silver dimers in the interaction region with the exponential fluorescence decay curve. The trace was further stretched to > 20 μs by the input impedance of the gated integrator, and thus presented no problems in synchronisation with the gate.

7.3 Results and Data Analysis

Prior to scanning with the ring laser, the location of the (0-0) band was verified using a low-resolution pulsed dye laser and the Burleigh wavemeter. The (0-0) band of the A←X system was then recorded using the ring dye laser over the range 22953-22978 cm^{-1} in a series of scans, each of 30 GHz (1 cm^{-1}) length with a 20 MHz scanning increment. The resetting accuracy of the ring dye laser was sufficient to permit end-to-end stacking of individual scans to generate a seamless spectrum of the complete origin band. Selected portions of the spectrum are shown in Figures 7.3 and 7.4. It should be noted at this stage that the line intensities recorded in different regions of the spectrum are not necessarily comparable, since the photomultiplier tube voltage was increased when scanning weaker, high-J features at the red end of the spectrum. Thus it was not possible to estimate the rotational temperature in the expansion by comparison of the observed and calculated intensities following the procedure outlined in Chapter 5. However, the observation that the spectrum persisted to J > 80 suggested that it could be in excess of 50 K at the point of probing.

The experimental spectral linewidth was observed to be ≃ 300 MHz, somewhat larger than the resolution calculated for the molecular beam-optical system. Laser-induced saturation broadening (see Section 2.4) may have made an

Figure 7.3 : Ring dye laser LIF spectrum of the (0-0) band of the A←X system of Ag_2 (P-branch)

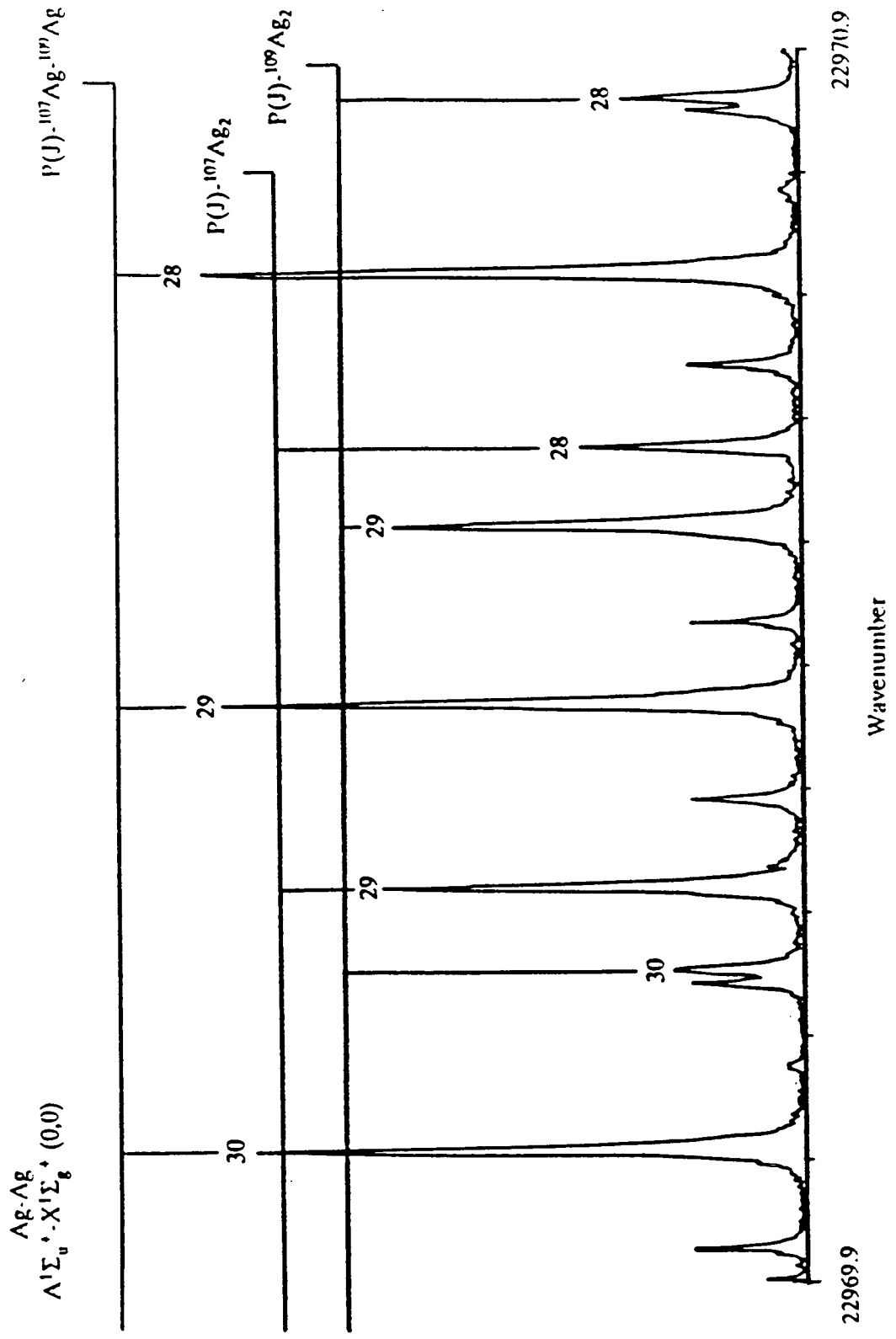

Figure 7.4 : Ring dye laser LIF spectrum of the (0-0) band of the A←X system of Ag_2 (R-bandhead)

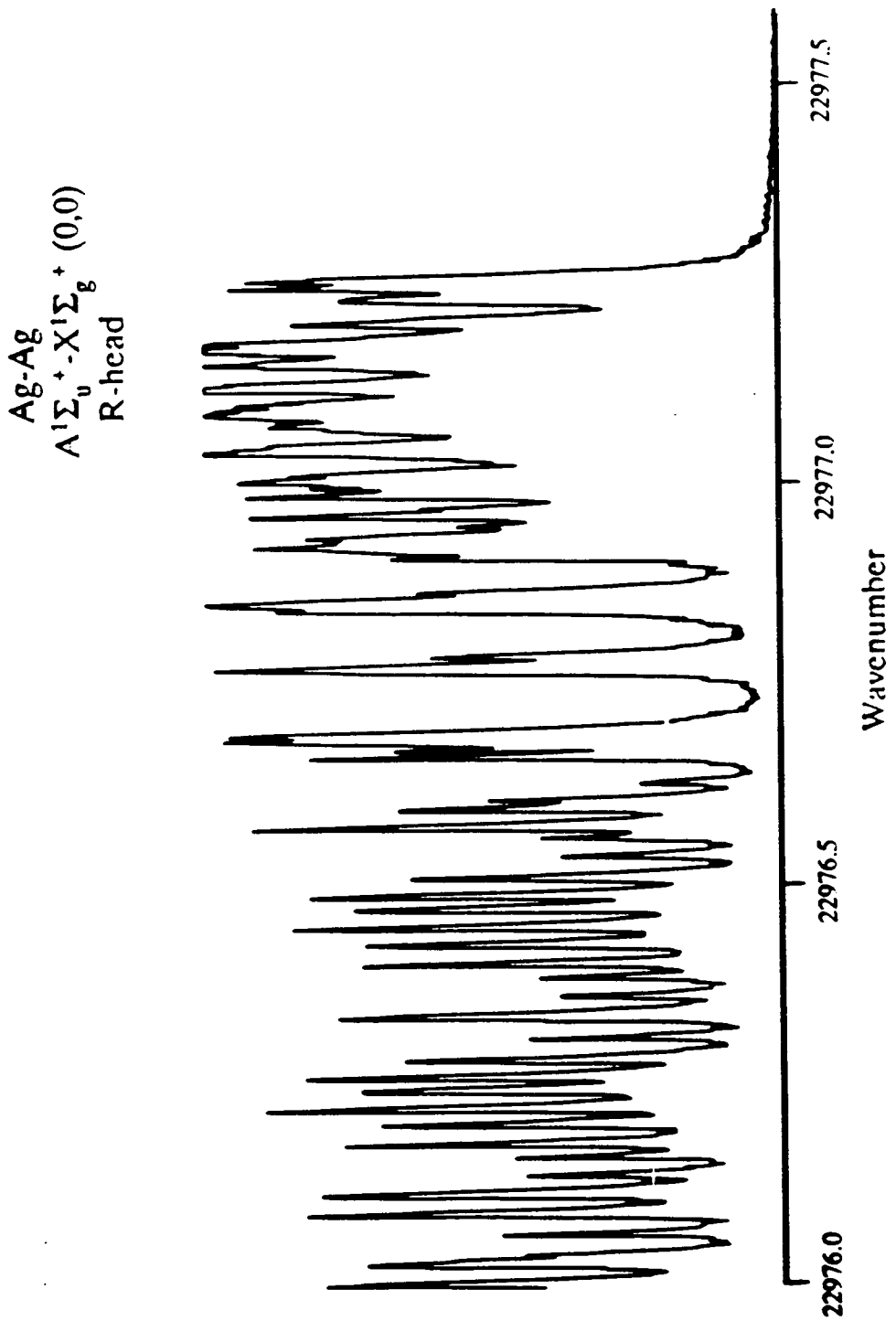

additional contribution to the observed linewidth. (The spectral energy density of the ring laser was calculated to be $\simeq$ 5.6 x 10^{-11} J m^{-3} Hz^{-1}, of similar magnitude to those of the pulsed laser sources used in the CuAg R2PI experiments described in Chapter 5, where transitions of comparable intensity were saturated.) In any case, the spectral resolution was adequate to resolve all P-branch lines from all three isotopomers, and a substantial portion of the R-branch.

Assignment of the spectrum was not trivial, and an *a priori* knowledge of molecular rotational constants and isotope shifts from the earlier R2PI work from this laboratory proved indispensable. Examination of the uncongested, low wavenumber wing of the spectrum revealed a distinct and regular progression of lines (see Figure 7.3). This was assigned to high-J members of the P-branch of $^{107}Ag^{109}Ag$ isotopomer, which is twice as abundant as either the $^{107}Ag_2$ or $^{109}Ag_2$ isotopomer. The possibility that alternate members of this series could be due to an R-branch progression returning from the R-bandhead was discounted: such an assignment would give an unacceptably large P-branch spacing at this displacement from the origin. The $^{107}Ag^{109}Ag$ P-branch could be followed with relative ease all the way to the P-R branch interval. Approximate values of the lower state rotational quantum number (J) were calculated using the known R2PI rotational constants and a crude estimate of the position of the rotationless origin band.

Since there is no nuclear spin intensity alternation in the spectrum due to $^{107}Ag^{109}Ag$, the correct numbering was established with reference to the corresponding $^{107}Ag_2$ and $^{109}Ag_2$ lines. The identity of lines due to the

homonuclear isotopomers was easily determined by calculating their approximate displacements from the central $^{107}Ag^{109}Ag$ lines. Since the nuclear spin of both silver isotopes is 1/2, the spectra of the homonuclear isotopomers will show an even:odd intensity alternation in the ratio 1:3 (see Appendix E). If a line in the spectrum of $^{107}Ag^{109}Ag$ is believed to arise from an odd-J rotational state, its $^{107}Ag_2$ and $^{109}Ag_2$ satellites should be relatively strong owing to their higher nuclear spin statistical weighting. Conversely, in the absence of any saturation effects, an even-J line arising from $^{107}Ag^{109}Ag$ will have weak homonuclear satellites. Figure 7.3 illustrates this phenomenon: $^{107}Ag^{109}Ag$ P(29) has two strong companions, $^{107}Ag_2$ P(29) and $^{109}Ag_2$ P(29), confirming the assignment. On the other hand, the satellites of $^{107}Ag^{109}Ag$ P(30) are manifestly much weaker. The more remote possibility that the assignment could have been in error by two rotational quanta in either direction was also tested. In this case, the rotational constants obtained upon least squares fitting of the data were completely unrealistic. A total of 74 P- and 84 R-branch lines in the spectrum of the $^{107}Ag^{109}Ag$ isotopomer were assigned. It was not possible to assign nearly the same number of lines for the homonuclear isotopomers with a high degree of confidence, and so the $^{107}Ag^{109}Ag$ analysis was completed independently of the other two isotopomers.

Accurate rotational constants were obtained from the LIF data by fitting the observed P- and R-branch line positions using a modified Lavenberg-Marquandt algorithm and a finite difference Jacobian. [46] The wavenumbers of the lines were calculated using the well-known expression:

$$\nu(J) = \nu_0 + F'(J + i) - F''(J)$$

where i= -1 and i= +1 refer to the P- and R-branch lines respectively. The rotational term values for both upper and lower states were assumed to follow the simple expression (for 0^+ states):

$$F(J) = B_v J(J + 1) - D_v J^2(J + 1)^2.$$

Table 7.2 gives the observed and calculated line positions, the residuals, and the correlation matrix for the fitted parameters. The random measurement error from the fit was 120 MHz, reassuringly well below the experimental accuracy of 200 MHz. Fitted molecular constants obtained from this analysis are given in Table 7.3. Quoted uncertainties represent one standard deviation (1σ).

Spectra were also recorded for portions of the (1-0), (2-0) and (0-1) bands, although these were not included in the analysis. The larger vibrational isotope shifts in these bands, far from simplifying assignment, led to spectra of even greater complexity. The large displacements between $^{107}Ag^{109}Ag$ lines and their homonuclear counterparts led to complex interleaving, and the full assignment and analysis has yet to be completed.

The consequent lack of rotational constants for a range of vibrational levels in the ground and excited states precluded the experimental determination of the vibration-rotation coupling constant α_e (see Chapter 5). Instead, if it is assumed that the diatomic potential can be represented by a Morse function, [30] the Pekeris relation may be used to estimate α_e, as described in Chapter 5. While the assumption may appear somewhat sweeping, the calculated α_e value is small compared to the precision of the bondlengths determined in the theoretical

Table 7.2 : Observed and calculated rotational line positions for the $^{107}Ag^{109}Ag$ $A(0_u^+) \leftarrow X(^1\Sigma_g^+)$ (0-0) band

J	OBSERVED	CALCULATED	RESIDUAL
		P-BRANCH	
1	22976.7306	22976.7334	-0.0028
2	22976.6336	22976.6272	0.0064
3	22976.5125	22976.5120	0.0005
4	22976.3867	22976.3878	-0.0011
5	22976.2533	22976.2548	-0.0015
6	22976.1107	22976.1129	-0.0022
7	22975.9689	22975.9620	0.0069
8	22975.8074	22975.8022	0.0052
9	22975.6389	22975.6335	0.0054
10	22975.4580	22975.4559	0.0021
11	22975.2715	22975.2693	0.0022
12	22975.0723	22975.0739	-0.0016
13	22974.8744	22974.8695	0.0049
14	22974.6573	22974.6562	0.0011
15	22974.4327	22974.4340	-0.0013
16	22974.2033	22974.2028	0.0005
17	22973.9686	22973.9628	0.0058
18	22973.7184	22973.7138	0.0046
19	22973.4542	22973.4559	-0.0017
20	22973.1920	22973.1891	0.0029
21	22972.9183	22972.9133	0.0050
22	22972.6289	22972.6286	0.0003
23	22972.3308	22972.3350	-0.0042
24	22972.0264	22972.0324	-0.0060
25	22971.7211	22971.7210	0.0001
26	22971.3976	22971.4006	-0.0030
27	22971.0662	22971.0712	-0.0050
28	22970.7363	22970.7329	0.0034
29	22970.3877	22970.3857	0.0020
30	22970.0265	22970.0296	-0.0031
31	22969.6650	22969.6645	0.0005
32	22969.2876	22969.2904	-0.0028
33	22968.9097	22968.9074	0.0023
34	22968.5186	22968.5155	0.0031
35	22968.1161	22968.1146	0.0015
36	22967.7120	22967.7048	0.0072
37	22967.2927	22967.2860	0.0067
38	22966.8637	22966.8583	0.0054
39	22966.4243	22966.4216	0.0027
40	22965.9768	22965.9760	0.0008
41	22965.5225	22965.5214	0.0011

J	OBSERVED	CALCULATED	RESIDUAL
42	22965.0553	22965.0578	-0.0025
43	22964.5834	22964.5853	-0.0019
44	22964.1025	22964.1038	-0.0013
45	22963.6098	22963.6133	-0.0035
46	22963.1045	22963.1138	-0.0093
47	22962.6098	22962.6054	0.0044
48	22962.0888	22962.0880	0.0008
49	22961.5694	22961.5616	0.0078
50	22961.0283	22961.0262	0.0021
51	22960.4856	22960.4819	0.0037
52	22959.9264	22959.9285	-0.0021
53	22959.3612	22959.3662	-0.0050
54	22958.7919	22958.7948	-0.0029
55	22958.2093	22958.2145	-0.0052
56	22957.6200	22957.6251	-0.0051
57	22957.0175	22957.0268	-0.0093
58	22956.4168	22956.4194	-0.0026
59	22955.8031	22955.8030	0.0001
60	22955.1713	22955.1776	-0.0063
61	22954.5414	22954.5432	-0.0018
62	22953.9003	22953.8997	0.0006
63	22953.2454	22953.2473	-0.0019
64	22952.5822	22952.5858	-0.0036
65	22951.9180	22951.9152	0.0028
66	22951.2337	22951.2356	-0.0019
67	22950.5496	22950.5470	0.0026
68	22949.8510	22949.8493	0.0017
69	22949.1438	22949.1425	0.0013
70	22948.4289	22948.4267	0.0022
71	22947.7018	22947.7019	-0.0001
72	22946.9719	22946.9680	0.0039
73	22946.2267	22946.2250	0.0017
74	22945.4773	22945.4729	0.0044
		R-BRANCH	
0	22976.9177	22976.9192	-0.0015
1	22976.9988	22976.9988	0.0000
2	22977.0636	22977.0694	-0.0058
3	22977.1365	22977.1311	0.0054
4	22977.1744	22977.1839	-0.0095
5	22977.2318	22977.2277	0.0041
6	22977.2538	22977.2626	-0.0088
7	22977.2837	22977.2887	-0.0050
8	22977.3025	22977.3057	-0.0032
9	22977.3112	22977.3139	-0.0027
10	22977.3112	22977.3132	-0.0020
11	22977.3025	22977.3035	-0.0010
12	22977.2837	22977.2849	-0.0012
13	22977.2538	22977.2574	-0.0036

J	OBSERVED	CALCULATED	RESIDUAL
14	22977.2213	22977.2209	0.0004
15	22977.1744	22977.1755	-0.0011
16	22977.1280	22977.1212	0.0068
17	22977.0534	22977.0580	-0.0046
18	22976.9866	22976.9858	0.0008
19	22976.9043	22976.9047	-0.0004
20	22976.8140	22976.8147	-0.0007
21	22976.7137	22976.7157	-0.0020
22	22976.6093	22976.6078	0.0015
23	22976.4908	22976.4909	-0.0001
24	22976.3626	22976.3651	-0.0025
25	22976.2289	22976.2304	-0.0015
26	22976.0833	22976.0867	-0.0034
27	22975.9358	22975.9341	0.0017
28	22975.7764	22975.7725	0.0039
29	22975.6076	22975.6020	0.0056
30	22975.4235	22975.4225	0.0010
31	22975.2347	22975.2340	0.0007
32	22975.0332	22975.0367	-0.0035
33	22974.8341	22974.8303	0.0038
34	22974.6166	22974.6150	0.0016
35	22974.3885	22974.3907	-0.0022
36	22974.1563	22974.1574	-0.0011
36	22973.9172	22973.9152	0.0020
38	22973.6624	22973.6640	-0.0016
38	22973.4009	22973.4039	-0.0030
40	22973.1333	22973.1347	-0.0014
41	22972.8571	22972.8566	0.0005
42	22972.5689	22972.5695	-0.0006
43	22972.2687	22972.2734	-0.0047
44	22971.9706	22971.9683	0.0023
45	22971.6524	22971.6542	-0.0018
46	22971.3248	22971.3311	-0.0063
47	22970.9934	22970.9990	-0.0056
48	22970.6619	22970.6580	0.0039
49	22970.3096	22970.3079	0.0017
50	22969.9488	22969.9488	0.0000
51	22969.5790	22969.5807	-0.0017
52	22969.1990	22969.2035	-0.0045
53	22968.8207	22968.8174	0.0033
54	22968.4267	22968.4222	0.0045
55	22968.0203	22968.0180	0.0023
56	22967.6123	22967.6048	0.0075
57	22967.1832	22967.1825	0.0007
58	22966.7580	22966.7512	0.0068
59	22966.3147	22966.3109	0.0038
60	22965.8627	22965.8615	0.0012
61	22965.4069	22965.4030	0.0039
62	22964.9359	22964.9355	0.0004
63	22964.4616	22964.4589	0.0027

J	OBSERVED	CALCULATED	RESIDUAL
64	22963.9735	22963.9733	0.0002
65	22963.4612	22963.4786	-0.0174
66	22962.9669	22962.9748	-0.0079
67	22962.4641	22962.4620	0.0021
68	22961.9430	22961.9400	0.0030
69	22961.4226	22961.4090	0.0136
70	00000.0000	22960.8689	0.0000
71	22960.3252	22960.3197	0.0055
72	22959.7619	22959.7614	0.0005
73	22959.1903	22959.1939	-0.0036
74	22958.6168	22958.6174	-0.0006
75	22958.0284	22958.0318	-0.0034
76	22957.4344	22957.4370	-0.0026
77	22956.8354	22956.8331	0.0023
78	22956.2159	22956.2200	-0.0041
79	22955.5987	22955.5979	0.0008
80	22954.9668	22954.9666	0.0002
81	22954.3238	22954.3261	-0.0023
82	22953.6754	22953.6765	-0.0011
83	22953.0177	22953.0177	0.0000

CORRELATION MATRIX

	B"	D"	0-0	B'	D'
B"	0.1000D+01	0.9116D+00	0.1230D+00	0.9980D+00	0.9178D+00
D"	0.9116D+00	0.1000D+01	0.1646D+00	0.9016D+00	0.9968D+00
0-0	0.1230D+00	0.1646D+00	0.1000D+01	0.7645D-01	0.1178D+00
B'	0.9980D+00	0.9016D+00	0.7645D-01	0.1000D+01	0.9126D+00
D'	0.9178D+00	0.9968D+00	0.1178D+00	0.9126D+00	0.1000D+01

Table 7.3 : Rotational constants for the A and X states of $^{107}Ag^{109}Ag$

$B_0' = 0.0442235(91)\ cm^{-1}$

$r_0' = 2.65745(26)$ Å

$B_0'' = 0.0486822(93)\ cm^{-1}$

$r_0'' = 2.53285(26)$ Å

$A(0_u^+)$ state :

$B_e' = 0.044292(10)\ cm^{-1}$

$\alpha_e' = 1.351(19) \times 10^{-4}\ cm^{-1}$

$r_e' = 2.65537(31)$ Å

$X(^1\Sigma_g^+)$ state :

$B_e'' = 0.048745(11)\ cm^{-1}$

$\alpha_e'' = 1.260(17) \times 10^{-4}\ cm^{-1}$

$r_e'' = 2.53118(28)$ Å

a - estimated from the Pekeris relation
Errors quoted are ± 1σ

treatments. These are normally quoted to 2 decimal places, and in the absence of error bounds it must be inferred that the uncertainty is at least 0.005 Å. Clearly, a rough estimation of α_e using the Pekeris relation hardly invalidates any comparisons.

7.4 Discussion

7.4.1 The X($^1\Sigma_g^+$) ground state

Numerous calculations on the ground state of silver dimer have been reported. [4]- [21] Table 7.4 summarises the salient results from a selection of these. To date, these investigations have been hampered by the lack of an experimental determination of the equilibrium bondlength, although some workers erroneously regard the semiempirical result quoted by Srdanov and Pesic [26] [28] as correct. It must be stressed that while semiempirical predictions of molecular parameters are a useful rough guide, their validity in heavy-atom cases such as the Group 1b transition metal dimers is open to question. Relativistic effects become increasingly important as one passes from Cu through Ag to Au. The relativistic contraction of the silver 5s atomic orbital (0.08 Å) [48] is more than twice that of the copper 4s orbital (0.03 Å), while that for the gold 6s orbital may be as high as 0.15 Å. [49] Furthermore, the 3d orbitals in copper, which play a secondary role in bonding, are substantially more contracted than the relatively diffuse 4d and 5d orbitals in silver and gold respectively. With such a complex interplay of factors determining the internuclear separation, the interpolative application of simple models should be viewed with some scepticism.

Table 7.4 : Theoretical determinations of the Ag_2 ground state spectroscopic parameters

Method	r_e(Å)	ω_e(cm^{-1})	D_e(eV)	Reference
HF + CI	2.76	134	-	[5]
HF + CI	2.72	-	1.13	[4]
RECP	2.71	144	-	[6]
RECP	2.68	131	0.94	[38]
RECP	2.62	172	1.33	[7]
RECP	2.65	169	-	[13]
RECP	2.62	242	1.12	[8]
RECP	2.60	178	1.10	[9]
PP + LSD	2.54	186	1.78	[15]
RECP	2.52	186	1.71	[11]
RP-HFS	2.52	203	2.04	[21]
RMP + LSD	2.50	214	2.1	[14]
Expt.	2.531[a]	192.4	1.65	[36]

a - this work

RMP - Relativistic model potential
RP-HFS - Relativistic perturbational Hartree-Fock-Slater
Other abbreviations defined in text

In comparing experimental and theoretical work on Ag_2, there are three molecular parameters of interest: the bondlength, the vibrational frequency and the dissociation energy. The bondlength, as determined in this work, stands up to direct comparison with the results of theoretical calculations, since *ab initio* treatments tend to determine this parameter more reliably than the other parameters. The vibrational constants for silver dimer were determined from a fairly extensive analysis of emission data, [24] and should be a fairly faithful representation of a substantial portion of the potential curve. However, inadequacies in the basis sets have a greater effect on the calculated values of ω_e than on calculated r_e values. The dissociation energy of Ag_2 (1.65(3) eV) was determined by Hilpert and Gingerich [50] using Knudsen effusion mass spectrometry (see Chapter 5). The "third law" method employed here is often subject to large errors due to indeterminate spectroscopic constants and contributions to the entropy from nearby excited states. In disilver the molecular constants are sufficiently well established, and any contribution from excited states so small that the third law determination is probably quite accurate. However, the theoretical dissociation energy may be quite sensitive to the long range behaviour of the atomic orbital functions. The basis sets used tend to be optimised for short internuclear separations comparable to the bondlength, and can often be of poor quality at long range. It thus seems prudent to test the viability of the various theoretical approaches principally by comparing the experimental and *ab initio* theoretical bondlengths.

McLean [4] and Shim and Gingerich [5] have performed non-relativistic all electron *ab initio* calculations on disilver. Although these lacked the

sophistication of a relativistic treatment, they demonstrate clearly how little hybridisation occurs upon bond formation: the valence d orbitals remain localised around the atoms, with the $s\sigma_g$ bonding orbital having >95% s character. With the inclusion of an estimated relativistic correction of -0.16 Å, the bondlength calculated by McLean (2.56 Å) approaches the experimental value (2.53 Å).

Pseudopotential methods, in which a potential is constructed to represent the X^+ atomic cores in a diatomic molecule, have proved of great utility in calculations on heavy atom dimers. An explicit treatment of the inner shell orbitals is avoided. In the case of silver dimer, the development of a sophisticated pseudopotential has proved quite fruitful. [15]- [19] This pseudopotential caters for the effects of core polarisation and core-core overlap, which can have a significant effect on bonding strength, particularly for large "floppy" cores such as silver. Correlation of the valence electrons remains a problem, although less so for Group 1b dimers than for other transition metal dimers, since the filled (n-1)d orbitals are rather non-bonding in character. Correlation is handled by local spin density (LSD) or configuration interaction methods. LSD treatments by Martins and Andreoni [20] (r_e = 2.51 Å), Salahub and co-workers [14] (2.50 Å) and Stoll *et al.* [15] (2.54 Å) are of particularly noteworthy accuracy.

Silver dimer is also well suited to theoretical studies using effective core potentials (ECPs), which may include relativistic effects (RECPs). [6]- [13] [38] In this case, a potential is constructed which treats only the $4d^{10}5s^1$ or $4s^24p^64d^{10}5s^1$ electrons in the valence space, with the inner shell electrons described by a core potential. This approach has received attention from a

number of workers, partly because of its ready extension to modelling of triatomic systems. [12] It has generally proved less accurate, consistently overestimating the bondlength by 0.1 Å in most cases. Inclusion of configuration interaction reduces the calculated bondlength towards the experimental value. More recently, Martin, [11] using an improved RECP basis set, has calculated a bondlength of 2.52 Å, in good agreement with the experimental value of 2.53 Å. This calculation employed a basis set in which all but the $4d^{10}5s^{1}$ valence electrons were replaced by a RECP.

Finally, Ziegler *et al.* [21] have used a perturbational Hartree-Fock-Slater approach to relativistic calculations on disilver, their calculated bondlength (2.52 Å) being in good agreement with the experimental value (2.53 Å).

7.4.2 The A(0_u^+) excited state

As was noted in Section 7.1, few calculations on electronically excited states of silver dimer have been reported. [33] [38]- [40] All investigators agree that the lowest singlet excited state in disilver is of $^1\Sigma_u^+$ symmetry, formed by a parallel $5s\sigma^* \leftarrow 5s\sigma$ promotion. This is a strongly-allowed transition, since it conforms to the spin ($\Delta S = 0$) and orbital angular momentum ($\Delta L = 0, \pm 1$) selection rule for molecules in a Hund's case (a) coupling scheme (see Chapter 5). The experimentally determined lifetime (< 40 ns) [37] is indicative of a transition with high oscillator strength. Although the calculation by Basch [38] does not give a satisfactory quantitative description of the other spectroscopic properties of the A and X states, his transition energy (2.59 eV) is in reasonable accord with the experimental value (2.85 eV). Normally, little store would be set by

the predictive power of extended Hückel methods in such a complex diatomic molecule as disilver. Nevertheless, Ozin and Klotzbücher [40] assign the A←X transition to an $s\sigma^*\leftarrow s\sigma$ promotion, at a reasonable assumed internuclear separation of 2.6 Å. Similarly, a SCF-Xα scattered wave calculation [33] predicts a $s\sigma^*\leftarrow s\sigma$ transition energy of 3.19 eV at the semi-empirically calculated bondlength of 2.47 Å. That the transition $5s\sigma^*\leftarrow 5s\sigma$ transition is calculated to be low-lying is perhaps not surprising. This all-valence excitation avoids opening up the 4d shell by core-valence promotions, a much more energetic process for silver. (Ozin calculates the $5s\sigma_u^*\leftarrow 4d\pi_g$ transition to be 5.65 eV.) Furthermore, transitions from $5s\sigma_g$ to molecular orbitals derived from 5p,5d orbitals will probably require more energy than $s\sigma^*\leftarrow s\sigma$ excitation.

In the limit of dissociation to atoms, the excitation $5s\sigma_u^*\leftarrow 5s\sigma_g$ does not involve a change in the population of any atomic orbital, and can be viewed as an electron transfer giving rise to the ion pair structure Ag^+Ag^-. The A state electronic configuration $(4d^{10})(4d^{10})(5s\sigma_g)^1(5s\sigma_u^*)^1$ correlates formally with the lowest ionic asymptotes: $Ag^+(^1S_0) + Ag^-(^1S_0)$. It is quite instructive to plot the coulombic attractive limb of the ionic curve [51] on a potential energy diagram for silver dimer, as described in Chapter 5 (see Figure 7.5). This figure gives a clear illustration of the probable importance of the ion-pair configuration in providing an accurate description of bonding in the A state. It is unlikely that this ionic state actually descends as deeply as the observed A state potential minimum. The repulsive inner limb of the potential will probably intersect it at a higher energy. Rather like the $A(0^+)$ state of CuAg and the $B(^1\Sigma_u^+)$ state of Cu_2, the spectroscopic properties of the A state of Ag_2 ($\omega_e, \omega_e x_e, D_e$) are not

Figure 7.5 : RKR potential curves for Ag_2

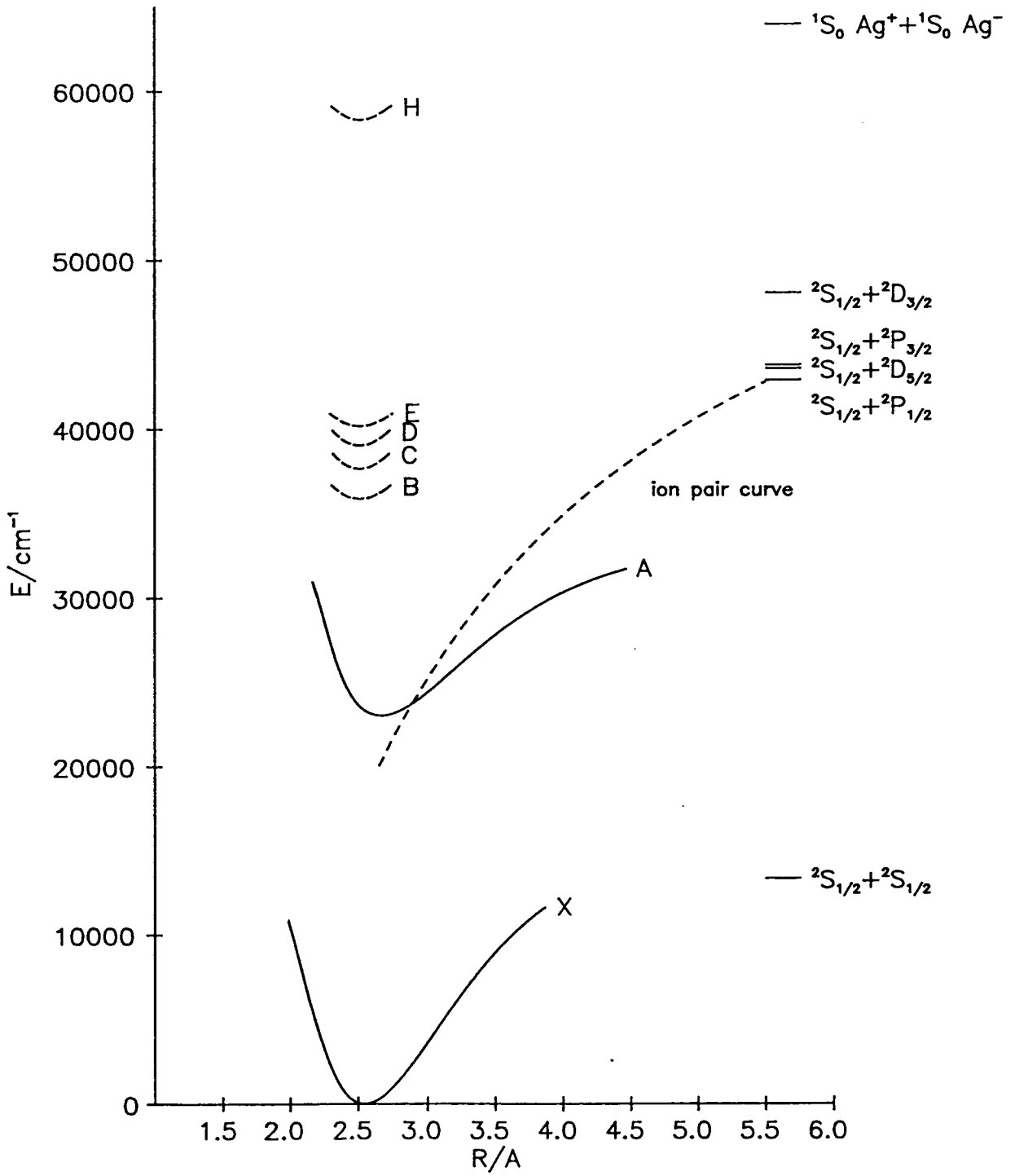

characteristic of an ion-pair state. It seems more plausible that the ionic configuration interacts with other, valence 0_u^+ states, giving rise to the experimentally observed A state. In the region of observation near the potential minimum, the A state will be an admixture of possibly several configurations. The involvement of other 0_u^+ states correlating with excited atomic asymptotes is now examined. The lowest excited limits of atomic silver are ^2P formed by 5p←5s promotion, and ^2D, by 5s←4d promotion. [52] Their energies and orbital occupancies are given in Table 7.5. In atomic copper, the ^2D limits lie well below the ^2P limits, reflecting the much lower ns←(n-1)d promotion energy. [52] The lowest excited states of dicopper can dissociate to $^2D + {}^2S$, although a Hund's case (c) description must be invoked at large internuclear separations since $^2D \leftarrow {}^2S$ transitions are only spin-orbit allowed. In silver, by way of contrast, the 5s←4d promotion energy is much greater, and the spin-orbit components of the ^2P and ^2D limits are interleaved.

Molecular 0_u^+ configurations derived from $^2D + {}^2S$ limits contain a d core vacancy. Their orbital occupancies can be described as follows:

$$^1\Sigma_u^+ : (d\sigma_g)^1(d\pi_u)^4(d\delta_g)^4(d\delta_u^*)^4(d\pi_g^*)^4(d\sigma_u^*)^2\ (s\sigma_g)^2(s\sigma_u^*)^1$$

$$^3\pi(0_u^+) : (d\sigma_g)^2(d\pi_u)^4(d\delta_g)^4(d\delta_u^*)^4(d\pi_g^*)^3(d\sigma_u^*)^2\ (s\sigma_g)^2(s\sigma_u^*)^1$$

where the latter 0^+ configuration arises from spin-orbit coupling. The atomic spin-orbit splitting in the ^2D states is large (4471.9 cm^{-1} [52]), which would be expected to favour a strong $0^+ \leftarrow 0^+$ promotion in Hund's case (c). However, an examination of the atomic transition intensities reveals that the $^2D \leftarrow {}^2S$ transition carries much less intensity than does either component of the fully-allowed

Table 7.5 : Lowest ^2P and ^2D atomic limits of silver[a]

Config.	Term	J	Energy / cm^{-1}
$4d^{10}\ 5s$	^2S	1/2	0.00
$4d^{10}\ 5p$	^2P	1/2	29552.05
		3/2	30472.71
$4d^9\ 5s^2$	^2D	5/2	30242.26
		3/2	34714.16

a - Reference [52]

$^2P \leftarrow ^2S$ transition. [53] It therefore appears unlikely that either of these d vacancy configurations have much effect in enhancing the A←X transition intensity. Furthermore, the formal bond order is reduced from 1 to 1/2 (ignoring weak d bonding) in both the ^2D-derived states, so that neither is liable to be strongly bound. Shallow well depths will restrict the extent to which these configurations can mix into the A state, which lies all of 2.55 eV below the $^2D + ^2S$ limits. Moreover, Butler's observation of a small electronic isotope shift [37] points to a lack of involvement of open d shell configurations in the A state, at least in the region near the potential minimum where these isotope shifts were measured.

The remaining limits which need be considered are $^2P + ^2S$, which give rise to two states of 0_u^+ symmetry:

$$^1\Sigma_u^+ : (4d^{10})(4d^{10})\ (5s\sigma_g)^1(5p\sigma_u^*)^1$$

$$^3\pi(0_u^+) : (4d^{10})(4d^{10})\ (5s\sigma_g)^1(5p\pi_u)^1$$

It is difficult to conceive of the $p\sigma^*$ configuration being much involved in the A state. The antibonding $p\sigma^*$ orbital which is populated is the most highly-excited 5p-derived molecular orbital. Excitation reduces the formal bond order to zero, and a repulsive, or at best weakly bound state results. The other 0_u^+ state is generated by spin-orbit coupling in a $(s\sigma)^1(p\pi^1)$ configuration. This state may be reasonably strongly bound: Basch [38] calculates that the $^3\pi_u$ state from $^2P + ^2S$ limits lies at 2.72 eV, close to the experimental transition energy of 2.85 eV. The small electronic isotope shifts observed in the R2PI work of Butler [37] are certainly consistent with a state dominated by filled d shell configurations, as described in Chapter 5. However, an intense $^3\pi(0_u^+) \leftarrow X(^1\Sigma_g^+)$ transition

necessitates strong spin-orbit coupling. Here, the ^2P spin-orbit multiplets are split by only 920.7 cm^{-1} [52], and the unperturbed state may tend more towards Hund's case (a) than case (c) coupling.

The most concrete conclusion which can be drawn from this rather limited study is that the A state is formed by an interaction of several configurations derived from the ^2D and ^2P excited atomic limits, and the lowest ion pair limit. Our current understanding of electronically-excited silver dimer is hazy and will remain so until the present body of work, both experimental and theoretical, is expanded. An obvious goal would be a comprehensive re-investigation of the many ultraviolet band systems which have been observed, with a view to determining bondlengths and state symmetries. Some of these states may well be the "ghost" companions of the A state, sharing some its characteristics. This work should be accompanied by high level *ab initio* calculations on the excited states of Ag_2, focusing on configurations arising from the ^2P and ^2D limits. Relativistic effects would hopefully be included, as spin-orbit coupling is clearly important. This is perhaps beyond the reach of current computational methods, and in the meantime experimentalists are likely to make more progress. It may be a very long time before even the lowest excited states of this problematic molecule can be laid to rest.

References

[1] Sayhun M. R. V., Photogr. Sci. Eng., **22**, p 317, (1978)
[2] Trautweiler F., Photogr. Sci. Eng., **12**, p 138, (1968)
[3] Morse M. D., Chem. Rev., **86**, p 1049, (1986)
[4] McLean A. D., J. Chem. Phys., **79**, p 3392, (1983)
[5] Shim I., Gingerich K. A., J. Chem. Phys., **79**, p 2903, (1983)
[6] Ross R. B., Ermler W. B., J. Phys. Chem., **89**, p 5202, (1985)
[7] Hay P. J., Martin R. L., J. Chem. Phys., **83**, p 5174, (1985)
[8] Basch H., Far. Symp. Chem. Soc., **14**, p 149, (1980)
[9] Walch S. P., Bauschlicher C. W. Jr., Langhoff S. R., J. Chem. Phys., **85**, p 5900, (1986)
[10] Klobukowski M., J. Comput. Chem., **4**, p 350, (1983)
[11] Martin R. L., J. Chem. Phys., **86**, p 5027, (1987)
[12] Bauschlicher C. W. Jr., Langhoff S. R., Partridge H., J. Chem. Phys., **91**, p 2412, (1989)
[13] Ross R. B., Pitzer R. M., *private communication*, ,
[14] Andzelm J., Radzio E., Salahub D. R., J. Chem. Phys., **83**, p 4573, (1985)
[15] Stoll H., Fuentealba P., Dolg M., Flad J., Szentpaly L. v., Preuss H., J. Chem. Phys., **79**, p 5532, (1983)
[16] Stoll H., Fuentealba P., Schwerdtfeger P., Flad J., Szentpaly L. v., Preuss H., J. Chem. Phys., **81**, p 2732, (1984)
[17] Flad. J., Igel G., Preuss H., Stoll H., Ber. Bunsenges. Phys. Chem., **88**, p 241, (1984)
[18] Flad J., Igel-Mann G., Preuss H., Stoll H., Chem. Phys., **90**, p 257, (1984)
[19] Flad J., Igel-Mann G., Preuss H., Stoll H., Surf. Sci., **54**, p 379, (1985)
[20] Martins J. L., Andreoni W., Phys. Rev. A, **28**, p 3637, (1983)
[21] Ziegler T., Snijders J. G., Baerends E. J., J. Chem. Phys., **74**, p 1271, (1981)
[22] Balasubramanian K., J. Phys. Chem., **93**, p 6585, (1989)
[23] Ruamps J., Compt. Rend. Hebd. Seances Acad. Sci., **238**, p 1489, (1954)
[24] Kleman B., Lindqvist S., Arkiv. fur Fysik, **9**, p 385, (1955)
[25] Gingerich K. A., Far. Symp. Chem. Soc., **14**, p 109, (1980)
[26] Brown C. M., Ginter M. L., J. Mol. Spec., **69**, p 25, (1978)
[27] Maheshwari R. C., Ind. J. Phys., **37**, p 368, (1963)
[28] Srdanov V. I., Pesic D. S., J. Mol. Spec., **90**, p 27, (1981)
[29] Shin-Piaw C., Loong Seng W., Yoke-Seng L., Nature, **209**, p 1300, (1966)
[30] Morse P. M., Phys. Rev., **34**, p 57, (1929)
[31] Clark C. H. D., Phys. Rev., **47**, p 238, (1935)
[32] Mitchell S. A., Ozin G. A., J. Phys. Chem., **88**, p 1425, (1984)
[33] Ozin G. A., Huber H., McIntosh D., Mitchell S. A., Norman J. G. Jr., Noodleman L., J. Am. Chem. Soc., **101**, p 3504, (1979)
[34] Mitchell S. A., Kenney-Wallace G. A., Ozin G. A., J. Am. Chem. Soc., **103**, p 6030, (1981)
[35] Grinter R., Armstrong S., Jayasooriya U. A., McCombie J., Norris D., Springall J. P., Far. Symp. Chem. Soc., **14**, p 94, (1980)
[36] Hopkins J. B., Langridge-Smith P. R. R., Morse M. D., Smalley R. E., *unpublished results*, ,

[37] Butler A. M., *Ph. D. thesis*, Edinburgh University, 1989.
[38] Basch H., J. Am. Chem. Soc., **103**, p 4657, (1981)
[39] Grinter R., Chem. Phys., **102**, p 187, (1986)
[40] Ozin G. A., Klotzbucher W. E., Inorg. Chem., **18**, p 2101, (1979)
[41] Cartwright P. C., *Ph. D. thesis*, Edinburgh University, 1989.
[42] Baldwin G. C., *An introduction to Nonlinear Optics*, Plenum Press, New York, 1969.
[43] Demtröder W., *Laser Spectroscopy: Basic Concepts and Instrumentation*, Springer Verlag, Berlin, 1982.
[44] Coherent Inc., *CR-699-29 manual*, Palo Alto Ca., 1984.
[45] Levy D .H., Ann. Rev. Phys. Chem., **31**, p 197, (1980)
[46] Simard B., Mitchell S. A., Hendel L. M., Hackett P. A., Farad. Disc. Chem. Soc., **86**, p 163, (1988)
[47] Levy D. H., Wharton L., Smalley R. E., *Chemical and Biochemical Applications of Lasers, Vol. II*, Academic Press, New York, 1977.
[48] Desclaux J. P., Atomic Data and Nuclear Data Tables, **12**, p 311, (1973)
[49] Lee Y. S., Ermler W. C., Pitzer K. S., McLean A. D., J. Chem. Phys., **70**, p 288, (1979)
[50] Hilpert K., Gingerich K. A., Ber. Bunsenges. Phys. Chem., **84**, p 739, (1980)
[51] Herzberg G., *Molecular Spectra and Molecular Structure I: Spectra of diatomic molecules*, 2nd. edition, van Nostrand, Princeton, 1950.
[52] Moore C. E., *Atomic energy levels*, NBS Circular 467, Washington D.C., 1971.
[53] Wiese W. L., Martin G. A., *Wavelengths and transition probabilities for atoms and atomic ions*, NBS Circular 68, Part II, Washington D.C., 1980.

Chapter 8
Bonding in the group 1b transition metal dimers

The purpose of this chapter is to draw together the results presented in Chapters 5,6 and 7, in an attempt to give a coherent picture of bonding in the Group 1b transition metal dimers. Because relativistic effects on bonding are so much greater in gold-containing dimers than in those containing just copper or silver, it seems logical to divide the discussion into two parts. The properties of the copper and silver dimers (Cu_2, CuAg and Ag_2) are compared in Section 8.1. Gold-containing dimers, which lay outside the experimental scope of this work, are surveyed and compared with the corresponding Cu,Ag species in Section 8.2.

The key to elucidating the bonding characteristics of a molecular system lies in the determination of its spectroscopic properties. In compiling this study, we concentrate (where possible) upon four distinct molecular parameters: the force constant (k_e), the equilibrium bondlength (r_e), the zero point dissociation energy (D_0) and the adiabatic ionisation potential.

The force constant (k_e) is simply a measure of the "stiffness" of the bond, and is related to the vibrational constant ω_e through the equation: [1]

$$k_e = 4\pi^2\omega_e^2\mu,$$

where μ is the reduced mass of the molecule.

Where possible, a direct spectroscopic determination of the equilibrium bondlength (r_e) is quoted. However, lack of data on excited vibrational levels of

the ground state often required the application of the Pekeris relation to calculate r_e from r_0 (see Chapter 5).

The neutral ground state dissociation energies (D_0) have been determined either spectroscopically or by effusion mass spectrometry. The reliability of the latter method for the determination of bond dissociation energies is often called into question when there are low-lying excited states nearby. [2] Thermal population of these states will affect the equilibrium concentration of dimer relative to monomer, which is used to determine the dissociation energy. The coinage dimers are spared these complications because they lack low-lying open d shell states in the immediate vicinity of the ground state.

Before making a detailed comparison of the data, the nature of the metal-metal bond in the Group 1b dimers is reviewed briefly. The relative contributions of d and s orbitals to a transition metal dimer bond are largely determined by the spatial extents and energies of these orbitals. In copper and silver, the (n-1)d shell lies well below the ns orbital, and the ground state configuration is $(n-1)d^{10}ns^1$ in each case (see Figure 5.6). [3]

In energetic terms, the separated atom configurations are "ready-made" for strong valence bonding interactions through the singly-occupied ns orbitals. A strong $s\sigma$ bond is formed, with a weak secondary interaction between the largely inert d cores. In proceeding across a transition period, both the (n-1)d and ns orbitals experience radial contraction due to the increasing nuclear charge. The (n-1)d orbitals are not so well shielded as the ns orbitals from the increasing nuclear charge as the ns orbitals, and are thus more severely contracted.

Calculations of the expectation values of the orbital radii, including relativistic corrections, reveal that the ratio $<r_{ns}>/<r_{(n-1)d}>$ increases from 2.33 to 3.17 in moving across the first period from Sc to Cu. [4] [5] The involvement of d orbitals in bonding therefore diminishes across a period, and for copper and silver these orbitals play a minor, if non-negligible role. In copper for example, $<r_{4s}> \simeq 1.55$ Å and $<r_{(n-1)d}> \simeq 0.49$ Å respectively (see Table 8.1). [4] [5] The equilibrium bondlength in the ground state of Cu_2 is determined spectroscopically to be 2.22 Å. [2] Clearly, while the 4s orbitals overlap appreciably, the 3d cores remain essentially non-penetrating.

For dimers containing only copper and silver, a clear picture of the generic bond emerges. Bonding is dominated by the nsσ bond formed by in-phase overlap of the singly-occupied ns atomic orbitals. The bond is modified by a weak repulsion between the fully-occupied d^{10} cores, to a degree determined by the extent of core-core overlap.

In gold, the situation is somewhat transformed by the very large relativistic contraction and stabilisation of the 6s orbital (see Table 8.1). (The origin of these effects was discussed in Chapter 5.) This contraction exerts a synergistic effect on the 5d orbitals, which expand and can become much more involved in bonding than in copper or silver (see Section 8.2).

8.1 Bonding in copper and silver dimers

8.1.1 The X($^1\Sigma_g^+$) ground states

Spectroscopic constants for the ground states of Cu_2, CuAg and Ag_2 are presented in Table 8.2. The pattern of equilibrium bondlengths is quite regular, the arithmetic mean of the the Cu_2 and Ag_2 bondlengths differing from r_e(CuAg) by only $\simeq$ 0.009 Å. The observation of such a simple trend in bondlength is perhaps unsurprising, since the same type of orbital interactions govern bonding in all three Cu,Ag species. While the replacement of a copper atom by a silver atom may alter the bond strength appreciably, the internuclear separation is still largely governed by the effective radii of the ns orbitals. The secondary bond-lengthening effect of core-core repulsions will also be roughly the mean of the homonuclear values. Morse [5] has pointed out that the regular pattern of bondlengths can be used to define "single-bond radii" for the coinage group, values of 1.110 Å (Cu) and 1.266 Å (Ag) being obtained.

The diatomic bondlengths may be compared with the effective ns orbital radii to determine the extent of ns overlap upon bond formation. Summing the relativistic radii of Table 8.1, and comparing with the experimental bondlengths reveal contractions of .878 Å (Cu_2), .856 Å (CuAg) and .815 Å (Ag_2).

Both the dissociation energies and the force constants increase in the order Ag_2 < CuAg < Cu_2, as shown in Table 8.2. This ordering is largely related to the size and stability of the bond-forming ns atomic orbitals. Spatially-compact ns orbitals will favour a strong sσ bond, since they facilitate substantial

Table 8.1 : Orbital radii of the group 1b atoms

Element	$<r_{(n-1)d}>$/Å	$<r_{ns}>$/Å	$<r_{ns}>/<r_{(n-1)d}>$
Cu	0.488	1.549	3.174
Ag	0.702	1.673	2.383
Au	0.808	1.543	1.910

Data from Reference [4], corrected for relativistic effects.

Table 8.2 : Spectroscopic constants for the Cu,Ag dimer ground states

Dimer	r_e/Å	$10^5 k_e$/dyn cm^{-1}	D_0/eV
Cu_2	2.2197[b]	1.319(1)[c]	2.01(8)[d]
CuAg	2.3664(71)[a]	1.240(19)[a]	1.76(10)[e]
Ag_2	2.53118(28)[a]	1.169(6)[f]	1.65(3)[g]

a - This work
b - Reference [6]
c - Reference [7]
d - Reference [8]
e - Reference [9]
f - Reference [10]
g - Reference [11]

concentration of bonding electron density near the nuclear line of centres defining the bond. Since the Ag(5s) orbital is more diffuse than the Cu(4s) orbital, the electron density is distributed over a greater volume, and is less strongly concentrated on axis upon bond formation. Thus the observed ordering of D_0 and k_e is crudely rationalised by appealing to a model whereby successive replacement of copper by silver leads to more diffuse bonding molecular orbitals, with a concomitant weakening of the bond. The observed ordering of bond strengths is reflected in the degree of ns overlap calculated above, which decreases in the order $Cu_2 > CuAg > Ag_2$.

A more subtle effect on bond strength may be traced to the differing spatial extents of the nd orbitals, and the differing core-core repulsions they generate. The ratio of the relativistically-corrected Hartree-Fock orbital radii $<r_{ns}>/<r_{(n-1)d}>$ decreases from 3.17 to 2.38 on passing from copper to silver. This effect is ascribed to the enhanced shielding of the 4d orbitals in silver by the $3d^{10}4s^2 4p^6$ orbitals, and the Ag(4d) orbitals are thus significantly more diffuse than the Cu(3d) orbitals. Relativistic contraction of all the s orbitals improves the shielding of the (n-1)d shell, allowing the latter to expand (see Chapter 5). Since relativistic effects are more pronounced for Ag than for Cu, their inclusion will heighten the discrepancy between the ratio of the radii for copper and silver. Thus the d cores in silver should exert a greater repulsive effect on each other than in copper, an effect which may be reflected in the observed order of bond strengths. Core-core repulsion is a manifestation of the weakly antibonding character of a fully-occupied d^{20} shell. The more diffuse the d orbital, the larger the antibonding interaction. It is interesting to note that although the

antibonding core interaction in disilver is larger than that in dicopper, the energetically lower-lying d shell in Ag_2 has much less influence on the molecular orbital character of the formally sσ bond. As Figure 5.6 demonstrates, the (n-1)d/ns energy gap in silver (8.62 eV) is almost twice that in copper (4.67 eV). [3] Therefore the amount of d character which can be mixed into the sσ bond will be reduced in silver dimer.

In the mixed dimer CuAg, the reduction in bond strength will arise mainly from the expansion of the sσ bonding molecular orbital when silver replaces copper. The energy mismatch between the Cu(4s) and Ag(5s) orbitals is small, 0.49 eV in the non-relativistic Hartree-Fock limit, diminishing with the inclusion of relativistic effects which preferentially stabilise the Ag(5s) orbital (see Figure 5.6). [3] This will effect a slight weakening of the bond. The Cu(3d) and Ag(4d) orbitals are separated by 3.46 eV in the NRHF limit (see Figure 5.6). This large energy gap leads to a very weak interaction between the two d cores, even though the Ag(4d) orbital is diffuse. The d shell in CuAg is therefore highly non-bonding and has little effect on the bond strength. $D_0(CuAg)$ appears to lie slightly closer to $D_0(Ag_2)$ than to $D_0(Cu_2)$. However, the substantial uncertainties associated with these measurements preclude any further deductions regarding the copper/silver character of the bond in CuAg. It would be similarly unwise to read too much into the difference between the force constants, given the subtle interplay of forces which may be operating.

8.1.2 Adiabatic ionisation potentials

Measurement of the adiabatic ionisation potentials sheds fresh light on the

bonding in the Cu,Ag dimers. Table 8.3 contains the measured IPs for Cu_2, CuAg and Ag_2, and the ion ground state dissociation energies inferred from these values. It should be noted that the IP of disilver measured by Hopkins *et al.* [12] is subject to confirmation as being the adiabatic IP. The observed trend $IP(Cu_2)$ > IP(CuAg) > $IP(Ag_2)$ can be rationalised by the same arguments used to explain the ground state bond strengths. The adiabatic ionisation potential measures the energy required for removal of an electron from the highest-lying $s\sigma$ orbital. This energy requirement decreases down the series Cu_2 → CuAg → Ag_2, as the electron is being ejected from a molecular orbital with progressively more character from the diffuse Ag(5s) orbital. This trend is also manifested in the atomic ionisation potentials, where IP(Ag) < IP(Cu). Electrons in valence orbitals lying closer to the positive core move in a stronger coulomb field, and require more energy for their removal.

The ionisation potential of CuAg is observed to lie closer to $IP(Cu_2)$ than to $IP(Ag_2)$. Again, this observation may have only limited significance, as subtle changes in the bond dissociation energies of the neutral and ionic ground states will affect the measured molecular ionisation potentials.

8.1.3 Dissociation energies of neutral and ionic ground states

With a knowledge of the atomic IP and the dissociation energy of the neutral ground state, measurement of the molecular adiabatic ionisation potential allows the dissociation energy of the ionic ground state to be determined. This procedure, using a simple thermochemical cycle, was applied in Chapter 6 to derive values for Cu_2^+ and $CuAg^+$.

Table 8.3 : Ionisation potentials of the Cu,Ag dimers

Dimer	IP	$D_0(M_2)$-$D_0(M_2^+)$	$D_0(M_2^+)$
Cu_2	7.90426(42)[a]	+0.17791(42)[b]	1.83(8)[d]
CuAg	7.78058(54)[a]	+0.20434(54)[b]	1.56(10)[d]
Ag_2	7.56(2)[c]	-0.02(2)[b]	1.67(50)[d]

Units of eV

a - This work
b - using atomic IPs from Reference [13]
c - Reference [12]
d - using $D_0(M_2)$ from Table 8.2

Spectroscopic determinations of $IP(M_2)$ and IP(M) can be carried out with extremely high accuracy, and thus the uncertainty in $D_0(M_2^+)$ is dictated largely by the error bound on $D_0(M_2)$. As recounted above, the lack of low-lying excited states in the Group 1b dimers makes determinations of $D_0(M_2)$ by effusion mass spectrometry quite reliable. (In the case of Cu_2, a dispersed fluorescence molecular beam study [8] enabled the thermodynamic measurement to be corroborated.) Of particular interest is to probe the extent to which the dissociation energy changes in going from the neutral to the ionic ground state. The use of the cycle to determine this change is unequivocal and highly accurate, since the difference in dissociation energies simply equals the difference in IP between atom and dimer:

$$D_0(M_2) - D_0(M_2^+) = IP(M_2) - IP(M).$$

Since both terms on the right hand side are measured with spectroscopic accuracy, ΔD_0 is determined very accurately.

The dissociation energies of the Cu,Ag dimer neutral and ion ground states are listed in Table 8.3. The differences in bond dissociation energy between neutral and dimer ion are only 0.21 eV (CuAg) and 0.18 eV (Cu_2). (The lower-lying $Cu + Ag^+$ limits were employed when calculating $D_0(CuAg^+)$.) As discussed in Chapter 6, the relatively minor reduction in bond strength which accompanies ionisation reflects the intimate involvement of low-lying $d^{19}(s\sigma)^2$ configurations in the ion ground states of both these molecules. Had the electronic configuration in the ion been entirely $d^{20}(s\sigma)^1$, the reduction in bond order upon ionisation from 1 to 1/2 would have a drastic bond-weakening effect. In CuAg, the d hole

states which mix into the ground state will be localised on copper, as the creation of a d vacancy in silver is a considerably more energetic process.

A recent electron spin resonance study on matrix-isolated Cu_2^+ implied that the unpaired electron possessed almost pure sσ character, with the dσ contribution being less than 1 %. [14] With virtually no $d^{19}(s\sigma)^2$ character in the ionic ground state, a bond substantially weaker than that in the neutral dimer would result. This result appears seriously at odds with the concurrent determinations of $D_0(Cu_2^+)$ both in this work and by Weisshaar's group, [15] their reported value for the ionic force constant being $\simeq$ 70 % of that in the neutral molecule. Also, a LCAO Xα calculation by Post and Baerends [16] found the valence electron in Cu_2^+ to have 76 % sσ and 20 % dσ character, and a pseudopotential calculation by Stoll *et al.* [18] determined $D_0(Cu_2^+)$ to be $\simeq$ 80 % of the neutral value. The glaring inconsistency between the solid matrix and gas phase results is disquieting. A possible explanation is the host-guest interaction which occurs in the solid phase. Perturbations induced by the matrix environment may alter the Cu_2^+ orbital energies with respect to the gas phase values.

The magnitude of the Ag_2^+ bond energy is even more problematic (see Table 8.3). Here, the difference in dissociation energies between the neutral and ion is almost zero, implying that Ag_2^+ and Ag_2 are equally strongly bound ! The possibility that Hopkins *et al.* [12] measured a vertical as opposed to the adiabatic ionisation potential offers no comfort: if the adiabatic IP is even lower than the measured value, the dissociation energy of the ion will be even larger than that of the neutral. Such a large ionic D_0 value points to ionisation by removal of a non-bonding electron, and might imply that d hole configurations

which retain the $(s\sigma)^2$ bond intact are heavily involved. However, unlike Cu_2 and CuAg, Ag_2 has no low-lying d vacancy states, as the s←d promotion energy is much greater in Ag and Ag^+. [13] Therefore $d^{19}(s\sigma)^2$ states are expected to make a diminished contribution in Ag_2^+, making the magnitude of $D_0(Ag_2^+)$ even harder to explain.

Some similarities may be drawn here between Ag_2 and the alkali dimers Na_2 and K_2, which are also primarily sσ-bonded. The dissociation energy of Na_2^+ is actually 32 % greater than that of Na_2, while that of K_2^+ is 50 % larger than that of the neutral. [17] It has been suggested that the increase in bond strength when a bonding electron is removed is connected with the existence of closed cores which exert a repulsive effect on the valence electrons. [18] Ionisation relieves part of the repulsive core-valence interaction, which more than cancels the halving of the formal bond order.

Theoretical calculations on Ag_2^+ are in disagreement. Basch [19], using a relativistic effective core potential (RECP), has calculated the dimer ion to be more deeply-bound than the neutral dimer, although his D_0 values are numerically in very poor agreement with experiment. Stoll *et al.*, [18] using pseudopotentials, obtained reasonably good agreement with the experimental dissociation energies of Cu_2 and Cu_2^+. The calculation gave $D_e(Ag_2) = 1.78$ eV and $D_e(Ag_2^+) = 1.40$ eV. That theoreticians cannot obtain satisfactory agreement with experiment (or with each other) demonstrates the peculiar nature of Ag_2^+. The effects which operate in Ag_2^+ may also be present in Cu_2^+ and $CuAg^+$, but are obscured by the influence of the low-lying copper d hole states. The "alkali analogy" may have some merit in explaining the curious bonding in the disilver

ion, but there is a clear mandate for further experimental and theoretical investigations of Ag_2^+. Threshold ionisation spectroscopic studies (TIS) on disilver are under way in our laboratory, and excited state photoelectron studies on Ag_2 would be particularly welcome.

8.1.4 Excited states

As should be abundantly clear from Chapters 5 to 7, the problem with making comparisons among the low-lying excited states of the Cu,Ag dimers is that the nature of the configurations of the various states are obscure. All the states examined are believed to be admixtures of several configurations, unlike the ground state which is well-described by the single configuration $d^{20}(s\sigma)^2$. The experimental evidence does not allow us to discern which, if any, is the dominant configuration in any of the excited states. Slight changes in the percentage composition of a state can radically alter ω_e and r_e, and thus we confine our comparisons to the more gross variations in bond dissociation energy.

The dissociation energies for the known low-lying 0^+ states of Cu_2, CuAg and Ag_2 are listed in Table 8.4. Both the A and B states of dicopper are included, since these are believed to interact *via* the somewhat nebulous "intruder" state (see Chapter 6 and Reference [20]). In each case, the states are believed to derive character from the lowest excited atomic asymptotes, and these are used in calculating $D_0(M_2^*)$ from a thermochemical cycle.

The most striking feature to emerge is that the $A(0_u^+)$ state of disilver is substantially more deeply bound than any of the low-lying states in Cu_2 or CuAg. The principal difference between Ag_2 and the copper-containing dimers is the

Table 8.4 : Dissociation energies of excited Cu,Ag dimers

Dimer	Dissn. limits[a]	D_0/eV[b]
Cu_2 $A(0_u^+)$	$^2D_{5/2} + {}^2S_{1/2}$	0.87(8)
Cu_2 $B(0_u^+)$	$^2D_{3/2} + {}^2S_{1/2}$	0.96(8)
CuAg $A(0^+)$	$^2D_{5/2}$(Cu) + $^2S_{1/2}$	0.57(10)
Ag_2 $A(0_u^+)$	$^2P_{1/2} + {}^2S_{1/2}$	2.47(3)

a - Reference [13]
b - Reference [2]

existence of low-lying $3d^9 4s^2$ excited limits in the latter. Mixing of the weakly-bonding $d^{19}(s\sigma)^2(s\sigma^*)^1$ configuration into the excited states of Cu_2 and CuAg creates a state only moderately strongly bound, which dissociates to ^2D + ^2S limits (see Figure 5.6). By contrast, in disilver, the corresponding $4d^9 5s^2$ limits are much higher-lying, as shown in Figure 7.5. That the A state of Ag_2 turns out to be considerably more strongly bound than the ground state suggests that it does not acquire much character from the configuration $d^{19}(s\sigma)^2(s\sigma^*)^1$. One of the higher-lying excited states of disilver (B - E), probably possesses more d hole character.

How then, are we to account for the anomalously deeply-bound $A(0_u^+)$ state of silver dimer ? Morse [5] has suggested that the the lowest ion pair limits are primarily responsible, an argument discussed in Chapter 7. Certainly, as can be seen in Figure 7.5, the attractive limb of the ion pair curve follows the A state quite closely, but the extent to which the ion pair state is bound is open to question. The other leading candidate is the $d^{20}(s\sigma)^1(p\pi)^1$ configuration, which is derived from the ^2P + ^2S limits, which are interleaved with the ^2D + ^2S limits in silver. Although completely bonding, the state arising from this configuration, $(\sigma)^1(\pi)^1$, is unlikely to be as deeply bound as the σ^2 ground state, owing to π overlap being poorer than σ overlap at long range.

There are clear parallels between the configuration responsible for the strong bonding of the A state of Ag_2, and the deeply-descending intruder state which influences the A and B states of copper dimer. These latter states would probably be deeply bound were it not for the intervention of the low-lying $3d^9 4s^2$ limits of copper. Whether the ion pair state or some other excited configuration is

responsible is a matter worthy of debate.

8.2 Bonding in gold-containing dimers

Gold-containing Group 1b dimers exhibit remarkable departures from the trends which might be naively expected by an extrapolation of the properties of the Cu,Ag dimers. The apparent anomalies can be traced to the operation of relativistic effects in gold which are many times more significant than those in copper or silver. The atomic numbers (Z) of the three Group 1b metals are 29 (Cu), 47 (Ag) and 79 (Au). Silver has 18 more electrons than copper. Gold, however, acquires 32 electrons more than silver, due to the additional filling of the 4f shell, which has descended deeply due to poor shielding of added charge. Chapter 5 outlined the origin of the relativistic effects responsible for the contraction and stabilisation of ns orbitals, and the concomitant expansion of high angular momentum orbitals such as (n-1)d. For the very highly-charged gold nucleus, these effects are quite severe, much more so than in either copper or silver. The 6s orbital radius in gold is contracted by 11 % relative to its non-relativistic value. [5] The net result is that gold forms extremely stable compounds through the overlap of tightly-contracted 6s orbitals, with the expanded 5d core much less inert than in copper or silver. A clear illustration of this effect is demonstrated by the variation in colour between bulk copper, silver and gold. The colour of the coinage metals arises from the ns←(n-1)d absorption band in the solid. The position of these bands will be largely the same as in the gas phase (see Figure 5.6 and Reference [13]). Copper appears reddish because the 4s←3d band lies in the visible region, so that solid copper reflects light at the

red end of the visible spectrum. In silver, the 5s←4d transition has shifted into the ultraviolet region, so that silver reflects all visible wavelengths, giving it a whitish hue. In gold, the dramatic relativistic stabilisation of the 6s orbital relative to 5d reduces the band gap into the visible region again, producing the visible absorption responsible for the yellow colour of gold.

The relativistic trend is also reflected in the variation in atomic ionisation potential, which drops from 7.73 eV (Cu) to 7.58 eV (Ag), but rises sharply to 9.23 eV (Au), indicating how tightly-bound is the 6s electron in gold. [13]

The preferential stabilisation of Au(6s) relative to Cu(4s) and Ag(5s) has important consequences for the bonding in Group 1b dimers involving gold atoms. Table 8.5 lists some of the spectroscopic constants of Au_2, CuAu and AgAu, as determined by experiment. The expectation that gold should be capable of forming exceptionally strong bonds is certainly borne out. The equilibrium bondlength in Au_2 is actually shorter than that in Ag_2, a remarkable testament to the extreme contraction of the Au(6s) orbital. As expected, the bond energies in the homonuclear dimers fall in the order $D_0(Ag_2) < D_0(Cu_2) < D_0(Au_2)$. (The relativistic contribution to the bond in Au_2 has been calculated to be $\simeq$ 1.0 eV. [21]) This same sequence is observed when molecular ionisation potentials or ion dissociation energies are compared. The order of bond strengths in the mixed dimers falls in the order $D_0(CuAg) < D_0(AgAu) < D_0(CuAu)$. Both mixed dimers which contain a gold atom are more deeply bound than CuAg, which lacks the stabilising effects of an Au(6s) orbital.

Bonding in the excited states of Au_2 and CuAu has been thoroughly reviewed by

Table 8.5 : Spectroscopic constants of Au-containing dimers

Dimer	r_e/Å	$10^5 k_e$/dyn cm^{-1}	$D_0(M_2)$/eV
Au_2 $X(^1\Sigma_g^+)$	2.4719	2.1179	2.29(2)
CuAu $X(^1\Sigma^+)$	2.3303	1.7528	2.36(4)
AgAu $X(^1\Sigma^+)$	-	-	2.06(10)

Dimer	$D_0(M_2^+)$/eV	IP/eV
Au_2	2.34(19)	9.18(19)
CuAu	1.36(7)	8.73(6)
AgAu	-	-

All data from Reference [5]

Morse. [5] Many of the excited states of CuAu have bondlengths within 0.02 Å of the ground state, and the $B(0_u^+)$ state has a vibrational frequency larger than the ground state. Less is known about the excited states of Au_2, but ω_e for the $A(1_u)$ state is greater than that in the $X(^1\Sigma_g^+)$ state. Such behaviour is in marked contrast to the low-lying excited states of Cu_2, CuAg and Ag_2, which without exception exhibit a marked reduction in vibrational frequency and substantial increase in bondlength compared to the ground state.

These differences are traceable to the peculiar activity of the 5d orbitals in gold, which because of their size and energetic proximity to the 6s orbital, can exert a considerable influence upon bonding. In Cu_2 and Ag_2, excitation of an essentially non-bonding d electron to form the configuration $d^{19}(s\sigma)^2(s\sigma^*)^1$, formally halves the overall bond order because of the semi-occupation of the antibonding σ^* orbital. Other excited configurations will be mixed in, but even these are incapable of reproducing the short and strong bonds observed in excited gold-containing dimers. In Au_2 and CuAu, the 5d-based molecular orbitals are much more involved in bonding, and excitation of an antibonding d electron can reduce the core-core repulsion considerably. When the electron is excited to the antibonding $s\sigma^*$ orbital, the two effects largely cancel, and the excited state acquires similar bonding properties to the ground state. This is, of course, an over-simplified view of bonding in gold-containing dimers which does not take into account admixture of other excited configurations. It does however, go a long way to explain the broad differences between excitation trends in Cu,Ag dimers and those in Au_2 and CuAu.

8.3 Critical Evaluation

The broad, unifying aim of the work presented in this thesis was to compare and contrast bonding in the copper-silver dimers using a variety of laser spectroscopies. In this, qualified success has been achieved.

Certainly, a wealth of spectroscopic information on the molecules Cu_2, CuAg and Ag_2 has been obtained to add to the rapidly-growing database on Group 1b dimers. However, as critical scrutiny of Chapter 8 reveals, no novel bonding features were discerned when CuAg was compared with its homonuclear parents. The spectroscopic properties of CuAg were largely those which were naively expected after examining Cu_2 and Ag_2. In a sense, this is hardly surprising. The electronic similarities between copper and silver are so great that it might have been more disconcerting to have found striking departures for CuAg. Deviations from established trends are only really seen in the spectroscopy of neutral and ionic gold-containing dimers, where substantial relativistic effects are known to operate.

The use of threshold ionisation spectroscopy (TIS) in bonding analysis is most suited to clusters containing at least one gold atom. Sharp differences between Au and Cu/Ag should lead to more localisation of electron density, and properties of the cluster should depart from the arithmetic mean of those of its constituents. For dimers, TIS has proved more valuable in the indirect determination of ion dissociation energies. For these species, $D_0(^+on)$ may be a more valid test of the characteristics of the valence orbitals than a determination of the ionisation potential alone. Proceeding to trimeric and higher clusters (

excited state spectroscopy permitting), multiple dissociation limits cloud the issue, and measuring the gross variation in IP may prove the more valuable approach here. Given the sheer high density of states in clusters beyond the dimer, it may prove difficult to unravel the detailed spectroscopy within a range of mixed neutral species to draw unequivocal conclusions about the bonding. TIS, combined with excited state photoelectron spectroscopy, both of which yield information on the ion, may give a clearer picture, provided that the adiabatic IP can be determined consistently using a variety of routes.

The success of much of the above hinges on the ability of theory to keep pace with experiment, and provide explanations more profound than the qualitative arguments used throughout this work. At the time of writing, *ab initio* calculations on even the Group 1b dimers lag well behind experiment Hopefully, the burgeoning of experimentation in this field, and recent developments in high-speed computing, will rectify this discrepancy soon.

The experimental community should not be content to rest on their laurels: there is a dearth of information on excited states of clusters larger than M_2, and on the ground states of cluster molecular ions. We eagerly anticipate high resolution electronic spectroscopy on the mixed Group 1b trimers, and excited-state photoelectron investigations of the known neutral dimers and trimers.

References

[1] Herzberg G., *Molecular Spectra and Molecular Structure. I : Spectra of diatomic molecules*, 2nd. edition, van Nostrand, Princeton, 1950.

[2] Morse M. D., Chem. Rev., **86**, p 1049, (1986)

[3] Clementi E., Roetti C., Atomic Data and Nucl. Data Tables, p 177, (1974)

[4] Desclaux J. P., Atomic Data and Nuclear Data Tables, **12**, p 311, (1974)

[5] Morse M. D., *Adv. Metal and Semiconductor Clusters. Vol. I : Spectry. and Dynamics*, to be published ,

[6] Lochet J., J. Phys. B, **11**, p L55, (1978)

[7] Ruamps J., C. R. Hebd. Seances Acad. Sci., **238**, p 1489, (1954)

[8] Rohlfing E. A., Valentini J. J., J. Chem. Phys., **84**, p 6560, (1986)

[9] Ackerman M., Stafford F. E., Drowart J., J. Chem. Phys., **33**, p 1784, (1960)

[10] Kleman B., Lindqvist S., Ark. Fys., **9**, p 385, (1955)

[11] Hilpert K., Gingerich K. A., Ber. Bunsenges. Phys. Chem., **84**, p 739, (1980)

[12] Hopkins J. B., Langridge-Smith P. R. R., Morse M. D., Smalley R. E., *unpublished results*, ,

[13] Moore C. E., *Atomic Energy Levels*, NBS Circular 467, Vol. III, Washington D. C., 1971.

[14] van Zee R. J., Weltner W. Jr., Chem. Phys. Lett., **162**, p 437, (1990)

[15] Sappey A. D., Harrington J. E., Weisshaar J. C., J. Chem. Phys., **91**, p 3854, (1989)

[16] Post D., Baerends E., Chem. Phys. Lett., **86**, p 176, (1982)

[17] Herrmann A., Schumacher E., Wöste L., J. Chem. Phys., **68**, p 2327, (1978)

[18] Stoll H., Fuentealba P., Dolg M., Flad J., Szentpaly L. v., Preuss H., J. Chem. Phys., **79**, p 5532, (1983)

[19] Basch H., J. Am. Chem. Soc., **103**, p 4657, (1981)

[20] Cartwright P. C., *Ph. D. thesis*, University of Edinburgh, 1989.

[21] Lee Y. S., Ermler W. C., Pitzer K. S., McLean A. D., J. Chem. Phys., **70**, p 288, (1979)

Appendix A
The $E(^3\Sigma_g^-) \leftarrow X(^3\pi_u)$ system of Al_2

The $E(^3\Sigma_g^-) \leftarrow X(^3\Pi_u)$ system of laser-vaporised, jet-cooled Al_2 has been observed using both LIF and R2PI spectroscopy. Bondybey and co-workers [1] obtained fluorescence excitation spectra of this system which showed triplet sub-bands (32 cm^{-1} spacing) corresponding to the three (Ω = 0,1,2) spin-orbit components in the ground state. Morse and co-workers [2] in a concurrent one colour R2PI investigation, found that the triplet structures collapsed to singlets when argon replaced helium as the quenching gas. The greater quenching efficiency of a heavier collision partner favours cooling into the lowest (Ω = 0) spin-orbit levels of the ground state.

We have also obtained intense 1+1 ionisation spectra of this system using the MB1 cluster rig (linear TOFMS). An Al rod was vaporised using low fluence (60 MW cm^{-2}) 532 nm radiation from the DCR-2 Nd:YAG laser, helium being used as the quenching gas. The E state lies more than half way to the ionisation limit (6.02 eV [3]), so that only one laser colour is required. 1 + 1 resonant ionisation was accomplished using the excimer-pumped dye laser system (EMG201MSC + FL3002EC) operating on the dye DMQ (346-377 nm, 360 nm peak with 8.5 % efficiency).

The resulting two photon ionisation spectrum (1 bar backing pressure) is displayed in Figure A.1. (The spectrum is not corrected for variation in laser power across the dye gain profile.) We make the intriguing observation that even when the helium pressure is reduced to 1 bar, there is still scant evidence for

Figure A.1 : One colour R2PI spectrum of the E←X system of Al_2

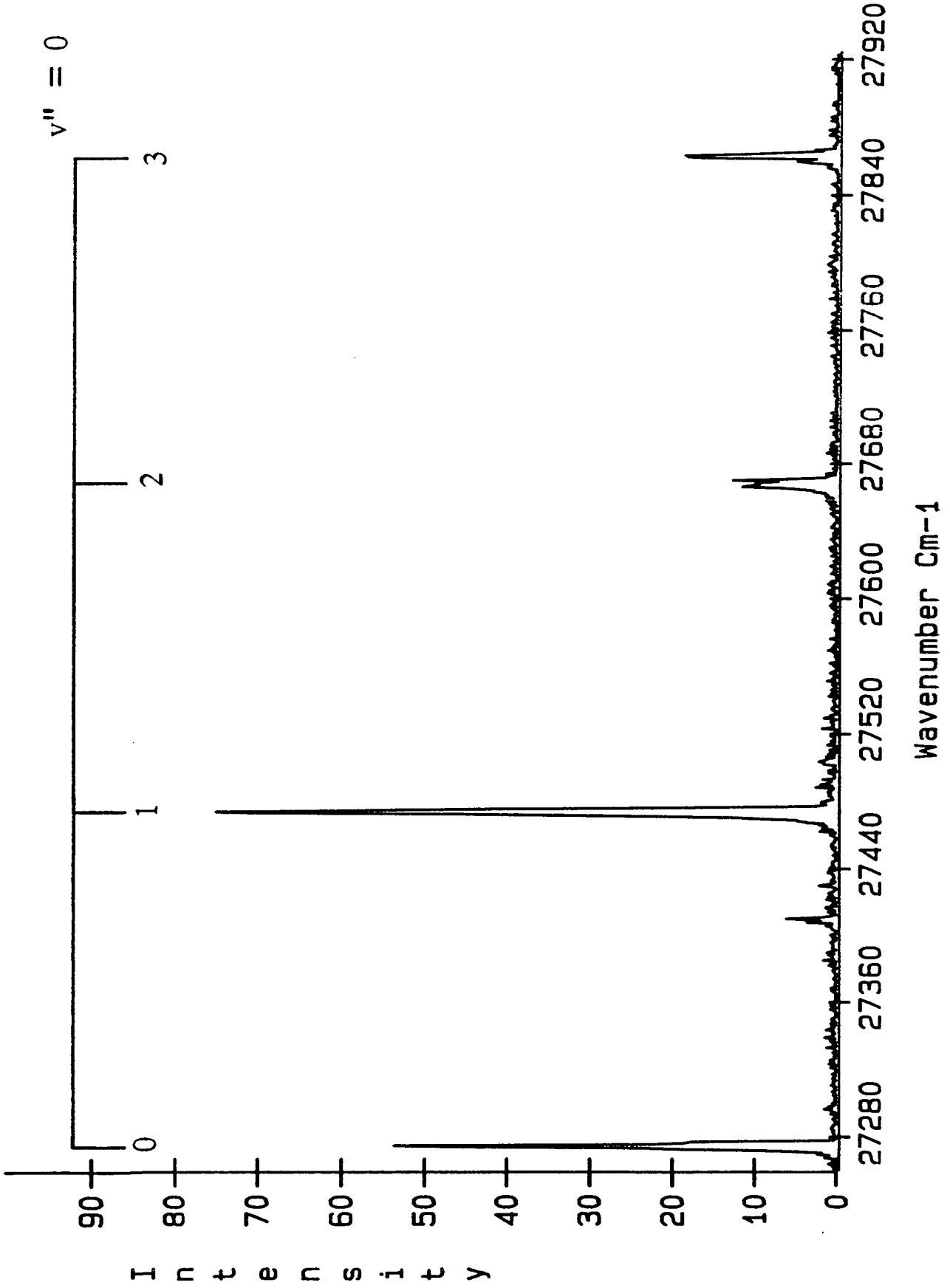

population of the $\Omega = 1$ and 2 spin-orbit states. In other words, efficient electronic quenching can occur with helium, even under very mild expansion conditions. The $\Omega = 2$ component of the (1-0) band is seen very weakly, displaced $\simeq 64$ cm^{-1} to the red of the $\Omega = 0$ component. Why only this feature appeared is not clear. Possibly a brief variation in source conditions occurred when scanning over this region.

References

[1] Cai M. F., Dzugan T. P., Bondybey V. E., Chem. Phys. Lett., **155**, p 430, (1989)

[2] Fu Zh., Lemire G. W., Bishea G. A., Morse M. D., *J. Chem. Phys.*, submitted for publication,

[3] Upton T., J. Phys. Chem., **90**, p 754, (1986)

Appendix B
Generation of electrostatic potential maps

The equilibrium electrical potential V at a point (x,y) in two dimensions is given by the solution of Laplace's equation: [1]

$$\partial^2 V/\partial x^2 + \partial^2 V/\partial y^2 = 0,$$

where V is the potential at the point with cartesian coordinates (x,y).

This equation is readily solved by a relaxation technique using fixed boundary conditions. The region of interest is subdivided into square cells by a mesh of unit length and width. Each cell vertex is assigned an initial potential. Vertices corresponding to the location of ion optical elements, and the mesh boundary, were not relaxed as the potential at these points is externally fixed. All other points were subjected to relaxation. For each relaxable point in turn, the potential is compared to that calculated from the average of its four nearest neighbours:

$$V_0(x,y) = 1/4 \, [\, V(x,y+g) + V(x,y-g) + V(x-g,y) + V(x,y-g) \,],$$

where g is the mesh length. (This equation follows from a Taylor series expansion of the potential at each point.) If the potential V(x,y) is not fully relaxed, further iterations are required. The total number of iterations required to achieve complete relaxation depends on the desired accuracy (typically 50 mV here).

For the MB1 linear extraction ion optics (Figure 4.6), the grounded copper cryoshield imposed a boundary condition. The MB2 reflectron extraction optics (Figure 4.10) lacked a cryoshield, and so the walls of the chamber formed the ground potential boundary instead.

The reflectron ion mirror and drift chamber (Figure 4.11) constituted a system with cylindrical symmetry, assuming that they were coaxial. This simplifies the problem to a system with cylindrical symmetry, requiring Laplace's equation to be recast in cylindrical coordinates:

$$\partial^2 V/\partial r^2 + 1/r.\partial V/\partial r + \partial^2 V/\partial z^2 = 0,$$

where z = the displacement along the axis, and r = the perpendicular distance from the axis. The resulting relaxation equation in cylindrical coordinates is:

$$V_0(r,z) = 1/4\,[\,(1+g/2r)V(r+g,z) + (1-g/2r)V(r-g,z) + V(r,z+g) + V(r,z-g)\,].$$

Two programs were employed to obtain the contour plots. One was written in FORTRAN 77 and implemented on the Edinburgh mainframe computer. The other was SIMION, a commercially-available package from the University of Iowa which was run on a Dell 325 PC. Although both programs gave the same results, the potential maps shown in Chapter 4 were generated using SIMION, as it executed more quickly and provided superior graphics.

References

[1] Klemperer O., *Electron Optics*, Cambridge University Press, 1953.

Appendix C
The RKR method for generating potential curves

Diatomic potential curves were generated from experimental molecular constants by the well-established Rydberg-Klein-Rees (RKR) inversion method. [1]- [3] The RKR method is based on an inversion of the first order phase integral (WKB approximation) for a particle in a one-dimensional potential. [4] Derived in this treatment are the Klein equations, which relate the turning points of the potential curve (r_{min}, r_{max}) to the experimental vibrational and rotational constants. These may be written most conveniently as:

$$f_v = c_1 \int_{vmin}^{v} (G(v) - G(v'))^{-1/2} dv'$$

$$g_v = 1/c_1 \int_{vmin}^{v} B(v)(G(v) - G(v'))^{-1/2} dv'$$

$$f_v = (r_{max} + r_{min})/2,$$

$$g_v = (1/r_{max} + 1/r_{min})$$

where c_1 is a constant depending on the reduced masses, and G(v) and B(v) are the conventional term value expressions for vibrational and rotational energy. A program which was developed by J. Telllinghuisen of Vanderbilt University was used to perform a numerical integration of these equations to obtain the turning points as a function of energy. The integrals are evaluated using a Gaussian quadrature which avoids estimating the intregrand at the limit G(v) = G(v'), where a singularity occurs. [5]

RKR potential curves tend to misbehave near dissociation if the vibration-rotation coupling constants have been imprecisely determined. The accuracy of the method is highly sensitive to changes in the data set of molecular constants employed, as has been pointed out by Tellinghuisen. [6] RKR-synthesised curves were required here for graphical depiction, or as input in Franck Condon factor calculations. In the former case, curves were rarely plotted up to the dissociation limit as the experimental constants had been determined only over a limited range. In the latter case, the transitions of interest involved low-lying vibrational levels, where the effects of imperfections in the data are least severe.

References

[1] Rydberg R., Z. Physik, **73**, p 376, (1931)
[2] Klein O., Z. Physik, **76**, p 226, (1932)
[3] Rees A. L. G., Proc. Phys. Soc., **59**, p 998, (1947)
[4] Kemble E. C., *Fundamental Principles of Quantum Mechanics*, McGraw-Hill, New York, 1937.
[5] Tellinghuisen J., J. Mol. Spectry., **44**, p 194, (1972)
[6] Tellinghuisen J., J. Mol. Spectry., **141**, p 258, (1990)

Appendix D
Calculation of Franck Condon factors

For a vibronic transition in absorption, the intensity is proportional to the square of the transition moment $\mathbf{R}_{ev}$, and is independent of the transition frequency: [1]

$$I_{abs} \alpha \mathbf{R}_{ev}^2.$$

In emission the expression is modified by a ν^3 term which arises because of the frequency dependence of the Einstein A coefficient:

$$I_{em} \alpha \nu^3 . \mathbf{R}_{ev}^2.$$

Explicitly, the Einstein A coefficient for a vibronic transition is given by: [2]

$$A = (64\Pi^4\nu^3/3hc^3)\mathbf{R}_{ev}^2.$$

The transition moment may be written as a product of the electronic transition moment $\mathbf{R}_e$ and the vibrational overlap integral $S_{v', v''}$: [3]

$$\mathbf{R}_{ev} = \mathbf{R}_e . S_{v', v''}$$

Explicitly, denoting electronic and vibrational wavefunctions by Ψ_e and Ψ_v respectively, the two terms in the expression for $\mathbf{R}_{ev}$ are:

$$\mathbf{R}_e = \int \Psi_e'^* \mu_e \Psi_e'' d\tau_e$$

where μ_e is the electric dipole moment operator,

$$S_{v',v''} = \int \Psi'_v \Psi''_v dr$$

R_e is almost independent of r over the limited range of non-zero overlap. Thus variations in the vibronic band intensities may be followed by evaluating $(S_{v',v''})^2$, the so-called Franck Condon factor (FCF). The vibrational overlap integral is simply a measure of the extent to which the vibrational wavefunctions of the two vibronic levels overlap one another. The calculated values of $(S_{v',v''})^2$ represent the probability of transitions between the levels v'' and v' when appropriate normalisation factors are included.

FCFs were calculated using a suite of programs written by K. P. Lawley. Potential energy surfaces for the two states involved in the transition are first generated using the RKR procedure described above. The vibrational eigenvalues and eigenfunctions are then calculated using the Numerov-Cooley method to solve the Schrödinger wave equation with the RKR potential as input. [4] [5] FCFs for particular vibronic transitions are evaluated by a numerical integration of the product of the relevant wavefunctions using Simpson's rule. [6] Further details of the method may be obtained from reference [7].

The original program was designed to simulate single vibronic level fluorescence to a range of lower state levels. When investigating progressions in absorption originating from a single lower state level, it was necessary to invert the order of the two states. Also, when simulating fluorescence, the program multiplied the calculated $(S_{v',v''})^2$ terms by the fourth power of the transition frequency to account for the ν^3 dependence of the Einstein A coefficient and the frequency dependence of the photodetector response. All calculations here concerned

photon absorption, the Einstein B coefficient for stimulated absorption being independent of frequency. [1] Furthermore, the signal intensity in photoionisation is independent of photon energy. Thus the ν^4 term was redundant, and the pure Franck Condon factors alone are used in any discussion of transition intensities.

References

[1] Herzberg G., *Molecular Spectra and Molecular Structure I: Spectra of diatomic molecules*, 2nd. edition, van Nostrand, Princeton, 1950.

[2] Lawley K. P., Jewsbury, Chem. Phys., **141**, p 225, (1989)

[3] Hollas J. M., *High Resolution Spectroscopy*, Butterworths, 1982.

[4] Numerov B., Publ. Observatoire Central Astrophys. Russ., **2**, p 188, (1933)

[5] Cooley J. W., Math. Computation, **15**, p 363, (1961)

[6] Kreysig E., *Advanced Engineering Mathematics*, 5th. edition, John Wiley, New York, 1983.

[7] Austin D. I., *Ph. D. thesis*, Edinburgh University, 1988.

Appendix E
Nuclear spin statistics

Rotation of a symmetrical linear molecule leads to an interchange of pairs of identical particles, such as the nuclei in a homonuclear diatomic. Constraints are imposed on overall symmetry of the molecular wavefunction by the Pauli Principle. [1] This states that the total wavefunction, inclusive of spin, must be antisymmetric with respect to the exchange of any pair of identical fermions (electrons or half-integral spin nuclei). The opposite principle holds for the exchange of identical bosons, with the overall wavefunction remaining symmetric. The Pauli Principle has important consequences for the distribution of rotational state populations in homonuclear diatomic molecules such as disilver.

Both isotopes of silver ^{107}Ag and ^{109}Ag, are fermions with nuclear spin of 1/2. Fermi-Dirac statistics are obeyed upon the interchange of identical nuclei in the homonuclear species $^{107}Ag_2$ and $^{109}Ag_2$. Exchange of the nuclear particles may be accomplished by applying a 180° (C_2) rotation to the whole molecule, which also rotates the electronic, vibrational, rotational and nuclear spin wavefunctions. Individual symmetry operations must be applied to the various wavefunctions to nullify the effects of the C_2 rotation, so that the overall operation reduces to a nuclear particle exchange or "relabelling".

The overall wavefunction for the molecule may be written as a product of constituent wavefunctions within the Born-Oppenheimer approximation as:

$$\Psi^{tot} = \psi^{el}\psi^{vib}\psi^{rot}\psi^{nuc}.$$

The effect of a 180° rotation on each component function is now investigated. The rotational wavefunction changes sign by $(-1)^J$ upon rotation, where J is the rotational quantum number. This operation must be applied to restore the original symmetry of the wavefunction. The original positions of the electrons may be regained by applying the operations $\sigma_{el} i_{el}$ (an inversion through the centre of mass followed by a reflection in the nuclear plane) successively to ψ^{el}. The vibrational wavefunction is unaltered upon rotation.

For fermion interchange, the effect of the "label exchange" operator on Ψ^{tot} can be described thus:

$$\mathbf{P}_e \Psi^{tot} = -\Psi^{tot}.$$

In terms of the component wavefunctions this becomes:

$$(\sigma_{el} i_{el} \psi^{el})(\psi^{vib})((-1)^J \psi^{rot})(p^{nuc} \psi^{nuc}) = -\Psi^{tot}$$

where p^{nuc} is the operator which exchanges the spin states of the nuclei. Since the ground state of silver dimer is $^1\Sigma_g^+$ the effect on the electronic wavefunction is simply $\sigma_{el} i_{el} \psi^{el} = \psi^{el}$. Hence we obtain the following simplified expression:

$$\mathbf{P}_e \Psi^{tot} = (-1)^J \psi^{rot} p^{nuc} \psi^{nuc} \psi^{vib} \psi^{el} = -\Psi^{tot}.$$

Clearly the numbering of the rotational levels (J) and their associated symmetry is intimately linked to the symmetry of the nuclear spin wavefunction ψ^{nuc}. To conform with the above equations, the effect of the operator p^{nuc} must be:

$p^{nuc}\psi^{nuc} = \psi^{nuc}$, when J is odd,

$p^{nuc}\psi^{nuc} = -\psi^{nuc}$, when J is even.

This immediately establishes that the nuclear spin wavefunctions are symmetric when J is odd, and antisymmetric when J is even. For spin 1/2 nuclei, two spin states may be formed: $m_I = 1/2$ (labelled α) and $m_I = -1/2$ (labelled β). Of the molecular spin wavefunctions which can be created from these, three are symmetric with respect to exchange ($\alpha\alpha$, $\beta\beta$ and $\alpha\beta+\beta\alpha$), and one is antisymmetric ($\alpha\beta-\beta\alpha$). Hence there are three times as many molecules in odd rotational states (even nuclear spin states) than in even ones. This readily explains the marked alternation in rotational line intensities observed for the homonuclear silver dimers $^{107}Ag_2$ and $^{109}Ag_2$.

References

[1] Atkins P. W., *Molecular Quantum Mechanics*, 2nd. edition, Oxford University Press, Oxford, 1983.

Appendix F
Courses and Conferences Attended

In accordance with the regulations of the Department of Chemistry, University of Edinburgh I have attended the following courses during my period of study:

1. Scientific German
2. FORTRAN 77 programming
3. 'C' programming
4. Laser Physics
5. Theoretical Chemistry
6. Mass Spectrometry
7. Signal Processing
8. Recent Advances in Physical Chemistry 1988
9. Recent Advances in Physical Chemistry 1989
10. Reaction Dynamics

In addition I have attended all Laser Chemistry research group meetings, departmental seminars, joint Edinburgh - Heriot-Watt laser chemistry group meetings, and the following conferences:

1. Symposium on Supersonic Jet Spectroscopy, The Royal Institution, London, December 1986
2. XI th. International Symposium on Molecular Beams, Edinburgh, July 1987.
3. Gordon Conference on Metal and Semiconductor Clusters, Holderness School, New Hampshire, USA, August 1987
4. Faraday Discussion No. 86, "Spectroscopy at low temperatures', Exeter, September 1988
5. Faraday Division, High Resolution Spectroscopy Group meeting, Birmingham, December 1988
6. Faraday Division, High Resolution Spectroscopy Group meeting, Nottingham, December 1989